Liquid Phase Dehydration of 1-Butanol to Di-n-butyl ether Experimental Performance, Modeling and Simulation of Ion Exchange Resins as Catalysts

María Ángeles Pérez-Maciá

Liquid Phase Dehydration of 1-Butanol to Di-n-butyl ether

Experimental Performance, Modeling and Simulation of Ion Exchange Resins as Catalysts

María Ángeles Pérez-Maciá

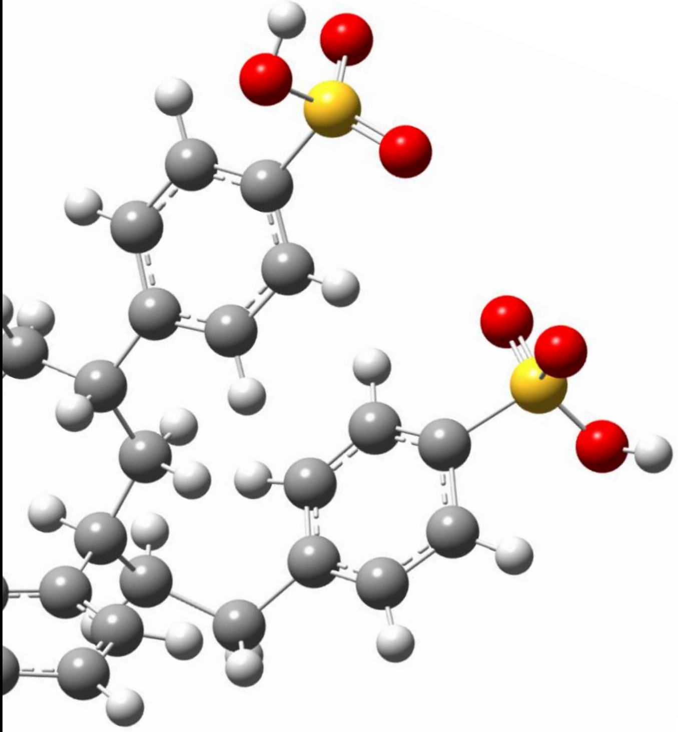

Universitat de Barcelona

Facultad de Química

Departamento de Ingeniería Química

LIQUID PHASE DEHYDRATION OF 1-BUTANOL TO DI-N-BUTYL ETHER.

EXPERIMENTAL PERFORMANCE, MODELING AND SIMULATION OF ION-EXCHANGE RESINS AS CATALYSTS.

Tesis Doctoral

María de los Ángeles Pérez Maciá

Dirigida por

Dra. Montserrat Iborra y Dr. Roger Bringué

Barcelona, 15 de septiembre de 2015

Programa de doctorado de *Ingeniería y Tecnologías Avanzadas*

La Dra. **MONTSERRAT IBORRA URIOS**, profesora titular del Departamento de Ingeniería Química de la Universidad de Barcelona y el Dr. **ROGER BRINGUÉ TOMÀS**, profesor lector del mismo departamento,

CERTIFICAN QUE:

El trabajo de investigación titulado “***LIQUID PHASE DEHYDRATION OF 1-BUTANOL TO DI-N-BUTYL ETHER. EXPERIMENTAL PERFORMANCE, MODELING AND SIMULATION OF ION-EXCHANGE RESINS AS CATALYSTS.***” constituye la memoria que presenta la Ingeniera Química María de los Ángeles Pérez Maciá para aspirar al grado de Doctor por la Universidad de Barcelona. Esta tesis doctoral se ha llevado a cabo dentro del programa de Doctorado “Ingeniería y Tecnologías Avanzadas” en el Departamento de Ingeniería Química de la Universidad de Barcelona.

Y para que así conste a los efectos oportunos, firman el presente certificado en Barcelona, 15 de septiembre de 2015.

Dra. Montserrat Iborra y Dr. Roger Bringué

Directores de la tesis doctoral

FOREWORD

The objectives of the present thesis can be summarized in two main subjects which are clearly represented in the title of this thesis: *Liquid phase dehydration of 1-butanol to di-n-butyl ether*. *Experimental performance, modeling and simulation of ion exchange resins as catalysts*.

In Chapters 1 and 2 the context of this thesis is defined and the materials and methods utilized in the subsequent chapters are introduced.

The next three chapters deal with the first main objective of this thesis, *Study of the liquid phase dehydration of 1-butanol to di-n-butyl ether over ion exchange resins*. The performance of poly(styrene-divinylbenzene), P(S-DVB), ion exchange resins in the synthesis of di-n-butyl ether from the dehydration of 1-butanol in liquid phase is addressed in Chapter 3. This chapter also discusses the influence of typical 1-butanol impurities (isobutanol or ethanol and acetone, depending on the production route) on the dehydration process. Chapter 4 is devoted to the thermodynamic equilibrium of 1-butanol dehydration. The experimental values of the equilibrium constants for the dehydration of 1-butanol to di-n-butyl ether and for potential side reactions determined by direct measurement of the composition of the liquid mixture at equilibrium are presented. Chapter 5 is dedicated to the chemical kinetics of the dehydration of 1-butanol to di-n-butyl ether over Amberlyst 70, shedding some light on the mechanism of di-n-butyl ether formation. Furthermore, the inhibitory effect of water is investigated.

The second general objective of this thesis, *Modeling and simulation of ion exchange resin*, has been developed in Chapters 6 and 7. Chapter 6 addresses the construction of a realistic model for P(S-DVB) networks. Furthermore, the relationship between the topology of highly crosslinked P(S-DVB) ion-exchange resins and their properties, especially the structural ones is studied by means of molecular dynamics simulations. Chapter 7 deals with the swelling of ion exchange resins in 1-butanol also by means of molecular dynamics simulations.

In Chapter 8 a concise summary of the results of this thesis is presented together with suggestions for future work.

Finally, at the end of this thesis an extended summary in Spanish can be found.

OBJECTIVES

(1) Check that sulfonic poly(styrene-divinylbenzene), P(S-DVB), ion exchange resins are suitable catalysts for the dehydration of 1-butanol to di-n-butyl ether, DNBE, in the liquid phase.

(2) Evaluate the influence of the morphological characteristics of P(S-DVB) resins on the synthesis of DNBE and, based on these results, select the most appropriate resin for industrial use.

(3) Study the influence that typical 1-butanol impurities have on the dehydration of 1-butanol.

(4) Evaluate the equilibrium constant of the dehydration reaction of 1-butanol to DNBE and main side reactions.

(5) Perform a kinetic study of the dehydration of 1-butanol to DNBE over the thermostable ion exchange resin Amberlyst 70 and propose a kinetic equation with mechanistical base.

(6) Develop a realistic atomistic model for the crosslinked network of P(S-DVB) ion exchange resins. The model must represent the heterogeneity of the macromolecular multi-chain networks.

(7) Study the influence of the polymer topology on the microscopic properties of the resin using molecular dynamic simulations.

(8) Study the swelling of ion-exchange resins in 1-butanol by means of molecular dynamics simulations.

TABLE OF CONTENTS

1. INTRODUCTION

1.1. Oil based economy

In the course of a century, technologies based on oil as a unique, easily handled fuel have shaped the world. Petroleum oil was recognized to be an essential source for illuminating oil in the 1860s followed by its use for heating and other applications including, eventually, electricity generation. It became essential for the production of transportation fuels after the introduction of internal combustion engines for cars and other vehicles, followed by planes and other means of transportation. Nowadays, oil remains the world's leading fuel supplying the 32.4% of the world primary energy consumption[1] and its use as a raw material for petrochemical and chemical products has also gained great significance.

The demand for oil continues to expand owing to a growing population and an increase in standard of living (see Figure 1.1). However, oil reserves are limited and the majority of the world's conventional oil reserves are located in the Middle East and other politically sensitive regions settings the trend for great uncertainty. The notion that the world is nearing a peak in oil supplies is a subject of great current interest and debate and, although there is much uncertainty over when oil production will peak as supplies are depleted, no one disagrees that the threat is real.

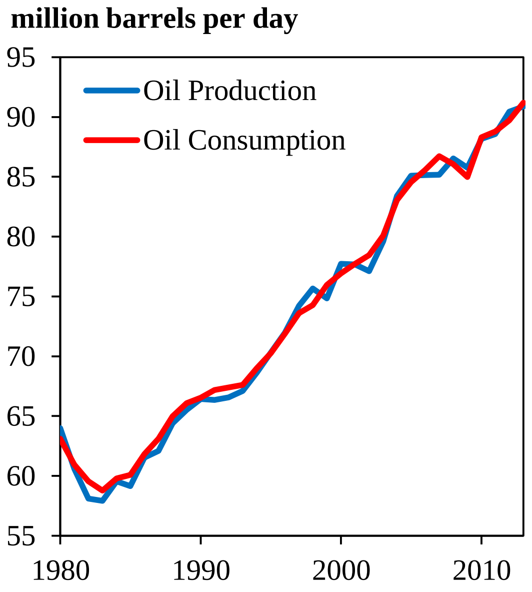

Source: U.S. Energy Information Administration. International Energy Statistics, April 2015.[2]

Figure 1.1. Total oil supply and total petroleum consumption 1980-2013.

Besides concerns about oil reserves limitation and the reliance on foreign resources, awareness of the importance of environmental issues (exhaust emissions, oil splits, climate change, etc.) has become more and more central to the thinking of the oil industry and regulators in the last decades. As a result, the European Union introduces increasingly stringent specifications for:

- Quality of petrol, diesel and gas-oil (Directive 2009/30/EC).
- Emissions from light passenger and commercial vehicles (Regulation EC 715/2007).
- Promotion of the use of energy from renewable sources, setting a mandatory 10% minimum target to be achieved by all Member States for the share of biofuels in transport petrol and diesel consumption by 2020 (Directive 2009/28/EC).

Although very efficient, diesel engines have had difficulties achieving desirable emission targets, especially for soot and NO_x formation.[3] Reformulation of diesel fuel to include oxygenates has proven to be an effective way to provide satisfactory engine power and cleaner exhaust without modification of existing diesel engines.[4-7]

1.2. Reformulation of diesel fuel

A number of different oxygenates have been considered as components for diesel fuel. These oxygenates include various alcohols, ethers and esters. Alcohols have several drawbacks: high water solubility, which can cause phase separation problems; high Reid vapor pressure (RVP), which may lead to the plugging of the fuel flow by increasing the vapor pressure; high volatility, which increases the volatile organic compounds emissions; high latent heat of vaporization, which raises cold start-up and drivability issues; and low heating value.[8] Vegetable oil methyl esters have a number of properties not typical of diesel fuels such as higher boiling point, viscosity, and surface tension that may contribute to increase the NO_x emissions.[9] On the contrary, ethers, especially linear monoethers, show good conditions to be added to diesel given its high cetane number, cold flow properties and mixture stability.[10] Linear ethers are also known to be effective additives to reduce diesel exhaust such as CO, particulate matter and unburned hydrocarbons and to substantially improve the trade-off between particulate and NO_x due to the presence of oxygen in the ether molecules.[11] Recently, di-n-butyl ether (DNBE) has been identified as an important candidate biofuel which can be produced from lignocellulosic biomass.[12,13]

1.3. Di-n-butyl ether (DNBE)

DNBE presents excellent properties to be blended with diesel fuel (see Table 1.1).[14] It has a particularly high cetane number (CN) indicating short ignition delay times which at the end translates into a relatively longer combustion process and thus less unburned hydrocarbons; its moderate boiling point allows facile vaporization of the fuel after injection while minimizing the volatile organic compounds emissions during transportation, storage and refueling; and its volumetric energy content is comparable to that of petroleum fuels providing satisfactory engine power in un-modified diesel engines. Besides, DNBE can be produced from lignocellulosic biomass such as residues from agriculture, energy crops and forest refuse. This residual biomass is produced in abundance and worldwide and it has no direct competition with food, thus being an attractive, inexpensive, renewable resource for the production of next generation biofuels.

Table 1.1. Properties of DNBE and diesel.

	Commercial Diesel	**DNBE**
Cetane Number	48-51	91-100
Boiling point [ºC]	170-380	144
Density [kg/m^3]	850	764
CP[a] [ºC]	-2	-13
CFPP[b] [ºC]	-15	-20
Flash point [ºC]	67	25

[a] CP (Cloud point): temperature where components form crystals and become visible forming a hazy or cloudy suspension.

[b] CFPP (Cold filter plugging point): lowest temperature at which a given volume of fuel passes through a standardized filtration device.

1.3.1. DNBE synthesis route

Linear symmetrical ethers can be produced by bimolecular dehydration of primary alcohols over acid catalysts.[15,16] Consequently, DNBE can be produced through the bimolecular dehydration of 1-butanol.

1.3.1.1. 1-butanol synthesis

1-butanol can be synthesized following biological or petrochemical routes:

Biological routes

Biobutanol can be produced from biomass by either fermentation or thermochemical routes, as it can be seen in Figure 1.2. Currently, biobutanol is being produced on industrial scale by the ABE fermentation process in which biomass fermentation by microorganisms of the genus Clostridium gives place to 1-butanol along with acetone and ethanol.[17,18]

Biobutanol can also be produced from biomass by condensation of bioethanol and/or biomethanol (Guerbet Catalysis).[19] Figure 1.2 shows that this route is still a developing technology which is not yet commercialized.[20] However, the company Abengoa developed and patented a catalyst that enables the manufacture of biobutanol competitively and, in November 2013, announced its plans to start commercial-scale production of butanol in 2015.[17]

The thermochemical routes for biobutanol production go through biomass gasification followed by syngas catalysis.

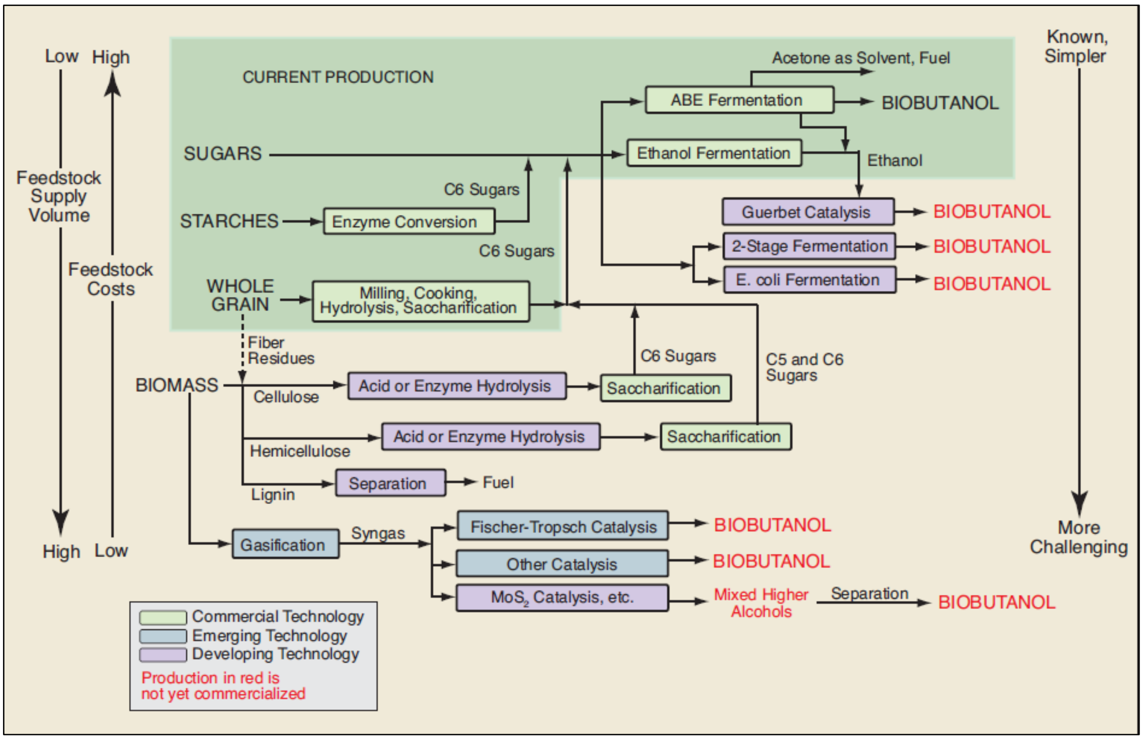

Figure 1.2. 1-Butanol biological synthesis routes (source: Carcone, 2009[20]).

Petrochemical route

Nowadays, the most important petrochemical route on industrial scale for the synthesis of 1-butanol is based on the Oxo process which consists of selective hydroformylation and hydrogenation of linear olefins from fluid catalytic cracking in the presence of Rh and Co phosphines.[21]

The reaction (see Figure 1.3) involves the addition of CO and hydrogen to the terminal double bond of propylene to yield n-butyraldehyde and iso-butyraldehyde. Subsequently, aldehydes are hydrogenated to yield 1-butanol. With this hydrogenation step 1-butanol is obtained together with 2-methyl-1-propanol (isobutanol) as byproduct.

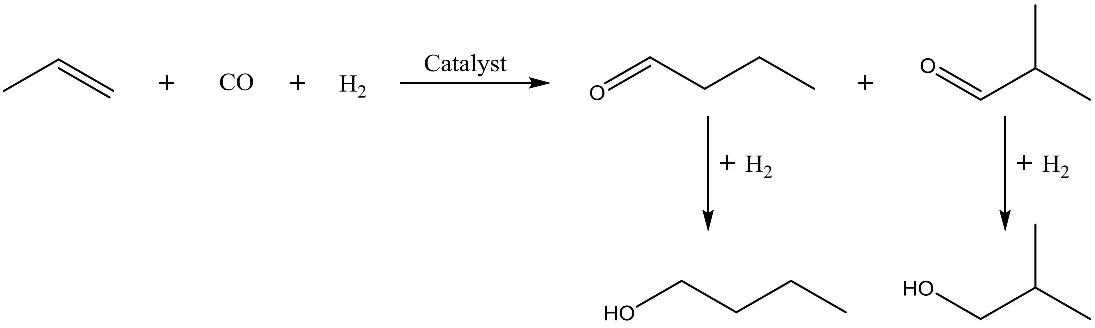

Figure 1.3. 1-Butanol petrochemical synthesis route.

1.3.1.2. Dehydration of 1-butanol to DNBE

As it was previously mentioned, di-n-butyl ether can be synthesized through the bimolecular dehydration of 1-butanol over an acid catalyst. So far, the dehydration of alcohols has been industrially catalyzed by sulfuric acid.[22] However, environmental concerns associated with safe handling and disposal of corrosive wastes (derived from product recuperation) have encouraged the development of safer and non-waste producing alternatives for applications in catalysis. There is also a strong economic driver to use a solid catalyst instead of a liquid. The advantages of a solid include reduced equipment corrosion; ease of product separation; less potential contamination in waste streams; and recycle of the catalyst. Using a solid may also increase the number of processing options such as a gas flow reactor and a fixed bed. The selectivity may also be improved in going to a solid acid catalyst. There are some examples available in the bibliography (Table 1.2) of the utilization of heterogeneous catalyst for the dehydration of 1-butanol.

Table 1.2. Published works on 1-butanol heterogeneous catalytic dehydration.

Catalyst	Operation conditions / Catalyst activity	Reference
$AlPO_4$	T = 300 ºC; P =1 atm; gas phase At high conversions the major products are butenes.	23
Zeolite H-ZSM-5	T = 105 – 185 ºC; P = 1 atm; gas phase Selectivity to ether decreases remarkably with increasing conversion.	24
Amorphous aluminosilicate	T = 105 – 185 ºC; P = 1 atm; gas phase Major products: butenes.	24
η alumina	T = 250 – 350 ºC; P = 0 – 4 MPa; gas phase Selectivity is highly dependent on conversion decreasing as 1-butanol conversion increases.	25
Niobium silicate	T = 150 – 300 ºC; P = 1 atm; gas phase High selectivity to butenes.	26
Heteropolyacids	T = 200 ºC; P = 30 bars; liquid phase Selectivity to DNBE higher than 80% 1-butanol conversions ranging from 30 to 80%	27, 28

As it can be seen in Table 1.2, all the works found in the bibliography regarding the catalytic dehydration of 1-butanol report high selectivity to butenes (except works carried out in liquid phase over heteropolyacids[27,28]). On the other hand, over the last years several works have demonstrated that acidic ion exchange resins are highly selective catalysts (97-99%) to produce linear symmetrical ethers from n-alcohols, avoiding byproducts as olefins.[29-32] However, to the best of our knowledge, the synthesis of di-n-butyl ether has not been reported on ion exchangers. Thus, one of the aims of this work is to study the liquid-phase dehydration of 1-butanol to DNBE over ion exchange resins.

1.4. Ion exchange resins as catalysts

Conventional ion exchange resins consist of a cross-linked polymer matrix with a relatively uniform distribution of ion-active sites (functional groups) throughout the polymeric structure. The polymeric matrix consists in hydrocarbon chains bonded together forming a three-dimensional hydrophobic structure, while functional groups are of hydrophilic nature. This structure makes ion exchange resins insoluble in solvents that do not break the carbon-carbon bonds of the matrix. Most ion exchange resins are based on cross-linked poly(styrene-divinylbenzene) copolymers, P(S-DVB) (Figure 1.4 shows a schematic representation of P(S-DVB) resins). Other ion exchanging materials include Nafion (a perfluorinated polymer containing sulfonic acid heads) and acrylic based resins.

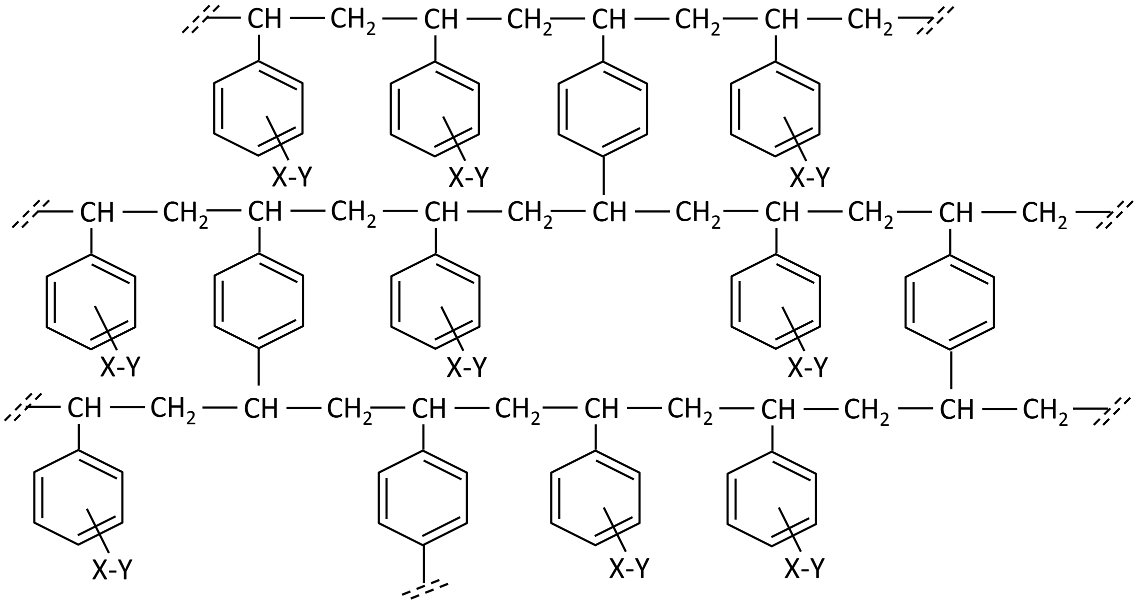

Figure 1.4. Schematic representation of the P(S-DVB) matrix. X-Y represents a functional group. Most common functional groups are SO_3^--H^+, CO_2^--Na^+, NR_3^+-Cl^-, NH_3^+-OH^-

All the experiments included in the present thesis were performed using P(S-DVB) resins functionalized with sulfonic acid groups.

Acidic styrene divinylbenzene resins

P(S-DVB) resins are commercially prepared in spherical (bead) form. A major large-scale industrial methodology for the production of P(S-DVB) resin beads is based on the suspension polymerization technique.[33] Typically, a styrene and DVB liquid mixture is dispersed as spherical liquid droplets (the dispersed or non-continuous phase) in an excess of an immiscible water phase (the continuous phase). The styrene–DVB mixture also contains a source of free radicals (the polymerization initiator) and the aqueous phase generally contains a low level of some dissolved 'suspension stabilizer' (a surface active species, often a water-soluble polymer) which helps to maintain the organic monomer droplets separate from each other.

After polymerization, the P(S-DVB) beads are functionalized to yield the finished resin. The aromatic rings of both monomers can react with several reagents, mainly the electrophilic ones, and at least one active group can be introduced in each aromatic ring, giving rise to resins with high exchange capacities.[34]

Based on their structure (which is determined principally by the conditions of polymerization of the backbone polymer), P(S-DVB) resins can be classified into two main groups:

Gel-type resins

When the co-monomer mixture in a polymerization suspension consists only of styrene and DVB (plus the polymerization initiator), the product generally results in hard glassy transparent resin beads. The percentage of DVB can be varied in principle from 0–100% but for most resin applications the range 0.5–8% is more usual. Gel type resins are composed of an amorphous crosslinked infinite network of interpenetrating polymer chains without permanent porosity and with very low surface area in the dry state (< 1 m^2/g). The diffusion of even small molecules through this polymeric glass is very slow. These materials will, however, swell in a 'good' solvent (i.e. a solvent with a solubility parameter similar to that of the polymer), with the percentage swelling typically being inversely related to the DVB content or nominal crosslinking ratio. Swelling creates space or 'solvent porosity' within the resin and allows ready access by small molecules to the polymer network.

Macroreticular resins

When the co-monomer mixture of styrene and DVB also contains an appropriate organic solvent (diluent or porogen) at some appropriate level then the internal structure (morphology) of the product resin beads can be very different to that of a gel-type resin. In particular, removal of the solvent or porogen at the end of the polymerization leads to rather heterogeneous or non-uniform polymeric matrices. In each macroreticular resin bead a well developed system of microgel particles or microspheres can be detected. These are of approximate spherical symmetry since this represents the form of lowest surface energy. Thus, macroporous resin beads (~ 50–500 μm diameter) are composed of a mass of microgel particles (typically ~ 1000 Å in diameter) and the molecular structure of an individual microgel particle is very similar to that of a whole gel-type resin bead. Therefore, to a good approximation, a macroporous resin particle can be regarded as comprised of a mass of tiny gel-type particles between which is a complex pore structure or labyrinth of channels (Figure 1.5). Thus, unlike gel-type resins, these materials possess a permanent network of pores (whose dimensions can be manipulated by the precise conditions used in polymerization) and a much higher surface area in the dry state, up to 100 m^2/g.

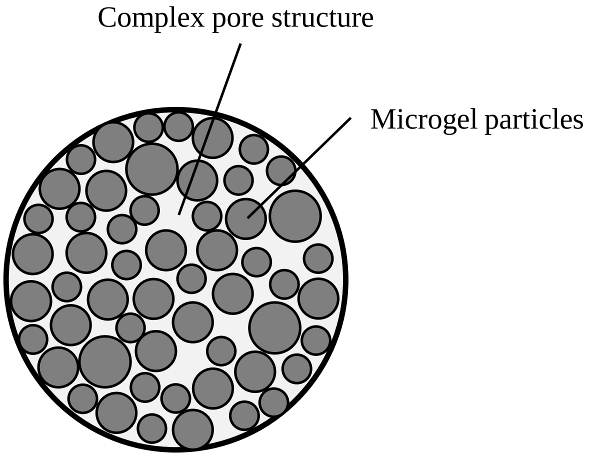

Figure 1.5. Schematic representation of a macroporous resin bead showing individual microgel particles.[33]

Provided that the surface of the pores is wetted with a compatible solvent, the pore structure of macroreticular resins can be accessed by essentially all solvents whether categorized as ‘good’ or ‘bad’. When a ‘good’ solvent is contacted with a macroporous resin then, as well as filling the pore volume, the solvent may also swell the polymer matrix to some extent (i.e. the microgel particles described above) creating new spaces.

Conventional porosimetric methods as mercury intrusion or nitrogen adsorption (in which samples must be completely dry) can not provide a complete description of the polymeric structure of ion exchange resins in the reaction medium. However, a useful description of the nature and characteristics of the spaces created as a consequence of resin swelling can be obtained from Inverse Steric Exclusion Chromatography (ISEC) data.[35-39]

1.5. Role of computational chemistry in the understanding of materials properties

The catalytic performance of ion exchange catalysts depends critically on both the nano-environment surrounding the active centers and their accessibility. Accessibility to the active centers in these materials depends greatly on the polymeric structure and is dramatically affected by the extent of swelling of the polymer mass in contact with the reaction medium. Because of the difficulty in experimentally determining the structure of the polymeric resins and the swollen-state morphology, exploitation of ion-exchange catalysts is still based on a trial and error approach rather than on a solid understanding and design of their parameters. To fully exploit the potential of ion exchange resins as catalyst, it is crucial to understand, describe and predict their behavior in the reaction medium. Employment of experimental techniques to get structural information of ion exchange resins is a complex task; therefore, computational chemistry and molecular modeling currently represent a useful way to investigate the properties and the behavior of these materials.

> *Computational chemistry* can be roughly defined as a set of theoretical methodologies (ranging from quantum mechanics of molecules to dynamics of large complex molecular aggregates) for investigating chemical problems on a computer. Thus progresses in computational chemistry have befallen closely with the headways in computer science. Over the past decade, computational power has increased by a factor of a million due to advances in hardware and software. This rate of improvement, which shows no sign of abating, has enabled the development of computer simulations and models of unprecedented fidelity.
>
> *Molecular modeling* designates the general process of describing complex chemical systems in terms of a realistic atomic model, with the goal being to understand and predict macroscopic properties based on detailed knowledge on an atomic scale.

State-of the-art computational tools allow scientists to calculate from first principles the interactions that dominate microstructural behavior and this microstructure controls a wide range of important properties, including swelling, strength, fatigue, high-temperatures performance, corrosion, radiation resistance. The amount of examples available in the bibliography of the utilization of computational chemistry to study the structural and dynamic properties of polymer networks is really vast.[40-49] However, in spite of this extensive literature, the relationship between the topology of highly crosslinked ion-exchange P(S-DVB) resins and their properties, especially the structural ones, remains unknown. In this thesis, computational chemistry techniques were used to get insight of the microscopic structure of P(S-DVB) ion exchange resins and to study the interaction resin/1-butanol.

The integration of theory, simulation, and experimentation will enhance ion exchange resins understanding and innovation.

Nomenclature

Abbreviations

ABE	Acetone-Butanol-Ethanol
CFPP	Cold filter plugging point
CP	Cloud point
CN	Cetane number
DNBE	Di-n-butyl ether
DVB	Divinylbenzene
ISEC	Inverse Steric Exclusion Chromatography
P(S-DVB)	Poly (styrene-divinylbenzene)
RVP	Reid vapor pressure

References

[1] BP Statistical review of world energy June 2014, 63rd edition. http://www.bp.com/statisticalreview (accessed April 2015).

[2] U.S. Energy information administration. International energy statistics. http://www.eia.gov/ (accessed April 2015).

[3] Ott, L. S.; Smith, B. L.; Bruno, T. J. Composition-explicit distillation curves of mixtures of diesel fuel with biomass-derived glycol ester oxygenates: A fuel design tool for decreased particulate emissions. *Energy Fuels* **2008**, *22*, 2518 - 2526.

[4] Nabi, M. N.; Kannan, D.; Hustad, J. E.; Rahman, M. M. Role of oxygenated fuel to reduce diesel emissions: A Review. *Proceedings of the International Conference on Mechanical Engineering*, Dhaka, Bangladesh, December 26-28, 2009.

[5] Golubkov, A. Motor fuel for diesel engines. Patent WO 2001018154 A1, March 15, 2001.

[6] Alander, T. J. A.; Leskinen, A. P.; Raunemaa, T. M.; Rantanen, L. Characterization of diesel particles: effects of fuel reformulation, exhaust aftertreatment, and engine operation on particle carbon composition and volatility. *Environ. Sci. Technol*. **2004**, *38*, 2707 -2714.

[7] Arteconi, A.; Mazzarini, A.; Di Nicola, G. Emissions from ethers and organic carbonate fuel additives: A Review. *Water, Air, Soil Pollut*. **2011**, *221*, 405 - 423.

[8] Sezer, I.; Bilgin, A. Effects of methyl tert-butyl ether addition to base gasoline on the performance and CO emissions of a spark ignition engine. *Energy Fuels* **2008**, *22*, 1341 - 1348.

[9] McCormick, R. L.; Ross, J. D.; Graboski, M. S. Effect of several oxygenates on regulated emissions from heavy-duty diesel engines. *Environ. Sci. Technol*. **1997**, *31* (4), 1144 - 1150.

[10] Pecci, G. C.; Clerici, M. G.; Giavazzi, F.; Ancillotti, F.; Marchionna, M.; Patrini, R. Oxygenated fuel diesel. Part-1 structure and properties correlations. *9th Int. Symp. Alcohol Fuels* **1991**, *1*, 321 - 326.

[11] Marchionna, M.; Patrini, R.; Giavazzi, F.; Pecci, G. C. Linear ethers as high-quality components for reformulated diesel fuels. *Symposium on Removal of Aromatics, Sulfur and Alkenes from Gasoline and Diesel*, 212th National Meeting, American Chemical Society: Washington DC, **1996**, 585 - 589.

[12] Mascal, M. Chemicals from biobutanol: technologies and markets. *Biofuel Bioprod. Bioref.* **2012**, *6*, 483-493.

[13] Harvey, B. G.; Meylemans, H. A. The role of butanol in the development of sustainable fuel technologies. *J. Chem. Technol. Biotechnol.* **2010**, *86*, 2–9.

[14] Cai, L.; Sudholt, A.; Lee, D. J.; Egolfopoulos, F. N.; Pitsch, H.; Westbrook, C. K.; Sarathy, S. M. Chemical kinetic study of a novel lignocellulosic biofuel: di-n-butyl ether oxidation in a laminar flow reactor and flames. *Combust. Flame* **2014**, *161*, 798–809.

[15] Starkey, L. S. In *Introduction to strategies for organic synthesis*, 2nd ed.; John Wiley & Sons, Inc., Hoboken: New Jersey, 2012; pp 67-71.

[16] Sheldon, R. A.; van Bekkum, H. In *Fine chemical through heterogeneous catalysis*, Wiley-VCH: Weinheim, Germany, 2001; Chapter 6.5.

[17] European biofuels technology platform. http://www.biofuelstp.eu/butanol.html (accessed April 2015)

[18] AIChE. BP, ABF, and DuPont unveil plans for grassroots biofuels plant. *Chem. Eng. Prog.* **2007**, *103*, 14.

[19] Tsuchida, T.; Sakuma, S.; Takeguchi, T.; Ueda, W. Direct synthesis of n-butanol from ethanol over nonstoichiometric hydroxyapatite. *Ind. Eng. Chem. Res.* **2006**, *45*, 8634-8642.

[20] Cascone, R. Biobutanol – A replacement for bioethanol? *Chem. Eng. Pro.* **2008**, *104* (8), S4 – S9.

[21] Report Abstract. Oxo Alcohols PERP06/07-8, February 2009. http://www.chemsystems.com

[22] Guilera, J. Ethyl octyl ether synthesis from 1-octanol and ethanol or diethyl carbonate on acidic ion-exchange resins. Ph.D. Thesis, University of Barcelona, June 2013.

[23] Bautista, F. M.; Delmon, B. 1-Butanol dehydration on $AlPO_4$ and modified $AlPO_4$: catalytic behavior and deactivation. *Appl. Catal., A.* **1995**, *130*, 47 – 65.

[24] Makarova, M. K.; Paukshtis, E. A.; Thomas, J. M.; Williams, C.; Zamaraev, K. I. Dehydration of n-butanol on zeolite H-ZSM-5 and amorphous aluminosilicate: detailed mechanistic study and the effect of pore confinement. *J. Catal.* **1994**, *149*, 36-51.

[25] Nel, R. J. J.; de Klerk, A. Dehydration of $C_5 – C_{12}$ linear 1-alchols over η – alumina to fuel ethers. *Ind. Eng. Chem. Res.* **2009**, *48*, 5230-5238.

[26] Brandão, P.; Philippou, A.; Rocha, J.; Anderson, M. W. Dehydrations of alcohols by microporous niobium silicate. *Catal. Lett.* **2002**, *80* (3-4), 99-102.

[27] Choi, J. H.; Kim, J. K.; Park, D. R.; Park, S.; Yi, J.; Song, I. K. Etherification of n-butanol to di-n-butyl ether over $H_3PMo_{12-x}W_xO_{40}$ (x=0, 3, 6, 9, 12) Keggin and $H_6P_2Mo_{18-x}W_xO_{62}$ (x=0, 3, 9, 15, 18) Wells–Dawson heteropolyacid catalysts. *Catal. Commun*. **2011**, *14*, 48-51.

[28] Kim, K. K.; Choi, J. H.; Song, J. H.; Yi, J.; Song, I. K. Etherification of n-butanol to di-n-butyl ether over $H_nXW_{12}O_{40}$ (X = Co^{2+}, B^{3+}, Si^{4+}, and P^{5+}) Keggin heteropolyacid catalysts *Catal. Commun*. **2012**, *27*, 5-8.

[29] Tejero, J.; Cunill, F.; Iborra, M.; Izquierdo, J. F.; Fité, C. Dehydration of 1-pentanol to di-n-pentyl ether over ion-exchange resin catalysts. *J. Mol. Catal. A: Chem*. **2002**, *182*, 541-554.

[30] Bringué, R.; Iborra, M.; Tejero, J.; Izquierdo, J. F.; Cunill, F.; Fité, C.; Cruz, V. F. Thermally stable ion-exchange resins as catalysts for the liquid-phase dehydration of 1-pentanol to di-n-pentyl ether (DNPE). *J. Catal*. **2006**, *244*, 33-42.

[31] Medina, E.; Bringué, R.; Tejero, J.; Iborra, M.; Fité, C. Conversion of 1-hexanol to di-n-hexyl ether on acidic catalysts. *Appl. Catal., A*. **2010**, *374*, 41-47.

[32] Casas, C.; Bringué, R.; Ramírez, E.; Iborra, M.; Tejero, J.; Liquid-phase dehydration of 1-octanol, 1-hexanol and 1-pentanol to linear symmetrical ethers over ion exchange resins. *Appl. Catal., A*. **2011**, *396*, 129-139.

[33] Sherrington, D. C. Preparation, structure and morphology of polymer supports. *Chem Commun*. **1998**, *21*, 2275–2286.

[34] Coutinho, F. M. B.; Rezende, S. M.; Soares, B. G. Characterization of sulfonated poly(styrene–divinylbenzene) and poly(divinylbenzene) and its application as catalysts in esterification reaction. *J. Appl. Polym. Sci*. **2006**, *102*, 3616–3627.

[35] Jerabek, K. in *Cross-evaluation of strategies, size-exclusion chromatography. (Inverse steric exclusion chromatography as a tool for morphology characterization)*, ACS Symposium Series 635, American Chemical Society, Washington, DC, USA, 1996; 211.

[36] Jerabek, K. Determination of pore volume distribution chromatography data from size exclusion. *Anal. Chem.* **1985**, *57*, 1595–1597.

[37] Jerabek, K. Characterization of swollen polymer gels using size exclusion chromatography. *Anal. Chem*. **1985**, *57*, 1598–1602.

[38] Centomo, P.; Jerabek, K.; Canova, D.; Zoleo, A.; Maniero, A. L.; Sassi, A.; Canton, P.; Corain, B.; Zecca, M. Highly hydrophilic copolymers of N,N-dimethylacrylamide, acrylamido-2-methylpropanesulfonic acid, and ethylenedimethacrylate: nanoscale morphology in the

swollen state and use as exotemplates for synthesis of nanostructured ferric oxide. *Chem. Eur. J.* **2012**, *18*, 6632 – 6643.

[39] Corain, B.; Zecca, M.; Jerabek, K. Catalysis and polymer networks - the role of morphology and molecular accessibility. *J. Mol. Catal. A Chem*. **2001**, *177*, 3–20.

[40] Koo, B.; Liu, Y.; Zou, J.; Chattopadhyay, A.; Dai, L. L. Study of glass transition temperature (T_g) of novel stress-sensitive composites using molecular dynamic simulation. *Modelling Simul. Mater. Sci. Eng*. **2014**, *22*, 065018.

[41] Edgecombe, S.; Linse, P. Monte Carlo simulation of two interpenetrating polymer networks: Structure, swelling, and mechanical properties. *Polymer* **2008**, *49*, 1981-1992.

[42] Bandyopadhyay A.; Odegard, G. M. Molecular modeling of crosslink distribution in epoxy

polymers. *Model. Simul. Mater. Sci. Eng.* **2012**, *20*, 045018.

[43] Kacar, G.; Peters, E. A. J. F.; de With, G. Multi-scale simulations for predicting material properties of a cross-linked polymer. *Comp. Mater. Sci*. **2015**, *102*, 68–77

[44] Soni, N. J.; Lin, P.-H.; Khare, R. Effect of cross-linker length on the thermal and volumetric properties of cross-linked epoxy networks: A molecular simulation study. *Polymer* **2012**, *53*, 1015-1019.

[45] Sacristan-Bermejo, J.; Mijangos-Ugarte, C. Influence of cross-linking density on the glass transition and structure of chemically cross-linked PVA: A molecular dynamics study. *Macromol. Theor. Simul*. **2009**, *18*, 317-327.

[46] Yang, S.; Qu, J. Computing thermomechanical properties of crosslinked epoxy by molecular dynamic simulations. *Polymer* **2012**, *53*, 4806-4817

[47] Lu, Z.-Y.; Hentschke, R. Computer simulation study on the swelling of a model polymer network by a chainlike solvent**.** *Phys. Rev. E*. **2002**, *65*, 041807.

[48] Khare, K. S.; Khare, R. Directed diffusion approach for preparing atomistic models of crosslinked epoxy for use in molecular simulations. *Macromol. Theor. Simul*. **2012**, *21*, 322-327.

[49] Jang, C.; Lacy, T. E.; Gwaltney, S. R.; Toghiani, H. Pittman, C. U. Jr. Relative Reactivity Volume Criterion for Cross-Linking: Application to Vinyl Ester Resin Molecular Dynamics Simulations. *Macromolecules* **2012**, *45*, 4876-4885.

2. MATERIALS AND METHODOLOGY

2.1. Chemicals

Detailed below are the chemical compounds used in this work:

Reactants

- 1-Butanol (≥ 99.4% pure; ≤ 0.1% butyl ether; ≤ 0.1% water) supplied by Acros Organic.
- Di-n-butyl ether (≥ 99.0% pure; ≤ 0.05% water) supplied by Acros Organics.
- 1-Butene (≥ 99.0% pure) supplied by Sigma Aldrich.
- *Cis*-2-butene (≥ 98.0% pure) supplied by TCI.
- 2-Methyl-1-propanol (≥ 99.45% pure; ≤ 0.05% water) supplied by Acros Organics.
- Acetone (≥ 99.8% pure; ≤ 0.2% water) supplied by Fisher Chemical.
- Ethanol (≥ 99.8% pure; ≤ 0.02% water; ≤ 0.02% methanol; ≤ 0.02% 2-butanol) supplied by Panreac.
- Deionised water (resistivity 18.2 mΩ·cm) was obtained in our laboratory.

Solvent

- 1,4-Dioxane (≥ 99.8% pure) supplied by Sigma Aldrich.

Titration analysis

- Hydrochloric acid 1M (Panreac).
- Sodium chloride chemically pure (Panreac).
- Sodium hydroxide 0.1 M (Panreac).
- Potassium biphtalate pure (Panreac).

Auxiliary gases

- Nitrogen (> 99.995 % pure) supplied by Abello Linde was used to pressurize the equipment.
- Helium (> 99.998 % pure) supplied by Abello Linde was used as carrier gas in the chromatograph.

2.2. Catalysts

All experiments conducted in this work were carried out using commercial P(S-DVB) ion exchange resins functionalized with sulfonic acid groups. Specifically, 13 P(S-DVB) resins supplied by Rohm and Hass (Amberlyst 15, Amberlyst 16, Amberlyst 35, Amberlyst 36, Amberlyst 70, Amberlyst 39, Amberlyst 31, Amberlyst 121 and Amberlyst 46), Purolite (CT482) and Aldrich (Dowex 50Wx8, Dowex 50Wx4 and Dowex 50Wx2) were used. Short names and properties are given in Table 2.1.

Table 2.1. Properties of tested catalysts.

Catalyst	Short name	Structure[a]	DVB%	Sulfonation Type[b]	Acidity[c] (meq.H^+/g)	T_{max}[d]. (ºC)
Amberlyst 15	A-15	M	20	M	4.81	120
Amberlyst 35	A-35	M	20	O	5.32	150
Amberlyst 16	A-16	M	12	M	4.8	130
Amberlyst 36	A-36	M	12	O	5.4	150
CT 482[e]	CT-482	M	Medium	M	4.25	190
Amberlyst 70[e]	A-70	M	8	M	2.65	190
Amberlyst 39	A-39	M	8	M	4.81	130
Dowex 50Wx8	Dow-8	G	8	M	4.83	150
Amberlyst 31	A-31	G	4	M	4.8	130
Dowex 50Wx4	Dow-4	G	4	M	4.95	150
Amberlyst 121	A-121	G	2	M	4.8	130
Dowex 50Wx2	Dow-2	G	2	M	4.83	150
Amberlyst 46	A-46	M	High	S	0.87	120

[a] Macroreticular structure (M) or gel-type structure (G)
[b] Monosulfonated (M), oversulfonated (O) or sulfonated only at the polymer surface (S)
[c] Titration against standard base following the procedure described by Fisher and Kunin[1].
[d] Information supplied by manufacturer.
[e] Chlorinated.

As it can be seen in Table 2.1, used resins can be classified according to different criterion:

Structure

Macroreticular resins include polymers with high crosslinking degree (A-15, A-35 and A-46), medium crosslinking degree (A-16, A-36, CT-482) and low crosslinking degree (A-39 and A-70). A characteristic property of macroreticular resins is that they present permanent porosity. The gel type resins include the catalyst Dow-8, Dow-4, A-31, Dow-2 and A-121 containing from 8 to 2 DVB%. In contrast with macroreticular resin, gel type resins do not present permanent porosity.

Sulfonation Type

Monosulfonated resins (A-15, A-16, CT-482, A-70, A-39, Dow-8, A-31, Dow-4, A-121 and Dow-2) present one sulfonic group per phenyl ring, whereas in oversulfonated resins (A-35 and A-36) the concentration of $–HSO_3$ groups has been increased beyond the usual limit of one group per benzene ring.[2] A-35 and A-36 are oversulfonated versions of A-15 and A-16, respectively. A-46 is a resin sulfonated exclusively at the polymer surface.

Thermal stability

A-70 and CT-482 present chlorine atoms in their aromatic nuclei which decreases the rate of desulfonation at high temperatures improving the thermal stability of these resins.[3]

Structural parameters of P(S-DVB) resins

Ion exchange resins swell in polar media and, as a result, morphology changes and non-permanent pores appear. Table 2.2 shows the morphological parameters of tested resins both in dry state and swollen in water. As seen, macroreticular resins present BET surface areas ranging between 0.02 – 57.4 m^2/g (pore volume between 0.0 – 0.328 cm^3/g). Nevertheless, the same resins show a surface area (and pore volume) increase up to 147 – 214 m^2/g (0.333 – 1.05 cm^3/g) when swelling in water making clear that new pores with lower pore diameter appear. A useful description of the nature and characteristics of these spaces can be obtained from Inverse Steric Exclusion Chromatography (ISEC) data. In macroreticular resins, part of these new open spaces in the range of mesopores (named "true pores") can be characterized by the cylindrical pore model (see Figure 2.1). On the other hand, gel type resins do not show true pores, as it can be concluded from Table 2.2. The cylindrical pore model, however, is not applicable to describe small spaces between polymer chains in the swollen polymer (micropores). A good view of the three-dimensional network of swollen polymer is given by the geometrical model developed by Ogston[4] in which micropores are described by spaces between randomly oriented rigid rods. The characteristic parameter of this model is the specific volume of the swollen polymer (volume of the free space plus that occupied by the skeleton), V_{sp}. The Ogston model also allows to distinguish between zones of swollen gel phase of different density or polymer chain concentration (total rod length per volume unit of swollen polymer, nm^{-2}). According to the Ogston model, the density of polymer chains is described as the total rod length per unit of volume. Figures 2.2a and b show the distribution of different polymer density zones of swollen catalysts in aqueous phase for macroreticular resins and gel-type resins, respectively. As seen, gel-type resins (Amberlyst 121, Dowex 50Wx2, Amberlyst 31 and Dowex 50Wx4) and macroreticular resins with low crosslinking degree (Amberlyst 70 and Amberlyst 39) show low polymer densities (0.2 – 0.8 nm^{-2}) typical of an expanded polymer whereas macroreticular resins with medium and high crosslinking degree (CT 482, Amberlyst 36, Amberlyst 16, Amberlyst 35, Amberlyst 15 and Amberlyst 46) present high chains concentration (1.5 - 2 nm^{-2}) characteristic of a very dense polymer mass. It is to be noted that Dowex 50Wx8, in spite of being a gel-type resin, shows zones with high polymer density (1.5 nm^{-2}). That behavior is probably due to its high DVB%.

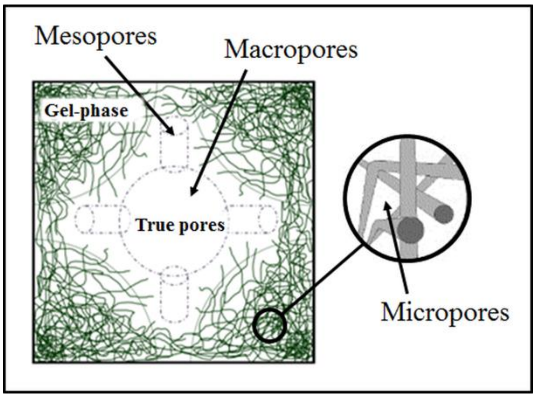

Figure 2.1. Schematic representation of the swollen polymer network.[5]

Table 2.2. Morphology of tested catalysts in the dry state and swollen in water.

Catalyst	ρ_s[a]	Dry state			Swollen in water (ISEC method)				
					"True Pores"			Gel polymer	
		S_{BET}[b]	V_{pore}[c]	d_{pore}[d]	S_{ISEC}[e]	V_{ISEC}[f]	d_{pore}[d]	V_{sp}	θ_{Total}[g]
	(g/cm^3)	(m^2/g)	(cm^3/g)	(nm)	(m^2/g)	(cm^3/g)	(nm)	(cm^3/g)	(%)
A-15	1.416	42.01	0.328	31.8	157	0.632	16.1	0.823	51.5
A-35	1.542	34.00	0.210	23.6	166	0.623	15.0	0.736	52.3
A-16	1.401	1.69	0.013	29.7	149	0.384	10.3	1.245	56.2
A-36	1.567	21.00	0.143	27.0	147	0.333	9.1	0.999	52.1
CT-482	1.538	8.7	0.06	26.8	214	1.051	18.5	1.081	69.5
A-70	1.520	0.02			176	0.355	8.1	1.15	56.3
A-39	1.417	0.09	2.9x10^{-4}	17.6	181	0.36	7.9	1.451	61.0
Dow-8	1.430	0.23						1.627	57.0
A-31	1.426	0.10	3.3x10^{-4}	15.3				1.933	63.7
Dow-4	1.426	0.01						1.92	63.5
A-121	1.428	0.02	3.5x10^{-4}	32.9				3.263	78.5
Dow-2	1.426	1.32						2.655	73.6
A-46	1.137	57.4	0.263	19.2	186	0.48	10.3	0.16	0.0

[a] Skeletal density measured by Helium displacement.
[b] BET (Brunauer-Emmet-Teller) surface area.
[c] Pore volume determined by adsorption-desorption of N_2 at 77 K.
[d] Mean pore diameter. Assuming pore cylindrical model: $4V_{pore}/S_{BET}$ or $4V_{ISEC}/S_{ISEC}$.
[e] Surface area determined from ISEC data.
[f] Pore volume determined from ISEC data.
[g] Porosity estimated as $100V_{pore}/(V_{pore}+(1/\rho_s))$ in dry state and as $100(V_{ISEC}+V_{sp}-(1/\rho_s))/(V_{ISEC}+V_{sp})$ in swollen state.

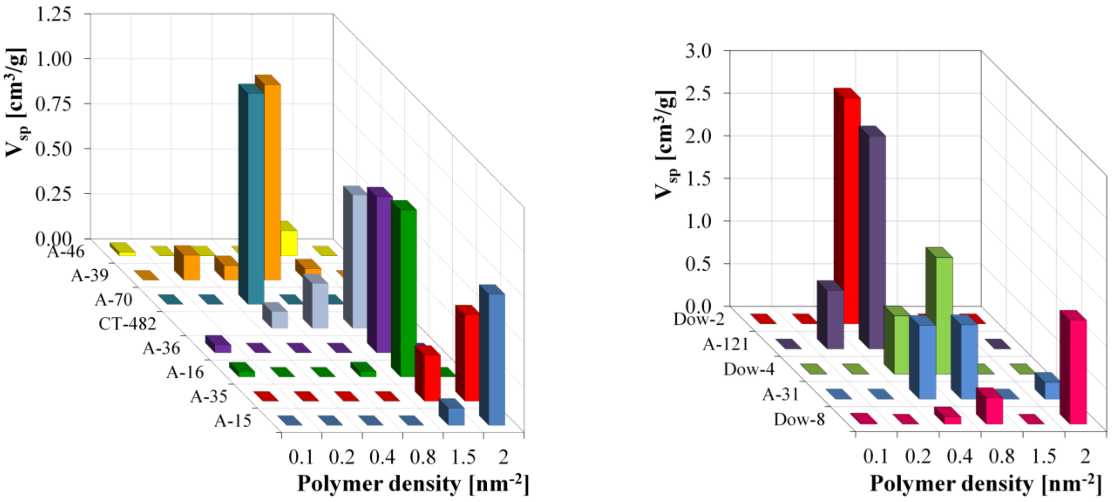

(a) **(b)**

Figure 2.2. ISEC pattern in water for (a) macroreticular and (b) gel-type resins.

Table 2.3 shows the particle size and the volume increase with respect to air for different catalysts swollen in water and 1-butanol. As it can be seen, size in water and 1-butanol is higher than in air as a consequence of swelling. However, for all the tested resins except for Amberlyst 46 the volume increase in 1-butanol is slightly lower than in water. As Table 2.3

shows, swelling increases as the resin DVB% decreases. Thus, Amberlyst 121 and Dowex 50Wx2 (2% of DVB content) present the highest swelling whereas Amberlyst 15 (20 % of DVB) and Amberlyst 40 (high % of DVB) show the lowest swelling.

Table 2.3. Mean d_p in different media and volume increase with respect to air.

	Mean d_p^a [µm]			Volume increase^b [%]	
Resin	Air	Water	1-butanol	Water	1-butanol
A-15	650	741	729	48	21
A-35			759		
A-70	551	783	729	187	132
A-39	540	768	724	188	141
A-121	441	824	718	552	332
A-31			660		
Dow-8	167	235	212	178	104
Dow-2	252	451	383	473	250
A-46	776	814	844	16	29

[a] Determined by laser diffraction (see Section 2.3.2)

[b] Calculated as $(V_{solvent}-V_{air})/V_{air}\cdot 100$ [%]

2.3. Experimental set up, analysis and procedure

2.3.1. Experimental set up

Experiments were carried out in a 100-mL-cylindrical autoclave made of 316 stainless steel (Autoclave Engineers, M010SS, maximum temperature: 232 ºC; pressure range: 0 – 150 bar). The autoclave was equipped with a pneumatic injection system for loading the catalyst, a magnetic drive stirrer and a 400 W electrical furnace for heating. Temperature and stirring speed were measured by a thermocouple located inside the reactor and by a tachometer. Both operation variables were controlled to ±1 K and ±1 rpm by an electronic control unit. One of the outlets of the reactor was connected directly to a liquid sampling valve, which injected 0.2 µL of pressurized liquid into a gas-liquid chromatograph. A scheme of the experimental set up is shown in Figure 2.3.

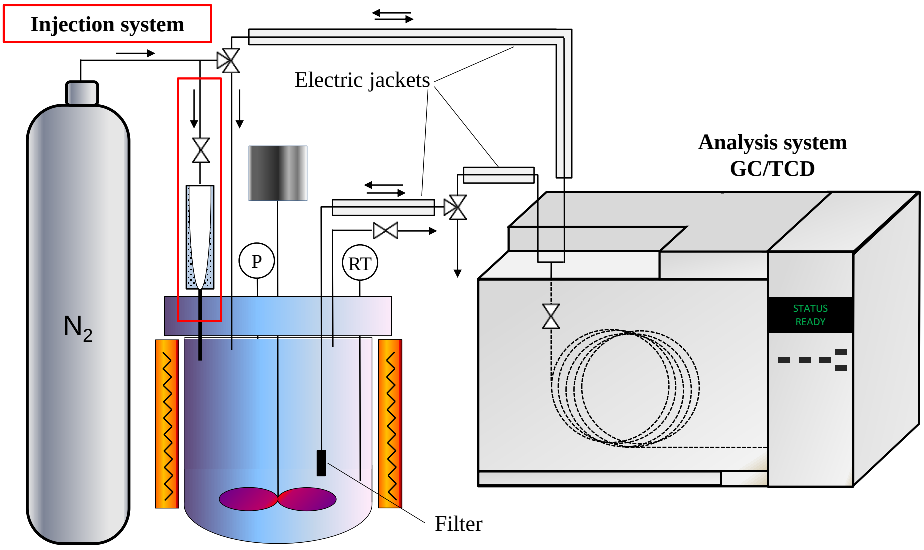

Figure 2.3. Scheme of the experimental set up.

2.3.2. Analysis

The composition of the reaction liquid mixture was analyzed in-line by a gas-liquid chromatograph (Agilent Technologies, 7820A) equipped with a TCD detector able to measure the presence of water. The capillary column used was a dimethylpolysiloxane HP-Pona (50 m x 0.200 mm x 0.50 μm). Helium was used as the carrier gas (70 $mL\cdot min^{-1}$, constant flow).

The oven was temperature programmed with a 5.5 min initial hold at 45 ºC followed by a 50 ºC/min ramp up to 180 ºC and held for 5 min. TCD temperature was set at 250 ºC.

A second GC equipped with a MS (Agilent GC/MS 5973) and chemical database software was used to identify all the species.

Chromatographic areas of each compound were correlated with the weigh percentage by means of calibration equations obtained from standard mixtures of known composition. These standard mixtures were prepared in a pressurizable deposit and injected in the GL chromatograph using the same injection system (valves and pipes) than that used in the analysis of the reaction medium.

Following, auxiliary devices used for catalyst characterization are presented.

Surface area

Catalyst surface area in dry state was obtained from N_2 adsorption-desorption isotherms recorded at 77 K (Accusorb ASAP 2020, Micrometrics) by the BET method. The samples were previously dried at 110 ºC under vacuum overnight.

Acid capacity

Acid capacity was determined following a modified Fisher-Kunin method.[1] For titration purposes a BRAND Digital Bürette was used.

Particle diameter

Particle diameter of resins swollen in 1-butanol was determined by a laser diffraction particle size analyzer (Beckman Coulter, LS 13 320). Resins samples, previously dried at 110 ºC at vacuum during 24 h, were placed in 1-butanol for 2 days to assure that resins were completely swollen. The optical model used in the analysis of the samples was the Fraunhofer diffraction pattern analysis.

2.3.3. Procedure

Catalyst pretreatment

Wet resins (as provided by the supplier) were dried at room temperature for 24 h followed by a mechanical sieving step in which resins were classified into four size fractions: < 0.4, 0.4 - 0.63, 0.63 - 0.8, and > 0.8. Afterwards, resin samples were dried at 110 ºC, firstly at 1 bar for 2 h and then at 10 mbar overnight (≈ 15 h). Guilera et al. showed that after this drying treatment the residual water content of the resin was < 3% (w/w).[6]

Dehydration experiments

Dehydration experiments can be grouped into six sets: preliminary experiments in which optimal experimental conditions were seek; catalyst screening where the influence of catalyst properties on the dehydration of 1-butanol were studied; thermal stability and reusability test; influence of typical 1-butanol impurities; thermodynamic equilibrium; and kinetic study. The procedure followed in all the cases was very similar although small differences existed among sets. Next, an introductory general procedure is described. For each set of experiments a detailed description of the procedure is described in the corresponding section.

Reaction mixture was charged in the reactor and, after checking for leaks, the selected stirring speed was set and the mixture was heated up to the working temperature. When the temperature set point was reached the catalyst was injected by means of pneumatic transport and the pressure was adjusted up to 40 bar by means of N_2 in order to ensure liquid phase medium. To follow the variation of the composition of the liquid mixture with time, liquid samples were taken out periodically and analyzed in-line as mentioned in Section 2.3.2.

2.4. Computational chemistry

Computational chemistry has proved to be a useful tool to model chemical phenomena (structure, properties, reactivity, etc.) via computer-implementation of the theoretical principles of classical and quantum mechanical physics. At the most fundamental level chemical phenomena are governed by the laws of quantum mechanics (QM). However, the computational effort in QM calculations increases as the fourth power the number of atoms and, therefore, its application to large molecules is expensive in terms of time and computer resources. For very large systems their properties must be modeled by classical methods. Classical methods treat molecules as a flexible collection of atoms held together by chemical bonds and do not provide electronic structure information.

In this work, molecular dynamics simulations were used to get insight of the microscopic structure of P(S-DVB) ion-exchange resins (see Chapter 6) and to study the interaction resin/1-butanol (see Chapter 7).

2.4.1. Molecular dynamic simulations

Molecular dynamic (MD) simulations reproduce the dynamical evolution of a system of N interacting atoms, at a molecular level, by solving Newton’s equations of motion:

$$F_i(t) = m_i \frac{\partial v_i(t)}{\partial t} \tag{2.1}$$

$$v_i(t) = \frac{\partial x_i(t)}{\partial t}, \qquad i = 1.....N. \tag{2.2}$$

For a given atom i, m_i, x_i, v_i and F_i are, respectively, the mass, the position, the velocity and the force acting on the atom.

The forces F_i can be calculated through Equation 2.3.

$$F_i = -\frac{\partial U(x_1, x_2, ..., x_N)}{\partial x_i} \tag{2.3}$$

being $U(x_1, x_2, ..., x_N)$ the potential energy of the system.

In molecular dynamics the potential energy of a system is calculated using a Force Field (see Section 2.4.1.1).

Equations 2.1 and 2.2 can be solved numerically integrating in small time steps by the so called leap-frog algorithm.[7] The leap-frog algorithm employs the Taylor expansions of the position vector (x_i) truncated at second order leading to:

$$v(t + \frac{1}{2}\Delta t) = v(t - \frac{1}{2}\Delta t) + \frac{\Delta t}{m} F(t) \tag{2.4}$$

$$x(t + \Delta t) = x(t) + \Delta t \cdot v(t + \frac{1}{2}\Delta t) \tag{2.5}$$

For numerical stability and accuracy in conserving the energy (rigorously, Newton's equations conserve the system total energy and therefore the numerical solutions should as well), one typically needs to pick a time step that is at least an order of magnitude smaller than the fastest time scale in the system. The time step in MD simulations is typically at the femtosecond level. This short time step together with the computer time required to perform one step of a calculation limit the total length of the simulation to several tens of nanoseconds.

In the present thesis, MD simulations were carried out in both, the canonical or NVT ensemble and the isobaric-isothermal or NPT ensemble. *Thermostats* and *barostats* were used to maintain the temperature and pressure in the required values. Their main characteristics are mentioned in Section 2.4.1.3.

In all the performed MD simulations the system was placed into a simulation box. In order to represent an infinite system and to eliminate surface effects, *periodic boundary conditions* (PBC) were applied i.e., the simulation box was replicated periodically in all directions so atoms outside the simulation box are simply images of the atoms simulated in that box. In this way, if an atom leaves the simulation box through the right wall, its image will enter the box through the left wall from the neighboring box (see Figure 2.4). This means that the resulting atomic model becomes periodic, with a periodicity equal to the dimensions of the box. The way in which non-bonded interactions (see next section) were computed when PBC were applied is described in Section 2.4.1.2.

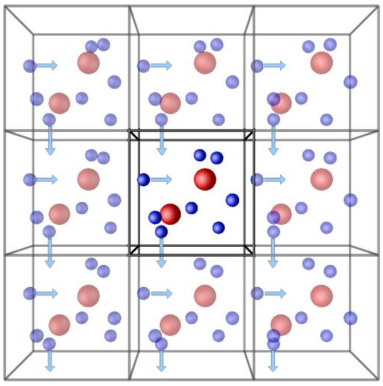

Figure 2.4. Periodic boundary conditions.[8]

2.4.1.1. Force Fields

Force-Field (FF) refers to the mathematical expression (called the potential function) and the parameters used to calculate the potential energy of a system of atoms (or coarse-grained particles) in molecular mechanics and molecular dynamics simulations.

In FF methods molecules are described by a “ball and spring” model with atoms having different sizes and “softness” and bonds having different lengths and “stiffness”. The potential function is written as a sum of terms including bonded terms for interactions of atoms that are linked by covalent bonds (bond-stretching, angle-bending and dihedrals) and nonbonded terms that describe the long-range electrostatic and van der Waals forces.

In the present thesis the following FF expression was employed:

$$U = \frac{1}{2}\sum_{\text{bonds}} k_{\text{b}}\left(b - b_0\right)^2 + \frac{1}{2}\sum_{\text{angles}} k_{\theta}\left(\theta - \theta_0\right)^2 + \sum_{\text{dihedrals}} k_{\varphi}\left(1 + \cos\left(n\varphi - \varphi_0\right)\right) + \sum_{\text{non-bonded}} 4\epsilon_{ij}\left(\left(\frac{\sigma_{ij}}{r_{ij}}\right)^{12} - \left(\frac{\sigma_{ij}}{r_{ij}}\right)^{6}\right) + \frac{q_i q_j}{4\pi\varepsilon_0\varepsilon_r r_{ij}} \tag{2.6}$$

In Equation 2.6 the first two sums represent the harmonic approximation for stretching and bending contributions, followed by a Fourier series expansion for the torsional term. In these bonding terms k_{b}, k_{θ} and k_{φ} are the bond, angle and dihedral angle force constants, respectively; b, θ and φ are the bond length, bond angle and dihedral angle, respectively; the subindex zero represents the equilibrium values for such geometric parameters; and n is the dihedral multiplicity. The second part of Equation 2.6 contains the van der Waals and electrostatic non-bonding interactions, which are represented, respectively, by the sum of 6-12 Lennard-Jones and Coulomb terms. In these contributions ϵ_{ij} is the depth of the potential well for the interaction of atoms *i* and *j*, σ_{ij} is the distance where the Lennard-Jones potential is exactly zero, q_i is the partial atomic charge of atom *i*, ε_0 is the electric constant, ε_r is the effective dielectric constant and r_{ij} is the distance separating atoms *i* and *j*.

The Lennard-Jones parameters between pairs of different atoms were obtained from the Lorentz-Berthelot mixing rules, in which σ_{ij} values are based on the arithmetic mean of σ_i and σ_j and ϵ_{ij} values are based on the geometric mean of ϵ_i and ϵ_j (Equations 2.7 and 2.8, respectively).

$$\sigma_{ij} = \frac{1}{2}(\sigma_{ii} + \sigma_{jj}) \tag{2.7}$$

$$\in_{ij} = (\in_{ii} \cdot \in_{jj})^{1/2} \tag{2.8}$$

Stretching, bending, torsional and van der Waals force field parameters were extracted from the general AMBER force field (GAFF).[9] Atomic charges were obtained from QM ab initio calculations according to the Restrained Electrostatic Potential (RESP) strategy.[10]

2.4.1.2. Non-bonded interactions

Evaluation of the non-bonded energy is by far the most time-consuming step. For a pairwise model the non-bonded contributions grow as the square of the number of atoms. However the majority of these non-bonded contributions are numerically very small, as the distance between the atom pairs is large. In Figure 2.5 it can be seen that the van der Waals interactions reproduced by a Lennard-Jones potential decays very rapidly and, at a distance of $2.5\sigma_{ij,}$ there is only 1% of the interaction at σ_{ij}. Thus, a considerable saving in computational time can be achieved by truncating the van der Waals potential. The introduction of a cutoff distance, beyond which the van der Waals energy is set to zero, is quite reasonable as the neglected contributions rapidly become small for any reasonable cutoff distance (see Figure 2.5 where the van der Waals potential has been truncated at 14 Å). To avoid duplicate interactions between atoms, the *minimum image convention* approximation where every atom in the original box interacts with the nearest elements that fall within the given cutoff is used. These interacting atoms may be in the original box or in the neighboring.

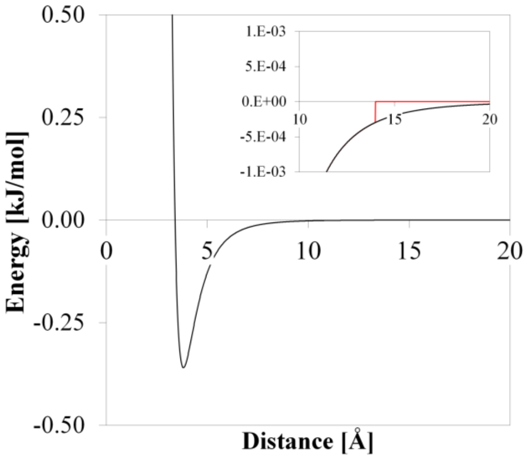

Figure 2.5. Lennard-Jones potential profile for σ_{ij} = 3.4 Å and ϵ_{ij} =0.36 kJ/mol . Red line corresponds to the cutoff-truncated aproximation.

Contrary to the van der Waals energy, which falls very rapidly, the other part of the non-bonded energy, the Coulomb interaction, does not decay that fast and the cutoff approximation may not be adequate. To account for the long range electrostatic interaction the so called Particle Mesh-Ewald summation (PME)[11,12] was used. The PME method calculates the infinite electrostatic interactions by splitting the summation in two terms: a direct sum of the short-ranged potential in real space and a summation in Fourier space of the long-ranged part. Since both summations converge quickly in their respective spaces (real and Fourier), they may be truncated with little loss of accuracy and great improvement in required computational time.

2.4.1.3. Temperature and pressure couplings

As it was previously mentioned, MD simulations were carried out in both, the NVT ensemble (whose thermodynamic state is characterized by a fixed number of atoms N, fixed volume V and fixed temperature T) and the NPT ensemble (fixed number of atoms N, pressure P and temperature T). In order to simulate constant temperature or constant pressure several algorithms were used:

Temperature coupling

In MD simulations the temperature of the system is computed from the system's total kinetic energy. Consequently, temperature can be controlled by adjusting the velocities of each atom. Two algorithms were used to control the temperature:

- The *Berendsen thermostat* couples the simulated system loosely to a constant bath. Such a coupling is accomplished by adding a frictional term to the equations of motion which drives the system (exponentially) toward the desired temperature. In practice, this coupling is achieved by scaling the velocities of the particles with a factor:

$$\lambda_T = \left[1 + \frac{\Delta t}{\tau_T}\left(\frac{T}{T_0} - 1\right)\right]^{\frac{1}{2}} \tag{2.9}$$

  where τ_T is the heat bath coupling time and T_0 is the set point temperature. A deeper description of the Berendsen thermostat can be found in Berendsen et al.[13]

  The Berendsen thermostat suppresses fluctuations of the kinetic energy of the system and thus does not give the correct thermodynamic ensemble. For this reason in this thesis systems were initially equilibrated using the Berendsen scheme, while properties were calculated using the widely known Nosé-Hoover thermostat, which correctly generates trajectories consistent with a canonical ensemble.

- In the *Nosé-Hoover thermostat* the idea is to consider the heat bath as an integral part of the system by addition of an artificial dynamical variable, associated with a mass as well as a velocity. The magnitude of the mass determines the coupling between the reservoir and the real system and so influences the temperature fluctuations. The artificial variable plays the role of a time-scaling parameter. A thorough description of the Nosé-Hoover thermostat can be found in Nosé[14] and Hoover[15].

Pressure coupling

Pressure coupling algorithms act to adjust box vectors and scale the coordinates of the atoms within the unit cell. In this work two algorithms were used to control the pressure:

- The *Berendsen barostat* couples the simulated system to a constant pressure bath. Similar to the temperature coupling, an extra term is added to the equations of motion that effects a pressure change. In practice this results in scaling the coordinates and the box length with a factor:

$$\mu_P = \left[1 + \frac{\Delta t}{\tau_P}\left(P - P_0\right)\right]^{\frac{1}{3}} \tag{2.10}$$

  where τ_P is the coupling time constant for the pressure scaling and P_0 is the set point pressure. A deeper description of the Berendsen barostat can be found in Berendsen et al.[13]

- The *Parrinello-Rahman barostat*. This method allows a variable simulation cell shape. Basically, the box vectors are set to follow an equation of motion, and the equations of motion of the particles are also changed as in the Nosé-Hoover thermostat. For an exhaustive derivation of the Parrinello-Rahman barostat and the related equations of motion, see the original paper of Parrinello and Rahman.[16]

2.4.2. Sorption of solvents by polymer matrices

The sorption of solvent molecules (*s*) in polymer matrices depends on the difference between the chemical potential of solvent molecules inside the polymer matrix ($\mu_{s,polymer}$) and the chemical potential of solvent molecules in the pure solvent system ($\mu_{s,pure}$). At equilibrium the two values are equal:

$$\mu_{s,polymer} = \mu_{s,pure} \tag{2.11}$$

In thermodynamics the chemical potential of a component *s* (μ_s) in a system may be defined as:

$$\mu_s = \left(\frac{\partial G}{\partial N_s}\right)_{P,T,N'} = \left(\frac{\partial A}{\partial N_s}\right)_{T,V,N'} \tag{2.12}$$

where G is the Gibbs energy of the system, A is the Helmholtz energy, N_s is the number of s molecules in the system, T is the absolute temperature, P is the pressure, V is the volume, and N designates the set of numbers $N_1, \ldots, N_c$, where N_i is the number of molecules of the ith species in the system. The set N' is the same as N but excludes the number N_s for the species s. However, a physical definition of the chemical potential requires the use of finite differences in Equation 2.12. For values of ΔN_s which do not sensibly affect the composition of the fluid, the ratio $\Delta A/\Delta N_s$ (or $\Delta G/\Delta N_s$) will not differ sensibly from the derivative on the right-hand side of Equation 2.12. Therefore, μ_s can be defined as the change in free energy produced by the subtraction or addition of a single molecule of solvent from the macroscopic system, while maintaining the temperature, volume and the numbers of molecules of the other species constant (canonical ensemble):

$$\mu_s = \Delta A = A(N_P, N_S + 1, V, T) - A(N_P, N_S, V, T) \tag{2.13}$$

In Equation 2.13 the system is considered to be composed by a polymer matrix (sub-index P) and the solvent. This equation states that the chemical potential μ_s can be estimated from the free energy difference between two systems: an initial system with N solvent molecules (System A) and a final system with N+1 solvent particles (System B).

The Helmholtz free energy A can be expressed in terms of the partition function Q:

$$A = -\beta^{-1} \ln Q(N,V,T) \qquad \text{with } \beta = 1/k_B T \tag{2.14}$$

where k_B is the Boltzman constant.

This equation forms the fundamental connection between thermodynamics and statistical mechanics in the canonical ensemble, from which it follows that calculating A is equivalent to estimating the value of Q. In general, evaluating Q is a very difficult undertaking. However, we are interested in free energy differences, ΔA, between two systems or states of a system, described by the partition functions Q_A and Q_B, respectively:

$$\Delta A = A_B - A_A = -\beta^{-1} \ln\left(\frac{Q_B(N+1,V,T)}{Q_A(N,V,T)}\right) \tag{2.15}$$

From Equation 2.15 classical statistical mechanics provides us with the following expression for the chemical potential:

$$\mu_s = k_B T \ln\left(\rho_{\mathrm{N,s}} \Lambda_{\mathrm{s}}^3\right) + \mu_s^{\mathrm{excess}} \tag{2.16}$$

A full derivation of this relation can be found in Ben-Naim.[17] In Equation 2.16 $\rho_{\mathrm{N,s}}$ is the number density $\rho_{\mathrm{N,s}} = (N_s + 1)/V$ and Λ_{s}^3 is the momentum partition function of the solvent.

Equation 2.16 may be interpreted as follows. The chemical potential is a measure of the change in the Helmholtz free energy caused by the addition of one solvent molecule to the system (at constant V, T and composition). The split of μ_s into two parts corresponds to the process of adding the solvent molecule in two steps. First the molecule is placed at a fixed position being the corresponding change in the Helmholtz energy μ_s^{excess} (the excess chemical potential). Next, the constraint imposed on the fixed position is released resulting in an additional change in the Helmholtz energy, $k_B T \ln\left(\rho_{N,s}\Lambda_s^3\right)$.[17]

Taking into account Equation 2.16, the equilibrium condition (Equation 2.11) can be written as Equation 2.17. Thus, given that the values of the number densities are known, evaluation of the excess part of the chemical potential is enough to determine the absorption of solvent molecules.

$$\mu_{s,polymer}^{excess} - \mu_{s,pure}^{excess} = k_B T \ln\left(\frac{\rho_{N,s,pure}}{\rho_{N,s,polymer}}\right) \tag{2.17}$$

In the next section an overview of several approaches to estimate the free energy change due to the process of inserting a molecule at a fixed position (i.e., the excess chemical potential, μ_s^{excess}), is presented. The reader who is interested in a thorough description of these methods is referred to the book *Free Energy Calculations. Theory and Applications in Chemistry and biology*.[18]

2.4.3. Free Energy Calculations

2.4.3.1. Free Energy Perturbation theory

Free-energy perturbation theory, as presented by Zwanzig in his paper[19], relates the free energy difference between an initial (reference, A) and a final (target, B) state of a system to an average of a function of their energy difference evaluated by sampling for the initial state:

$$\Delta A = A_B - A_A = -\beta^{-1} \ln\left\langle \exp\left[-\beta\cdot\left(\mathcal{H}_B - \mathcal{H}_A\right)\right]\right\rangle_A \tag{2.18}$$

Here $\mathcal{H}_A$ and $\mathcal{H}_B$ are respectively the Hamiltonian of the system at the initial and final state and $\langle ... \rangle_A$ denotes an ensemble average over configurations sampled from the reference state. This is the fundamental FEP (Free Energy Perturbation) formula. It states that ΔA can be estimated by sampling only equilibrium configurations of the reference state.

The particle-insertion method of Widom is an application of Equation 2.18 to obtain the excess chemical potential of a system with N particles (state A) by inserting a test particle, N+1 (state B):

$$\mu_s^{excess} = \Delta A = -\beta^{-1} \ln \left\langle e^{-\beta B_{N+1}} \right\rangle_N \tag{2.19}$$

Where $B_{N+1} = \sum_{i=1}^{N} U_{i,N+1}$ is the total potential energy of interaction between the test particle and the *N* particles of the system. The brackets $\langle ... \rangle_N$ denote the canonical ensemble average over the original *N*-particle system (without the test particle).

Thus, the excess chemical potential (μ_s^{excess}) can be calculated from the potential energy change of the system with *N* particles, caused by the insertion of a test particle of species *i* into the system at randomly chosen positions.

Practical limits of the perturbation formalism

Particle insertion method works very well in many circumstances but it may run into difficulties in systems with large solutes or at high density or with strong or long-range interactions, e.g., between dipolar species. In these systems, it becomes increasingly unlikely that a test particle can be successfully inserted. That is, it is more probable that a randomly chosen position will yield a large, positive value of the potential energy due to repulsive overlaps between the test particle and the host particles of the system. These insertions will contribute negligibly to μ_s^{excess} because of the exponential function in Equation 2.19. Consequently, it will be difficult to know sufficiently well the low energy tail of the distribution resulting in inaccurate estimates of Δ*A*.

2.4.3.2. Thermodynamic Integration

The thermodynamic integration method (TI) assumes that the Hamiltonian of the evolving system can be defined as a function of a continuously varying parameter, *λ*. The parameterized Hamiltonian $\mathcal{H}_\lambda$ is defined such that when λ = 0, $\mathcal{H}_\lambda = \mathcal{H}_A$ (corresponding to the starting state of the system) and when λ = 1, $\mathcal{H}_\lambda = \mathcal{H}_B$ (corresponding to the final state of the system). $\mathcal{H}_\lambda$ interpolates smoothly between the two Hamiltonian functions. The free energy *A* becomes itself a function of λ and we have

$$\frac{dA}{d\lambda} = \left\langle \frac{\partial \mathcal{H}_\lambda}{\partial \lambda} \right\rangle_\lambda \tag{2.20}$$

$\langle ... \rangle_\lambda$ represents an ensemble average at a particular λ value.

Standard TI assumes that one obtains full equilibration along the λ path which allows the calculation of the free energy difference by integrating the derivative of the Hamiltonian with respect to λ:

$$\Delta A = A_{\lambda=1} - A_{\lambda=0} = \int_0^1 \left\langle \frac{\partial \mathcal{H}_\lambda}{\partial \lambda} \right\rangle_\lambda d\lambda \tag{2.21}$$

In the particular case of estimating the excess chemical potential of the specie *s* by TI, the coupling parameter λ slowly introduces (or removes) the binding energy B_{N+1} (attractive and repulsive interactions) between an *s* particle *N*+1 and all other particles in the system.

Practical Limits of Thermodynamic Integration

TI relies on exhaustively sampling phase space at each intermediate λ point to meet the requirement of being always in equilibrium and fully reversible, a requirement which is difficult to meet in complex systems.

The thermodynamic integration technique has been used extensively to calculate the free energy changes of adding molecules to dense liquids, or changing a small group of atoms on a molecule into another group of atoms. Nowadays these free energy calculations can be performed very accurately. When, however, the thermodynamic integration method is used to compute the excess chemical potential of the solvent *s* in a polymer matrix, the accuracy could become quite poor. In these cases the major problem to overcome is related to the sampling of the state in which the coupled *s* molecule is completely (or almost completely) interacting. When the interaction between the penetrant molecule *s* and the polymer structure is sufficiently strong the *s* molecule may end up in a local free minimum, that is, the solvent molecule occupies a cavity in the polymer from which it does not move away during the simulation thus, poorly sampling the phase space.

2.4.3.3. Non-equilibrium method

Nonequilibrium methods for equilibrium free energy calculations are based on Jarzynski's nonequilibrium work theorem:[20]

$$\exp(-\beta \Delta A_{AB}) = \left\langle \exp(-\beta W_{AB}) \right\rangle_A \tag{2.22}$$

Jarzynski relates the work W_{AB} that is being performed on a system when going from state A to state B (along a coordinate λ) with the free energy change, irrespective of the reversibility of the sampling. He finds that the exponentially averaged work of repeated sampling of the path from A to B is equal to the free energy difference between A and B. The angular bracket in (2.22) denotes averaging over a canonical ensemble of the initial state A.

In principle, Equation 2.22 permits the calculation of free energy differences from repeated "fast-growth" TIs at arbitrarily fast growth rates. The two limiting cases are the instantaneous change which corresponds to standard perturbation from an equilibrium ensemble (Equation 2.18) and the infinitely slow change (Equation 2.21).

Practical limits of the nonequilibrium equality

The limitations of Equation 2.22 are in spirit similar to the typical perturbation sampling problem: accurate estimates of the exponential work average exp($-\beta W_{AB}$) are difficult. For any finite number of repetitions, this average tends to be dominated by the few smallest values W_{AB} observed. This is consequence of the strong nonlinearity of the exponential function to be averaged. The number of fast experiments required to sample the (exponentially rarely occurring) tails of the work distribution function grows exponentially with the amount of irreversible work performed during the experiment. This means that sampling the relevant (favorable) paths between A and B becomes very difficult.

Nomenclature

Notation

A	Helmholtz free energy
b	Bond length
b_0	Equilibrium bond length
B_{N+1}	Total potential energy of interaction between the test particle and the N particles of the system
d_p	Particle diameter
d_{pore}	Mean pore diameter. Assuming pore cylindrical model
F_i	Force acting on the atom i
G	Gibbs free energy
$\mathcal{H}_i$	Hamiltonian of the system at state i
$\mathcal{H}_\lambda$	Parameterized Hamiltonian
k_b	Bond force constant
k_B	Boltzman constant
k_θ	Angle force constant
k_φ	Dihedral angle force constant
m_i	Mass of atom i
n	Dihedral multiplicity
N	Number of molecules in the system
N_i	Number of molecules of the ith species
P	Pressure
P_0	Set point pressure
q_i	Partial atomic charge of atom i
Q	Partition function
r_{ij}	Distance separating atoms i and j
s	solvent
S_{BET}	BET surface area
S_{ISEC}	Surface area determined from ISEC data
t	Time
T	Temperature
T_0	Set point temperature
T_{max}	Maximum operation temperature
U	Potential energy of the system
$U_{i,N+1}$	Potential energy of interaction between the test particle (N+1) and the i particle of the system
v_i	Velocity of atom i

V_{ISEC}	Pore volume determined from ISEC data
V	Volume
V_{air}	Volume of a resin particle in air
V_{pore}	Pore volume determined by adsorption-desorption of N_2 at 77 K
V_{sp}	Specific volume of the swollen polymer
$V_{solvent}$	Volume of a resin particle swollen in a solvent
W_{AB}	Work performed on a system when going from state A to state B
x_i	Position of atom *i*

Greek symbols

β	$(k_B \cdot T)^{-1}$
ΔA	Helmholtz free energy change
ΔG	Gibbs free energy change
ΔN_s	Change of the number of molecules of *s*
Δt	Time step
ϵ_{ij}	Depth of the potential well for the interaction of atoms *i* and *j*
ε_0	Electric constant
ε_r	Effective dielectric constant
θ	Bond angle
θ_0	Equilibrium bond angle
θ_{Total}	Porosity
λ	Coupling parameter
Λ_s^3	Momentum partition function of the solvent
λ_T	Velocity scaling factor (Berendsen thermostat)
μ_P	Coordinates scaling factor (Berendsen barostate)
μ_{s}	Chemical potential of the solvent *s*
μ_s^{excess}	Excess chemical potential of the solvent *s*
ρ_{s}	Skeletal density measured by Helium displacement
$\rho_{\mathrm{N,s}}$	Number density of compound *s*
σ_{ij}	Distance between atoms *i* and *j* where the Lennard-Jones potential is exactly zero
τ_P	Coupling time constant for the pressure scaling (Berendsen barostate)
τ_T	Heat bath coupling time (Berendsen thermostat)
φ	Dihedral angle
φ_0	Equilibrium dihedral angle

Abbreviations

BET	Brunauer-Emmet-Teller
DVB	Divinyl benzene
FEP	Free energy perturbation
FF	Force field
GAFF	General Amber force field
GC	Gas chromatography
ISEC	Inverse steric exclusion chromatography
MD	Molecular dynamics
MS	Mass spectrometry
NPT	Isobaric-isothermal ensemble
NVT	Canonical ensemble
PBC	Periodic boundary conditions
PME	Particle Mesh-Ewald
P(S-DVB)	Poly(styrene-divinylbenzene)
QM	Quantum mechanics
RESP	Restrained electrostatic potential
TCD	Thermal conductivity detector
TI	Thermodynamical integration

References

[1] Fisher, S.; Kunin, R. Routine exchange capacity determinations of ion exchange resins. *Anal. Chem*. **1955**, *27*, 1191-1194.

[2] Tejero, J.; Cunill, F.; Iborra, M.; Izquierdo J. F.; Fité, C. Dehydration of 1-pentanol to di-n-pentyl ether over ion-exchange resin catalysts. *J. Mol. Catal. A: Chem*. **2002**, *182-183*, 541-554.

[3] Costin, C. R. Thermally stable resins prepared by bromination or chlorination of aromatic polymer beads followed by sulphonation. U.S. Patent 4,269,943, May 26, 1981.

[4] Ogston, A. G. The spaces in a uniform random suspension of fibres. *Trans. Faraday Soc*. **1958**, *54*, 1754-1757.

[5] Jerabek, K. in *Cross-evaluation of strategies, size-exclusion chromatography. (Inverse steric exclusion chromatography as a tool for morphology characterization)*, ACS Symposium Series 635, American Chemical Society, Washington, DC, USA, 1996; 211.

[6] Guilera, J.; Bringué, R.; Ramírez, E.; Iborra, M.; Tejero, J. Synthesis of ethyl octyl ether from diethyl carbonate and 1-octanol over solid catalysts. A screening study. *Appl. Catal., A*. **2012**, *413– 414*, 21– 29.

[7] Jensen, F. *Introduction to computational chemistry*, 2nd Ed.; John Willey & Sons Ltd: England, 2007, pp 452.

[8] Central Michigan University. Interactive Structure Analysis of Amorphous and Crystalline Systems (I.S.A.A.C.S) web: isaacs.sourceforge.net/phys/pbc.html (accessed 5th May, 2015)

[9] Wang, J.; Wolf, R. M.; Caldwell, J. W.; Kollman, P. A.; Case, D. A. Development and testing of a general amber force field. *J. Comput. Chem*. **2004**, *25* (9), 1157-1174.

[10] Cieplak, P.; Cornell, W.; Bayly, C. I.; Kollman, P. A. A well-behaved electrostatic potential based method using charge restraints for deriving atomic charges: the RESP model *J. Comput. Chem*. **1995**, *16*, 1357-1377.

[11] Darden, T.; York, D.; Pedersen, L. Particle mesh Ewald: An $N\cdot\log(N)$ method for Ewald sums in large systems. J. *Chem. Phys*. **1993**, *98*, 10089–10092.

[12] Essmann, U.; Perera, L.; Berkowitz, M. L.; Darden, T.; Lee, H.; Pedersen, L. G. A smooth particle mesh Ewald method. *J. Chem. Phys*. **1995**, *103*, 8577–8592.

[13] Berendsen, H. J. C.; Postma, J. P. M.; van Gunsteren, W. F.; DiNola, A.; Haak, J. R. Molecular dynamics with coupling to an external bath. *J. Chem. Phys*. **1984**, *81* (8), 3684-3690.

[14] Nosé, S. A unified formulation of the constant temperature molecular dynamics methods. *J. Chem. Phys.* **1984**, *81* (1), 511-519.

[15] Hoover, W. G. Canonical dynamics: Equilibrium phase-space distributions. *Phys. Rev. A.* **1985**, *31* (3), 1695-1697.

[16] Parrinello, M.; Rahman, A. Polymorphic transitions in single crystals: A new molecular dynamics method. *J. Appl. Phys*. **1981**, *52*, 7182-7190.

[17] Ben-Naim, A. *Solvation Thermodynamics*, 1st ed.; Springer Science + Business Media: New York, 1987; pp 123-132.

[18] *Free energy calculations. Theory and applications in chemistry and biology*; Chipot. C.; Pohorille, A., Eds.; Springer Series in Chemical Physics 86; Springer-Verlag: Berlin Heidelberg, 2007.

[19] Zwanzig, R. W. High-temperature equation of state by a perturbation method. I. Non-polar gases. *J. Chem. Phys*. **1954**, *22*, 1420-1426.

[20] Jarzynski, C., Nonequilibrium equality for free energy differences. *Phys. Rev. Lett*. **1997**, *78*, 2690-2693.

3. SYNTHESIS OF DI-N-BUTYL ETHER FROM 1-BUTANOL OVER ACIDIC ION EXCHANGE RESINS[*]

---

[*] Results presented in this chapter have been published in:

Pérez, M. A.; Bringué, R.; Iborra, M.; Tejero, J.; Cunill, F. Ion exchange resins as catalysts for the liquid-phase dehydration of 1-butanol to di-n-butyl ether. *Appl. Catal., A*. **2014,** *482*, 38-48.

3.1. Introduction

Linear symmetrical ethers can be synthesized by bimolecular dehydration of primary alcohols over acid catalysts.[1,2] During the alcohol dehydration reaction both an intermolecular dehydration (ether formation) and an intramolecular dehydration (olefin formation) may occur. The prevailing pathway depends on the reaction conditions as well as the reactant and catalyst used. Different solid acids have been tested as catalysts in the dehydration of 1-butanol: zeolites[3], aluminum phosphates[4], amorphous aluminosilicates (AAS)[3], microporous niobium silicates[5], and α-alumina[6] have been tested in gas phase whereas heteropolyacids[7,8] have been tested in liquid phase. In the gas phase selectivity proved to be highly dependent on conversion. Over $AlPO_4$ (fixed-bed reactor, atmospheric pressure, T = 300 ºC) the dehydration of 1-butanol gave place mainly to butenes at 1-butanol conversions >75 % suggesting that the intramolecular dehydration of 1-butanol to 1-butene and the subsequent isomerization to *trans*-2-butene and *cis*-2-butene took place.[4] Butene was the major product for the dehydration reaction on AAS over the whole range of temperature tested (flow microreactor, 105 – 185 ºC, 1 atm).[3] At the same set-up and experimental conditions, selectivity to ether over H-ZSM-5 was higher than on AAS at about 2% alcohol conversion, but it decreased remarkably on increasing 1-butanol conversion.[3] In the dehydration of $C_5 – C_{12}$ linear alcohols over η- alumina (fixed bed reactor, 250 – 350 ºC, 0 – 4 MPa, WHSV = 1 – 4 h^{-1}) it was observed that temperatures as high as 300 ºC were necessary to achieve over 60 % conversion of 1-butanol; selectivity to ethers being lower than 30%.[6] Finally, 1-butanol also dehydrated selectively to butenes over microporous niobium silicate (150 – 300 ºC, 1 atm).[5] On the contrary, the liquid phase etherification of 1-butanol to di-n-butyl ether on heteropolyacids with different heteroatoms (200 ºC, 30 bars) showed that 1-butanol dehydrates selectively to di-n-butyl ether achieving over 80% ether selectivity with 1-butanol conversions ranging from 30 to 80%.[8]

Over the last years, it has been found that acidic ion-exchange resins are able to catalyze the dehydration of primary alcohols to linear symmetrical ethers with high selectivity (97-99%), avoiding byproducts as olefins.[9-12] However, the synthesis of di-n-butyl ether has not been reported on ion-exchangers. Thus, the aim of this chapter was to study the liquid-phase dehydration of 1-butanol to DNBE over ion-exchange resins of different morphology and discuss the relationship between resins properties and their catalytic behavior. Furthermore, the thermal stability of the resins as well as the influence of typical 1-butanol impurities were studied.

3.2. Materials and experimental procedure

Tested catalysts were acidic styrene-codivinylbenzene ion exchange resins: the monosulfonated macroreticular resins Amberlyst 15, Amberlyst 16 and Amberlyst 39 (high, medium and low crosslinking degree, respectively); the oversulfonated macroreticular resins Amberlyst 35 (high crosslinking degree) and Amberlyst 36 (medium crosslinking degree) which are oversulfonated versions of Amberlyst 15 and Amberlyst 16 respectively; the chlorinated macroreticular resins Amberlyst 70 and CT482; the macroreticular resin sulfonated exclusively at the polymer surface Amberlyst 46; and the monosulfonated gel-type resins Dowex 50Wx8, Dowex 50Wx4, Amberlyst 31, Dowex 50Wx2 and Amberlyst 121 containing from 8 to 2 DVB%. The most relevant properties for this study are given in Table 3.1. A comprehensive characterization of all the resins can be found in Section 2.2.

Table 3.1. Properties of tested catalysts.

Catalyst	Short name	DVB%	Acidity[a] (meq.H^+/g)	V_{sp}[b] (cm^3/g)
Amberlyst 15	A-15	20	4.81	0.823
Amberlyst 35	A-35	20	5.32	0.736
Amberlyst 16	A-16	12	4.8	1.245
Amberlyst 36	A-36	12	5.4	0.999
CT482	CT-482	Medium	4.25	1.081
Amberlyst 70	A-70	8	2.65	1.15
Amberlyst 39	A-39	8	4.81	1.451
Dowex 50Wx8	Dow-8	8	4.83	1.627
Amberlyst 31	A-31	4	4.8	1.933
Dowex 50Wx4	Dow-4	4	4.95	1.92
Amberlyst 121	A-121	2	4.8	3.263
Dowex 50Wx2	Dow-2	2	4.83	2.655
Amberlyst 46	A-46	High	0.87	0.16

[a] Titration against standard base following the procedure described by Fisher and Kunin.[28]

[b] Specific volume of the swollen polymer (volume of the free space plus that occupied by the skeleton) obtained from Inverse Steric Exclusion Chromatography (ISEC) data.

Dehydration tests were performed in the autoclave described in Section 2.3.1.Wet resins (as provided by the supplier) were dried at room temperature for 24 h prior to mechanical sieving. Resin samples with bead size between 0.40 – 0.63 mm were dried at 110 ºC, firstly at 1 bar for 2 h and then at 10 mbar for 15 h. 70 ml of 1-butanol were charged in the reactor and heated to 150 ºC. The reaction mixture was pressurized to 40 bar by means of N_2 in order to assure the liquid phase reaction medium. The stirring speed was set at 500 rpm and the mass of loaded catalyst used was 1 g. After reaching the working temperature, the dry catalyst was injected by means of pneumatic transport. That moment was considered the starting point of reaction. To follow the variation of concentration of reactants and products with time, liquid samples were taken out hourly and analyzed in-line as mentioned in Section 2.3.2. Total length of the experiments was 7 h. In all the experiments mass balance was accomplished within ±8%.

The operating conditions were selected based on the experience acquired over previous studies carried out by other members of the research group.[9-12] As can be seen in these works, a temperature of 150 ºC was selected in order to achieve measurable reaction rates and, as a result, to obtain medium to large alcohol conversions using a moderate amount of catalysts and avoiding the negative effects of having an excessive load in the reactor. At 150 ºC it is possible to see differences in the catalytic behavior of the resins and, as a consequence, to select a resin (or several) that could be of industrial interest. Regarding the temperature stability of the resins (see Table 2.1), results gathered in Section 3.5 indicate that obtained data were hardly influenced by serious damage of resins morphology. On the other hand, performing experiments at the same temperature at which the previous studies were carried out allows us to study the influence of alcohol length chain on catalyst performance during the dehydration reaction (see Section 3.4). As for operating pressure (40 bar), it was selected in order to ensure that the reaction was carried out in the liquid phase. Previous simulations performed with the software Chemcad showed that an operating pressure of 40 bar ensures that reaction medium is always in the liquid-phase even when the amount of olefins (the most volatile compounds in the system), is high. Finally, at 500 rpm, 1 g of catalyst and bead size of 0.40 – 0.63 mm the dehydration of 1-butanol to di-n-butyl ether takes place free of the influence of mass transfer limitations or solid distribution effects (see Section 5.3.1).

In each experiment, 1-butanol conversion (X_{BuOH}), selectivity to products (S_j, the subscript j corresponding to each formed product) and DNBE yield (Y_{DNBE}) were estimated as follows:

$$X_{\mathrm{BuOH}} = \frac{\text{mol of 1-butanol reacted}}{\text{initial mol of 1-butanol}} \times 100 \quad [\text{\% mol/mol}] \tag{3.1}$$

$$S_{\mathrm{DNBE}} = \frac{\text{mol of 1-butanol reacted to form DNBE}}{\text{mol of 1-butanol reacted}} \times 100 \quad [\text{\% mol/mol}] \tag{3.2}$$

Selectivity to olefins ($S_{\text{1-butene}}$, $S_{\text{(E)2-butene}}$ and $S_{\text{(Z)2-butene}}$) branched ether 1-(1-methylpropoxy) butane ($S_{\text{BuOBu'}}$) and 2-butanol ($S_{\text{2-BuOH}}$) were defined similarly.

$$Y_{\mathrm{DNBE}} = \frac{\text{mol of 1-butanol reacted to form DNBE}}{\text{initial mol of 1-butanol}} \times 100 \quad [\text{\% mol/mol}] \tag{3.3}$$

In addition, initial reaction rate of DNBE formation (r^0_{DNBE}) was computed from the function of the experimental curve of DNBE mole (n_{DNBE}) vs. time according to:

$$r^0_{\mathrm{DNBE}} = \frac{1}{W_{\mathrm{cat}}} \left(\frac{dn_{\mathrm{DNBE}}}{dt} \right)_{t=0} \tag{3.4}$$

Initial turnover frequency for DNBE formation (TOF^0_{DNBE}) was estimated by dividing r^0_{DNBE} by the acid capacity:

$$TOF^0_{\mathrm{DNBE}} = \frac{r^0_{\mathrm{DNBE}}}{\text{acid capacity}} \tag{3.5}$$

3.3. Results and discussion

3.3.1. Reaction scheme of the catalytic dehydration of 1-butanol to DNBE

Dehydration of 1-butanol over the ion exchange resins tested leads to the formation of di-n-butyl ether as main product. Detected byproducts were C_4 olefins (1-butene, *trans*- and *cis*-2-butene), the branched ether 1-(1-methylpropoxy) butane and, in a much smaller amount, 2-butanol.

Figure 3.1 shows the evolution of the liquid phase composition over the course of an experiment conducted on Amberlyst 15. The products distribution on all tested resins is similar although it should be pointed out some significant differences: (1) over macroreticular resins with low crosslinking degree (Amberlyst 39 and Amberlyst 70) and gel type resins (Amberlyst 31, Amberlyst 121, Dowex 50x4 and Dowex 50x2) 2-butanol was not detected; (2) after 7 hours reaction time most resins showed higher selectivity to 2-butenes than to 1-butene except for Amberlyst 70, Amberlyst 121 and Dowex 50x2. This fact may be due to the very low total amount of butenes formed on these resins.

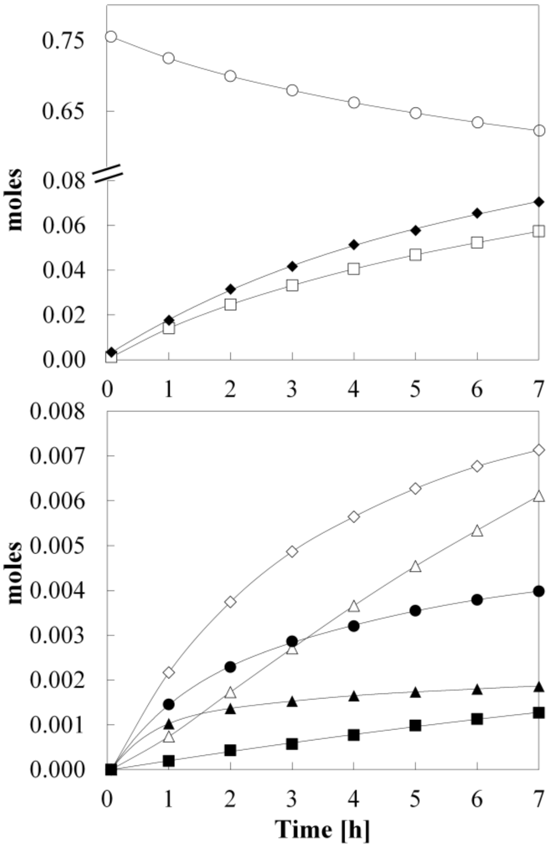

Figure 3.1. Evolution of the composition of the reaction medium with time. (○) 1-butanol, (♦) water, (□) DNBE, (▲) 1-butene, (◊) *trans*-2-butene, (●) *cis*-2-butene, (Δ) 1-(1-methylpropoxy) butane, (■) 2-butanol. 1g of Amberlyst 15, catalyst bead size = 0.400 - 0.630 mm, T = 150 °C, P = 40 bar, 500 rpm.

Distribution of products suggests the reaction network shown in Figure 3.2. Dehydration of 1-butanol to di-n-butyl ether is the main reaction (R1). Dehydration to olefins is the main side reaction (R2). The fact that at very low olefins concentration the major C_4 product was 1-butene whereas when the olefins concentration increases 2-butenes are favored, especially *trans*-2-butene, indicates that 1-butanol dehydrates to 1-butene which in turn isomerizes to *trans*-2-butene and *cis*-2-butene (R3), the *trans*-isomer being thermodynamically more stable. The resin sites are also active for catalyzing the reverse reactions of (R1) and (R2), ether hydrolysis (R4) and olefins hydration (R5). When olefins hydration takes place, the alcohol that is formed is no longer a primary alcohol. In addition to double bond isomerization, 2-butenes could be formed by hydration of 1-butene to 2-butanol and its subsequent dehydration, giving place to any of the three C_4 olefins. From the fact that 1-(1-methylpropoxy) butane was detected over all the resins despite the nonexistence of 2-butanol on some catalysts, it is inferred that the branched ether could be preferably formed by 1-butanol reaction with a C_4 olefin (R6) instead of by the reaction between 1-butanol and 2-butanol. Furthermore, the absence of 2,2'-oxydibutane indicates that intermolecular dehydration of two molecules of 2-butanol is not taking place, probably due to the low concentration of the secondary alcohol in the reaction medium.

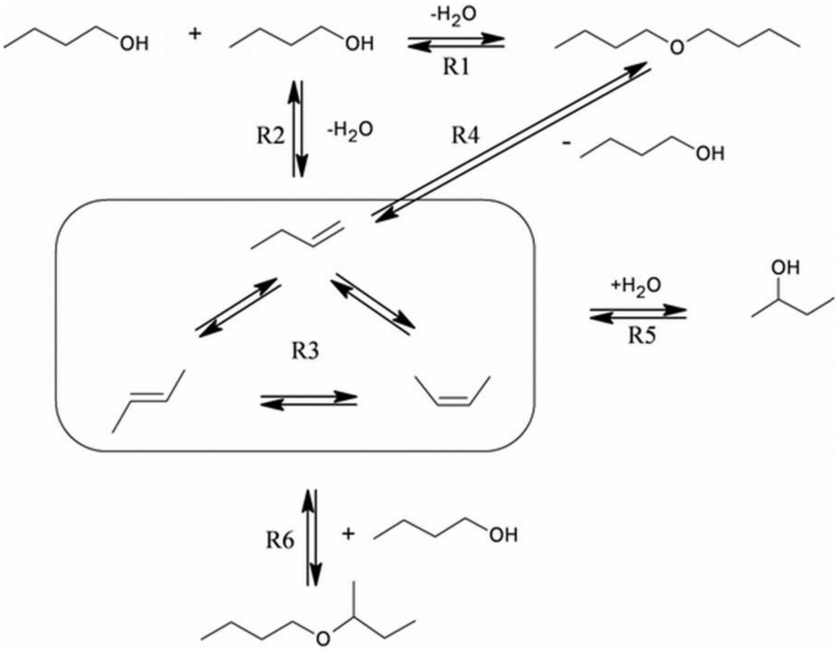

Figure 3.2. Scheme of reaction network.

3.3.2. Influence of resin morphology on 1-butanol conversion, initial reaction rate, selectivity to DNBE and DNBE yield

Table 3.2 shows 1-butanol conversion, selectivity to DNBE and byproducts, and yield of DNBE at 7 h reaction time. Initial reaction rate and turnover frequency of DNBE synthesis are also given. The data has a relative experimental error lower than ±4% for X_{BuOH}, ± 1% for S_{DNBE}, ± 5% for Y_{DNBE} and ± 7% for r^0_{DNBE} and TOF^0_{DNBE}. Due to the low concentration of byproducts in the reaction medium, $S_{\mathrm{byproducts}}$ data has in some cases a relative experimental error up to ± 20%.

Table 3.2. Conversion of 1-butanol, selectivity to DNBE and byproducts, yield to DNBE at 7 h reaction, initial reaction rate and turnover frequency for DNBE formation (1 g catalyst, catalyst bead size = 0.400 - 0.630 mm, T = 150 ºC, P = 40 bar).

Catalyst	X_{BuOH} %	S_{DNBE} %	$S_{1\text{-}Butene}$ %	$S_{(E)2\text{-}Butene}$ %	$S_{(Z)2\text{-}Butene}$ %	$S_{2\text{-}BuOH}$ %	$S_{BuOBu'}$ %	Y_{DNBE} %	r^0_{DNBE} mol/h kg	TOF^0_{DNBE} mol/h eq H^+
A-15	18.4	81.7	1.27	4.89	2.74	0.890	8.56	15.0	15.6	3.25
A-35	22.2	74.8	1.38	6.35	3.46	1.33	12.7	16.6	22.9	4.30
A-16	19.9	92.9	0.753	1.65	0.994	0.343	3.33	18.5	17.2	3.59
A-36	23.2	86.4	0.934	3.30	1.87	0.725	6.76	20.1	28.1	5.20
CT-482	19.3	95.8	0.707	0.917	0.634	0.215	1.74	18.4	15.8	3.72
A-70	14.1	98.7	0.479	0.120	0.096	trace	0.595	14.0	10.3	3.90
A-39	19.4	97.1	0.613	0.559	0.407	0.0798	1.21	18.8	16.1	3.21
Dow-8	19.4	96.2	0.644	0.795	0.551	0.191	1.60	18.7	15.8	3.26
A-31	18.9	98.1	0.513	0.321	0.235	0.0431	0.759	18.5	14.5	3.02
Dow-4	18.6	98.4	0.481	0.265	0.215	trace	0.679	18.3	13.8	2.79
A-121	17.6	99.1	0.423	0.0118	trace	0	0.440	17.5	13.2	2.75
Dow-2	18.4	98.9	0.379	0.151	0.136	0	0.458	18.2	12.7	2.64
A-46	3.25	98.7	trace	trace	trace	0	1.32	3.21	1.64	1.88

Taking into account that extended-duration experiments (>72 h) showed that equilibrium conversions are higher than 85% at the working conditions, it is seen that at the end of the experiments the reaction medium is still far from equilibrium. From data of Table 3.2 it can be concluded that the most active resins are the oversulfonated resins Amberlyst 36 and Amberlyst 35, whereas the most selective ones are Amberlyst 121 > Dowex 50Wx2 > Amberlyst 70 > Amberlyst 46 > Dowex 50Wx4 > Amberlyst 31. Resins Amberlyst 16 > Amberlyst 36 > Amberlyst 15 > Amberlyst 35 show the lowest selectivity to ether.

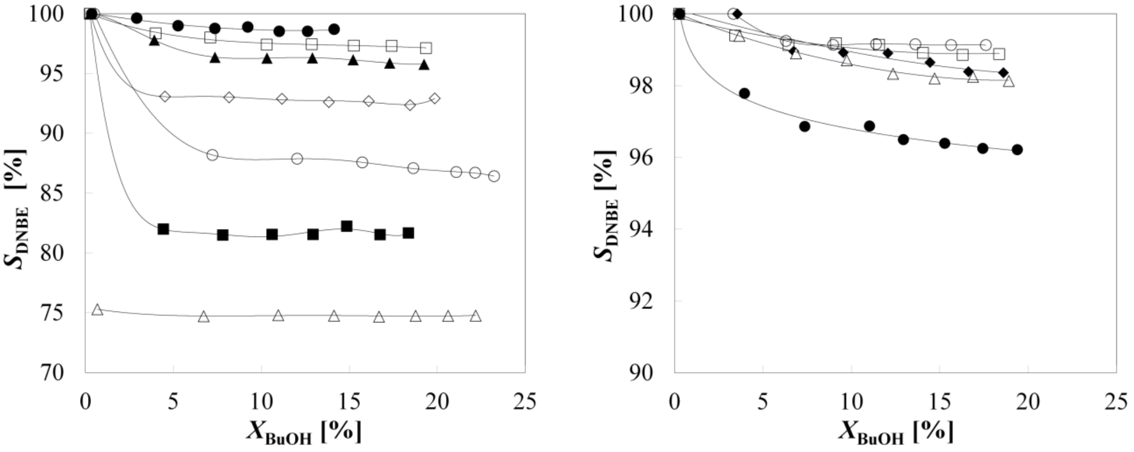

(a) (b)

Figure 3.3. S_{DNBE} as a function of 1-butanol conversion, X_{BuOH}.
(a) macroreticular resins: (●) A-70, (□) A-39, (▲) CT-482, (◊) A-16, (○) A-36, (■) A-15, (Δ) A-35.
(b) gel-type resins: (○) A-121, (□) Dow-2, (♦) Dow-4, (Δ) A-31, (●) Dow-8.
1 g catalyst, catalyst bead size = 0.400 – 0.630 mm, T = 150 ºC, P = 40 bar, 500 rpm.

By plotting the selectivity to DNBE as a function of X_{BuOH} (Figure 3.3) it is shown that, for all tested resins, S_{DNBE} initially decreases and then stabilizes. As a consequence, it can be concluded that at these alcohol conversions the differences observed in S_{DNBE} after 7 h of reaction time are not due to the different reaction extent on each catalyst. On the contrary, they are a consequence of the resins properties, in particular morphology and acid capacity.

In order to gain insight into the role that acid capacity and polymer morphology play on resins behavior, the response surfaces for conversion and selectivity as a function of acid capacity and V_{sp} (which, together with polymer chain density, is a suitable way of characterizing the polymeric structure of the resins gel type phase) have been represented in Figure 3.4. As seen, acid capacity is the parameter which plays the most important role regarding resins activity as it can be inferred from the almost vertical arrangement of colors in the response surface of Figure 3.4a. Nevertheless, selectivity to DNBE is influenced by both acid capacity and resin structure as it can be drawn from the diagonal arrangement of colors in the response surface of Figure 3.4b.

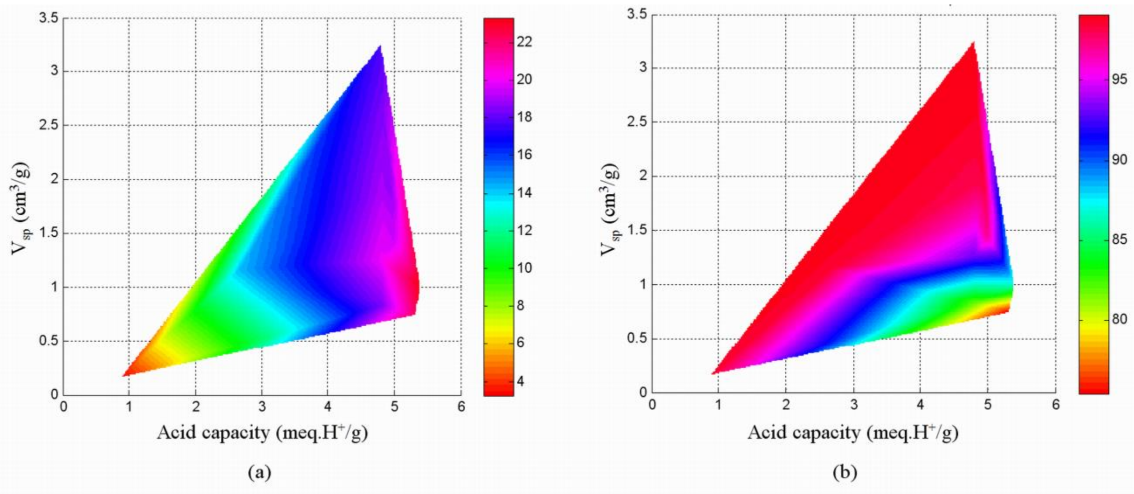

(a)
(b)

Figure 3.4. Response surfaces for: (a) 1-butanol conversion; (b) selectivity to DNBE as a function of V_{sp} and acid capacity.
t = 7 h, 1 g catalyst, catalyst bead size = 0.400 – 0.630 mm, T = 150 ºC, P = 40 bar, 500 rpm.

With the aim of achieving a deeper knowledge regarding the influence that acid capacity and polymer morphology have on resins behavior, obtained data have been arranged as shown in Figure 3.5. In this way it is easy to compare on one hand, the behavior of resins having the same acid capacity but different polymeric structure and, on the other hand, resins with similar values of swollen polymer volume but different acid capacity. Data corresponding to Amberlyst 46 have been omitted in Figures 3.5a, c and d for the sake of clarity.

From Figure 3.5 it can be assumed that a higher acid capacity is essential for a more active catalyst (Figures 3.5a and c) but it also seems to affect the catalyst selectivity to DNBE in a negative way (Figure 3.5b). Regarding polymer morphology, it plays a decisive role on resin selectivity to DNBE and, although not as significant as acid capacity, it also influences catalytic activity. These facts can be observed by comparing resins with similar acid capacity but different pore structure: (1) Amberlyst 35 and Amberlyst 36 (5.3 meq.H$^+$/g), and (2) Amberlyst 15, Amberlyst 16, Amberlyst 39, Dowex 50Wx8, Amberlyst 31, Dowex 50Wx4, Amberlyst 121 and Dowex 50Wx2 (around 4.8 meq.H$^+$/g). It can be seen that, as V_{sp} rises, S_{DNBE} progressively increases until reaching an almost constant value of about 98 – 99% with gel-type resins containing ≤ 4 % DVB (Figure 3.5b). However, in spite of the improvement in catalytic activity observed when the V_{sp} increases from 0.823 cm^3/g (Amberlyst 15) to 1.245 cm^3/g (Amberlyst 16) a further increase in V_{sp} leads to a slight reduction of the resin activity (Figures 3.5a and c).

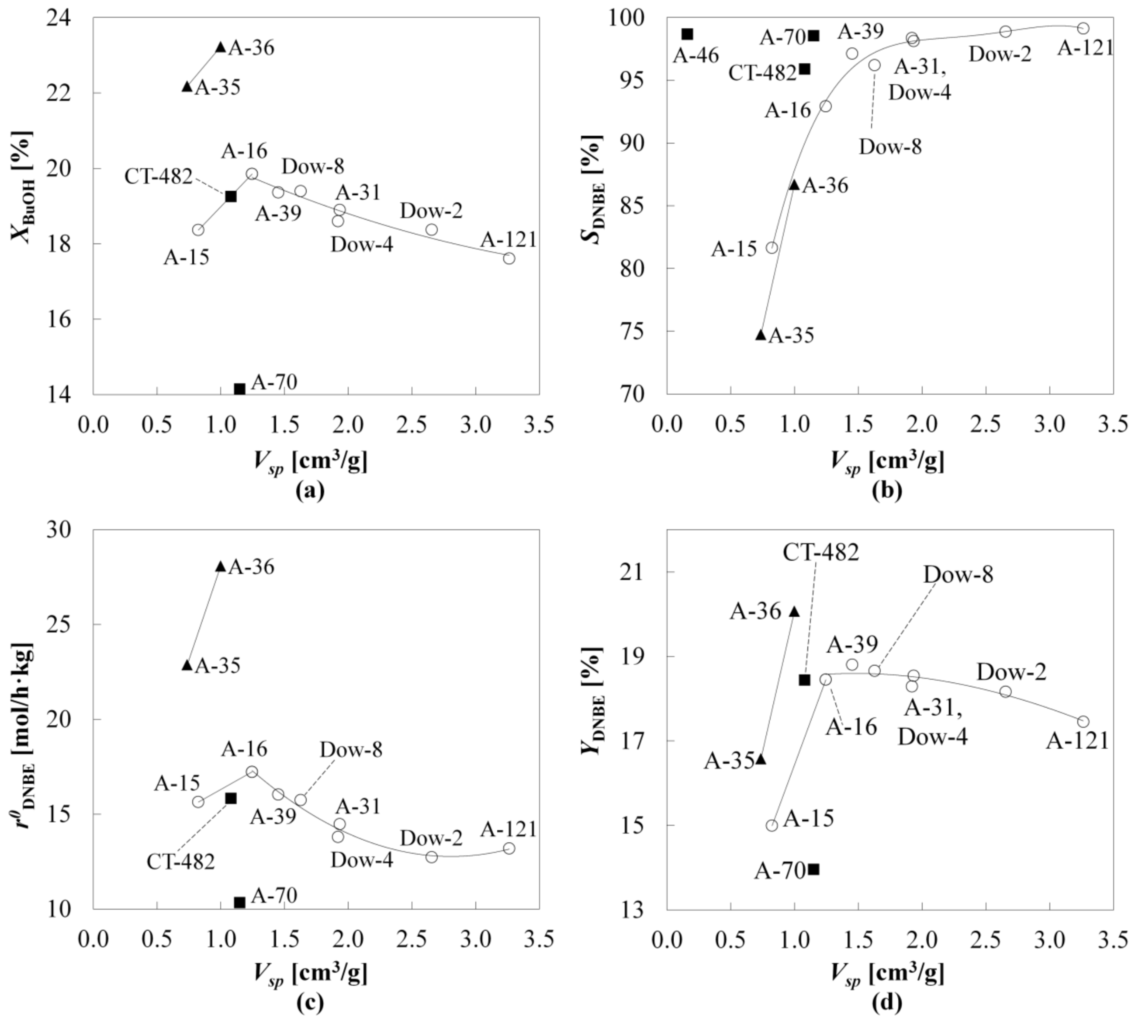

Figure 3.5. Influence of V_{sp} on: (a) 1-BuOH conversion; (b) selectivity to di-n-butyl ether; (c) initial reaction rate for DNBE synthesis; (d) DNBE yield.
(○) resins with 4.8 meq.H+/g; (♦) resins with 5.3 meq.H+/g; (■) resins with other values of acid capacity.
t = 7 h, 1 g catalyst, catalyst bead size = 0.400   0.630 mm, T = 150 °C, P = 40 bar, 500 rpm.

It is a well-established fact that the alcohol dehydration reaction occurs mainly in the swollen polymer mass.[9] Dehydration to ether follows an S_N2 reaction mechanism in which 2 alcohol molecules are involved, whereas dehydration to olefins occurs by a monomolecular reaction of elimination, E1.[13] As Figure 2.2 shows, the tested resins have zones of different density or polymer chain concentration in the swollen polymer mass ranging from 0.1 to 2.0 nm/nm^3. Very high polymer concentration (2 nm/nm^3) entails a very dense polymer mass, poorly accessible to 1-butanol which leads to a lower catalytic activity. Furthermore, in this dense polymer zone the S_N2 reaction is limited to a great extent by steric hindrance and the occurrence of the E1 reaction increases, hence giving place to lower S_{DNBE}. On the other hand, low polymer concentration corresponding to a greatly expanded polymer enhances selectivity to DNBE. However, too low polymer concentration gives place to a significant distance among its active centers. In this case the probability of disposing the precise orientation of sulfonic groups to form the reaction intermediate lessens and resins activity decreases. Thus, medium values of polymer chain concentration may favor 1-butanol conversion. That could explain the behavior observed in Figures 3.5a and c where, among resins with acid capacity around 4.8 meq. H$^+$/g, Amberlyst 16 (V_{sp} = 1.245 cm^3/g; polymer density = 0.8 – 1.5 nm/nm^3) shows a 1-butanol conversion and initial reaction rate higher than those determined on gel-type resins (which have higher V_{sp} but polymer densities ranging between 0.2 – 0.8 nm/nm^3). TOF^{0}_{DNBE} data (Table 3.2) confirm that resins with medium V_{sp} values show higher reaction rates per catalytic site.

As for the thermostable resins Amberlyst 70 and CT482, the latter has a V_{sp} of 1.081 cm^3/g and an acid capacity of 4.25 meq. H$^+$/g (Table 3.1). This value of acid capacity is not very different from 4.8 meq. H$^+$/g and, as seen in Figures 3.5a and c, catalytic activity of resin CT482 is in agreement with data obtained for resins with 4.8 meq. H$^+$/g. Amberlyst 70 shows lower 1-butanol conversion because of its low acid capacity (2.65 meq. H$^+$/g, Table 3.1). Furthermore, it can be seen that selectivity to the linear ether over Amberlyst 70, as well as over Amberlyst 46, is equal to the maximum S_{DNBE} value found which corresponds to the gel-type resins Amberlyst 121 and Dowex 50Wx2. This high selectivity (and therefore, high DNBE content in the final product) is extremely desirable from an environmental standpoint, in addition to the obvious impact on capital requirements and operating costs.

As seen in Figure 3.5d the highest DNBE yield is achieved on Amberlyst 36, nonetheless, gel-type resins and Amberlyst 70 are more selective to the linear ether which makes them more appropriate for industrial use. Among them, Amberlyst 70 can be considered as the most suitable catalyst due to its thermal stability.

Finally, Figure 3.6 shows the combined effect of acid capacity and V_{sp} on S_{DNBE} for all tested resins. As can be seen, S_{DNBE} correlates quite well with the ratio acid capacity/V_{sp} showing that selectivity to DNBE increases as the number of acid sites per volume unit of swollen polymer (acid density) decreases.

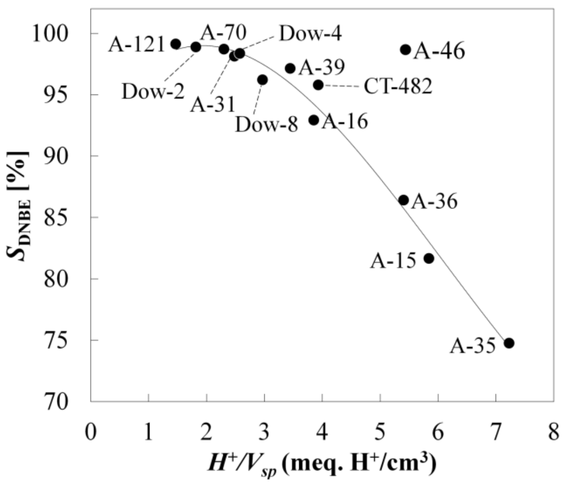

Figure 3.6. Selectivity to di-n-butyl ether as a function of H^+/V_{sp}.
t = 7 h, 1 g catalyst, catalyst bead size = 0.400 – 0.630 mm, T = 150 ºC, P = 40 bar, 500 rpm.

3.4. Comparison with DNPE, DNHE and DNOE

The liquid phase dehydration of 1-pentanol[9,10], 1-hexanol[11] and 1-octanol[12] over ion exchange resins have been studied in previous works. In this section, a comparative study between these three systems and the dehydration of 1-butanol is presented. Figure 3.7 and Figure 3.8 show, respectively, the alcohol conversion and the selectivity to the linear ether for the four systems. As it can be seen, in macroreticular resins with high and medium crosslinking degree (Amberlyst 15, Amberlyst 35, Amberlyst 16 and Amberlyst 36) alcohol conversion and selectivity to the corresponding ether depend on the size of the alcohol: the lower the size of the alcohol molecule, the higher the alcohol conversion and the selectivity to the linear ether. This trend is considerably lower over macroreticular resins with low crosslinking degree (Amberlyst 70 and Amberlyst 39) and is almost nonexistent over the gel type resins (Amberlyst 31, Amberlyst 121 and Dowex 50Wx4). Gel type resins are able to swell enough as to accommodate without problems even the higher alcohols. However, macroreticular resins present a polymeric structure more rigid and poorly accessible. In these resins the lower size of the alcohol (and the corresponding linear ether) enhances the accessibility to the active center and the formation of the ether.

Regarding resin Amberlyst 46 (sulfonated exclusively at the polymer surface), differences in alcohol conversion and selectivity between the four systems are not important. In this resin active centers are located on the catalyst surface, therefore accessibility of alcohol molecules to the active centers is not influenced by the size of the reactant. Furthermore, over the catalyst surface the formation of the linear ether is not sterically hindered with respect to olefin formation.

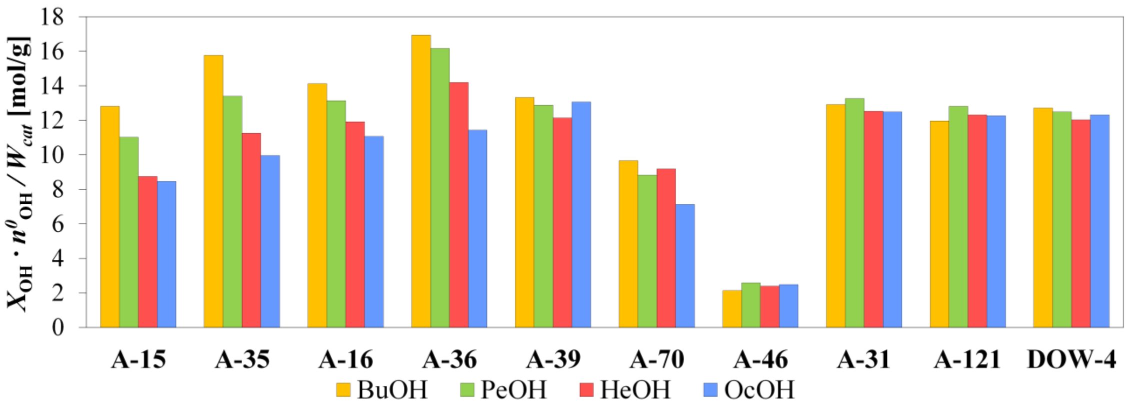

Figure 3.7. Alcohol conversion ($X_{OH} \cdot n^0_{OH}/W_{cat}$) for 1-butanol, 1-pentanol, 1-hexanol and 1-octanol dehydration at 6 h of reaction and 423 K.

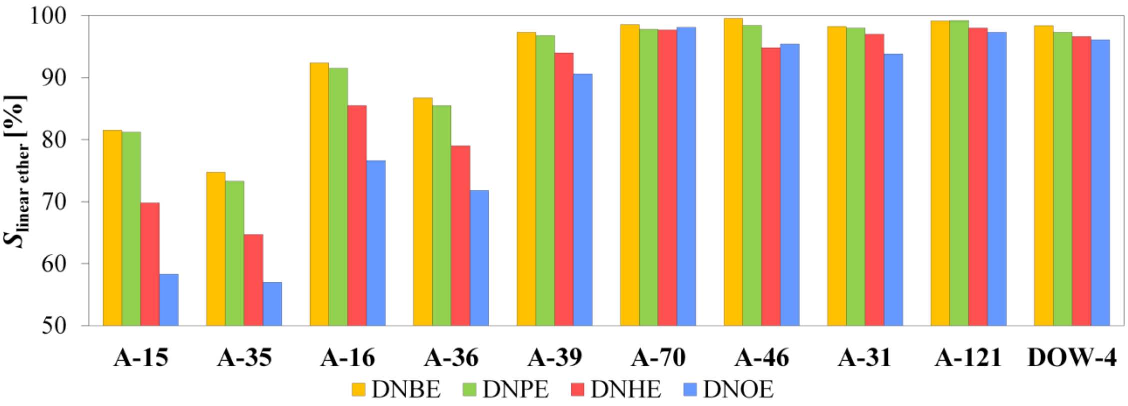

Figure 3.8. Selectivity to linear ether for 1-butanol, 1-pentanol, 1-hexanol and 1-octanol dehydration at 6 h of reaction and 423 K.

3.5. Thermal stability and reusability

An additional series of experiments was performed over Amberlyst 31 and Amberlyst 15 to test their thermal stability and reusability. These two resins were selected because they have a maximum operating temperature (120 and 130 ºC respectively) very much lower than 150 ºC.

Each resin was used for three cycles. In the first cycle fresh catalyst was used following the experimental procedure described in Section 3.2. After a 7 h experiment the reactor was cooled at the room temperature, catalyst was filtered out from the reaction medium, washed with 25 ml of methanol, dried at ambient temperature for 24 h then dried at 110 ºC, firstly at 1 bar for 2 h and then at 10 mbar for 15 h before being subjected to a new reaction cycle.

Afterwards, BET surface area and acid capacity were measured and compared to those of fresh catalyst.

As shown in Table 3.3, both resins experience some loss of sulfonic acid groups after 3 cycles (fresh resin plus two reused cycles; 21 h of accumulated working time). BET surface area increases moderately in the case of Amberlyst 15.

Table 3.3. Acid capacity and BET surface area of fresh and reused catalysts after 3 reaction cycles.
7 h, 150 ºC, 40 bar

Catalyst	Acid site loss[a] (%)	S_{BET}[b] (m^2/g)	
		Fresh	Reused
Amberlyst 15	11.6 ± 3.3	42.01	43.7
Amberlyst 31	8.6 ± 1.9	0.10	0.10

[a] Titration against standard base following the procedure described by Fisher and Kunin.[14]
[b] BET (Brunauer-Emmet-Teller) surface area.

Despite the small morphological and acid capacity change, the performance of the two resins remains constant throughout the 3 cycles, as it can be seen in Figure 3.9, pointing out that results gathered in Section 3.3.2 are not influenced by thermal deactivation and resins can be reused a few cycles. In order to take into account the differences in initial alcohol and catalyst mass (due to small catalyst losses during the process of resin recovering and cleaning), the factor $X_{BuOH}{\cdot}n^0_{BuOH}/W_{cat}$ is used instead of X_{BuOH}. The differences observed for r^0_{DNBE} between data in Figure 3.9 and values gathered in Table 3.2 for Amberlyst 31 and Amberlyst 15 are due to the fact that in this series of experiments the injector was not used. Thus, catalyst was charged into the reactor and then heated to 150 ºC; the moment at which this temperature was reached was considered as the beginning of the experiment (zero time). It is to be noted that despite this change of methodology the results are quite similar. It is concluded from these reuse experiments that data reported in Table 3.2 are reliable. It can be accepted that accessible zone of resins increases on losing active centers, and this effects are mutually balanced. However, as resins show a clear trend to morphological instability it is suitable to use in industrial applications resins with high thermal stability such as Amberlyst 70.

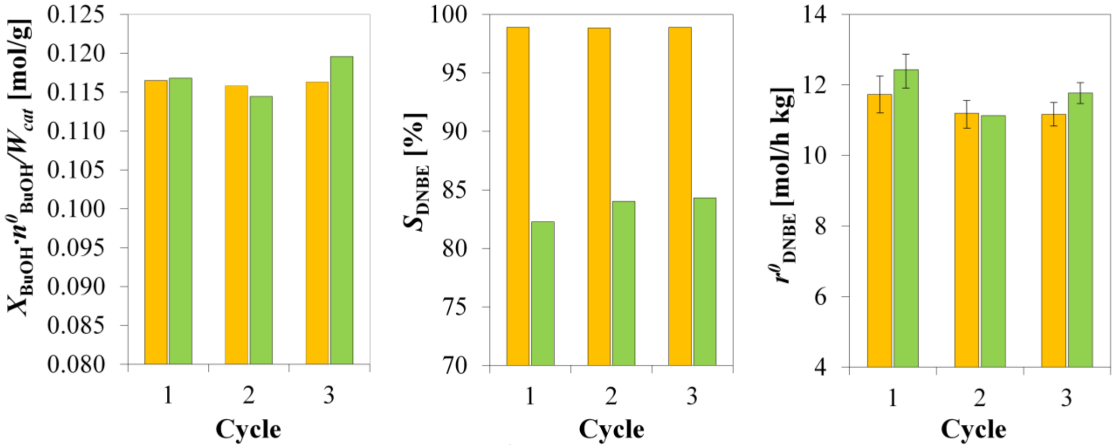

Figure 3.9. Conversion of 1-butanol ($X_{BUOH}{\cdot}n^0_{BuOH}/W_{cat}$) and selectivity to DNBE (S_{DNBE}) at 7 h reaction and initial reaction rate for DNBE formation in reusability tests.
(green) Amberlyst 15, (orange) Amberlyts 31
1 g catalyst, catalyst bead size = 0.400 – 0.630 mm, T = 150 ºC, P = 40 bar.

3.6. Influence of typical 1-butanol impurities

Nowadays two important routes on industrial scale for the synthesis of 1-butanol are a petrochemical route based on the Oxo process and the ABE (Acetone-Butanol-Ethanol) fermentation process (see Section 1.3.1.1 for details). If 1-butanol is produced by the Oxo process the main impurity is 2-methyl-1-propanol (isobutanol) whereas if it is produced by the ABE fermentation process the impurities are ethanol and acetone.

The aim of this section is to report the influence of typical 1-butanol impurities on the dehydration of 1-butanol to DNBE. For that, a set of experiments was carried out with different mixtures of 1-butanol:isobutanol (95:5 and 90:10 % w/w) and 1-butanol:ethanol:acetone (95:2.5:2.5 and 90:5:5 % w/w) over the highly selective resins Amberlyst 70, Amberlyst 31 and Amberlyst 121. The experimental procedure and reaction conditions were the same as those described in Section 3.2.

3.6.1. Influence of 2-methyl-1-propanol (isobutanol)

Figure 3.10 shows the influence of isobutanol presence on the dehydration of 1-butanol to DNBE at 7 h reaction time. As seen, the trend is very similar over the three tested resins: the selectivity to DNBE decreases upon increasing the initial concentration of the branched alcohol mainly due to the increase in 1-(1-methylpropoxy) butane formation (R7). It is quoted in the open literature that alcohols can undergo alkyl group transpositions.[15] In primary alcohols, after protonation to form the alkyloxonium ion, steric hindrance interferes in the direct displacement of the leaving group (water) by the nucleophile; instead water leaves at the same time as the alkyl group shifts from the adjacent carbon to skip the formation of the unstable primary carbocation. This mechanism is known as “Concerted Alkyl Shift” (Figure 3.11). Thus, the increasing amounts of 1-(1-methylpropoxy) butane detected when isobutanol is initially present in the reaction medium is explained by the reaction of 1-butanol with the secondary carbocation which results from isobutanol dehydration and alkyl group shift. The rearrangement of products during isobutanol dehydration in the presence of strong Brönsted acid sites is also reported by Kotsarenko and Malysheva.[16] 1-(2methylpropoxy) butane was also detected in the reaction medium over the three tested resins when isobutanol was added into the feed composition. This new branched ether is formed when a molecule of isobutanol reacts with a molecule of 1-butanol (R8).

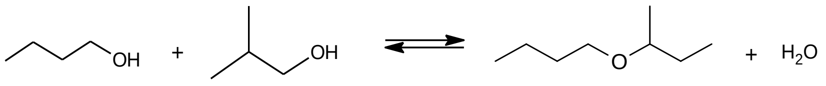

(R7)

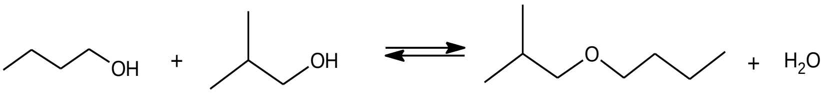

(R8)

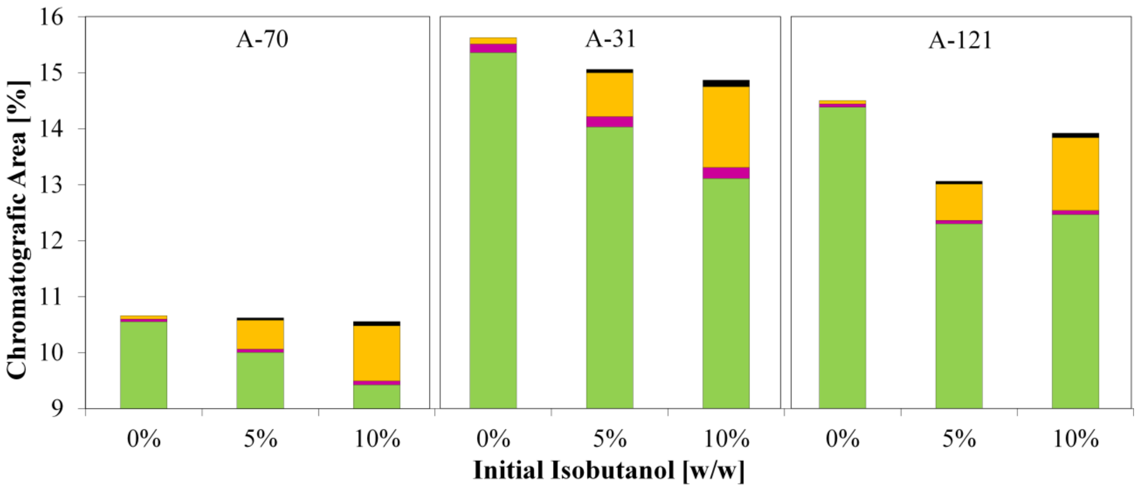

Figure 3.10. Influence of 2-methyl propanol on the dehydration of 1-butanol to DNBE at 7 h reaction. (🟩) DNBE, (🟪) Olefins, (🟨) 1-(1-methylpropoxy) butane, (■) 1-(2-methylpropoxy) butane. *T* = 150 ºC, *P* = 40 bar, 500 rpm, 1 g catalyst, catalyst bead size = 0.400 – 0.630 mm.

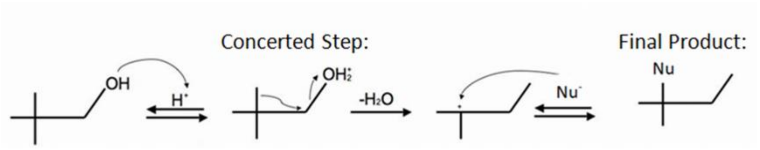

Figure 3.11. Mechanism of Concerted Alkyl Shift.

No significant change was observed in olefins concentration despite the addition of isobutanol to the reaction medium. Olefin 2-methyl propene (isobutylene) consequence of isobutanol intramolecular dehydration was not detected at these reaction conditions, probably due to the low isobutanol initial concentration and conversion extent. However, even though the amount of olefins, which are the most problematic byproduct, hardly changes by the isobutanol presence in the initial reaction mixture, it should be avoided as it increases the formation of branched ethers which present worse performance properties than the linear ether.[17]

3.6.2. Influence of ethanol and acetone

Two new byproducts were mainly detected when ethanol and acetone were added into the feed composition: the major one was ethyl butyl ether (EBE) which is formed by the dehydration reaction between a molecule of 1-butanol and a molecule of ethanol (R9); the other one, detected only in very low amounts, was di-ethyl ether (DEE) which is the product of ethanol intermolecular dehydration (R10).

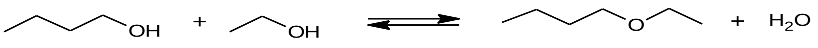

(R9)

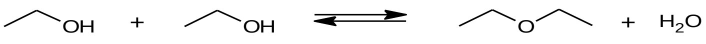

(R10)

As it can be seen in Figure 3.12 selectivity to DNBE decreased whereas EBE formation increased when the initial amount of ethanol rises even at high 1-butanol:ethanol initial ratios. Similarly, in the dehydration reaction of 1-octanol/ethanol mixtures at 150 ºC over acidic ion exchangers, ethers with lower molecular weight are preferentially formed.[18] Under the present experimental conditions the small amount of DEE detected is due to the high initial 1-butanol:ethanol ratios. DEE must be avoided as it cannot be blended directly into commercial diesel fuels.

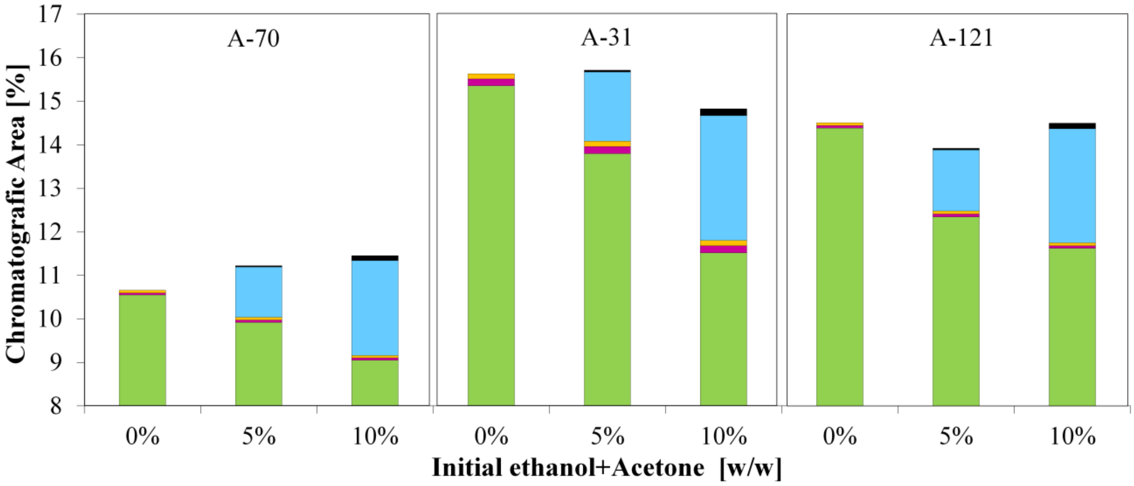

Figure 3.12. Influence of ethanol and acetone on the dehydration of 1-butanol to DNBE at 7 h reaction. (🟩) DNBE, (🟪) Olefins, (🟨) 1-(1-methylpropoxy) butane, (🟦) Ethyl butyl ether, (■) Diethyl ether. *T* = 150 ºC, *P* = 40 bar, 500 rpm, 1 g catalyst, catalyst bead size = 0.400 – 0.630 mm.

Regarding acetone reactivity, its condensation/dehydration forming mesityl oxide (MSO) and water over Amberlyst 16 in the temperature range 100 – 120 ºC has been quoted.[19] Still, under the current experimental conditions acetone hardly react and only very low amounts of 2-propanol were detected (always less than 0.04% chromatographic area/g of catalyst). 2-Propanol could be the product of the acetone hydrogenation catalyzed by a component of stainless steel tubing's and reactor walls such as nickel or iron. The amount of olefins (1-butene, *trans*-2-butene and *cis*-2-butene) and the branched ether 1-(1-methylpropoxy) butane did not experiment significant changes despite ethanol/acetone addition. Comparing the catalytic behavior of the three resins it can be concluded that, as found when isobutanol was added, the presence of ethanol and acetone in the medium does not change significantly the general trend observed when 1-butanol is free of impurities.

3.7. Conclusions

Sulfonic S/DVB resins were shown to be suitable catalysts for the dehydration reaction of 1-butanol to di-n-butyl ether in the liquid phase. Activity (reaction rate and conversion of 1-butanol) was enhanced with higher acid capacity (oversulfonated resins) and with medium values of swollen polymer volume (0.823 – 1.245 cm^3/g). Very high polymer concentration results in a very dense polymer mass, poorly accessible to 1-butanol. On the contrary, very low polymer concentration corresponds to a greatly expanded polymer which results in a large distance between its active centers. As a result, the probability of disposing the precise conformation of sulfonic groups to form the reaction intermediate lessens and 1-butanol conversion decreases. Amberlyst 36 (oversulfonated, medium values of %DVB) proved to be the most active catalysts tested. However, gel-type resins (which have a flexible morphology and are able to greatly swell in the reaction medium) and the resins Amberlyst 70 and Amberlyst 46 were more selective to DNBE; the resin Amberlyst 121 being the most selective. DNBE formation follows an S_N2 reaction mechanism in which two molecules of 1-butanol are involved, whereas dehydration to butenes occurs through a monomolecular reaction of elimination, E1. As a consequence, in highly expanded polymers the S_N2 reaction is not limited by steric hindrance yielding higher selectivity to the linear ether. In addition, a clear relationship between selectivity and H^+/V_{sp} ratio was observed; the resins with lowest H^+/V_{sp} being the most selective.

The presence of 2-methyl-1-propanol in the initial reactant mixture enhanced the formation of branched ethers, which have worse properties as diesel components than linear ones. However no significant changes were observed in the concentration of olefins which are the most troublesome byproducts regarding the sought properties for fuel additives. On the other hand, the presence of ethanol and acetone leaded to the formation of ethyl butyl ether and, in a much lesser extent, di-ethyl ether. Di-ethyl ether must be avoided as it cannot be blended directly into commercial diesel fuels.

Nomenclature

Notation

n_{DNBE}	Mole of di-n-butyl ether
n^{0}_{DNBE}	Initial mole of di-n-butyl ether
r^{0}_{DNBE}	Initial reaction rate of DNBE formation
S_j	Selectivity to product *j*
t	Time
TOF^{0}_{DNBE}	Initial turnover frequency for DNBE formation
V_{sp}	Volume of swollen polymer mass
W_{cat}	Mass of catalyst
X_{BuOH}	Conversion of 1-butanol
Y_{DNBE}	Yield to di-n-butyl ether

Abbreviations

2-BuOH	2-Butanol
ABE	Acetone-Butanol-Ethanol
AAS	Amorphous aluminosilicates
BET	Brunauer-Emmet-Teller
BuOH	1-Butanol
BuOBu’	1-(1-methylpropoxy) butane
DEE	Di-ethyl ether
DNBE	Di-n-butyl-ether
EBE	Ethyl butyl ether
ISEC	Inverse Steric Exclusion Chromatography
MSO	Mesityl oxide
WHSV	Weight hourly space velocity

References

[1] Starkey, L. S. Synthesis of ethers. *Introduction to strategies for organic synthesis*, John Wiley & Sons, Inc.: Hoboken, New Jersey, 2012.

[2] Sheldon, R. A.; van Bekkum, H. Solid acid catalysis: miscellaneous. *Fine chemical through heterogeneous catalysis*, Wiley-VCH Verlag GmbH: Weinheim, Germany, 2000.

[3] Makarova, M. A.; Paukshtis, E. A.; Thomas, J. M.; Williams, A.; Zamaraev, K. I. Dehydration of n-butanol on zeolite H-ZSM-5 and amorphous aluminosilicate: detailed mechanistic study and the effect of pore confinement. *J. Catal*. **1994**, *149*, 36-51.

[4] Bautista, F. M.; Delmon, B. 1-Butanol dehydration on $AlPO_4$ and modified $AlPO_4$: catalytic behaviour and deactivation. *Appl. Catal., A.* **1995**, *130*, 47-65.

[5] Brandão, P.; Philippou, A.; Rocha, J.; Anderson, M. W. Dehydration of alcohols by microporous niobium silicate AM-11. *Catal. Lett*. **2002**, *80* (3-4), 99-102.

[6] Nel, R. J. J.; de Klerk, A. Dehydration of C_5-C_{12} linear 1-alcohols over η-alumina to fuel ethers. *Ind. Eng. Chem. Res*. **2009**, *48*, 5230-5238.

[7] Choi, J. H.; Kim, J. K.; Park, D. R.; Park, S.; Yi, J.; Song, I. K. Etherification of n-butanol to di-n-butyl ether over $H_3PMo_{12-x}W_xO_{40}$ (x=0, 3, 6, 9, 12) Keggin and $H_6P_2Mo_{18-x}W_xO_{62}$ (x=0, 3, 9, 15, 18) Wells–Dawson heteropolyacid catalysts. *Catal. Commun*. **2001**, *14*, 48-51.

[8] Kim, J. K.; Choi, J. H.; Song, J. H.; Yi, J.; Song, I. K. Etherification of n-butanol to di-n-butyl ether over $H_nXW_{12}O_{40}$ (X = Co^{2+}, B^{3+}, Si^{4+}, and P^{5+}) Keggin heteropolyacid catalysts. *Catal. Commun*. **2012**, *27*, 5-8.

[9] Tejero, J.; Cunill, F.; Iborra, M.; Izquierdo, J. F.; Fité, C. Dehydration of 1-pentanol to di-n-pentyl ether over ion-exchange resin catalysts. *J. Mol. Catal. A: Chem*. **2002**, *182,* 541-554.

[10] Bringué, R.; Iborra, M.; Tejero, J.; Izquierdo, J. F.; Cunill, F.; Fité, C.; Cruz, V. F. Thermally stable ion-exchange resins as catalysts for the liquid-phase dehydration of 1-pentanol to di-n-pentyl ether (DNPE). *J. Catal*. **2006**, *244*, 33-42.

[11] Medina, E.; Bringué, R.; Tejero, J.; Iborra, M.; Fité, C. Conversion of 1-hexanol to di-n-hexyl ether on acidic catalysts. *Appl. Catal., A*. **2010**, *374*, 41-47.

[12] Casas, C.; Bringué, R.; Ramírez, E.; Iborra, M.; Tejero, J. Liquid-phase dehydration of 1-octanol, 1-hexanol and 1-pentanol to linear symmetrical ethers over ion exchange resins. *Appl. Catal., A*. **2011**, *396*, 129-139.

[13] Olah, G. H.; Shamma, T.; Surya-Prakash, G. K. Dehydration of alcohols to ethers over Nafion-H, a solid perfluoroalkanesulfonic acid resin catalyst. *Catal. Lett*. **1997**, *46*, 1-4.

[14] Fisher, S.; Kunin, R. Routine exchange capacity determinations of ion exchange resins. *Anal. Chem*. **1955**, *27*, 1191-1194.

[15] Vollhardt, K.P.C.; Schore, N. E. Transposiciones de carbocationes. *Química Orgánica*, 2nd Edition; Ed. Omega: Barcelona, Spain, 2000.

[16] Feeley, O. C.; Johansson, M. A.; Herman, R. G.; Klier, K. Isobutene from isobutanol/methanol mixtures over inorganic acid catalysts, *Prepr. Div. Fuel Chem*. ACS. **1992**, *37*, 1817–1824.

[17] Pecci, G. C.; Clerici, M. G.; Giavazzi, F.; Ancillotti, F.; Marchionna, M.; Patrini, R. In *Oxygenated diesel fuels-structure and properties correlation*, Proceeding of the IX International Symposium on Alcohol Fuels, Firenze, Italy, 1991; vol. 1, pp. 321–335.

[18] Guilera, J.; Bringué, R.; Ramirez, R.; Iborra, M.; Tejero, J. Comparison between ethanol and diethyl carbonate as ethylating agents for ethyl octyl ether synthesis over acidic ion-exchange resins. *Ind. Eng. Chem. Res*. **2012**, *51*, 16525-16530.

[19] du Toit, E.; Schwarzer, R.; Nicol, W. Acetone condensation on a cation exchange resin catalyst: the pseudo equilibrium effect. *Chem. Eng. Sci*. **2004**, *59*, 5545-5550.

4. THERMODYNAMIC EQUILIBRIUM[*]

In this house, we obey the laws of Thermodynamics!

-- Homer Simpson.

---

[*] Results presented in this chapter have been published in:

Pérez-Maciá, M. A.; Bringué, R.; Iborra, M.; Tejero, J.; Cunill, F. Thermodynamic equilibrium for the dehydration of 1-butanol to di-n-butyl ether. *Chem. Eng. Res. Des.* **2015**, *102*, 186–195.

4.1. Introduction

In the previous chapter it was demonstrated that di-n-butyl ether can be successfully synthesized through the bimolecular dehydration of 1-butanol over acidic ion-exchange resins. Among the tested resins, Amberlyst 70 proved to be the most suitable catalyst for industrial use due to its high selectivity to DNBE and its thermal stability, up to 463 K.

In order to develop a potential industrial process a reliable knowledge of the chemical equilibrium and the kinetics of the reactions is required. However, to the best of our knowledge, equilibrium data for the liquid-phase DNBE synthesis have not been reported yet and the few kinetic studies on 1-butanol dehydration have been carried out at experimental conditions in which butenes (resulting from 1-butanol intramolecular dehydration) are the main products.

To overcome the lack of thermodynamic data, in this chapter experimental values of the equilibrium constant of 1-butanol to di-n-butyl ether and water determined by direct measurement of the composition of the liquid mixture at equilibrium are presented. The equilibrium constants of potential side reactions (intramolecular dehydration of 1-butanol to 1-butene, isomerization of 1-butene to *cis*-2-butene and *trans*-2-butene, olefins hydration to 2-butanol and 1-(1methylpropoxy) butane formation from the reaction between 1-butanol and the olefins) were also determined. From these values, thermodynamic properties such as the standard enthalpy change $\Delta_r H^0_{(l)}$, the standard entropy change $\Delta_r S^0_{(l)}$ and the standard Gibbs energy $\Delta_r G^0_{(l)}$ of reactions were computed and compared with estimated and experimental values found in data banks. Whenever possible, recommended values for these thermochemical properties, as well as for the standard enthalpy of formation ($\Delta_f H^0_{(l)}$) and for the standard molar entropy ($S^0_{(l)}$) for the compounds present in the system are provided.

The liquid-phase kinetics of the synthesis of DNBE from 1-butanol, necessary for reactor design purposes, will be addressed in the next chapter.

4.2. Experimental procedure

Preliminary experiments carried out at 423 K and 40 bar showed that, when starting from pure 1-butanol, equilibrium conversions are higher than 85%. Because an important amount of di-n-butyl ether and water was expected in the reaction medium and given their immiscibility, 1,4-dioxane was used as a solvent to avoid liquid phase separation. The selection of the solvent was made taking into account its stability under the working conditions (blank experiments showed that 1,4-dioxane does not undergo any chemical reaction); its lack of influence on the catalyst structure[1]; and because it was found in previous works that the use of this solvent does not alter the value of the chemical equilibrium constant.[2]

Wet resin Amberlyst 70 (as provided by the supplier) was dried at 383 K, firstly at 1 bar during 2 h and then at 10 mbar overnight. The catalyst and 70 ml of different mixtures of 1,4-dioxane, 1-butanol, DNBE, water, 1-butene, *cis*-2-butene and 2-butanol, with a composition presumably close to the equilibrium composition, were charged into the reactor. The mass of loaded catalyst ranged from 1 to 7 g. In order to adjust the time needed to reach the equilibrium at the different working temperatures a higher amount of catalyst in experiments carried out at low temperature was used. After checking for leaks, the stirring speed was set at 500 rpm and the mixture was heated up to the working temperature (413 – 463 K). When the temperature set point was reached the pressure was adjusted up to 40 bar by means of N_2 in order to ensure liquid phase medium.

To follow the variation of the composition of the liquid mixture with time, liquid samples were taken out periodically and analyzed in-line as mentioned in Section 2.3.2. Experiments were considered finished when the calculated equilibrium constants had the same value along time, within the limits of experimental uncertainties.

4.3. Results and discussion

4.3.1. Equilibrium constants

In the previous chapter it was showed that the dehydration of 1-butanol over ion exchange resins gives place to di-n-butyl ether and water as the main products. Besides DNBE, some side products were detected in the reaction medium. Following, all the reactions that take part in the reaction medium are enumerated.

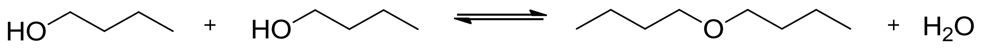

··· R1*

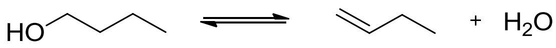

……………………………..…………….. R2*

……………………….. R3


……………………………………………………..… R4

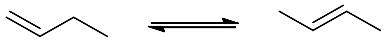
……………………………………………………..… R5*

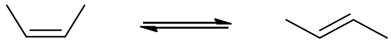
……………………………………………………..… R6*

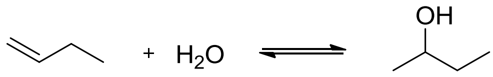

…………………..…..………………… R7*

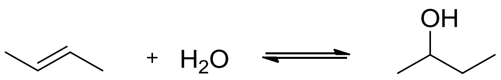

………………………………………… R8

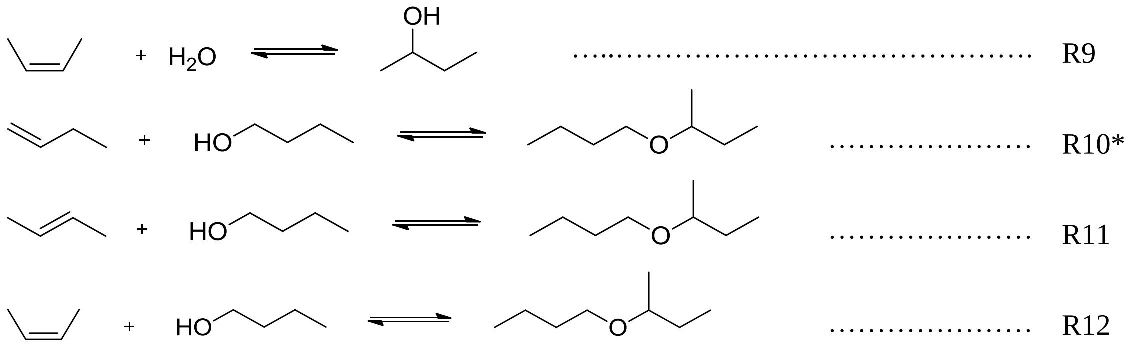

Scheme 4.1

R1 is the bimolecular dehydration of 1-butanol to DNBE and water; 1-butene can be formed by intramolecular dehydration of 1-butanol, R2, or by DNBE decomposition, R3. DNBE decomposition produces also 1-butanol. 1-butene isomerizes to *cis*-2-butene, R4, and *trans*-2-butene, R5. Furthermore, *cis*-2-butene can isomerize to *trans*-2-butene, R6, and vice versa. The olefins can react with water to produce 2-butanol, R7-R9, or with 1-butanol to produce 1-(1-methylpropoxy) butane, R10-R12. More details about byproducts formation was given in Section 3.3.1.

It should be noted that from the group of reactions proposed only 6 reactions are stoichiometrically independent. One of the possible combinations of stoichiometrically independent reactions is the group formed by the reactions marked with an asterisk (*) in Scheme 4.1. The rest of the reactions and the corresponding relation between equilibrium constants, $K_{eq,i}$, can be obtained as follows:

$$[R_3]=[R_2]-[R_1] \qquad K_{eq,3}=\frac{K_{eq,2}}{K_{eq,1}} \tag{4.1}$$

$$[R_4]=[R_5]-[R_6] \qquad K_{eq,4}=\frac{K_{eq,5}}{K_{eq,6}} \tag{4.2}$$

$$[R_8]=[R_7]-[R_5] \qquad K_{eq,8}=\frac{K_{eq,7}}{K_{eq,5}} \tag{4.3}$$

$$[R_9]=[R_7]+[R_6]-[R_5] \qquad K_{eq,9}=\frac{K_{eq,7}\,K_{eq,6}}{K_{eq,5}} \tag{4.4}$$

$$[R_{11}]=[R_{10}]-[R_5] \qquad K_{eq,11}=\frac{K_{eq,10}}{K_{eq,5}} \tag{4.5}$$

$$[R_{12}]=[R_{10}]+[R_6]-[R_5] \qquad K_{eq,12}=\frac{K_{eq,10}\,K_{eq,6}}{K_{eq,5}} \tag{4.6}$$

The degree of ideality of the reaction medium is an important factor in a thermodynamic study and, because of the important dissimilarity between the compounds present in the medium, the system is expected to deviate from ideality. To account for these deviations, the activity coefficients of all the species, γ_j, were estimated by the UNIFAC-Dortmund predictive method.[3-6] This method was selected because it presents the following advantages in front of the group contribution methods UNIFAC or ASOG: (1) better description of the temperature dependence; (2) better description of the real behavior in the dilute region; (3) it can be applied more reliably for systems involving molecules with very different size.

As an example of a typical experiment, Figure 4.1 shows the evolution of the activities for all the species detected in the reaction medium at 423 K. It must be pointed out that 1,4-dioxane has the higher activity ($a_{\text{dioxane}} \approx 0.69$) because of its high concentration in the medium followed by water ($a_{\text{water}} \approx 0.32$) whose high activity is due to its high activity coefficient (in all experiments higher than 2). Activities of 1-(1-methylpropoxy) butane, 2-butanol and 1-butene were in all cases very low due to their low concentration in the reaction medium.

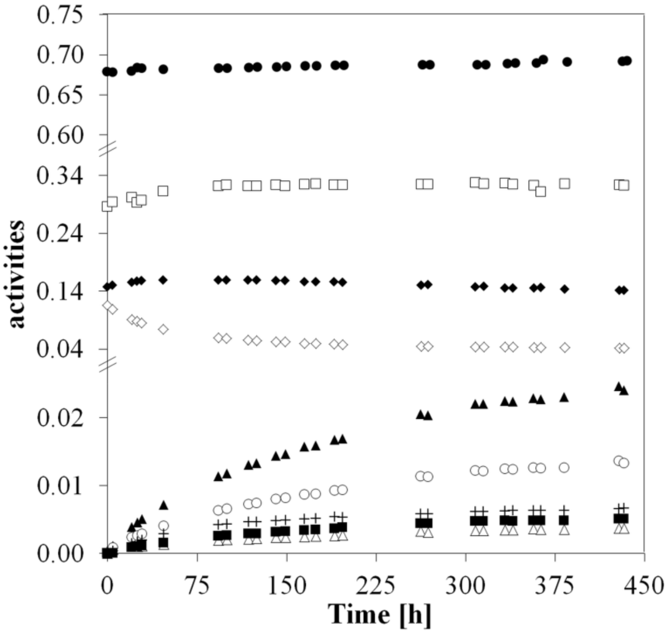

Figure 4.1. Evolution of activities over time (1g of catalyst, T = 423 K, P = 40 bar, 500 rpm).
(●) Dioxane; (□) Water; (♦) DNBE; (◊) 1-butanol; (▲)*trans*-2-butene; (o) *cis*-2-butene;
(+) 1-(1-methylpropoxy) butane; (■) 2-butanol; (Δ) 1-butene.

In all experiments a slightly decrease in the DNBE activity and a very slow increase in the 1-butene activity were observed. This fact indicates that both intramolecular dehydration of 1-butanol (R1) and DNBE decomposition (R3) could have not reached the chemical equilibrium at the end of the experiment. The increase in 1-butene activity gives place to a slight increase of 2-butenes (reactions R4 and R5), 2-butanol (reactions R7, R8 and R9) and 1-(1-methylpropoxy) butane (reactions R10, R11 and R12).

Because the reaction follows a parallel-series scheme, it was rather difficult to achieve a constant composition for all the species present in the medium. For this reason, it was considered that the system was in equilibrium when the computed values of $K_{eq,i}$ were constant, within the limits of the experimental error. Thermodynamic equilibrium constants $K_{eq,i}$ were computed from activities according to Equation 4.7 where $K_{\gamma,i}$ and $K_{x,i}$ are, respectively, the equilibrium constants of reaction i in terms of activity coefficients and molar fractions of the species that take part in the reaction.

$$K_{eq,i} = \prod_{j=1}^{S} \left(a_j\right)_e^{\nu_j} = \prod_{j=1}^{S} \left(\gamma_j\right)_e^{\nu_j} \left(x_j\right)_e^{\nu_j} = \prod_{j=1}^{S} \left(\gamma_j\right)_e^{\nu_j} \prod_{j=1}^{S} \left(x_j\right)_e^{\nu_j} = K_{\gamma,i} K_{x,i} \tag{4.7}$$

Time evolution of the so-calculated equilibrium constants (see Figure 4.2) shows that, after 450 h of running, both 1-butanol intramolecular dehydration (R2, Figure 4.2b) and DNBE decomposition (R3, Figure 4.2c), had not reached the chemical equilibrium, as mentioned above. However, the formation of 1-butene was rather slow, allowing a quick readjustment of the compositions for the rest of the reactions. This fact can be corroborated by observing that $K_{eq,i}$ were constant within the limits of the experimental error for the rest of studied reactions. Thus, it was considered that these reactions were in pseudo-equilibrium state. It should be pointed out that, despite the very low amount of 2-butanol and 1-(1-methylpropoxy) butane detected in the reaction medium, the reactions involving these two compounds reached the chemical equilibrium quickly (see Figures 4.2e and f) in contrast with the main reaction where the amount of DNBE was considerably higher but the corresponding reaction needed a longer time to reach the equilibrium (see Figure 4.2a).

Table 4.1 gathers the values of $K_{\gamma,i}$ and $K_{x,i}$ and the equilibrium constants $K_{eq,i}$ for the group of stoichiometrically independent reactions marked with an asterisk (*) in Scheme 4.1. It can be observed that $K_{x,i}$ decreases with temperature for all the reactions with exception of R1, where $K_{x,1}$ remains constant within the limits of the experimental error.

In a similar way, $K_{\gamma,i}$ decreases with temperature for all the reactions. In reactions where water participates (R1, bimolecular dehydration of 1-butanol to di-n-butyl ether, and R7-R9, hydration of olefins to 2-butanol) the values of $K_{\gamma,i}$ are significantly different from unity showing the non-ideality of the mixture. On the other hand, the values of $K_{\gamma,i}$ corresponding to olefins isomerization (R4-R6) are very close to unity. In these reactions only olefins are involved which have very similar activity coefficients.

Regarding $K_{eq,i}$, the equilibrium constant for the bimolecular dehydration of 1-butanol to DNBE (R1) is high enough to state that the reaction is shifted to the ether formation at equilibrium. Furthermore, as it was mentioned before, the formation of 1-butene was extremely slow and the highest amount of 1-butene detected at the end of the experiments was rather low. Consequently, the amount of the other byproducts was also very low. All this assures a good conversion level of 1-butanol to ether in industrial etherification processes. Moreover, $K_{eq,1}$ hardly changes with temperature, pointing out that conversion is quite promising to produce the ether in all the experimental temperature range.

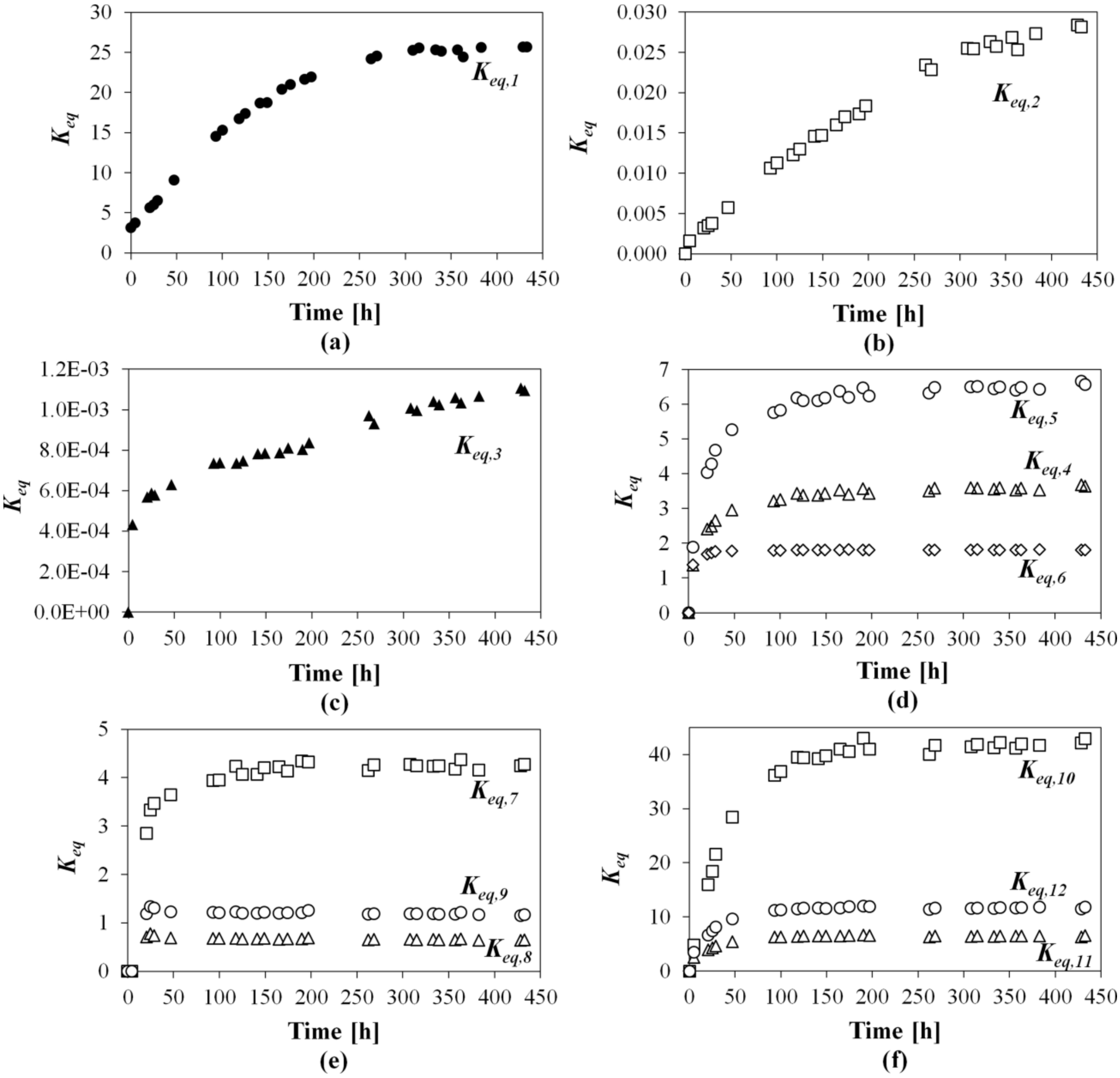

Figure 4.2. Evolution of the equilibrium constants with time for the experiment shown in Figure 4.1 (1g of catalyst, T = 423 K, P = 40 bar, 500 rpm): (a) (●) $K_{eq,1}$; (b) (□) $K_{eq,2}$; (c) (▲) $K_{eq,3}$; (d) (Δ) $K_{eq,4}$, (o) $K_{eq,5}$, (◊) $K_{eq,6}$; (c) (□) $K_{eq,7}$, (Δ) $K_{eq,8}$, (o) $K_{eq,9}$; (d) (□) $K_{eq,10}$, (Δ) $K_{eq,11}$, (o) $K_{eq,12}$

Data corresponding to the intramolecular dehydration of 1-butanol to 1-butene (R2), which is also part of the group of stoichiometrically independent reactions marked with an asterisk in Scheme 4.1, is not included in Table 4.1 because the reaction did not reach the chemical equilibrium, as above mentioned. Despite that, it should be pointed out that the results suggest that the dehydration of 1-butanol to 1-butene is an endothermic reaction. This fact is in agreement with the general pattern found in literature about dehydration of alcohols to olefins.[1,7,8]

For the rest of the reactions gathered in Table 4.1 it can be observed that $K_{eq,i}$ decreases with temperature indicating that they are exothermic reactions. Olefins isomerization is shifted to 2-butenes formation and, among them, *trans*-2-butene is thermodynamically favored as it can be inferred from the $K_{eq,6}$ values of R6 (isomerization *cis* - *trans*).

Table 4.1. Mean values and standard uncertainties of the equilibrium constants determined in the temperature range of 413-463 K and 40 bar. (R1) bimolecular dehydration of 1-butanol to di-n-butyl ether, (R5) isomerization of 1-butene to *trans*-2-butene, (R6) isomerization of *cis*-2-butene to *trans*-2-butene, (R7) hydration of 1-butene to 2-butanol and (R10) reaction between 1-butene and 1-butanol to yield 1-(1-methyl propoxy) butane.

	T [K]	$K_{x,i}$	$K_{\gamma,i}$	$K_{eq,i}$
R1	413	12.8 ± 0.7	2.19 ± 0.01	28.0 ± 1.1
	423	12.7 ± 0.2	2.18 ± 0.01	27.7 ± 0.2
	433	13.0 ± 0.7	2.09 ± 0.03	27.2 ± 1.8
	443	12.7 ± 0.3	2.03 ± 0.05	25.9 ± 1.2
	453	13.7	1.94	26.6
	463	14.6 ± 0.6	1.92 ± 0.03	28.1 ± 1.3
R5	413	6.6 ± 0.1	1.06224 ± 0.00003	7.0 ± 0.1
	423	6.0 ± 0.4	1.058 ± 0.003	6.4 ± 0.4
	433	5.8 ± 0.3	1.052 ± 0.005	6.0 ± 0.3
	443	5.48 ± 0.02	1.04 ± 0.01	5.70 ± 0.03
	453	5.1	1.01	5.1
	463	4.65 ± 0.07	0.99 ± 0.01	4.62 ± 0.07
R6	413	1.848 ± 0.002	1	1.848 ± 0.002
	423	1.813 ± 0.002	1	1.813 ± 0.002
	433	1.775 ± 0.003	1	1.775 ± 0.003
	443	1.742 ± 0.002	1	1.742 ± 0.002
	453	1.702	1	1.702
	463	1.6747 ± 0.0002	1	1.6747 ± 0.0002
R7	413	15.9 ± 0.3	0.3565 ± 0.0003	5.7 ± 0.1
	423	11.7 ± 1.0	0.357 ± 0.008	4.2 ± 0.3
	433	8.9 ± 0.6	0.35 ± 0.01	3.1 ± 0.1
	443	7.15 ± 0.04	0.32 ± 0.03	2.3 ± 0.2
	453	5.4	0.28	1.5
	463	4.0 ± 0.1	0.27 ± 0.01	1.08 ± 0.06
R10	413	63.7 ± 0.5	0.95 ± 0.01	60.4 ± 0.1
	423	46.4 ± 2.0	0.91 ± 0.03	42.3 ± 0.4
	433	30.9 ± 3.2	0.91 ± 0.03	28.2 ± 2.2
	443	23.4	0.74	17.4
	453	16.5	0.69	11.3
	463	11.5 ± 0.4	0.65 ± 0.03	7.5 ± 0.2

Equation 4.7 is deduced considering that fugacity of liquids is a weak function of pressure and assuming that the fugacity of the liquid at the working temperature and pressure is equal to the fugacity of the liquid at the working temperature and at 1 bar of pressure. However, at high pressures this assumption can be inaccurate. In order to take into account the deviations in $K_{eq,i}$ due to the difference between the working pressure (40 bar) and the pressure at the standard state (1 bar), the Poynting correction factor K_Γ was evaluated as follows:[9]

$$K_\Gamma = \exp\left(\frac{P\text{-}1}{RT} \sum_{j=1}^{S} \nu_j V_{\mathrm{m},j} \right) \tag{4.8}$$

where P is the working pressure and ν_j and $V_{\mathrm{m},j}$ are respectively the stoichiometric coefficient and the molar volume of compound j.

At this point it is important to emphasize that previous simulations with the software Chemcad[10] were carried out in order to select the working pressure. These simulations showed that working at 40 bar ensures that, for the temperature range studied, the reaction medium is in liquid phase even when the amount of olefins, which are the most volatile compounds in the system, is high. Thus, the liquid phase was assured throughout the experiment. However, the working conditions are very close to the critical region of pure butenes being the critical points of butenes: 419.6 K and 40.2 bar for 1-butene; 428.6 K and 39.9 bar for *trans*-2-butene; and 435.6 K and 42.0 bar for *cis*-2-butene.[11] Accurate fluid properties in states near a pure component's vapor-liquid critical point are difficult to obtain both from experiments and from models.[12] For this reason molar volumes $V_{\mathrm{m},j}$ of butenes were not determined and consequently, the Poynting correction factor K_Γ was evaluated only for the main reaction, the bimolecular dehydration of 1-butanol to di-n-butyl ether.

Table 4.2 gathers the calculated Poynting correction factor K_Γ for the reaction of 1-butanol dehydration to ether at different temperatures (the molar volumes of 1-butanol, di-n-butyl ether and water was estimated by the Hankinson-Brobst-Thomson method[12]). As it can be seen, K_Γ values ranged from 0.983 to 0.978. Thus, the effect of K_Γ on the $K_{eq,1}$ ($K_{eq,1} = K_{x,1}{\cdot}K_{\gamma,1}{\cdot}K_\Gamma$) was lower than the experimental uncertainty. Therefore, it can be assumed that the effect of the working pressure on the equilibrium constant is negligible and the equilibrium constant is only a function of temperature.

Table 4.2. Molar volumes of 1-butanol DNBE and water; and K_Γ correction factor of DNBE synthesis reaction, calculated by Hawkinson-Brobst-Thomson (HBT) method.[12]

T [K]	$V_{\mathrm{m,BuOH}}$ [l/mol]	$V_{\mathrm{m,DNBE}}$ [l/mol]	$V_{\mathrm{m,H2O}}$ [l/mol]	K_Γ
413	0.105	0.175	0.019	0.983
423	0.106	0.177	0.019	0.982
433	0.108	0.180	0.020	0.981
443	0.111	0.184	0.020	0.980
453	0.113	0.187	0.020	0.979
463	0.116	0.191	0.021	0.978

4.3.2. Standard Gibbs free energy, enthalpy, and entropy of reactions

Data corresponding to the standard Gibbs free energy ($\Delta_r G^0_{i,(\mathrm{l})}$), enthalpy ($\Delta_r H^0_{i,(\mathrm{l})}$) and entropy ($\Delta_r S^0_{i,(\mathrm{l})}$) for the chemical reactions involved in the system under study are, in most cases, unavailable in the literature. A theoretical estimation of these thermochemical properties can be obtained as follows: (1) $\Delta_r H^0_{i,(\mathrm{l})}$ can be estimated from the standard heats of formation of the reactants and products involved in reaction *i*; (2) $\Delta_r S^0_{i,(\mathrm{l})}$ can be estimated form the standard molar entropies of the reactants and products involved in reaction *i*; and (3) $\Delta_r G^0_{i,(\mathrm{l})}$ can be estimated from Equation 4.9:

$$\Delta_r G^0_{i,(l)} = \Delta_r H^0_{i,(l)} - \Delta_r S^0_{i,(l)} \cdot T \tag{4.9}$$

Table 4.3. Thermochemical data of species involved in the reaction network. Standard formation enthalpy ($\Delta_f H^0_{(l)}$), standard vaporization enthalpy ($\Delta_{vap} H^0$) and standard molar entropy ($S^0_{(l)}$).

	$\Delta_f H^0_{(g)}$ kJ·mol^{-1}	**$\Delta_{vap} H^0$ kJ·mol^{-1}**	**$\Delta_f H^0_{(l)}$ kJ·mol^{-1}**	**$S^0_{(g)}$ J·mol^{-1}·K^{-1}**	**$S^0_{(l)}$ J·mol^{-1}·K^{-1}**
1-butanol			**-328 ± 4**[d]		**225.73**[i]
DNBE		45[b]	**-378 ± 1**[e]	506.65[c]	**421.04**[j]
Water			**-285.83**[f]		**69.95 ± 0.03**[f]
1-butene	-0.63 ± 0.79[a]	20.88[b]	**-21.51 ± 0.79**[g]		**229.06**[k]
trans-2-butene	-10.8 ± 1[a]	21.97[b]	**-32.77 ± 1**[g]		**163.5**[k]
cis-2-butene	-7.7 ± 1.3[a]	22.7[b]	**-30.4 ± 1.3**[g]		**220**[k]
2-butanol			**-342.7 ± 0.59**[h]		**213.1**[l]
1-(1-methylpropoxy) butane		43.61 ± 0.85[c]	**-390.7**[c]	509.84[c]	**424.61**[j]

[a] Prosen et al.[13]
[b] Majer and Svoboda.[14]
[c] Estimated by a modified Benson method.[21]
[d] NIST average of values.
[e] Colomina et al.[15]
[f] Chase.[16]
[g] Estimated according to the common definition $\Delta_f H^0_{(l)} = \Delta_f H^0_{(g)} - \Delta_{vap} H^0$.
[h] Chao and Rossini.[17]
[i] Counsell et al.[18]
[j] Calculated by the equation proposed by Stull et al.[22]
[k] Takeda et al.[19]
[l] Andon et al.[20]

Table 4.3 gathers thermochemical data corresponding to the species involved in the reaction network. Most of these values were obtained from the open literature; however, to the best of our knowledge the values of the standard enthalpy of formation for 1-(1-methylpropoxy) butane and the liquid molar entropy of di-n-butyl ether and 1-(1-methylpropoxy) butane are not available. The standard enthalpy of formation was estimated by the improved Benson's group-additivity method[21] and the molar entropies of the two ethers by the procedure described by Stull et al.[22] (Equations 4.10 to 4.13).

$$S^0_{j,(l)} = S^0_{j,(g)} - \Delta_v S^0_j - \Delta_c S^0_j - \Delta_{ig} S^0_j \tag{4.10}$$

where

$$\Delta_v S^0_j = \frac{\Delta_{vap} H_j}{T} \tag{4.11}$$

$$\Delta_c S^0_j = -R\,ln\left(\frac{P^0}{P^s_j}\right) \tag{4.12}$$

$$\Delta_{ig} S^0_j = \frac{27}{32}\frac{R T^3_{c,j}}{P_{c,j} T^3} P^0 \tag{4.13}$$

Equation 4.10 involves, for compound j, the entropy change due to phase change ($\Delta_v S^0_j$), the effect of vapor compression from the saturation pressure P^s_j (vapor pressure at standard temperature) to the standard pressure P^0 (1.013 bar) ($\Delta_c S^0_j$) and the deviation of ideality of the vapor at 298.15 K and 1.013 bar ($\Delta_{ig} S^0_j$).

The thermochemical data gathered in Table 4.3 allows estimating the *theoretical* standard enthalpy ($\Delta_r H^0_{i,(l)}$), entropy ($\Delta_r S^0_{i,(l)}$) and Gibbs free energy ($\Delta_r G^0_{i,(l)}$) of the reactions at 298.15 K shown in Table 4.4. In order to corroborate these theoretically estimated values, the *experimental* standard enthalpy ($\Delta_r H^0_{i,(l)}$), entropy ($\Delta_r S^0_{i,(l)}$) and Gibbs free energy ($\Delta_r G^0_{i,(l)}$) of the reactions were also estimated from the values of the equilibrium constants. As it is well known, the thermodynamic equilibrium constant of the chemical reaction i is related to the Gibbs free energy change ($\Delta_r G^0_i$) as follows:

$$\ln K_{eq,i} = \left(\frac{-\Delta_r G_i^0}{RT} \right) \tag{4.14}$$

Substituting Equation 4.9 in 4.14 the temperature dependence of the equilibrium constant can be expressed by

$$\ln K_{eq,i} = \frac{-\Delta_r H_i^0}{RT} + \frac{\Delta_r S_i^0}{R} \tag{4.15}$$

Thus, assuming that the enthalpy change of reaction does not vary over the temperature range, it is possible to obtain the experimental values of $\Delta_r H^0_{i,(l)}$ and $\Delta_r S^0_{i,(l)}$ by fitting Equation 4.15 to the experimental (obtained from composition at equilibrium) values of $K_{eq,i}$.

The resulting fitted linear models obtained by least squares regression are shown in Table 4.4. Figure 4.3 shows the experimental values of ln $K_{eq,i}$ versus $1/T$ for the reactions in pseudo-equilibrium state (dots), the values predicted by the corresponding fitted linear models (solid line) and the confidence intervals at the 95% confidence level for the values predicted by these models (dotted lines). For each model an F-test was performed to evaluate its accuracy from a statistical standpoint. In all cases the F-test proved that the linear models represented adequately reactions equilibrium data.

Table 4.4. Standard enthalpy ($\Delta_r H^0_{i,(l)}$), entropy ($\Delta_r S^0_{i,(l)}$) and Gibbs energy ($\Delta_r G^0_{i,(l)}$) for the reactions in pseudo-equilibrium state of Scheme 4.1.

Reaction	Linear model	Thermodynamic properties	From linear model	Theoret.	Literat. data
R1	$\ln K_{eq,1}=\left(\frac{37\pm357}{T}\right)+\left(3.2\pm0.8\right)$	$\Delta_r H^0_1$ [kJ·mol^{-1}]	-0.3 ± 2.9	-7.8 ± 9.8	
		$\Delta_r S^0_1$ [J·mol^{-1}·K^{-1}]	26.8 ± 6.7	39.5	
		$\Delta_r G^0_1$ [kJ·mol^{-1}]	-8.3 ± 5.0	-19.6 ± 9.0	
R4	$\ln K_{eq,4}=\left(\frac{1169\pm240}{T}\right)-\left(1.5\pm0.6\right)$	$\Delta_r H^0_4$ [kJ·mol^{-1}]	-9.7 ± 2.0	-8.9 ± 2.1	
		$\Delta_r S^0_4$ [J·mol^{-1}·K^{-1}]	-12.4 ± 4.6	-9.1	
		$\Delta_r G^0_4$ [kJ·mol^{-1}]	-6.0 ± 3.4	-6.2 ± 2.1	
R5	$\ln K_{eq,5}=\left(\frac{1561\pm284}{T}\right)-\left(1.8\pm0.7\right)$	$\Delta_r H^0_5$ [kJ·mol^{-1}]	-13.0 ± 2.4	-11.3 ± 1.8	-12.6 ± 0.84[a]
		$\Delta_r S^0_5$ [J·mol^{-1}·K^{-1}]	-15.1 ± 5.4	-65.6	
		$\Delta_r G^0_5$ [kJ·mol^{-1}]	-8.5 ± 4.0	8.3 ± 1.8	
R6	$\ln K_{eq,6}=\left(\frac{382\pm23}{T}\right)-\left(0.31\pm0.05\right)$	$\Delta_r H^0_6$ [kJ·mol^{-1}]	-3.2 ± 0.2	-2.4 ± 2.3	-4 ± 2[b]
		$\Delta_r S^0_6$ [J·mol^{-1}·K^{-1}]	-2.6 ± 0.4	-56.5	
		$\Delta_r G^0_6$ [kJ·mol^{-1}]	-2.4 ± 0.3	14.5 ± 2.3	
R7	$\ln K_{eq,7}=\left(\frac{6407\pm477}{T}\right)-\left(13.7\pm1.1\right)$	$\Delta_r H^0_7$ [kJ·mol^{-1}]	-53.3 ± 4.0	-35.4 ± 1.4	
		$\Delta_r S^0_7$ [J·mol^{-1}·K^{-1}]	-113.9 ± 9.1	-85.9	
		$\Delta_r G^0_7$ [kJ·mol^{-1}]	-19.3 ± 6.7	-9.8 ± 1.4	
R8	$\ln K_{eq,8}=\left(\frac{4875\pm321}{T}\right)-\left(12.0\pm0.7\right)$	$\Delta_r H^0_8$ [kJ·mol^{-1}]	-40.5 ± 2.4	-24.1 ± 1.6	
		$\Delta_r S^0_8$ [J·mol^{-1}·K^{-1}]	-99.4 ± 6.1	-20.4	
		$\Delta_r G^0_8$ [kJ·mol^{-1}]	-10.9 ± 4.5	-18.0 ± 1.6	
R9	$\ln K_{eq,9}=\left(\frac{5262\pm312}{T}\right)-\left(12.3\pm0.7\right)$	$\Delta_r H^0_9$ [kJ·mol^{-1}]	-43.8 ± 2.6	-26.5 ± 1.9	
		$\Delta_r S^0_9$ [J·mol^{-1}·K^{-1}]	-102.0 ± 6.0	-76.9	
		$\Delta_r G^0_9$ [kJ·mol^{-1}]	-13.3 ± 4.4	-3.6 ± 1.9	
R10	$\ln K_{eq,10}=\left(\frac{8204\pm459}{T}\right)-\left(15.7\pm1.1\right)$	ΔrH^0_{10} [kJ·mol^{-1}]	-68.2 ± 3.8	-41.2 ± 4.8	
		$\Delta_r S^0_{10}$ [J·mol^{-1}·K^{-1}]	-130.2 ± 8.8	-30.2	
		$\Delta_r G^0_{10}$ [kJ·mol^{-1}]	-29.4 ± 6.4	-32.2 ± 4.8	
R11	$\ln K_{eq,11}=\left(\frac{6453\pm429}{T}\right)-\left(13.4\pm1.0\right)$	$\Delta_r H^0_{11}$ [kJ·mol^{-1}]	-53.7 ± 3.6	-29.9 ± 5.0	
		$\Delta_r S^0_{11}$ [J·mol^{-1}·K^{-1}]	-111.5 ± 8.2	35.4	
		$\Delta_r G^0_{11}$ [kJ·mol^{-1}]	-20.4 ± 6.0	-40.5 ± 5.0	
R12	$\ln K_{eq,12}=\left(\frac{6826\pm461}{T}\right)-\left(13.7\pm1.1\right)$	$\Delta_r H^0_{12}$ [kJ·mol^{-1}]	-56.8 ± 3.8	-32.3 ± 5.3	
		$\Delta_r S^0_{12}$ [J·mol^{-1}·K^{-1}]	-113.9 ± 8.8	-21.1	
		$\Delta_r G^0_{12}$ [kJ·mol^{-1}]	-22.8 ± 6.5	-26.0 ± 5.3	

[a] Meyer and Stroz.[23]

[b] NIST average of values.[24]

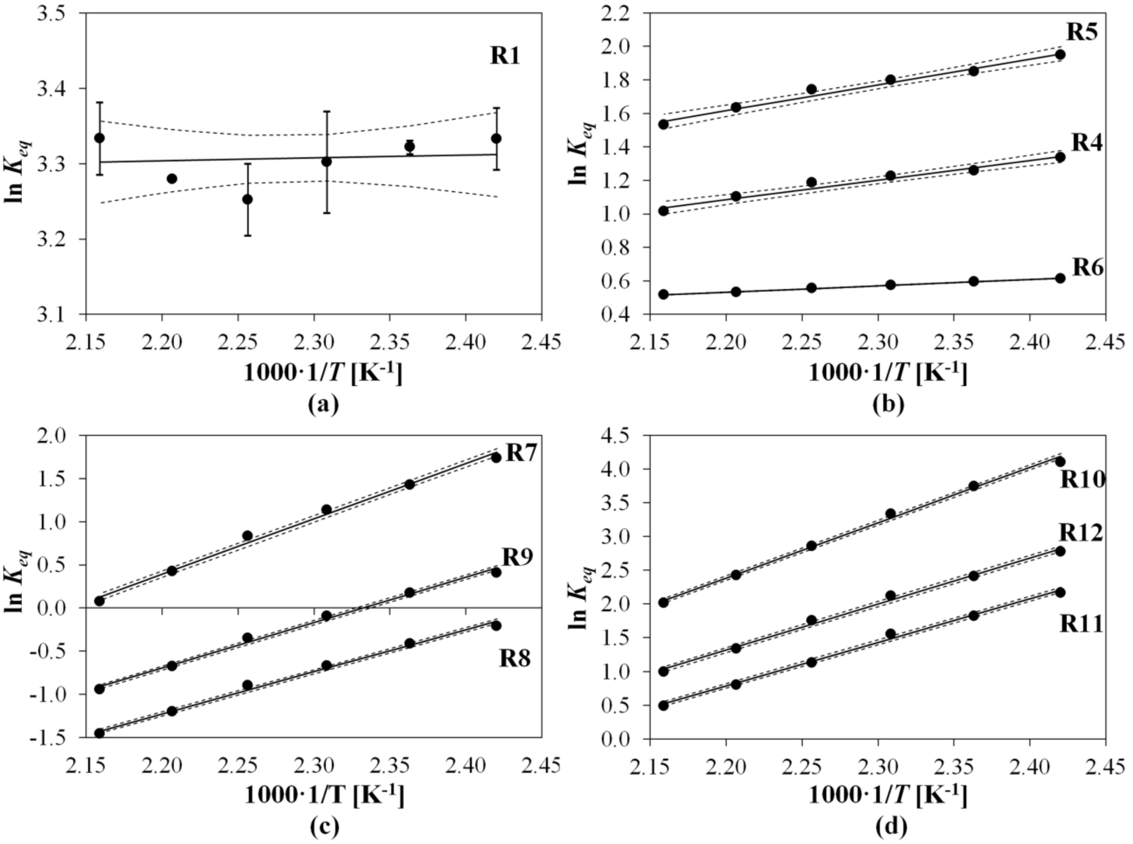

Figure 4.3. ln $K_{eq,i}$ versus $1/T$ for: (a) bimolecular dehydration of 1-butanol to DNBE; (b) olefins isomerization; (c) olefins hydration to 2-butanol; (d) 1-(1-methylpropoxy) butane formation. Dots refer to mean experimental values; solid lines refer to values predicted with Equation 4.15; and dotted lines refer to the intervals at 95% confidence level for predicted values.

Table 4.4 shows the values of $\Delta_r H^0_{i,(l)}$ and $\Delta_r S^0_{i,(l)}$ obtained from Equation 4.15, and $\Delta_r G^0_{i,(l)}$ computed from Equation 4.9 for each reaction. $\Delta_r H^0_{i,(l)}$ and $\Delta_r S^0_{i,(l)}$ are, as a matter of fact, average values in the temperature range 413-463 K, and it is assumed that they hardly change with temperature so that such values are representative that the ones at 298.15 K. $\Delta_r G^0_{i,(l)}$ was estimated at 298.15 K by means of Equation 4.9. Experimental values reported in the literature (Literat. data) as well as theoretical values (Theoret.) of $\Delta_r H^0_{i,(l)}$ (estimated from the standard heats of formation, Table 4.3), $\Delta_r S^0_{i,(l)}$ (estimated form the standard molar entropies, Table 4.3) and $\Delta_r G^0_{i,(l)}$ (estimated from Equation 4.9) are also included in Table 4.4.

Next, the conclusions deduced by comparing the experimental values of $\Delta_r H^0_{i,(l)}$, $\Delta_r S^0_{i,(l)}$ and $\Delta_r G^0_{i,(l)}$ with theoretical values (and with literature data when available) are discussed.

4.3.2.1. Bimolecular dehydration of 1-butanol to DNBE

The theoretical $\Delta_r H^0_{1,(l)} = -7.8 \pm 9.8$ kJ·mol^{-1} estimated from the standard heats of formation presents a low absolute value suggesting that the exothermicity of the bimolecular dehydration of 1-butanol to di-n-butyl ether and water is very low, being almost an athermic reaction. This fact agree with the experimentally determined $\Delta_r H^0_{1,(l)} = -0.3 \pm 2.9$ kJ·mol^{-1} and is also in agreement with the constancy of $K_{eq,1}$ with temperature (see Table 4.1). Furthermore, the experimental $\Delta_r H^0_{1,(l)}$ found in this work is in the trend shown by the values of other linear symmetrical dialkyl ether found in the literature (see Table 4.5).[1,7,8] From the experimental $\Delta_r H^0_{1,(l)}$ in Table 4.4 and $\Delta_f H^0_{j,(l)}$ of 1-butanol and water in Table 4.3 a value of $\Delta_f H^0_{\mathrm{DNBE,(l)}}$ = -370.5 ± 10.9 kJ·mol^{-1} at 298.15 K for DNBE can be obtained. This value agrees with that obtained by Colomina et al.[15] from combustion enthalpies, enforcing the reliability of the experimental equilibrium data obtained for the main reaction.

The experimental $\Delta_r S^0_{1,(l)}$ found in this work (26.8 ± 6.7 J·mol^{-1}·K^{-1}) is lower than the theoretical value (39.5 J·mol^{-1}·K^{-1}). As mentioned above, the theoretical $\Delta_r S^0_{1,(l)}$ was obtained using the value of $S^0_{\mathrm{DNBE,(g)}}$ estimated by an improved Benson group-additive method[21] and Equations 4.10 to 4.13.[22] To the best of our knowledge, no experimental value of $S^0_{\mathrm{DNBE,(l)}}$ has been published yet. From the experimental $\Delta_r S^0_{1,(l)}$ in Table 4.4 and $S^0_{\mathrm{j,(l)}}$ of 1-butanol and water in Table 4.3 a value of $S^0_{\mathrm{DNBE,(l)}}$ = 408.3 ± 6.8 J·mol^{-1}·K^{-1} at 298.15 K for DNBE can be obtained. This value is slightly lower (3%) than that predicted by the modified Benson method (421.04 J·mol^{-1}·K^{-1}).

Table 4.5 shows the $\Delta_r H^0_{i,(l)}$, $\Delta_r S^0_{i,(l)}$ and $\Delta_r G^0_{i,(l)}$ for the intermolecular dehydration of 1-butanol (present work), 1-pentanol[7], 1-hexanol[1], and 1-octanol[8]. A clear trend can be observed for the three thermochemical properties. Both $\Delta_r H^0_{i,(l)}$ and $\Delta_r G^0_{i,(l)}$ becomes less negative (less exothermic) as the length of the ether decreases. On the other hand, $\Delta_r S^0_{i,(l)}$ increases as the length of the ether decreases. It should be pointed out that, for the four reactions, the theoretical value of $\Delta_r H^0_{i,(l)}$ overestimates the one experimentally found.

Table 4.5. Standard enthalpy ($\Delta_r H^0_{i,(l)}$), entropy ($\Delta_r S^0_{i,(l)}$) and Gibbs energy ($\Delta_r G^0_{i,(l)}$) changes for the synthesis reaction of di-n-butyl ether (DNBE), di-n-pentyl ether (DNPE), di-n-hexyl ether (DNHE) and di-n-octyl ether (DNOE) in the liquid phase assuming $\Delta_r H^0_{i,(l)}$ constant over the temperature range 423-463K.

	$\Delta_r H^0_{i,(l)}$ kJ mol^{-1}		**$\Delta_r S^0_{i,(l)}$ J mol^{-1} K^{-1}**		**$\Delta_r G^0_{i,(l)}$ kJ mol^{-1}**	
	Experim.	**Theoret.**	**Experim.**	**Theoret.**	**Experim.**	**Theoret.**
DNBE	-0.3 ± 2.9	-7.8 ± 9.8	26.8 ± 6.7	39.5	-8.3 ± 5.0	-19.6 ± 9.0
DNPE[7]	-6.5 ± 0.6	-17.8	18.1 ± 1.4	-48.4	-11.9 ± 1.1	-3.4
DNHE[1]	-8.5 ± 0.2	-11.9	15.2 ± 0.5	13	-13.0 ± 0.4	-15.8
DNOE[8]	-13.5 ± 1.7	-15.9	14.0 ± 4.0	-15.5	-17.7 ± 2.1	-11.3

4.3.2.2. Olefins isomerization

The experimental values of $\Delta_r H^0_{i,(l)}$ corresponding to olefins isomerization are in agreement with both, those found in the literature and the estimated theoretical values.

Regarding $\Delta_r S^0_{i,(l)}$, the experimental value corresponding to the isomerization of 1-butene to *cis*-2-butene (R4) is also in agreement with the theoretical one. However, the experimental

$\Delta_r S^0_{i,(l)}$ of both the isomerization of 1-butene to *trans*-2-butene (R5) and the isomerization of *cis*-2-butene to *trans*-2-butene (R6) are lower than the theoretical values. Some discrepancies about the standard entropy at 298.15 K of the *trans*-2-butene isomer ($S^0_{\text{trans-2-butene,(l)}}$) can be found in the literature.[19,25] From the equilibrium data of this work it is possible to compute $S^0_{\text{trans-2-butene,(l)}}$ by two ways: (1) from the experimental $\Delta_r S^0_{5,(l)}$ in Table 4.4 and $S^0_{\text{1-butene,(l)}}$ shown in Table 4.3 a value of $S^0_{\text{trans-2-butene,(l)}} = 214.3 \pm 5.3$ J·mol^{-1}·K^{-1} is obtained; (2) from the experimental $\Delta_r S^0_{6,(l)}$ in Table 4.4 and $S^0_{\text{cis-2-butene,(l)}}$ shown in Table 4.3 a value of $S^0_{\text{trans-2-butene,(l)}} = 217.4 \pm 0.4$ J·mol^{-1}·K^{-1} is obtained. From these two values a mean $S^0_{\text{trans-2-butene,(l)}} = 215.8 \pm 2.9$ J·mol^{-1}·K^{-1} was computed. This value is slightly higher than that reported by Guttman and Pitzer[25] (205.39 J·mol^{-1}·K^{-1}) and slightly lower than that estimated by the improved Benson group-additive method (221.78 J·mol^{-1}·K^{-1}).

4.3.2.3. Olefins hydration to 2-butanol

Experimental values of $\Delta_r H^0_{i,(l)}$, $\Delta_r S^0_{i,(l)}$ and $\Delta_r G^0_{i,(l)}$ for the hydrations of olefins to 2-butanol differ significantly from the theoretical values. Following the same reasoning as described with previous reactions the mean values $\Delta_f H^0_{\text{2-butanol,(l)}} = -359.9 \pm 4.1$ kJ·mol^{-1} and $S^0_{\text{2-butanol,(l)}} = 185.9 \pm 7.2$ J·mol^{-1}·K^{-1} for 2-butanol were obtained at 298.15 K which are, respectively, 5% and 13% lower than the data found in the literature. These differences can be ascribed to uncertainty in chemical analysis (olefins and 2-butanol were minor components at equilibrium).

4.3.2.4. 1-(1-Methylpropoxy) butane formation

Like in olefins hydration, experimental values of $\Delta_r H^0_{i,(l)}$, $\Delta_r S^0_{i,(l)}$ and $\Delta_r G^0_{i,(l)}$ for the 1-(1-methylpropoxy) butane formation differ significantly from the theoretical values. Following the same procedure, the mean value $\Delta_f H^0_{\text{BuOBu',(l)}} = -415.8 \pm 8.8$ kJ·mol^{-1} and $S^0_{\text{BuOBu',(l)}} = 328.3 \pm 8.5$ J·mol^{-1}·K^{-1} were obtained for 1-(1-methylpropoxy) butane at 298.15 K. These values are, respectively, 6.4% and 22.7% lower than the values estimated by an improved Benson group-additive method. The important differences observed can be attributed to both the uncertainty in chemical analysis (olefins and 1-(1-methylpropoxy) butane were minor components) and a poor estimate of 1-(1-methylpropoxy) butane formation enthalpy and molar entropy by the improved Benson group-additive method.

4.4. Conclusions

The equilibrium constant for the bimolecular dehydration of 1-butanol to di-n-butyl ether and water was experimentally determined. Its value was found to be high enough to state that the reaction is shifted to the ether formation at equilibrium. Furthermore, the formation of 1-butene was extremely slow and, consequently, the rest of secondary products were also found in very low concentrations. As a consequence, a good conversion level of 1-butanol to the linear ether could be expected in industrial etherification processes.

The equilibrium constant for the dehydration reaction of 1-butanol to di-n-butyl ether and water was found to be independent of the operating temperature within the limits of the experimental error. That explains the very low value of the enthalpy change of reaction found (practically zero), which is in the trend showed by the reaction enthalpy change of other lineal symmetrical di-alkyl ethers found in the literature. From equilibrium data a value of $\Delta_f H^0_{\text{DNBE,(l)}}$ = -370.5 ± 10.9 kJ·mol^{-1} for DNBE was obtained at 298.15 K which agree with that one found in literature data bank within the limits of the experimental error.

Some differences between the values of $\Delta_r S^0_{(l)}$ for the dehydration of 1-butanol to di-n-butyl ether computed from equilibrium data and estimated from standard molar entropies were observed. Based on this fact, the value $S^0_{(l)}$ = 408.3 ± 6.8 J·mol^{-1}·K^{-1} for DNBE is proposed. This value is slightly lower than that predicted by the modified Benson method (421.04 J·mol^{-1}·K^{-1}).

Isomerizations between olefins proved to be exothermic with an $\Delta_r H^0_{(l)}$ of -9.7 ± 2.0 J·mol^{-1}·K^{-1} for the isomerization of 1-butene to *cis*-2-butene, -13.0 ± 2.4 J·mol^{-1}·K^{-1} for the isomerization of 1-butene to *trans*-2-butene and -3.2 ± 0.2 J·mol^{-1}·K^{-1} for the isomerization of *cis*-2-butene to *trans*-2-butene. These values are in agreement with those estimated from the standard formation enthalpies. Some disagreements regarding the value of the standard molar entropy of *trans*-2-butene can be found in the literature. From equilibrium data, the value $S^0_{(l)}$ = 215.8 ± 2.9 J·mol^{-1}·K^{-1} for *trans*-2-butene is proposed.

Side reactions of olefins hydration and branched ether synthesis were proved to be also exothermic.

Nomenclature

Notation

a_j	Activity of compound *j*
$K_{eq,i}$	Equilibrium constant of reaction *i*
$K_{\gamma,i}$	Equilibrium constant of reaction *i* in term of activity coefficients
$K_{x,i}$	Equilibrium constant of reaction *i* in term of molar fraction
K_{Γ}	Poynting correction factor
P	Pressure
P^0	Standard pressure
$P_{c,j}$	Critical pressure of compound *j*
P^s_j	Vapor pressure at standard temperature
R	Ideal gas constant
$S^0_{j,(\mathrm{l})}$	Standard molar entropy of compound *j* (in liquid phase)
T	Temperature
$T_{c,j}$	Critical temperature of compound *j*
v_j	Stoichiometric coefficient of compound *j*
$V_{m,j}$	Molar volume of compound *j*
x_j	Molar fraction of compound *j*

Greek symbols

γ_j	Activity coefficients of compound *j*
$\Delta_c S^0_j$	Entropy change due to the effect of vapor compression from P^s_j to P^0
$\Delta_f H^0_{j,(\mathrm{l})}$	Standard formation enthalpy of compound *j*(in liquid phase)
$\Delta_{ig} S^0_j$	Entropy change due to the deviation of ideality of the vapor at 298.15 K and 1.013 bar
$\Delta_r G^0_{i,(\mathrm{l})}$	Standard Gibbs free energy for the chemical reaction *i*
$\Delta_r H^0_{i,(\mathrm{l})}$	Standard enthalpy for the chemical reaction *i*
$\Delta_r S^0_{i,(\mathrm{l})}$	Standard entropy for the chemical reaction *i*
$\Delta_{vap} H^0$	Standard vaporization enthalpy
$\Delta_v S^0_j$	Entropy change due to phase change for compound *j*

Abbreviations

BuOH	1-Butanol
BuOBu’	1-(1-methylpropoxy)butane
DNBE	Di-n-butyl ether

DNHE	Di-n-hexyl ether
DNPE	Di-n-pentyl ether
DNOE	Di-n-octyl ether
HBT	Hawkinson-Brobst-Thomson

References

[1] Bringué, R.; Tejero, J.; Iborra, M.; Fité, C.; Izquierdo, J. F.; Cunill, F. Study of the chemical equilibrium of the liquid-phase dehydration of 1-hexanol to di-hexyl ether. *J. Chem. Eng. Data* **2008**, *53*, 2854-2860.

[2] Delion, A.; Torck, B.; Hellin, M. Equilibrium constant for the liquid-phase hydration of isobutylene over ion-exchange resin. *Ind. Eng. Chem. Process Des. Dev*. **1986**, *25*, 889-893.

[3] Weidlicht, U.; Gmehling, J. A modified UNIFAC model. 1. Prediction of VLE, h^E, and γ^∞. *Ind. Eng. Chem. Res.* **1987**, *26* (7), 1372-1381.

[4] Gmehling, J.; Li, J.; Schiller M. A modified UNIFAC model. 2. Present parameter matrix and results for different thermodynamic properties. *Ind. Eng. Chem. Res*. **1993**, *32*, 178-193.

[5] Gmehling, J.; Lohmann, J.; Jakob, A.; Li, J.; Joh, R. A modified UNIFAC (Dortmund) model. 3. Revision and extension. *Ind. Eng. Chem. Res.* **1998**, *37*, 4876-4882.

[6] Jakob, A.; Grensemann, H.; Lohmann, J.; Gmehling, J. Further development of modified UNIFAC (Dortmund): revision and extension 5. *Ind. Eng. Chem. Res.* **2006**, *45*, 7924-7933.

[7] Bringué, R.; Tejero, J.; Iborra, M.; Izquierdo, J.F.; Fite, C.; Cunill, F. Experimental study of the chemical equilibria in the liquid-phase dehydration of 1-pentanol to di-n-pentyl ether. *Ind. Eng. Chem. Res*. **2007**, *46*, 6865-6872.

[8] Casas, C.; Fité, C.; Iborra, M.; Tejero, J.; Cunill, F. Chemical equilibrium of the liquid-phase dehydration of 1-octanol to 1-(octyloxy)octane. *J. Chem. Eng. Data* **2013**, *58*, 741-748.

[9] Smith, J. M.; Van Ness, H. C. Chemical reaction equilibria. *Introduction to chemical engineering thermodynamics*, 4th ed.; McGraw-Hill: Singapore, 1987.

[10] http://www.chemstations.com/ (accessed March 2012)

[11] Tsonopoulos, C.; Ambrose, D., Vapor-liquid critical properties of elements and compounds. 6. Unsaturated aliphatic hydrocarbons. *J. Chem. Eng. Data* **1996**, *41*, 645-656.

[12] Poling, B. E.; Prausnitz, J. M.; O'Connell, J. P. Volumetric properties of mixtures. *The properties of gases and liquids*, 5th ed.; McGraw-Hill Companies, 2001.

[13] Prosen, E.J.; Maron, F.W.; Rossini, F.D. Heats of combustion, formation, and isomerization of ten C_4 hydrocarbons. *J. Res. NBS*, **1951**, *46*, 106-112.

[14] Majer, V.; Svoboda, V. *Enthalpies of vaporization of organic compounds: A critical review and data compilation*. Blackwell Scientific Publications, Oxford, 1985.

[15] Colomina, M.; Pell, A.S.; Skinner, H.A.; Coleman, D.J. Heats of combustion of four dialkylethers. *Trans. Faraday Soc*. **1965**, *61*, 2641.

[16] Chase, M.W., Jr., *NIST-JANAF Thermochemical tables*, 4th Edition; *J. Phys. Chem. Ref. Data*, Monograph 9, **1998**, 1-1951.

[17] Chao, J.; Rossini, F.D. Heats of combustion, formation, and isomerization of nineteen alkanol. *J. Chem. Eng. Data* **1965**, *10*, 374-379.

[18] Counsell, J.F.; Hales, J.L.; Martin, J.F. Thermodynamic properties of organic oxygen compounds. Part 16. Butyl alcohol. *Trans. Faraday Soc.* **1965**, *61*, 1869-1875.

[19] Takeda, K.; Yamamuro, O.; Suga, H. Thermodynamic study of 1-butene. Exothermic and endothermic enthalpy relaxations near the glass transition. *J. Phys. Chem. Solids* **1991**, *22*, 607-615.

[20] Andon, R.J.L.; Connett, J.E.; Counsell, J.F.; Lees, E.B.; Martin, J.F. Thermodynamic properties of organic oxygen compounds: xxvii racemate of - butan-2-ol and (+)-butan-2-ol. *J. Chem. Soc. A*. **1971**, 661-664.

[21] Verevkin S. P. Improved Benson increments for the estimation of standard enthalpies of formation and enthalpies of vaporization of alkyl ethers, acetals, ketals, and ortho esters. *J. Chem. Eng. Data* **2002**, *47*, 1071-1097.

[22] Stull, D. R.; Westrum, E. F., Jr.; Sinke, G. C. *The chemical thermodynamics of organic compounds*; John Wiley: New York, 1969.

[23] Meyer, E.F.; Stroz, D.G. Thermodynamics of n-butene isomerization. *J. Am. Chem. Soc.* **1972**, *94*, 6344-6347.

[24] http://webbook.nist.gov/chemistry/ (accessed June 2014)

[25] Guttman, L.; Pitzer, K.S. *trans*-2-Butene. The heat capacity, heats of fusion and vaporization, and vapor pressure. The entropy and barrier to internal rotation. *J. Am. Chem. Soc.* **1945**, *67*, 324-327.

5. KINETIC STUDY[*]

With two adjustable parameters, I can fit an elephant.

With three, a running elephant.

-- Anonymous.

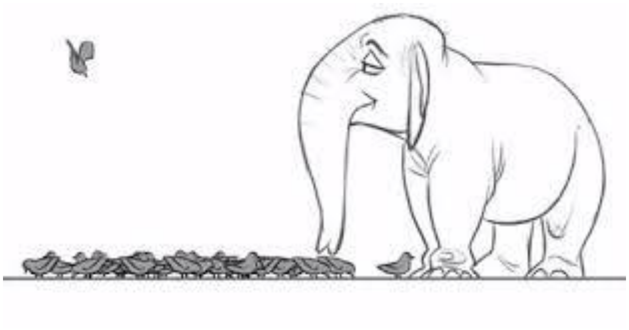

---

[*] Results presented in this chapter have been accepted in:

Pérez-Maciá, M. A.; Bringué, R.; Iborra, M.; Tejero, J.; Cunill, F. Kinetic study of 1-butanol dehydration to di-n-butyl ether over Amberlyst 70. *AIChE J.*

5.1. Introduction

As it was previously mentioned, a proper knowledge of the thermodynamics and the chemical kinetics of the reactions involved in a system are essential for the development of a profitable manufacturing process. Thermodynamics set the composition toward which the kinetic process is moving, thus it places a maximum limit on the product yield that may be obtained. In Chapter 4 the thermodynamics of the dehydration of 1-butanol over Amberlyst 70 were studied. From this work it was concluded that a good conversion level of 1-butanol to the linear ether can be expected.

The present chapter is devoted to the chemical kinetics of the dehydration of 1-butanol to DNBE over Amberlyst 70. Few are the kinetic studies on 1-butanol dehydration that can be found in the literature and most of them have been carried out at experimental conditions in which butenes (resulting from 1-butanol intramolecular dehydration) are the main products.[1] Those studies in which the dehydration of 1-butanol gave place to DNBE are: (1) Olaofe and Yue[1] studied the kinetics of 1-butanol dehydration over three types of zeolites in gas phase in the temperature range 473 – 573 K and 1-butanol pressures up to 0.6 bar. At these conditions the main products were both butenes and DNBE. For the dehydration of 1-butanol to di-n-butyl ether they considered a power law kinetic model as well as three Hougen-Watson type kinetic expressions assuming the surface reaction as the rate controlling step and that the adsorption of water and ether was negligible against the adsorption of 1-butanol. They concluded that empirical power functions rate expressions satisfactorily correlated the reaction rate data of the dehydration of 1-butanol to DNBE and found an activation energy of 54 – 142 kJ/mol (depending on the used zeolite); (2) Krampera and Beránek[2] studied the kinetics of individual reactions for the dehydration of 1-butanol over alumina in gas phase at 433 K. For di-n-butyl ether formation they proposed a Langmuir-Hinshelwood-Hougen-Watson mechanism where the irreversible surface reaction of two adsorbed molecules of 1-butanol was the rate limiting step and assuming the adsorption of water and ether negligible against the adsorption of 1-butanol. Sow et al.[3] studied the kinetics of 1-butanol dehydration to DNBE in liquid phase (at 433, 453 and 473 K under autogenerated pressure) over three sulfonated mesoporous silica and organosilica catalysts and a Y-zeolite. In their study they only considered a kinetic rate expression based on a mechanism where one molecule of 1-butanol adsorbs on an active site, the irreversible surface reaction being the rate limiting step and assuming the adsorption of alcohol and ether to be negligible against the adsorption of water. The values of the activation energies that they obtained ranged between 95 – 97 kJ/mol.

The aim of this chapter was to perform a comprehensive kinetic analysis in order to find a mechanism that represents the dehydration of 1-butanol to DNBE over Amberlyst 70 in liquid phase at the temperature range of 413 – 463 K. Particular emphasis was placed on high water contents given its inhibitory effect.[4-7] The reaction rate models considered in this work were based on the Langmuir-Hinshelwood-Hougen-Watson (LHHW) and the Eley Rideal (ER) formalisms.

The LHHW formalism has been the subject of much discussion and criticism.[8] First, the heat of adsorption of many adsorbate-adsorbent systems varies with the surface coverage of the adsorbate. Given that the Langmuir isotherm does not account for interactions between adsorbates, it is therefore doubtful that the behavior of an adsorbate in multicomponent systems would follow a Langmuir isotherm under reaction conditions. However, the LHHW equation derived from the Langmuir isotherm often provides a good fit of the rate data. Other types of isotherms accounting for the variation of heat of adsorption with coverage have been applied to kinetic studies and were found to fit experimental data with an equal amount of accuracy. Indeed, as the quote at the beginning of this chapter denotes, it is not difficult to obtain a good fit to rate data of rate expressions with a number of adjustable parameters, usually more than three. Second, the postulation of a different mechanism or rate determining steps may lead to the same form of rate equations in the LHHW kinetic framework. Third, the adsorption constant found by fitting the LHHW equations to experimental data are rarely equal to adsorption constants measured from chemisorption experiments. These criticisms led to the opinion that the LHHW formalism is nothing more than a systematic data fitting technique. An alternative are the empirical power-law rate expressions that have wide applicability, provide a straight forward relationship between rate and reactant concentration, and are easy to fit to experimental data with conventional techniques. However, LHHW kinetics provides insight into the mechanism of the reaction and may lead to a fundamental understanding of the reaction. In fact, LHHW rate forms or modifications of it are widely used and accepted for correlation of rates of catalytic reactions.

5.2. Experimental procedure

Wet resin Amberlyst 70 was dried at room temperature for 24 h prior to mechanical sieving. Afterwards, resin samples with bead size between 0.40 - 0.63 mm were dried following the procedure described in Section 2.3.3.

70 mL of 1-butanol, or 1-butanol/water, or 1-butanol/DNBE were charged in the reactor and heated to the working temperature (413-463 K). The pressure was kept at 40 bar with N_2 to ensure that the reaction medium was in liquid phase over the whole temperature range and the stirring speed was set at the selected value (300-700 rpm). Once the corresponding working temperature was reached, the dried catalyst was injected by means of pneumatic transport

considering this time as the starting point of reaction. Liquid composition was analyzed hourly during 7 h. For more information about experimental setup and procedure see Section 2.3.

Reaction rates of DNBE formation were obtained by differentiating the function of the DNBE moles produced vs time (Equation 5.1). A rational function was used to describe the relationship between n_{DNBE} and t.

$$r_{\mathrm{DNBE}}(t)=\frac{1}{W_{\mathrm{cat}}}\left(\frac{dn_{\mathrm{DNBE}}}{dt}\right) \tag{5.1}$$

5.3. Results and discussion

5.3.1. Preliminary experiments

In order to check that the overall observed reaction rates were not influenced by mass transfer limitations or solid distribution effects, a set of preliminary experiments was conducted based on a factorial design of experiments.[9] In this set the three factors studied were the stirring speed, N_{stir}, the catalyst particle size, d_p, and the mass of loaded catalyst, W_{cat}. Each of the three factors was studied at two levels, i.e. following a 2^3 factorial design. Table 5.1 shows the experimental matrix for the 2^3 factorial design. Some of the eight formulations were replicated (denoted with an *) and four additional runs (last 4 rows) were carried out at 500 rpm, 1g of catalyst with particle size between 0.4-0.63 mm (these values were selected because, under these operation conditions, the dehydration of 1-pentanol and 1-octanol over Amberlyst 70 were not influenced by mass transfer limitations[10,11]). The last column in Table 5.1 shows the initial rate of DNBE formation obtained experimentally for each run. The order in which the runs were carried out was randomized to avoid systematic errors. All tests were performed at 40 bar and the highest temperature of the range explored, which corresponds to the catalyst maximum operating temperature (463 K).

The obtained results have been represented in the boxplot of Figure 5.1 for a first visual data analysis. In this figure, the bottom and top of the box are the first and third quartiles, and the band inside the box is the second quartile (the median). The whiskers of the boxplot indicate the range of the observations. From a visual inspection, it is difficult to ascertain if any of the three factors studied have a significant influence over the observed reaction rates. Therefore, in order to evaluate the influence of the studied factors on the reaction rate, a linear regression model (Equation 5.2) which considered as regressor variables the main effects (N_{stir}, d_p, W_{cat}) as well as the interaction effects ($N_{stir}\cdot d_p$; $N_{stir}\cdot W_{cat}$; $d_p\cdot W_{cat}$; $N_{stir}\cdot d_p\cdot W_{cat}$) was fitted to data of Table 5.1 by the least square method.

Table 5.1. 2^3 experimental design used to determine the optimum operational conditions.

Factors			**Coded Factors**			r^0_{DNBE} **[mol/h·kg]**
N_{stir} **[rpm]**	$W_{cat.}$ **[g]**	d_p**[mm]**	**A**	**B**	**C**	
300	0.504	< 0.4	-1	-1.0	-1	147.7
700	0.502	< 0.4	1	-1.0	-1	150.4
300	2.067	< 0.4	-1	1.1	-1	163.6
300*	2.044	< 0.4	-1	1.1	-1	152.2
700	2.018	< 0.4	1	1.0	-1	161.0
300	0.53	0.63-0.8	-1	-1.0	1	142.2
300*	0.516	0.63-0.8	-1	-1.0	1	145.9
700	0.505	0.63-0.8	1	-1.0	1	147.6
300	2.023	0.63-0.8	-1	1.0	1	147.7
300*	2.024	0.63-0.8	-1	1.0	1	146.3
700	2.028	0.63-0.8	1	1.0	1	149.2
700*	2.034	0.63-0.8	1	1.0	1	149.7
500	1.012	0.4-0.63	0	-0.3	0	155.2
500	1.011	0.4-0.63	0	-0.3	0	152.5
500	1.022	0.4-0.63	0	-0.3	0	153.8
500	1.001	0.4-0.63	0	-0.3	0	146.9

[a] From the four central point replicates an initial reaction rate mean value of 152.1 mol/h·kg (standard deviation = 3.7 mol/h·kg) at 190 ºC can be obtained.

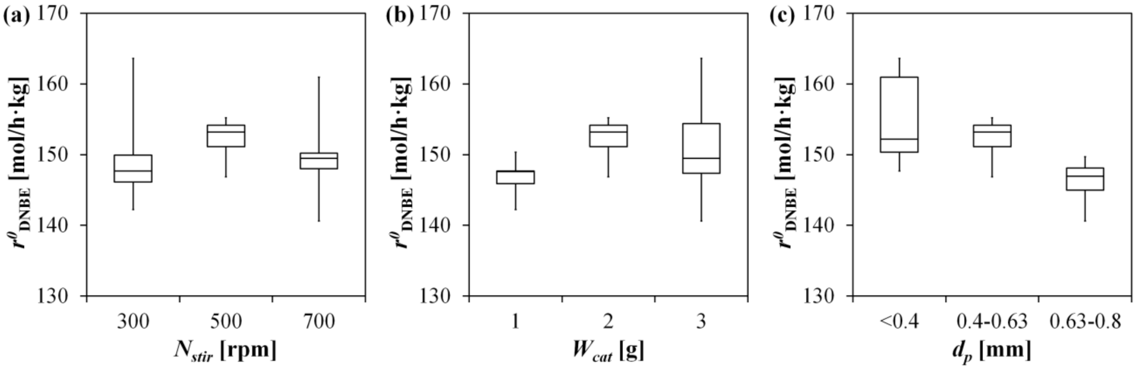

Figure 5.1. Main effect of (a) the stirring speed; (b) the mass of loaded catalyst; (c) the particle size. The bottom and top of the box are the first and third quartiles, and the band inside the box is the second quartile (the median). The whiskers of the boxplot indicate the range of the observations.

$$\hat{r}^0_{\text{DNBE}} = 150.93 + 1.235\cdot(N_{stir}) + 2.445\cdot(W_{cat}) - 4.051\cdot(d_p) - 0.472\cdot(N_{stir}\cdot W_{cat}) - 0.341\cdot(N_{stir}\cdot d_p) - 2.271\cdot(W_{cat}\cdot d_p) - 0.677\cdot(N_{stir}\cdot W_{cat}\cdot d_p) \tag{5.2}$$

To evaluate whether the linear model (Equation 5.2) represented the experimental data satisfactorily from a statistical standpoint, a *Test for the lack of fit*[12] was performed. The test statistic for lack of fit is:

$$F_0 = \frac{SS_{LOF}/(m-p)}{SS_{PE}/(n-m)} \tag{5.3}$$

where:

SS_{LOF} is the sum of squares due to the lack of fit which is computed from the average of the n_i observations at the ith level of the regressor variables ($\overline{r^0_{\mathrm{DNBE},i}}$) and the fitted values ($\hat{r}^0_{\mathrm{DNBE},i}$) as:

$$SS_{LOF} = \sum_{i=1}^{m} n_i \left(\overline{r^0_{\mathrm{DNBE},i}} - \hat{r}^0_{\mathrm{DNBE},i} \right)^2 \tag{5.4}$$

SS_{PE} is the sum of squares due to pure error computed from the jth observation of the response at the ith level of the regressor variables ($r^0_{\mathrm{DNBE},ij}$) and $\overline{r^0_{\mathrm{DNBE},i}}$:

$$SS_{PE} = \sum_{i=1}^{m} \sum_{j=1}^{n_i} \left(r^0_{\mathrm{DNBE},ij} - \overline{r^0_{\mathrm{DNBE},i}} \right)^2 \tag{5.5}$$

m is the number of levels of the regressor variables.

p is the number of regression coefficients.

n is the total number of observations.

By computing SS_{PE} and SS_{LOF} it was possible to compare the test statistic F_0 with the critical value of the $F_{distribution}$ to ascertain if both variances were statistically different. From Table 5.2 it can be concluded that $F_0 < F_{distribution}$ for a probability of 95 %. Thus, there is not evidence of the lack of fit of the model.

Table 5.2. Lack of fit test for the regression model of Equation 5.2. (α = 0.95)

Source of Variation	***SS***	***Degree of Freedom***	***Mean Square***	F_0	$F_{\alpha,m-p,n-m}$
Lack of fit	21.69	2	10.85	0.458	4.737
Pure Error	165.77	7	23.68		

To determine whether the regressor variables contributed significantly to the model a *Test for significance of regression*[12] was performed. The test procedure involves computing the statistic F_0 as follows:

$$F_0 = \frac{SS_R/k}{SS_E/(n-k-1)} \tag{5.6}$$

where:

SS_R is the sum of squares due to the regression which is computed from the average of the total n observations ($\overline{r^0_{\mathrm{DNBE}}}$) and the fitted values ($\hat{r}^0_{\mathrm{DNBE},i}$) as:

$$SS_R = \sum_{i=1}^{n} \left(\overline{r^0_{\mathrm{DNBE}}} - \hat{r}^0_{\mathrm{DNBE},i} \right)^2 \tag{5.7}$$

SS_E is the sum of squares due to the error computed from the *i*th observation of the response ($r^0_{\mathrm{DNBE},i}$) and the fitted values ($\hat{r}^0_{\mathrm{DNBE},i}$) as:

$$SS_E = \sum_{i=1}^{n} \left(r^0_{\mathrm{DNBE},i} - \hat{r}^0_{\mathrm{DNBE},i} \right)^2 \tag{5.8}$$

k is the number of regressor variables.

Table 5.3. Test for significance of regression (α = 0.95)

Source of Variation	***SS***	***Degree of Freedom***	***Mean Square***	F_0	$F_{\alpha,k,n-k-1}$
Regression	377.26	7	53.894	2.608	3.293
Error	185.97	9	20.663		
Total	563.22	16			

From the results gathered in Table 5.3 it can be concluded that $F_0 < F_{distribution}$ (for a probability of 95%), thus none of the regressor variables contributed to the model, i.e. in the range of operation variables studied (N_{stir} = 300 – 700 rpm, d_p = 0.4 – 0.8 mm and W_{cat} = 0.5 - 2 g) the reaction rate values can be considered the same within the limits of experimental error.

Therefore, the selected operation conditions to carry out the kinetic experiments were: N_{stir} = 500 rpm, W_{cat} = 1 g of Amberlyst-70 and d_p = 0.4 – 0.63 mm.

5.3.2. Modeling of kinetic data

The reaction rate models considered in this work were based on the Langmuir-Hinshelwood-Hougen-Watson (LHHW) and the Eley Rideal (ER) formalisms. These formalisms, as well as the kinetic expressions derived from different rate limiting step (RLS) and quasi-steady states assumptions are discussed next.

Mechanism 1: Langmuir-Hinshelwood-Hougen-Watson (LHHW) formalism.

In the LHHW mechanism two alcohol molecules, each one adsorbed on an adjacent active site, react to yield the ether. The elementary steps for this model are shown in the following equations, in which σ represents an active site and BuOHσ, DNBEσ and $H_2O\sigma$ correspond, respectively, to 1-butanol, di-n-butyl ether and water chemisorbed on an only active site.

$$\mathrm{BuOH} + \sigma \xrightleftharpoons{K_{\mathrm{BuOH}}} \mathrm{BuOH}\sigma$$

$$2\,\mathrm{BuOH}\sigma + n_\sigma(\sigma) \xrightleftharpoons{K_s} \mathrm{DNBE}\sigma + \mathrm{H_2O}\sigma + n_\sigma(\sigma)$$

$$\mathrm{DNBE}\sigma \xrightleftharpoons{1/K_{\mathrm{DNBE}}} \mathrm{DNBE} + \sigma$$

$$H_2O\sigma \xrightleftharpoons{1/K_{H_2O}} H_2O + \sigma$$

Mechanism 2: Eley Rideal formalism where DNBE remains adsorbed (ER$_{DNBE}$)

The ER formalism assumes that only one of the two reacting molecules of 1-butanol adsorbs on the surface and reacts with other one directly from the bulk yielding DNBE and water. The formed DNBE molecule remains adsorbed on the surface while water is immediately released into solution:

$$BuOH + \sigma \xrightleftharpoons{K_{BuOH}} BuOH\sigma$$

$$BuOH + BuOH\sigma + n_\sigma(\sigma) \xrightleftharpoons{K_S} DNBE\sigma + H_2O + n_\sigma(\sigma)$$

$$DNBE\sigma \xrightleftharpoons{1/K_{DNBE}} DNBE + \sigma$$

Mechanism 3: Eley Rideal formalism where water remains adsorbed (ER$_{H2O}$)

As in mechanism 2, 1-butanol from solution reacts directly with 1-butanol adsorbed on the surface of the catalyst but, in this case, the ether is immediately released to the liquid phase and water remains adsorbed:

$$BuOH + \sigma \xrightleftharpoons{K_{BuOH}} BuOH\sigma$$

$$BuOH + BuOH\sigma + n_\sigma(\sigma) \xrightleftharpoons{K_S} DNBE + H_2O\sigma + n_\sigma(\sigma)$$

$$H_2O\sigma \xrightleftharpoons{1/K_{H_2O}} H_2O + \sigma$$

In the three mechanisms it was taken into account the possibility that n_σ additional active sites (with $n_\sigma = 0$, 1 or 2) could participate in the surface reaction.

Each of the elementary steps that take part in the reaction mechanisms just described can be considered as the rate limiting step. If the chemical reaction rate on the surface is considered the RLS, it is assumed that adsorption of species is maintained in a quasi-equilibrium state all the time. On the contrary, if the RLS is considered to be the adsorption of the reactant or the desorption of a product then, it is assumed that the chemical reaction between adsorbed species is in quasi-equilibrium. Table 5.4 gathers the kinetic models derived from the three reaction mechanisms depending on the elementary step that is considered as the RLS. $\hat{k}$ is the forward rate constant for the surface reaction; k_j and K_j are, respectively, the adsorption rate constant and the adsorption equilibrium constant of compound j; K_{eq} is the thermodynamic equilibrium constant which was experimentally determined in the previous chapter. All the rate expressions of Table 5.4 may be expressed as a combination of three terms, the kinetic, the driving potential and the adsorption term[13,14]:

Table 5.4. Kinetic models with n_σ additional active centers participating in the surface reaction ranging from 0 to 2.

	Reaction Mechanisms		
RLS	**LHHW**	**ER with DNBE adsorption**	**ER with H_2O adsorption**
1-butanol adsorption	LHHW-RLS1	ER_{DNBE}-RLS1	ER_{H2O}-RLS1
	$r_{DNBE}=\dfrac{k_{BuOH}\left(a_{BuOH}-\left(\dfrac{a_{DNBE}\cdot a_{H_2O}}{K_{eq}}\right)^{0.5}\right)}{1+K_{BuOH}\left(\dfrac{a_{DNBE}\cdot a_{H_2O}}{K_{eq}}\right)^{0.5}+K_{DNBE}\cdot a_{DNBE}+K_{H_2O}\cdot a_{H_2O}}$	$r_{DNBE}=\dfrac{k_{BuOH}\left(a_{BuOH}-\dfrac{a_{DNBE}\cdot a_{H_2O}}{K_{eq}\cdot a_{BuOH}}\right)}{1+K_{BuOH}\cdot\left(\dfrac{a_{DNBE}\cdot a_{H_2O}}{K_{eq}\cdot a_{BuOH}}\right)+K_{DNBE}\cdot a_{DNBE}}$	$r_{DNBE}=\dfrac{k_{BuOH}\left(a_{BuOH}-\dfrac{a_{DNBE}\cdot a_{H_2O}}{K_{eq}\cdot a_{BuOH}}\right)}{1+K_{BuOH}\cdot\left(\dfrac{a_{DNBE}\cdot a_{H_2O}}{K_{eq}\cdot a_{BuOH}}\right)+K_{H_2O}\cdot a_{H_2O}}$
Surface reaction	LHHW-RLS2	ER_{DNBE}-RLS2	ER_{H2O}-RLS2
	$r_{DNBE}=\dfrac{\hat{k}\cdot K_{BuOH}^2\left(a_{BuOH}^2-\dfrac{a_{DNBE}\cdot a_{H_2O}}{K_{eq}}\right)}{\left(1+K_{BuOH}\cdot a_{BuOH}+K_{DNBE}\cdot a_{DNBE}+K_{H_2O}\cdot a_{H_2O}\right)^{2+n_\sigma}}$	$r_{DNBE}=\dfrac{\hat{k}\cdot K_{BuOH}\left(a_{BuOH}^2-\dfrac{a_{DNBE}\cdot a_{H_2O}}{K_{eq}}\right)}{\left(1+K_{BuOH}\cdot a_{BuOH}+K_{DNBE}\cdot a_{DNBE}\right)^{1+n_\sigma}}$	$r_{DNBE}=\dfrac{\hat{k}\cdot K_{BuOH}\left(a_{BuOH}^2-\dfrac{a_{DNBE}\cdot a_{H_2O}}{K_{eq}}\right)}{\left(1+K_{BuOH}\cdot a_{BuOH}+K_{H_2O}\cdot a_{H_2O}\right)^{1+n_\sigma}}$
DNBE desorption	LHHW-RLS3	ER_{DNBE}-RLS3	
	$r_{DNBE}=\dfrac{k_{DNBE}\left(K_{eq}\dfrac{a_{BuOH}^2}{a_{H_2O}}-a_{DNBE}\right)}{1+K_{BuOH}\cdot a_{BuOH}+K_{DNBE}\cdot\left(K_{eq}\dfrac{a_{BuOH}^2}{a_{H_2O}}\right)+K_{H_2O}\cdot a_{H_2O}}$	$r_{DNBE}=\dfrac{k_{DNBE}\left(K_{eq}\dfrac{a_{BuOH}^2}{a_{H_2O}}-a_{DNBE}\right)}{1+K_{BuOH}\cdot a_{BuOH}+K_{DNBE}\cdot\left(K_{eq}\dfrac{a_{BuOH}^2}{a_{H_2O}}\right)}$	
H_2O desorption	LHHW-RLS4		ER_{H2O}-RLS3
	$r_{DNBE}=\dfrac{k_{H_2O}\left(K_{eq}\dfrac{a_{BuOH}^2}{a_{DNBE}}-a_{H_2O}\right)}{1+K_{BuOH}\cdot a_{BuOH}+K_{DNBE}\cdot a_{DNBE}+K_{H_2O}\cdot\left(K_{eq}\dfrac{a_{BuOH}^2}{a_{DNBE}}\right)}$		$r_{DNBE}=\dfrac{k_{H_2O}\left(K_{eq}\dfrac{a_{BuOH}^2}{a_{DNBE}}-a_{H_2O}\right)}{1+K_{BuOH}\cdot a_{BuOH}+K_{H_2O}\cdot\left(K_{eq}\dfrac{a_{BuOH}^2}{a_{DNBE}}\right)}$

Each kinetic model has been identified with the initials of the mechanism (LHHW, ER_{DNBE} or ER_{H2O}) followed by RLS# where # indicates the number corresponding to the elementary step that is being considered the Rate Limiting Step.

$$r_{\text{DNBE}} = \frac{\text{kinetic term} \times \left(\text{driving potential term}\right)}{\left(\text{adsorption term}\right)^{m_\sigma}} \tag{5.9}$$

When the surface reaction is considered the RLS, the *kinetic term* is the product of the surface reaction rate constant for the forward reaction and a power of the 1-butanol adsorption equilibrium constant which depends on the considered mechanism. If the adsorption of 1-butanol or the desorption of one of the products is the RLS, the kinetic term is the rate constant of the rate limiting adsorption/desorption process. The *driving potential term* accounts, in all rate expressions, for how far the thermodynamic equilibrium is, and it must become zero when the equilibrium is reached. Finally, the *adsorption term* accounts for all the species that are adsorbed on surface sites. The exponent on the adsorption term for the cases where the surface reaction is considered the RLS is equal to the number of active sites participating in the surface reaction. When the adsorption/desorption of a single species is the RLS, the corresponding element in the adsorption term is modified according to the surface reaction involved.

Simplified kinetic models were derived from the general kinetic models of Table 5.4 by assuming the amount of free active sites very low compared with the occupied ones (thus the unity present in the adsorption term can be removed), and/or the adsorption of alcohol, ether and/or water to be negligible. This way, 82 different kinetic models were obtained, which have been included in the Appendix that can be found at the end of this chapter.

All the models where fitted to reaction rate data by minimizing the sum of squared relative errors (*SSRE*, Equation 5.10) using the Levenberg-Marquardt algorithm[15,16] which is implemented in Matlab. We consider the relative error to be a more meaningful measure[17,18] than the sum of squared errors ($\sum (r_{\text{exp}} - r_{cal})^2$), given that the range of rate values is large ($r_{\text{DNBE}} \approx 2 - 135$ mol/h·kg).

$$SSRE = \sum \left(\frac{r_{\text{exp}} - r_{cal}}{r_{\text{exp}}} \right)^2 \tag{5.10}$$

The dependence of the kinetic parameters with the temperature was considered to follow the Arrhenius law (Equation 5.11) for the rate constants ($\hat{k}$ and k_j), and the van't Hoff law (Equation 5.12) for the adsorption constants (K_j). Both expressions were reparametrized in order to avoid strong binary correlation between parameters.[19] T_{ref} is defined as the midpoint T value in the analyzed range of temperatures.

$$\hat{k}, k_j = A \cdot \exp\left[-\frac{E_A}{R} \left(\frac{1}{T} - \frac{1}{T_{ref}} \right) \right] \tag{5.11}$$

$$K_j = \exp\left[\frac{\Delta S_j}{R} - \frac{\Delta H_j}{R}\left(\frac{1}{T} - \frac{1}{T_{ref}}\right)\right] \quad (5.12)$$

The temperature dependence of the thermodynamic equilibrium constant was found to be (see previous chapter):

$$K_{eq} = \exp\left[\frac{37.0}{T} + 3.2\right] \quad (5.13)$$

Whenever possible, rate and adsorption constants were grouped for mathematical fitting purposes. Equations 5.14-5.17 show, by way of example, how the constants association was done for the kinetic model LHHW-RLS2/1b (see Appendix) which stemmed from the LHHW formalism when the following assumptions were made: (1) the surface reaction was considered the RLS; (2) the number of active centers participating in the reaction was 3; and (3) the amount of free active sites was very low compared with the occupied ones.

$$r_{\text{DNBE}} = \frac{k^{*}\cdot\left(a_{\text{BuOH}}^{2} - \dfrac{a_{\text{DNBE}}\cdot a_{\text{H}_2\text{O}}}{K_{eq}}\right)}{\left(a_{\text{BuOH}} + K_1\cdot a_{\text{DNBE}} + K_2\cdot a_{\text{H}_2\text{O}}\right)^{3}} \quad (5.14)$$

With

$$k^{*} = \hat{k}\cdot\frac{K_{\text{BuOH}}^{2}}{K_{\text{BuOH}}^{3}} = \hat{k}\cdot K_{\text{BuOH}}^{-1} \quad (5.15)$$

$$K_1 = \frac{K_{\text{DNBE}}}{K_{\text{BuOH}}} \quad (5.16)$$

$$K_2 = \frac{K_{\text{H}_2\text{O}}}{K_{\text{BuOH}}} \quad (5.17)$$

5.3.2.1. Experiments starting from pure 1-butanol

A series of experiments with pure 1-butanol was conducted in the temperature range 413 - 463 K. Each experiment was, at least, duplicated (being the relative error corresponding to DNBE formation rates lower than 5%). Figures 5.2a and b represent, respectively, 1-butanol conversion and selectivity to di-n-butyl ether as a function of the reaction time for all the temperatures tested. From Figure 5.2a it could be concluded that the normalized 1-butanol conversion is strongly influenced by reaction temperature increasing from a value of 4% at 413 K to more than a tenfold (≈ 46%) at 463 K (after 7 h of experiment). However, it must be taken into account that the system is far away from the equilibrium position. In the previous chapter it was found that the dehydration of 1-butanol to DNBE is a slightly exothermic reaction (almost athermic). Thus it is expected that, with time, the curves of conversion for all the tested temperatures tend to a very close value (not exactly the same value due to the existence of secondary reactions which are influenced by the temperature reaction).

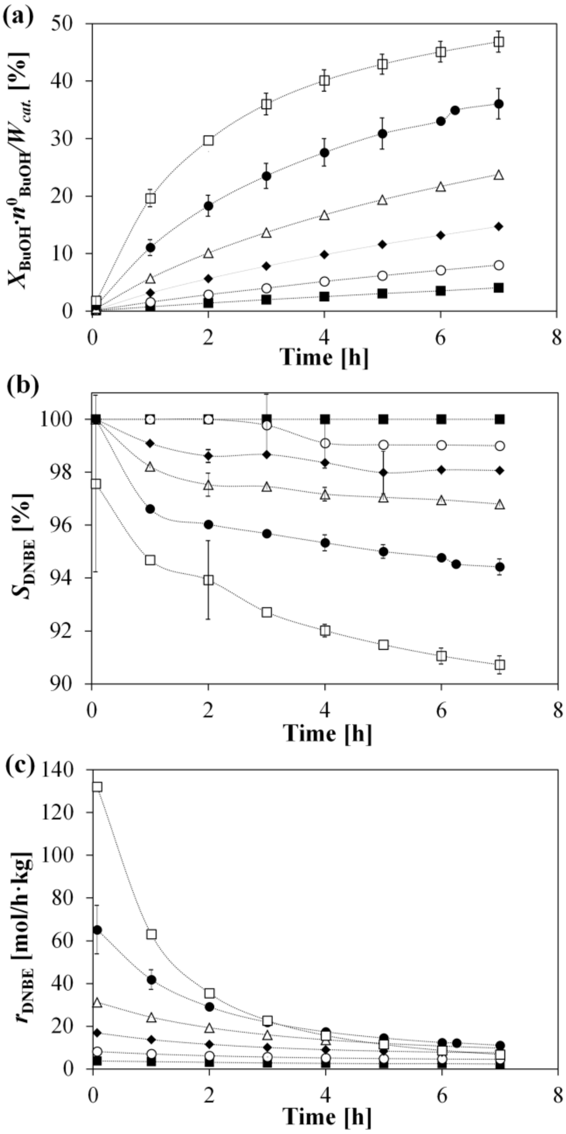

Figure 5.2. (a) 1-butanol conversion; (b) selectivity to DNBE; and (c) reaction rate of DNBE synthesis as a function of temperature: (■) 413 K; (○) 423 K; (♦) 433 K; (Δ) 443 K; (●) 453 K; (□) 463 K. Experiments starting from pure 1-butanol, 1 g of catalyst, $d_p = 0.4 – 0.63$ mm, 40 bar, 500 rpm. The error bars indicate the confidence interval at a 95% probability level. Most error bars are smaller than markers.

Selectivity to DNBE also depends on the reaction temperature although in all cases was higher than 90%. As it can be seen, after some time selectivity reaches a plateau. The time needed to reach this plateau and the value to which the selectivity tends depends on the operating temperature: a higher reaction temperature results in longer times to reach a constant (in experiments run at the higher temperatures, 443 – 463 K, selectivity was still moderately decreasing after 7 h) and lower selectivity to DNBE, other detected products being butenes, 2-butanol and the branched ether 1-(1-methylpropoxy) butane (a detailed scheme of the reaction network can be found in Section 3.3.1). Nevertheless, for all the tested temperatures the catalyst is very selective to the linear ether.

Figure 5.2c shows the reaction rate of DNBE synthesis along the experiments as a function of temperature. As expected, the initial reaction rate is highly dependent on temperature doubling its value with each 10 K rise. However, reaction rate decreases along time (more sharply when the reaction temperature is high) and after 7 h the reaction rate for all the tested temperatures is very similar with values in the range of 2.3 - 11.1 mol/h·kg. This decrease could be due to an inhibition effect caused by the reaction products (it is well known that released water adsorbs strongly on acidic sites influencing the reaction rate[4-7]).

Given the important dissimilarity between the compounds presents in the medium, the system deviates from ideality. In order to take into account this non-ideality, the kinetic analysis was carried out as a function of activities instead of concentrations. The activity coefficients were estimated by the UNIFAC-Dortmund predictive method.[20-23]

Figure 5.3 shows the dependence of the reaction rate as a function of activities of 1-butanol (a_{BuOH}), water (a_{H2O}) and di-n-butyl ether (a_{DNBE}). Due to the fact that a_{BuOH}, a_{H2O} and a_{DNBE} are not independent variables, it is difficult to analyze the influence that each activity has on the reaction rate. However, from Figure 5.3 it can be concluded that a decrease in $a_{BuOH,}$ which is associated with an increase in a_{H2O} and a_{DNBE}, affects negatively the DNBE reaction rate for all the temperatures tested.

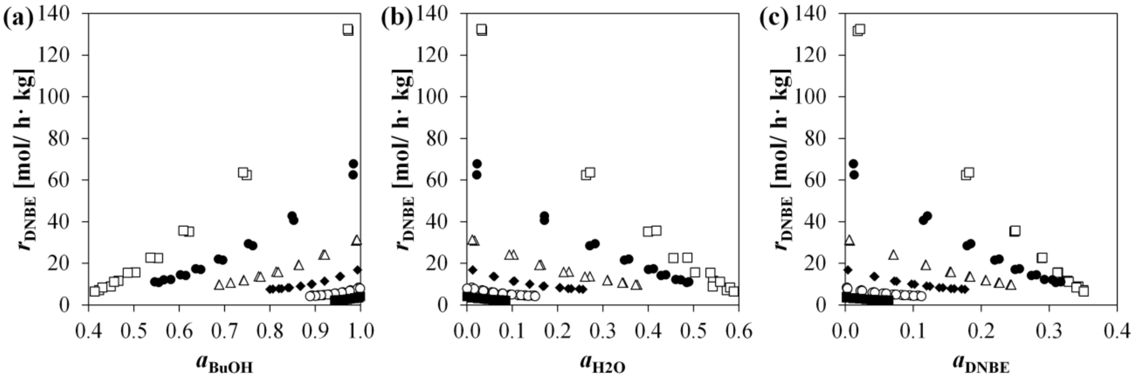

Figure 5.3. Reaction rate of DNBE synthesis as a function of (a) 1-butanol activity; (b) water activity; (c) DNBE activity. (■) 413 K, (○) 423 K, (♦) 433 K, (Δ) 443 K, (●) 453 K, (□) 463 K. Experiments starting from pure 1-butanol, 1 g of catalyst, d_p = 0.4 – 0.63 mm, 40 bar, 500 rpm.

General (Table 5.4) and simplified models (Appendix) were fitted to experimental data corresponding to runs starting from pure 1-butanol. Several kinetic models with physicochemical meaning (positive activation energy and negative adsorption enthalpy and adsorption entropy) fitted the experimental data satisfactorily. Models, fitted parameters, confidence intervals for a 95% of probability, sum of squared relative errors and goodness of the fit (R^2_{adj}) for the best kinetic models are gathered in Table 5.5. Among these models, LHHW-RLS4/1b (Equation 5.19) and LHHW-RLS3/1b (Equation 5.20) present the lowest sum of squared relative errors (*SSRE*) and the lowest parameter uncertainty Δ (calculated with Equation 5.18, with ε_i being the uncertainty of parameter β_i and *p* de number of parameters in the model). Both equations stem from a LHHW formalism in which the rate limiting step is considered to be the desorption of one of the products (water and ether respectively) and assuming the amount of free active sites to be negligible. On the other hand, model LHHW-RLS2/1b (Equation 5.21) stems from a LHHW formalism where the surface reaction is considered the rate limiting step.

$$\Delta = \left[\sum_{i=1}^{p} \left(\frac{\varepsilon_i}{\beta_i} \right)^2 \right]^{0.5} \tag{5.18}$$

Table 5.5. Best kinetic models for experiments starting from pure 1-butanol.

LHHW-RLS4/1b
RLS: water desorption. Assuming negligible the amount of free active sites.

$$r_{\mathrm{DNBE}} = \frac{\frac{k_{\mathrm{H_2O}}}{K_{\mathrm{H_2O}}}\left(K_{eq}\frac{a_{\mathrm{BuOH}}^2}{a_{\mathrm{DNBE}}} - a_{\mathrm{H_2O}}\right)}{\frac{K_{\mathrm{BuOH}}}{K_{\mathrm{H_2O}}}\cdot a_{\mathrm{BuOH}} + \frac{K_{\mathrm{DNBE}}}{K_{\mathrm{H_2O}}}\cdot a_{\mathrm{DNBE}} + K_{eq}\frac{a_{\mathrm{BuOH}}^2}{a_{\mathrm{DNBE}}}} \qquad (5.19)$$

$SSRE$ = 0.59	R^2_{adj} = 0.99	Δ = 0.60

Parameters

A	E_A [kJ/mol]	$\Delta S_{\mathrm{BuOH}} - \Delta S_{\mathrm{H2O}}$ [J/mol·K]	$\Delta H_{\mathrm{BuOH}} - \Delta H_{\mathrm{H2O}}$ [kJ/mol]	$\Delta S_{\mathrm{DNBE}} - \Delta S_{\mathrm{H2O}}$ [J/mol·K]	$\Delta H_{\mathrm{DNBE}} - \Delta H_{\mathrm{H2O}}$ [kJ/mol]
24.2±1.0	112.8±3.5	38.9±1.9	-50.7±17.8	44.8±2.8	48.0±22.7

LHHW-RLS3/1b
RLS: DNBE desorption. Assuming negligible the amount of free active sites.

$$r_{\mathrm{DNBE}} = \frac{\frac{k_{\mathrm{DNBE}}}{K_{\mathrm{DNBE}}}\left(K_{eq}\frac{a_{\mathrm{BuOH}}^2}{a_{\mathrm{H_2O}}} - a_{\mathrm{DNBE}}\right)}{\frac{K_{\mathrm{BuOH}}}{K_{\mathrm{DNBE}}}\cdot a_{\mathrm{BuOH}} + K_{eq}\frac{a_{\mathrm{BuOH}}^2}{a_{\mathrm{H_2O}}} + \frac{K_{\mathrm{H_2O}}}{K_{\mathrm{DNBE}}}\cdot a_{\mathrm{H_2O}}} \qquad (5.20)$$

$SSRE$ = 0.60	R^2_{adj} = 0.99	Δ = 0.65

Parameters

A	E_A [kJ/mol]	$\Delta S_{\mathrm{BuOH}} - \Delta S_{\mathrm{DNBE}}$ [J/mol·K]	$\Delta H_{\mathrm{BuOH}} - \Delta H_{\mathrm{DNBE}}$ [kJ/mol]	$\Delta S_{\mathrm{H2O}} - \Delta S_{\mathrm{DNBE}}$ [J/mol·K]	$\Delta H_{\mathrm{H2O}} - \Delta H_{\mathrm{DNBE}}$ [kJ/mol]
24.7±1.1	110.7±4.0	37.3±1.3	-53.9±16.5	36.0±3.4	47.9±27.1

LHHW-RLS2/1b
RLS: surface reaction. Assuming negligible the amount of free active sites.

$$r_{DNBE} = \frac{\hat{k}\cdot\frac{K_{\mathrm{BuOH}}^2}{K_{\mathrm{BuOH}}^{2+\mathrm{n}}}\left(a_{\mathrm{BuOH}}^2 - \frac{a_{\mathrm{DNBE}}\cdot a_{\mathrm{H_2O}}}{K_{eq}}\right)}{\left(a_{\mathrm{BuOH}} + \frac{K_{\mathrm{DNBE}}}{K_{\mathrm{BuOH}}}\cdot a_{\mathrm{DNBE}} + \frac{K_{\mathrm{H_2O}}}{K_{\mathrm{BuOH}}}\cdot a_{\mathrm{H_2O}}\right)^{2+\mathrm{n}_\sigma}} \qquad (5.21)$$

n_σ	**0**	**1**	**2**
$SSRE$:	0.94	0.96	1.01
R^2_{adj}:	0.97	0.98	0.97
Δ:	1.79	1.99	2.59
Parameters			
A:	25.4±1.1	25.5±1.1	25.6±1.1
E_A [kJ/mol]:	118.5±3.9	118.7±4.0	118.9±4.1
$\Delta S_{\mathrm{DNBE}} - \Delta S_{\mathrm{BuOH}}$ [J/mol·K]:	6.9±2.6	4.1±3.6	2.2±4.3
$\Delta H_{\mathrm{DNBE}} - \Delta H_{\mathrm{BuOH}}$ [kJ/mol]:	-26.3±26.4	-27.3±28.9	-28.0±29.7
$\Delta S_{\mathrm{H2O}} - \Delta S_{\mathrm{BuOH}}$ [J/mol·K]:	-12.8±15.3	-10.0±12.1	-8.3±9.8
$\Delta H_{\mathrm{H2O}} - \Delta H_{\mathrm{BuOH}}$ [kJ/mol]:	116.7±92.2	83.4±12.1	66.6±48.4

It must be pointed out that the concentration of alcohol, ether and water in the reaction medium are not independent variables, thus a_{BuOH}, a_{DNBE} and a_{H2O} are reciprocally dependent. Figure 5.4 shows the relation between water and DNBE activity. As it can be seen, the ratio $a_{\mathrm{H2O}}/a_{\mathrm{DNBE}}$ is almost constant along the experiments for all the temperatures tested (except for time = 0) with values ranging between 1.3 and 1.8, belonging the highest ratios to the highest temperatures. This tendency is in accordance with the lower selectivity observed for higher temperatures being water also produced through side-reactions. The significant high ratios observed at time = 0 h are probably due to residual water in the dry catalyst or in the reactant. Due to the fact that the ratio a_{H2O}/a_{DNBE} is almost constant, models LHHW-RLS4/1b (Equation 5.19) and LHHW-RLS3/1b (Equation 5.20) are equivalent. Similarity between fitted parameters of both models (Table 5.5) corroborates it. This fact makes impossible to differentiate, from this set of experiments, which of the two mechanisms prevails.

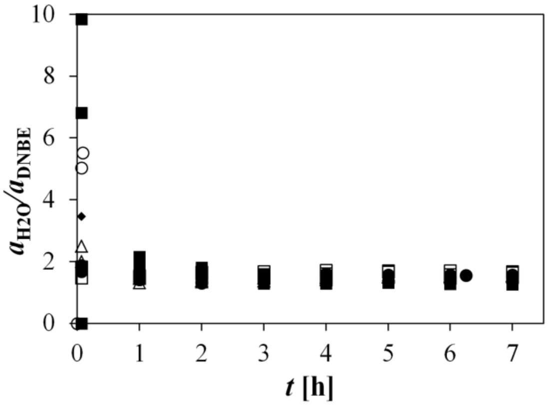

Figure 5.4. Evolution of the ratio a_{H2O}/a_{DNBE} with time for experiments starting from pure 1-butanol. (■) 413 K, (○) 423 K, (♦) 433 K, (Δ) 443 K, (●) 453 K, (□) 463 K. Experiments starting from pure 1-butanol, 1 g of catalyst, d_p = 0.4 – 0.63 mm, 40 bar, 500 rpm.

Distribution of residual of fitted models gathered in Table 5.5 must also be taken into account. As it can be seen in Figure 5.5a the model fits the experimental data satisfactorily. However, residuals do not show a random distribution. From Figure 5.5b it can be concluded that residuals corresponding to experiments performed at 463 K account significantly in the total sum of residuals. Data shown in Figure 5.5 corresponds to model LHHW-RLS4/1b (Equation 5.19) but for the rest of models gathered in Table 5.5 the trends are very similar. Two circumstances may be the cause of the important difference observed between the models fitting to data corresponding to 463 K runs and to data corresponding to the rest of temperatures: (1) a temperature increase may lead to a change of the rate limiting step, thus a change of the kinetic model and/or (2) the considerable amount of water produced in experiments carried out at high temperatures (at 463 K the amount of water can reach up to 0.25 molar fraction) play an important role on the catalytic reaction.

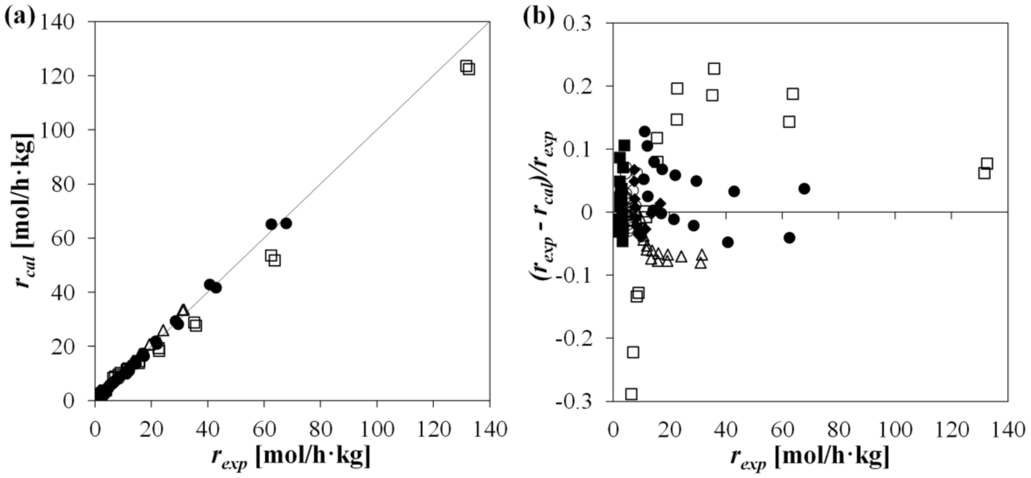

Figure 5.5. (a) Calculated reaction rates by model LHHW-RLS4/1b (Equation 5.19) versus experimental rates; (b) residuals distribution. (■) 413 K, (○) 423 K, (♦) 433 K, (Δ) 443 K, (●) 453 K, (□) 463 K. Experiments starting from pure 1-butanol, 1 g of catalyst, d_p = 0.4 – 0.63 mm, 40 bar, 500 rpm.

5.3.2.2. Experiments starting from 1-butanol/water and 1-butanol/DNBE mixtures.

To stress the effect of reaction products on the reaction rate and to break the constancy of the ratio a_{H2O}/a_{DNBE} a set of experiments starting from mixtures of 1-butanol/water and 1-butanol/DNBE was performed at 413, 433 and 453 K. Figure 5.6 shows the values of the ratio a_{H2O}/a_{DNBE} for all the performed experiments. As it can be seen, for experiments starting from pure 1-butanol, a_{H2O}/a_{DNBE} is constant with both reaction time and temperature. However, when starting from mixtures of 1-butanol/water and 1-butanol/DNBE this trend is broken.

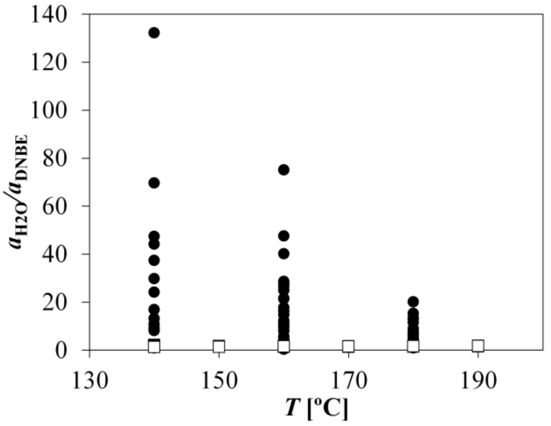

Figure 5.6. Ratio a_{H2O}/a_{DNBE} for: (□) experiments starting from pure 1-butanol; (●) experiments starting from 1-butanol/water mixtures. For each temperature the values of a_{H2O}/a_{DNBE} for different reaction time have been repesented.

Figure 5.7 shows the effect of water and DNBE on the initial reaction rate as a function of the initial amount of water and DNBE in the mixture (% w/w). In Figure 5.7a it can be seen that the initial reaction rate is highly sensitive to water content decreasing as the amount of water in the initial mixture increases. This trend is in agreement with the inhibitor character attributed to water. On the other hand, Figure 5.7b indicates that the effect of DNBE on the initial reaction rate is not remarkable suggesting that the adsorption of the ether may be negligible.

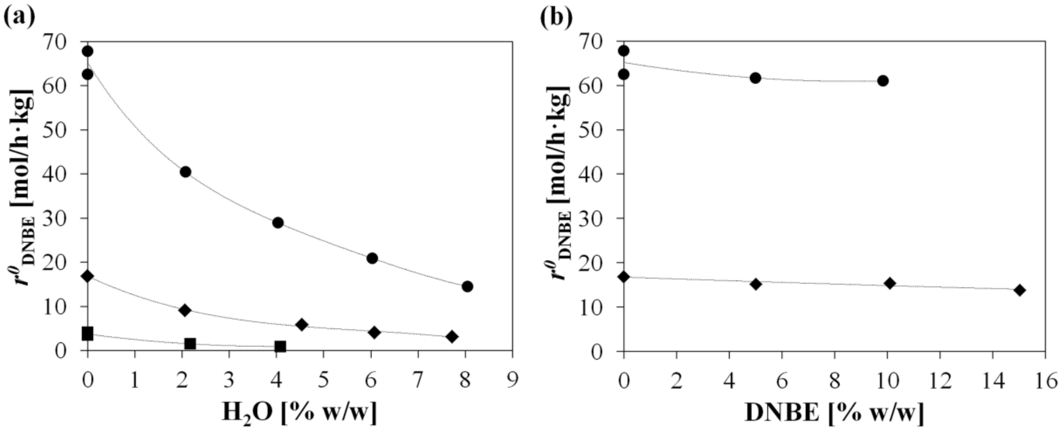

Figure 5.7. Influence of (a) water and (b) DNBE on the initial reaction rate of DNBE formation. (■) 413 K, (♦) 433 K, (●) 453 K, 1 g of catalyst, d_p = 0.4 – 0.63 mm, 40 bar, 500 rpm.

Besides reducing the initial reaction rate of DNBE synthesis, water also affects the catalyst selectivity. As it can be seen in Figure 5.8, mixtures with higher initial amount of water present, after 7 hours of experiment, lower selectivity to DNBE. The drop in DNBE selectivity is due to an increase in the formation of olefins and the secondary alcohol, however, selectivity to the branched ether, 1-(1-methylpropoxy) butane, is not affected. Water molecules adsorb preferentially on the active sites, blocking them. As the number of active sites blocked by water increases, the probability of finding two or more molecules of 1-butanol absorbed on the catalyst surface close enough decreases reducing the extent of the bimolecular dehydration of 1-butanol and enhancing the intramolecular dehydration to yield the olefin 1-butene. Data of Figure 5.8 corresponds to experiments performed at 453 K. For lower temperatures (413 and 433 K) the amount of water in the initial mixture does not have a significant effect on the products distribution which may be due to the fact that the intramolecular dehydration of 1-butanol to 1-butene is enhanced at high temperatures. The presence of DNBE in the starting mixture does not have any significant effect on the product distribution either.

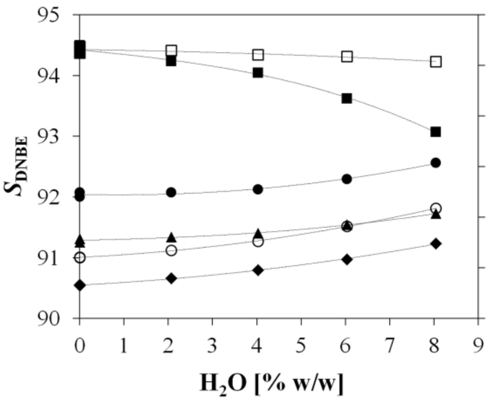

Figure 5.8. Selectivity to products after 7 h reaction as a function of initial water content.
T = 463 K, 1 g of catalyst, d_p = 0.4 – 0.63 mm, 40 bar, 500 rpm.
(■) DNBE, (○) 1-butene, (♦) 2-butanol,
(▲) *cis*-2-butene, (●) *trans*-2-butene,
(□) 1-(1-methylpropoxy)butane.

General (Table 5.4) and simplified models (Appendix) were fitted to data corresponding to experiments starting from mixtures of 1-butanol/water and 1-butanol/DNBE. Data of experiments performed with pure 1-butanol were not included in this analysis with the aim of facilitate differentiation among models that are equivalent when the relationship between activities is almost constant. Best kinetic models are gathered in Table 5.6.

As it can be concluded from the results gathered in Table 5.6, the fact of breaking the constancy of a_{H2O}/a_{DNBE} makes possible to differentiate between models that in the previous set of experiments (pure 1-butanol) were equivalent. In contrast to results gathered in Table 5.5, the model which stems from a LHHW formalism where the desorption of water is considered de rate limiting step and assuming the amount of free active sites negligible (LHHW-RLS4/1b, see Equation 5.19) does not fit satisfactorily experimental data (with *SSRE* higher than 20). Nevertheless, the LHHW model where the rate limiting step is considered to be the desorption of DNBE (LHHW-RLS3/1b, see Equation 5.20) still does. LHHW models obtained assuming that the surface reaction is the rate limiting step, LHHW-RLS2/1b (Equation 5.21) (considering the amount of free active sites negligible) and LHHW-RLS2/3b (Equation 5.22) (considering negligible both the amount of free active sites and the adsorption of DNBE) with n_σ = 0, 1 and 2 also fit adequately data (except for LHHW-RLS2/3b with n_σ = 2 where the *SSRE* is 2.36) however, uncertainty of parameters corresponding to model LHHW-RLS2/1b with n_σ = 0 and 1 is significant. It should be noted that all these models (Table 5.6) include in their denominator the term of water adsorption.

Table 5.6. Best kinetic models for experiments starting from mixtures 1-butanol/water and 1-butanol/DNBE.

LHHW-RLS3/1b (see Equation 5.20) RLS: DNBE desorption. Assuming negligible the amount of free active sites.					
SSRE = 0.36		$R^2_{\mathrm{adj}} = 1.00$		$\Delta = 2.53$	
Parameters					
A	E_A [kJ/mol]	$\Delta S_{\mathrm{BuOH}} - \Delta S_{\mathrm{DNBE}}$ [J/mol·K]	$\Delta H_{\mathrm{BuOH}} - \Delta H_{\mathrm{DNBE}}$ [kJ/mol]	$\Delta S_{\mathrm{H2O}} - \Delta S_{\mathrm{DNBE}}$ [J/mol·K]	$\Delta H_{\mathrm{H2O}} - \Delta H_{\mathrm{DNBE}}$ [kJ/mol]
14.4±0.8	117.8±6.7	33.6±1.8	-18.4±18.5	38.9±0.9	3.9±9.1

LHHW-RLS2/1b (see Equation 5.21) RLS: surface reaction. Assuming negligible the amount of free active sites.			
$\boldsymbol{n_\sigma}$	**0**	**1**	**2**
SSRE:	0.52	0.45	0.43
R^2_{adj}:	0.98	0.98	0.98
Δ:	13.59	6.61	1.89
Parameters			
A:	16.9 ± 1.0	16.9 ± 0.8	16.9 ± 0.8
E_A [kJ/mol]:	120.7 ± 5.8	122.7 ± 4.7	123.9 ± 4.4
$\Delta S_{\mathrm{DNBE}} - \Delta S_{\mathrm{BuOH}}$ [J/mol·K]:	-16.7 ± 7.9	-9.5 ± 1.9	-7.8 ± 1.1
$\Delta H_{\mathrm{DNBE}} - \Delta H_{\mathrm{BuOH}}$ [kJ/mol]:	-59 ± 162	3.4 ± 21.8	10.2 ± 12.0
$\Delta S_{\mathrm{H2O}} - \Delta S_{\mathrm{BuOH}}$ [J/mol·K]:	4.9 ± 0.5	2.0 ± 0.3	0.2 ± 0.3
$\Delta H_{\mathrm{H2O}} - \Delta H_{\mathrm{BuOH}}$ [kJ/mol]:	463.2 ± 6159	2.8 ± 4.3	4.0 ± 3.4

LHHW-RLS2/3b
RLS: surface reaction.
Assuming negligible the amount of free active sites and the adsorption of DNBE.

$$r_{\mathrm{DNBE}} = \frac{\hat{k} \cdot \dfrac{K^2_{\mathrm{BuOH}}}{K^{2+n}_{\mathrm{BuOH}}} \left(a^2_{\mathrm{BuOH}} - \dfrac{a_{\mathrm{DNBE}} \cdot a_{\mathrm{H_2O}}}{K_{eq}} \right)}{\left(a_{\mathrm{BuOH}} + \dfrac{K_{\mathrm{H_2O}}}{K_{\mathrm{BuOH}}} \cdot a_{\mathrm{H_2O}} \right)^{2+n_\sigma}} \qquad (5.22)$$

$\boldsymbol{n_\sigma}$	**0**	**1**	**2**
SSRE:	0.54	1.02	2.36
R^2_{adj}:	0.98	0.98	
Δ:	2.35	0.70	
Parameters			
A:	16.1 ± 0.7	14.2 ± 0.7	
E_A [kJ/mol]:	122.1 ± 5.4	125.2 ± 6.5	
$\Delta S_{\mathrm{H2O}} - \Delta S_{\mathrm{BuOH}}$ [J/mol·K]:	4.6 ± 0.4	1.2 ± 0.5	
$\Delta H_{\mathrm{H2O}} - \Delta H_{\mathrm{BuOH}}$ [kJ/mol]:	2.5 ± 6.0	10.7 ± 6.1	

Figure 5.9 shows the comparison between the calculated and experimental reaction rates, as well as the residual distribution, for the two models of Table 5.6 which present the lowest *SSRE* (LHHW-RLS3/1b and LHHW-RLS2/1b with $n_\sigma = 2$). For the models LHHW-RLS2/3b with $n_\sigma = 0$ and 1 the trends are very similar. As it can be seen, the model LHHW-RLS3/1b (Figures 5.9a and c) fits the experimental data satisfactorily with a random distribution of

residuals. However, in Figure 5.9b it can be observed that, at 453 K, model LHHW-RLS2/1b with n_σ = 2 overestimates low and high values of reaction rates and, on the other hand, underestimates medium values of reaction rates. Consequently, the residuals do not show a completely random distribution (Figure 5.9d).

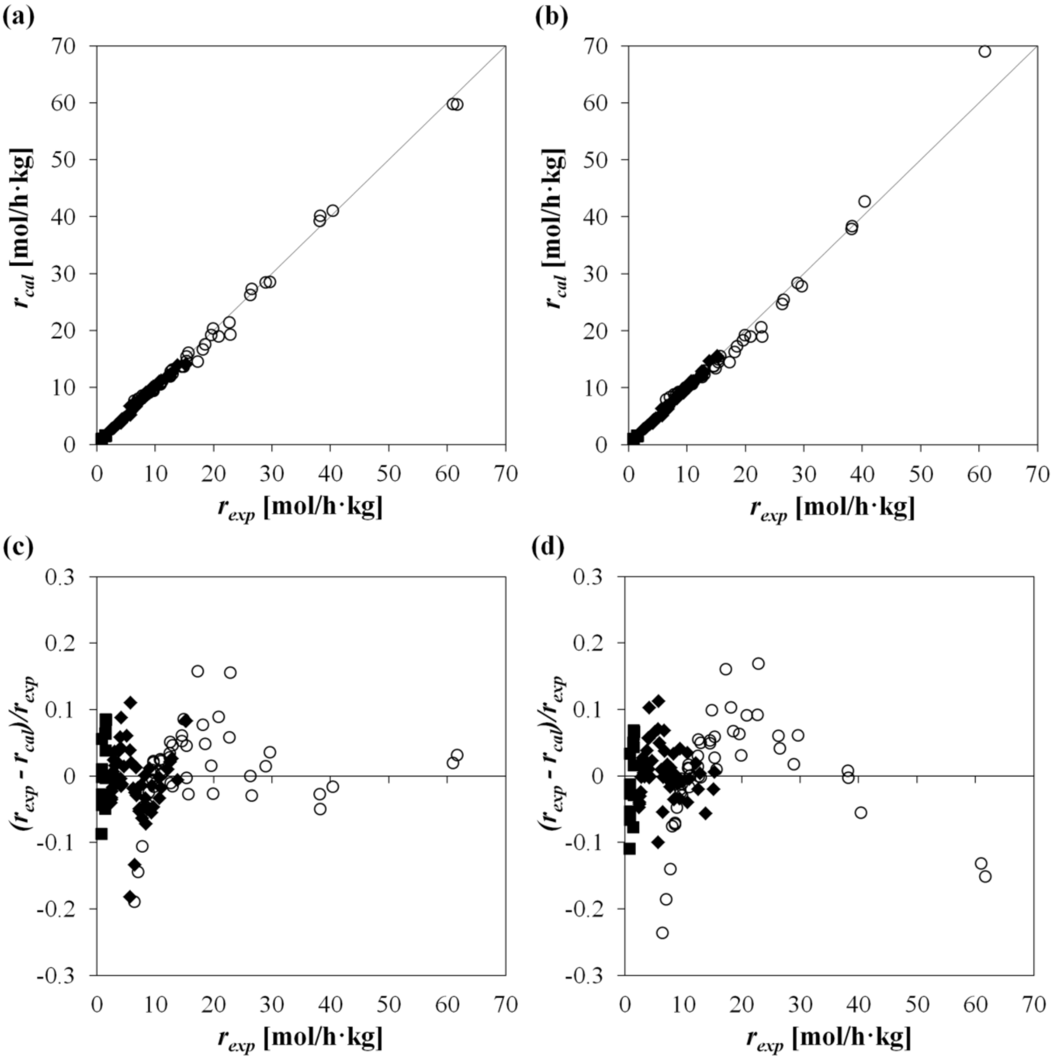

Figure 5.9. Calculated reaction rates by models (a) LHHW-RLS3/1b (Equation 5.20) and (b) LHHW-RLS2/1b (Equation 5.21) with n_σ = 2 versus experimental rates; residuals distribution for models (c) LHHW-RLS3/1b and (d) LHHW-RLS2/1b with n_σ = 2.
(■) 413 K, (♦) 433 K, (○) 453 K. Experiments starting from mixtures 1-butanol/water and 1-butanol/DNBE, 1 g of catalyst, d_p = 0.4 – 0.63 mm, 40 bar, 500 rpm.

Apparent activation energies computed by models LHHW-RLS3/1b and LHHW-RLS2/1b from experiments starting from mixtures of 1-butanol/water and 1-butanol/DNBE (Table 5.6) are slightly higher than values computed by the same model but from experiments starting from pure 1-butanol (Table 5.5). This fact is in agreement with the inhibiting effect attributed to water.[4-7] In the next section, general and simplified kinetic models where modified in order to introduce the inhibiting effect of water.

5.3.3. Modified kinetic models

Several authors have reported the strong inhibition effect of water in reactions carried out over ion exchange resins.[4-7] In those works, water is considered to adsorb preferentially on the sulfonic groups, blocking the adsorption of reactants and thus, suppressing the catalytic reaction. The common approach to model the water inhibition effect is to modify the rate constant in such a way that only the fraction of available active sites (not blocked by water molecules, 1- θ_{H2O}) are taken into account. The fraction of acid sites blocked by water molecules (θ_{H2O}) can be expressed by an adsorption isotherm. In Table 5.7 three correction factors derived from Langmuir (Equations 5.24 and 5.25) and Freundlich (Equations 5.23) adsorption isotherms are shown. In these expressions m_σ is the total number of active sites taking part in the rate-limiting step.

Table 5.7. Correction factors to represent water inhibiting effect on reaction rate

Equation	Correction factor	Comments	Ref.
(5.23)	$\left(1\text{-}K_w \cdot a_{H_2O}^{1/\alpha}\right)^{m_\sigma}$ with $\alpha = K_\alpha/T$	Freundlich isotherm.	5
(5.24)	$\left(\frac{1}{1+K_w \cdot a_{H_2O}}\right)^{m_\sigma}$	Langmuir isotherm where a molecule of water adsorbs on one active site.	7
(5.25)	$\left(\frac{1}{1+K_w \cdot a_{H_2O}^{0.5}}\right)^{m_\sigma}$	Langmuir isotherm where a molecule of water adsorbs on two active sites.	6

Three new sets of models were obtained by adding the three correction factors gathered in Table 5.7 to both the general kinetic models (Table 5.4) and the simplified kinetic models (Appendix). In all the cases the variation of K_w with temperature was supposed to be:

$$K_w = \exp\left[K_{w_1} - K_{w_2}\left(\frac{1}{T} - \frac{1}{T_{ref}}\right)\right] \tag{5.26}$$

Modified models were fitted to experimental data. The fact of adding the correction factors defined by Equations 5.24 and 5.25 did not improve the fittings. However, the correction factor derived from the Freundlich adsorption isotherm (Equation 5.23) provides important improvements.

For experiments starting from pure 1-butanol, modified models (including the Freundlich correction factor) that best fit rate data are the same as those obtained when the correction factor was not included (Table 5.5) but eliminating the term of water adsorption from the denominator of Equation 5.20 and 5.21 (or, given the equivalence between models due to the constancy of the ratio a_{H2O}/a_{DNBE}, the term of DNBE adsorption in the denominator of Equation 5.19 and

5.21). Models with the Freundlich correction factor present lower *SSRE* (mainly due to an improvement of the fitting to data corresponding to experiments carried out at 463 K); however, the uncertainty of the fitted parameter is higher.

When models including the Freundlich correction factor were fitted to rate data corresponding to experiments starting from mixtures 1-butanol/products, in contrast to the results obtained in the fitting of the models without correction factor (Table 5.6), modified models that do not include a water adsorption term in the denominator (LHHW-RLS2/2b, Equation 5.27, and LHHW-RLS4/2b, Equation 5.28) are the ones that best fit the experimental data (see Table 5.8). Model LHHW-RLS4/2b stems from a LHHW formalism where the desorption of water is considered the RLS and assuming negligible the amount of free active sites and the adsorption of DNBE. Model LHHW-RLS2/2b stems from a LHHW formalism where the RLS is the surface reaction and considering the amount of free active sites and the adsorption of water negligible. Furthermore, model LHHW-RLS2/1b also has very low values of *SSRE* but the uncertainty of the parameters is higher.

From the results gathered in Table 5.6 and Table 5.8 it can be concluded that water effect must be included in the model either by means of the Freundlich correction factor (i.e., considering that water molecules block the active sites reducing the number of available ones), or in the adsorption term. Nevertheless, including the Freundlich correction factor gives better results because not only reduces the *SSRE* but also achieve a better residual distribution (models in which the Freundlich correction factor is not included show higher residuals in experiments performed at higher temperatures). Taking into account both approaches simultaneously does not improve the fitting and besides introduces more parameters to the models.

These conclusions agree with the results obtained in the set of experiments starting from pure 1-butanol (both, when the Freundlich factor is included and when is not). Thus, we can conclude that the models that best fit the experimental data (for the whole range of water activity and temperature explored) are:

$$r_{\mathrm{DNBE}} = \frac{\hat{k}\cdot\dfrac{K_{\mathrm{BuOH}}^{2}}{K_{\mathrm{BuOH}}^{2+n_{\sigma}}}\left(a_{\mathrm{BuOH}}^{2} - \dfrac{a_{\mathrm{DNBE}}\cdot a_{\mathrm{H_2O}}}{K_{eq}}\right)}{\left(a_{\mathrm{BuOH}} + \dfrac{K_{\mathrm{DNBE}}}{K_{\mathrm{BuOH}}}\cdot a_{\mathrm{DNBE}}\right)^{2+n_{\sigma}}}\left(1\text{-}K_{w}a_{\mathrm{H_2O}}^{1/\alpha}\right)^{2+n_{\sigma}} \qquad (5.27)$$

$$r_{\mathrm{DNBE}} = \frac{\dfrac{k_{\mathrm{H_2O}}}{K_{\mathrm{H_2O}}}\left(K_{eq}\dfrac{a_{\mathrm{BuOH}}^{2}}{a_{\mathrm{DNBE}}} - a_{\mathrm{H_2O}}\right)}{\dfrac{K_{\mathrm{BuOH}}}{K_{\mathrm{H_2O}}}\cdot a_{\mathrm{BuOH}} + K_{eq}\dfrac{a_{\mathrm{BuOH}}^{2}}{a_{\mathrm{DNBE}}}}\left(1\text{-}K_{w}a_{\mathrm{H_2O}}^{1/\alpha}\right) \qquad (5.28)$$

With $\alpha = K_{\alpha} / T$

Table 5.8. Best *modified* kinetic models for experiments starting from mixtures 1-butanol/water and 1-butanol/DNBE.

LHHW-RLS2/1b (see Equation 5.21)
RLS: surface reaction. Assuming negligible the amount of free active sites.

n_σ	0	1	2
SSRE:	0.14	0.15	0.16
R^2_{adj}:	1.00	1.00	1.00
Δ:	3.21	1.37	1.59
Parameters			
A:	16.6 ± 0.6	16.6 ± 0.6	16.6 ± 0.6
E_A [kJ/mol]:	114.6 ± 3.9	115.9 ± 3.7	116.7 ± 3.7
$\Delta S_{DNBE}–\Delta S_{BuOH}$ [J/mol·K]:	-11.4 ± 2.4	-8.3 ± 1.0	-7.1 ± 0.7
$\Delta H_{DNBE}–\Delta H_{BuOH}$ [kJ/mol]:	20.5 ± 24.7	-19.5 ± 10.8	19.0 ± 7.0
$\Delta S_{H2O}–\Delta S_{BuOH}$ [J/mol·K]:	4.0 ± 0.4	1.3 ± 0.3	-0.3 ± 0.3
$\Delta H_{H2O}–\Delta H_{BuOH}$ [kJ/mol]:	-14.3 ± 5.3	-9.4 ± 4.3	-6.4 ± 3.7
K_{w1}:	-0.19 ± 0.55	-0.64 ± 0.65	-0.99 ± 0.70
K_{w2}:	5714 ± 2112	7572 ± 2902	8670 ± 3475
K_α:	65.4± 26.5	88.3 ± 26.6	86.8 ± 27.6

LHHW-RLS2/2b
RLS: Surface reaction.
Assuming negligible the amount of free active sites and the adsorption of H_2O.

$$r_{DNBE} = \frac{\hat{k}\cdot\frac{K^2_{BuOH}}{K^{2+n_\sigma}_{BuOH}}\left(a^2_{BuOH} - \frac{a_{DNBE}\cdot a_{H_2O}}{K_{eq}}\right)}{\left(a_{BuOH} + \frac{K_{DNBE}}{K_{BuOH}}\cdot a_{DNBE}\right)^{2+n_\sigma}}\left(1\text{-}K_w a^{1/\alpha}_{H_2O}\right)^{2+n_\sigma} \quad (5.27)$$

n_σ	0	1	2
SSRE:	0.22	0.23	0.24
R^2_{adj}:	0.99	0.99	0.99
Δ:	0.81	0.53	0.41
Parameters			
A:	16.4 ± 0.8	16.3 ± 0.7	16.3 ± 0.7
E_A [kJ/mol]:	123.2 ± 2.3	123.2 ± 2.4	123.2 ± 2.5
$\Delta S_{DNBE}–\Delta S_{BuOH}$ [J/mol·K]:	-9.5 ± 1.5	-7.6 ± 0.8	-6.7 ± 0.6
$\Delta H_{DNBE}–\Delta H_{BuOH}$ [kJ/mol]:	34.0 ± 14.5	25.5 ± 8.2	22.5 ± 5.8
K_{w1}:	-0.10 ± 0.02	-0.23 ± 0.02	-0.32 ± 0.02
K_{w2}:	265 ± 166	415 ± 164	527 ± 156
K_α:	550.0 ± 34.8	499.6 ± 25.5	477.4 ± 21.0

LHHW-RLS4/2b
RLS: Desorption of water.
Assuming negligible the amount of free active sites and the adsorption of DNBE.

$$r_{DNBE} = \frac{\frac{k_{H_2O}}{K_{H_2O}}\left(K_{eq}\frac{a^2_{BuOH}}{a_{DNBE}} - a_{H_2O}\right)}{\frac{K_{BuOH}}{K_{H_2O}}\cdot a_{BuOH} + K_{eq}\frac{a^2_{BuOH}}{a_{DNBE}}}\left(1\text{-}K_w a^{1/\alpha}_{H_2O}\right) \quad (5.28)$$

SSRE = 0.25 R^2_{adj} = 0.99 Δ = 1.50

Parameters

A	E_A [kJ/mol]	$\Delta S_{BuOH} – \Delta S_{H2O}$ [J/mol·K]	$\Delta H_{BuOH} – \Delta H_{H2O}$ [kJ/mol]	K_{w1}	K_{w2}	K_α
19.2±1.4	121.8±2.2	22.7±1.9	55.8±17.5	0.08±0.02	56.8±81.8	991±108

Equation 5.27 stems from a LHHW formalism in which two adjacent adsorbed molecules of 1-butanol (from the results it is difficult to distinguish the number of additional active sites – 0, 1 or 2 – that participate in the surface reaction) react to yield ether and water, being the surface reaction the rate limiting step. The formed water remains in the catalyst surface blocking the active centers. Equation 5.27 assumes that the number of unoccupied sites is not significant and that the adsorption of water is negligible. Equation 5.28 stems from a mechanism in which the rate limiting step is the desorption of water and where the adsorption of DNBE is negligible (which agrees with the fact that adding DNBE to the reaction medium does not influence the reaction rate, Figure 5.7b) and the number of unoccupied sites is not significant. From Equation 5.28 it is not possible to discern if the mechanism corresponds to a LHHW formalism or to a ER-H_2O formalism as both lead to the same form of the rate equation (see in the Appendix the models LHHW-RLS4/2b and ER_{H2O}-RLS3/1b).

5.3.4. General kinetic models

With the aim of finding a set of parameters that represent a wider range of activities, Equations 5.27 and 5.28 were fitted to all the experimental data simultaneously. Results are gathered in Table 5.9.

Table 5.9. Best *modified* kinetic models for all experimental data.

<table>
<tr><th colspan="4">LHHW-RLS2/2b (see Equation 5.27)
RLS: Surface reaction.
Assuming negligible the amount of free active sites and the adsorption of H_2O.</th></tr>
<tr><td>n_σ</td><td>0</td><td>1</td><td>2</td></tr>
<tr><td>*SSRE*:</td><td>1.24</td><td>1.38</td><td>1.50</td></tr>
<tr><td>R^2_{adj}:</td><td>0.99</td><td>0.99</td><td>0.99</td></tr>
<tr><td>Δ:</td><td>2.50</td><td>0.84</td><td>0.54</td></tr>
<tr><th colspan="4">Parameters</th></tr>
<tr><td>*A*:</td><td>25.4 ± 1.1</td><td>24.9 ± 1.0</td><td>24.7 ± 1.0</td></tr>
<tr><td>E_A [kJ/mol]:</td><td>121.7 ± 1.8</td><td>122.2 ± 1.9</td><td>122.6 ± 2.0</td></tr>
<tr><td>$\Delta S_{DNBE}-\Delta S_{BuOH}$ [J/mol·K]:</td><td>-9.6 ± 1.7</td><td>-7.2 ± 0.9</td><td>-6.3 ± 0.7</td></tr>
<tr><td>$\Delta H_{DNBE}-\Delta H_{BuOH}$ [kJ/mol]:</td><td>61.2 ± 12.9</td><td>42.6 ± 7.5</td><td>36.1 ± 5.4</td></tr>
<tr><td>K_{w1}:</td><td>-0.08 ± 0.03</td><td>-0.20 ± 0.03</td><td>-0.29 ± 0.02</td></tr>
<tr><td>K_{w2}:</td><td>73.3 ±180.4</td><td>233.1 ± 184.6</td><td>364.2 ± 178.6</td></tr>
<tr><td>K_α:</td><td>563.2 ± 42.4</td><td>499.4 ± 31.5</td><td>471.8 ± 26.2</td></tr>
</table>

<table>
<tr><th colspan="7">LHHW-RLS4/2b (see Equation 5.28)
RLS: Desorption of water.
Assuming negligible the amount of free active sites and the adsorption of DNBE.</th></tr>
<tr><td colspan="2">*SSRE* = 1.34</td><td colspan="3">R^2_{adj} = 0.98</td><td colspan="2">Δ = 2.54</td></tr>
<tr><th colspan="7">Parameters</th></tr>
<tr><td>*A*</td><td>E_A
[kJ/mol]</td><td>$\Delta S_{BuOH}-\Delta S_{H2O}$
[J/mol·K]</td><td>$\Delta H_{BuOH}-\Delta H_{H2O}$
[kJ/mol]</td><td>K_{w1}</td><td>K_{w2}</td><td>K_α</td></tr>
<tr><td>29.7±2.1</td><td>121.3±1.8</td><td>22.8±2.0</td><td>83.7±15.4</td><td>0.09±0.02</td><td>36.8±92.5</td><td>1018±128</td></tr>
</table>

Figures 5.10a and b show the reaction rate of DNBE formation estimated by models LHHW-RLS2/2b (Equation 5.27) with $n_\sigma = 0$ and LHHW-RLS4/2b (Equation 5.28), including the Freundlich correction factor, against the experimental reaction rate. As it can be seen, both fittings are very similar. Figures 5.10c and d show the residual distribution for the two models.

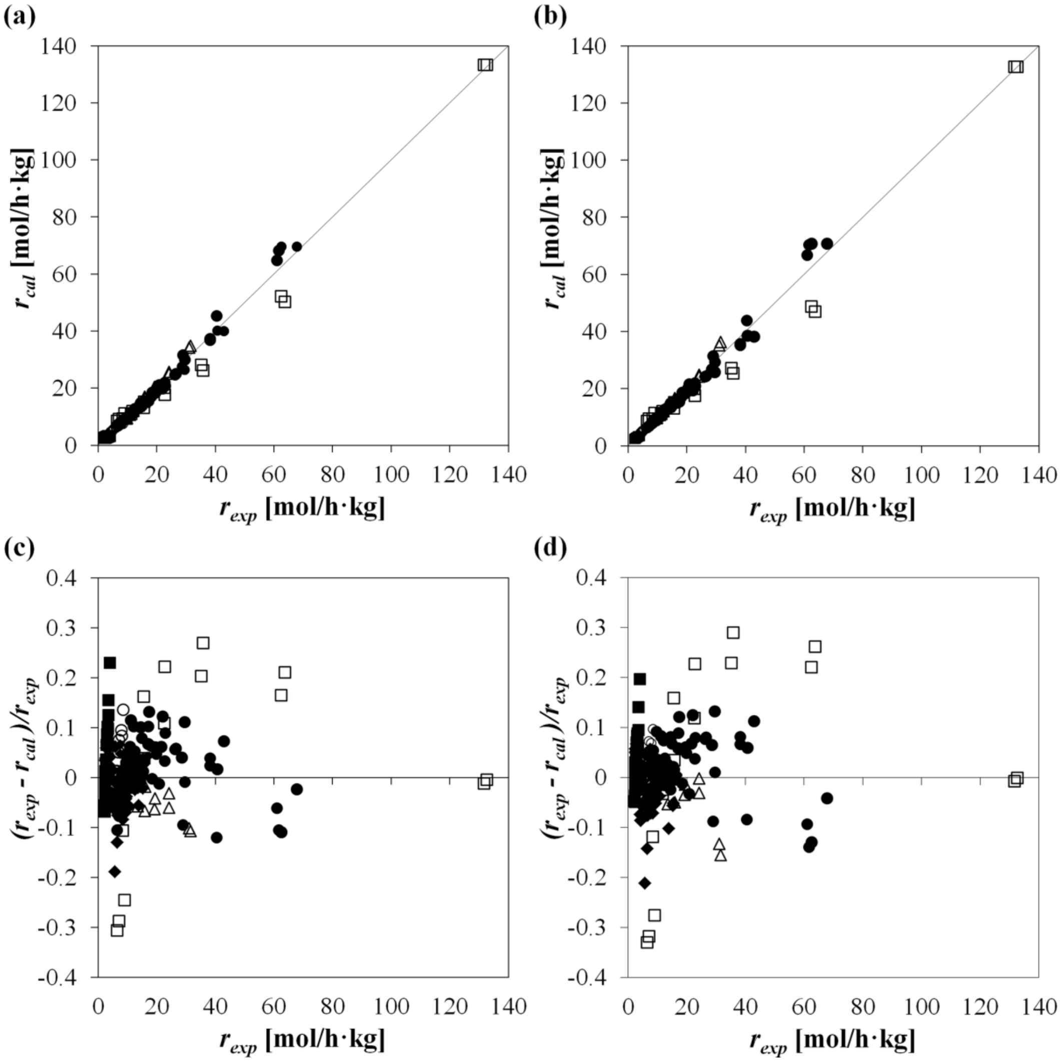

Figure 5.10. Calculated reaction rates by the *modified* models (a) LHHW-RLS2/2b (Equation 5.27) with $n_\sigma = 0$ and (b) LHHW-RLS4/2b (Equation. 5.28) versus experimental rates; residuals distribution for models (c) LHHW-RLS4/2b with $n_\sigma = 0$ and (d) LHHW-RLS2/2b.
(■) 413 K, (○) 423 K, (♦) 433 K, (Δ) 443 K, (●) 453 K, (□) 463 K. Rate data corresponding to all the experiments, 1 g of catalyst, d_p = 0.4 – 0.63 mm, 40 bar, 500 rpm.

Figure 5.11 plots the values of the Freundlich correction factor, $1\text{-}K_w a_{\mathrm{H_2O}}^{1/\alpha}$, as used in models LHHW-RLS2/2b (with $n_\sigma = 0$) and LHHW-RLS4/2b (Table 5.9), versus a_{H2O} for all the temperatures tested. In both models the correction factor decreases on increasing a_{H2O} and seems to be independent on the operating temperature (which explains the high uncertainty associated with the parameter K_{w2}, see Table 5.9, indicating little sensitivity to this parameter in the fit).

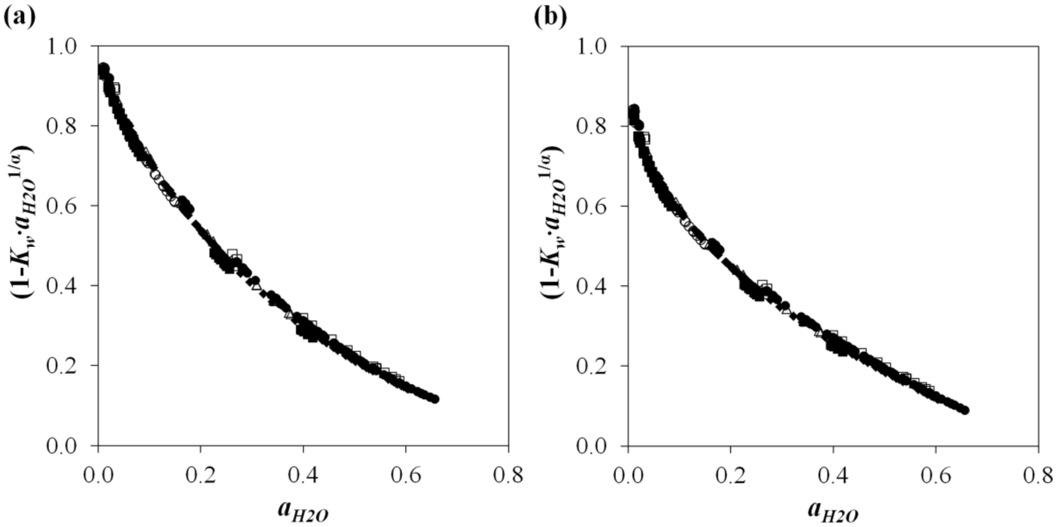

Figure 5.11. Freundlich factor corresponding to models (a) LHHW-RLS2/2b with $n_\sigma = 0$ and (b) LHHW-RLS4/2b vs. a_{H2O} at different temperatures.
(■) 413 K, (○) 423 K, (♦) 433 K, (Δ) 443 K, (●) 453 K, (□) 463 K. All the experiments, 1 g of catalyst, d_p = 0.4 – 0.63 mm, 40 bar, 500 rpm.

Similar values of apparent activation energies (Table 5.9) were found for all the models (≈ 122 ± 2 kJ/mol). This value is slightly higher than those reported for the dehydration reactions over Amberlyst 70 of 1-pentanol to di-n-pentyl ether[10] (114.0±0.1 kJ/mol) and 1-octanol to di-n-octyl ether[11] (110±5 kJ/mol) and very similar to that reported for the dehydration of 1-hexanol to di-n-hexyl ether[24] (121 ±3 kJ/mol). Regarding the molar adsorption enthalpy differences, it is possible to see that adsorption of 1-butanol is stronger (more exothermic) than that of DNBE (models LHHW-RLS2/2b) but weaker than that of water (model LHHW-RLS4/2b). For model LHHW-RLS2/2b, the positive value of the difference between the free energy change for DNBE adsorption (ΔG_{DNBE}) and the free energy change for 1-butanol adsorption (ΔG_{BuOH}), calculated as $(\Delta G_{DNBE} - \Delta G_{BuOH}) = (\Delta H_{DNBE} - \Delta H_{BuOH}) - T(\Delta S_{DNBE} - \Delta S_{BuOH})$ indicates that ΔG_{BuOH} is more negative than ΔG_{DNBE}, being the 1-butanol adsorption a more favored process than DNBE adsorption. In a similar way, for model LHHW-RLS4/2b, the positive value of $\left(\Delta G_{BuOH} - \Delta G_{H_2O}\right)$ indicates that the adsorption of water over the catalyst is a more favored process than 1-butanol adsorption. This trend is in agreement with the polarity of the compounds and the high water affinity of the resin.

5.4. Conclusions

The reaction rate of 1-butanol dehydration to di-n-butyl ether was found to be very sensitive to temperature and to water presence. Two kinetic models are proposed to explain the dehydration of 1-butanol to di-n-butyl ether over Amberlyst 70. One of them stems from a LHHW formalism in which two adsorbed molecules of 1-butanol react to yield ether and water, being the reversible surface reaction the rate limiting step and where the adsorption of water is negligible. The other one stems from a mechanism in which the rate limiting step is the desorption of water and where the adsorption of DNBE is negligible. The two models present several characteristics in common: (1) the strong inhibiting effect of water is taken into account by means of a correction factor derived from a Freundlich adsorption isotherm (water is not included in the adsorption term); (2) the number of free active sites is found to be negligible compared to the occupied ones; (3) both models present similar values of *SSRE* and apparent activation energies (122 ± 2 kJ/mol).

Appendix

Table S1. Simplified kinetic models for the LHHW formalism considering the rate limiting step (RLS) the adsorption of 1-butanol

LHHW – RLS: 1-butanol adsorption	
LHHW-RLS1/1a	**LHHW-RLS1/1b**
$r_{\mathrm{DNBE}}=\dfrac{k_{\mathrm{BuOH}}\left(a_{\mathrm{BuOH}}-\left(\dfrac{a_{\mathrm{DNBE}}\cdot a_{\mathrm{H_2O}}}{K_{eq}}\right)^{0.5}\right)}{1+K_{\mathrm{BuOH}}\left(\dfrac{a_{\mathrm{DNBE}}\cdot a_{\mathrm{H_2O}}}{K_{eq}}\right)^{0.5}+K_{\mathrm{DNBE}}\cdot a_{\mathrm{DNBE}}+K_{\mathrm{H_2O}}\cdot a_{\mathrm{H_2O}}}$	$r_{\mathrm{DNBE}}=\dfrac{\dfrac{k_{\mathrm{BuOH}}}{K_{\mathrm{BuOH}}}\left(a_{\mathrm{BuOH}}-\left(\dfrac{a_{\mathrm{DNBE}}\cdot a_{\mathrm{H_2O}}}{K_{eq}}\right)^{0.5}\right)}{\left(\dfrac{a_{\mathrm{DNBE}}\cdot a_{\mathrm{H_2O}}}{K_{eq}}\right)^{0.5}+\dfrac{K_{\mathrm{DNBE}}}{K_{\mathrm{BuOH}}}\cdot a_{\mathrm{DNBE}}+\dfrac{K_{\mathrm{H_2O}}}{K_{\mathrm{BuOH}}}\cdot a_{\mathrm{H_2O}}}$
LHHW-RLS1/2a	**LHHW-RLS1/2b**
$r_{\mathrm{DNBE}}=\dfrac{k_{\mathrm{BuOH}}\left(a_{\mathrm{BuOH}}-\left(\dfrac{a_{\mathrm{DNBE}}\cdot a_{\mathrm{H_2O}}}{K_{eq}}\right)^{0.5}\right)}{1+K_{\mathrm{BuOH}}\left(\dfrac{a_{\mathrm{DNBE}}\cdot a_{\mathrm{H_2O}}}{K_{eq}}\right)^{0.5}+K_{\mathrm{DNBE}}\cdot a_{\mathrm{DNBE}}}$	$r_{\mathrm{DNBE}}=\dfrac{\dfrac{k_{\mathrm{BuOH}}}{K_{\mathrm{BuOH}}}\left(a_{\mathrm{BuOH}}-\left(\dfrac{a_{\mathrm{DNBE}}\cdot a_{\mathrm{H_2O}}}{K_{eq}}\right)^{0.5}\right)}{\left(\dfrac{a_{\mathrm{DNBE}}\cdot a_{\mathrm{H_2O}}}{K_{eq}}\right)^{0.5}+\dfrac{K_{\mathrm{DNBE}}}{K_{\mathrm{BuOH}}}\cdot a_{\mathrm{DNBE}}}$
LHHW-RLS1/3a	**LHHW-RLS1/3b**
$r_{\mathrm{DNBE}}=\dfrac{k_{\mathrm{BuOH}}\left(a_{\mathrm{BuOH}}-\left(\dfrac{a_{\mathrm{DNBE}}\cdot a_{\mathrm{H_2O}}}{K_{eq}}\right)^{0.5}\right)}{1+K_{\mathrm{BuOH}}\left(\dfrac{a_{\mathrm{DNBE}}\cdot a_{\mathrm{H_2O}}}{K_{eq}}\right)^{0.5}+K_{\mathrm{H_2O}}\cdot a_{\mathrm{H_2O}}}$	$r_{\mathrm{DNBE}}=\dfrac{\dfrac{k_{\mathrm{BuOH}}}{K_{\mathrm{BuOH}}}\left(a_{\mathrm{BuOH}}-\left(\dfrac{a_{\mathrm{DNBE}}\cdot a_{\mathrm{H_2O}}}{K_{eq}}\right)^{0.5}\right)}{\left(\dfrac{a_{\mathrm{DNBE}}\cdot a_{\mathrm{H_2O}}}{K_{eq}}\right)^{0.5}+\dfrac{K_{\mathrm{H_2O}}}{K_{\mathrm{BuOH}}}\cdot a_{\mathrm{H_2O}}}$
LHHW-RLS1/4a	**LHHW-RLS1/4b**
$r_{\mathrm{DNBE}}=\dfrac{k_{\mathrm{BuOH}}\left(a_{\mathrm{BuOH}}-\left(\dfrac{a_{\mathrm{DNBE}}\cdot a_{\mathrm{H_2O}}}{K_{eq}}\right)^{0.5}\right)}{1+K_{\mathrm{BuOH}}\left(\dfrac{a_{\mathrm{DNBE}}\cdot a_{\mathrm{H_2O}}}{K_{eq}}\right)^{0.5}}$	$r_{\mathrm{DNBE}}=\dfrac{\dfrac{k_{\mathrm{BuOH}}}{K_{\mathrm{BuOH}}}\left(a_{\mathrm{BuOH}}-\left(\dfrac{a_{\mathrm{DNBE}}\cdot a_{\mathrm{H_2O}}}{K_{eq}}\right)^{0.5}\right)}{\left(\dfrac{a_{\mathrm{DNBE}}\cdot a_{\mathrm{H_2O}}}{K_{eq}}\right)^{0.5}}$

Table S2. Simplified kinetic models for the LHHW formalism considering the rate limiting step (RLS) the surface reaction. n_σ is the number of additional active centers participating in the surface reaction ranging from 0 to 2

LHHW – RLS: Surface reaction	
LHHW-RLS2/1a $r_{\mathrm{DNBE}}=\frac{\hat{k}\cdot K_{\mathrm{BuOH}}^2\left(a_{\mathrm{BuOH}}^2-\frac{a_{\mathrm{DNBE}}\cdot a_{\mathrm{H_2O}}}{K_{eq}}\right)}{\left(1+K_{\mathrm{BuOH}}\cdot a_{\mathrm{BuOH}}+K_{\mathrm{DNBE}}\cdot a_{\mathrm{DNBE}}+K_{\mathrm{H_2O}}\cdot a_{\mathrm{H_2O}}\right)^{2+n_\sigma}}$	**LHHW-RLS2/1b** $r_{\mathrm{DNBE}}=\frac{\hat{k}\cdot\frac{K_{\mathrm{BuOH}}^2}{K_{\mathrm{BuOH}}^{2+n_\sigma}}\left(a_{\mathrm{BuOH}}^2-\frac{a_{\mathrm{DNBE}}\cdot a_{\mathrm{H_2O}}}{K_{eq}}\right)}{\left(a_{\mathrm{BuOH}}+\frac{K_{\mathrm{DNBE}}}{K_{\mathrm{BuOH}}}\cdot a_{\mathrm{DNBE}}+\frac{K_{\mathrm{H_2O}}}{K_{\mathrm{BuOH}}}\cdot a_{\mathrm{H_2O}}\right)^{2+n_\sigma}}$
LHHW-RLS2/2a $r_{\mathrm{DNBE}}=\frac{\hat{k}\cdot K_{\mathrm{BuOH}}^2\left(a_{\mathrm{BuOH}}^2-\frac{a_{\mathrm{DNBE}}\cdot a_{\mathrm{H_2O}}}{K_{eq}}\right)}{\left(1+K_{\mathrm{BuOH}}\cdot a_{\mathrm{BuOH}}+K_{\mathrm{DNBE}}\cdot a_{\mathrm{DNBE}}\right)^{2+n_\sigma}}$	**LHHW-RLS2/2b** $r_{\mathrm{DNBE}}=\frac{\hat{k}\cdot\frac{K_{\mathrm{BuOH}}^2}{K_{\mathrm{BuOH}}^{2+n_\sigma}}\left(a_{\mathrm{BuOH}}^2-\frac{a_{\mathrm{DNBE}}\cdot a_{\mathrm{H_2O}}}{K_{eq}}\right)}{\left(a_{\mathrm{BuOH}}+\frac{K_{\mathrm{DNBE}}}{K_{\mathrm{BuOH}}}\cdot a_{\mathrm{DNBE}}\right)^{2+n_\sigma}}$
LHHW-RLS2/3a $r_{\mathrm{DNBE}}=\frac{\hat{k}\cdot K_{\mathrm{BuOH}}^2\left(a_{\mathrm{BuOH}}^2-\frac{a_{\mathrm{DNBE}}\cdot a_{\mathrm{H_2O}}}{K_{eq}}\right)}{\left(1+K_{\mathrm{BuOH}}\cdot a_{\mathrm{BuOH}}+K_{\mathrm{H_2O}}\cdot a_{\mathrm{H_2O}}\right)^{2+n_\sigma}}$	**LHHW-RLS2/3b** $r_{\mathrm{DNBE}}=\frac{\hat{k}\cdot\frac{K_{\mathrm{BuOH}}^2}{K_{\mathrm{BuOH}}^{2+n_\sigma}}\left(a_{\mathrm{BuOH}}^2-\frac{a_{\mathrm{DNBE}}\cdot a_{\mathrm{H_2O}}}{K_{eq}}\right)}{\left(a_{\mathrm{BuOH}}+\frac{K_{\mathrm{H_2O}}}{K_{\mathrm{BuOH}}}\cdot a_{\mathrm{H_2O}}\right)^{2+n_\sigma}}$
LHHW-RDS2/4a $r_{\mathrm{DNBE}}=\frac{\hat{k}\cdot K_{\mathrm{BuOH}}^2\left(a_{\mathrm{BuOH}}^2-\frac{a_{\mathrm{DNBE}}\cdot a_{\mathrm{H_2O}}}{K_{eq}}\right)}{\left(1+K_{\mathrm{DNBE}}\cdot a_{\mathrm{DNBE}}+K_{\mathrm{H_2O}}\cdot a_{\mathrm{H_2O}}\right)^{2+n_\sigma}}$	**LHHW-RLS2/4b** $r_{\mathrm{DNBE}}=\frac{\hat{k}\cdot\frac{K_{\mathrm{BuOH}}^2}{K_{\mathrm{DNBE}}^{2+n_\sigma}}\left(a_{\mathrm{BuOH}}^2-\frac{a_{\mathrm{DNBE}}\cdot a_{\mathrm{H_2O}}}{K_{eq}}\right)}{\left(a_{\mathrm{DNBE}}+\frac{K_{\mathrm{H_2O}}}{K_{\mathrm{DNBE}}}\cdot a_{\mathrm{H_2O}}\right)^{2+n_\sigma}}$
LHHW-RLS2/5a $r_{\mathrm{DNBE}}=\frac{\hat{k}\cdot K_{\mathrm{BuOH}}^2\left(a_{\mathrm{BuOH}}^2-\frac{a_{\mathrm{DNBE}}\cdot a_{\mathrm{H_2O}}}{K_{eq}}\right)}{\left(1+K_{\mathrm{BuOH}}\cdot a_{\mathrm{BuOH}}\right)^{2+n_\sigma}}$	**LHHW-RLS2/5b** $r_{\mathrm{DNBE}}=\frac{\hat{k}\cdot\frac{K_{\mathrm{BuOH}}^2}{K_{\mathrm{BuOH}}^{2+n_\sigma}}\left(a_{\mathrm{BuOH}}^2-\frac{a_{\mathrm{DNBE}}\cdot a_{\mathrm{H_2O}}}{K_{eq}}\right)}{\left(a_{\mathrm{BuOH}}\right)^{2+n_\sigma}}$
LHHW-RLS2/6a $r_{\mathrm{DNBE}}=\frac{\hat{k}\cdot K_{\mathrm{BuOH}}^2\left(a_{\mathrm{BuOH}}^2-\frac{a_{\mathrm{DNBE}}\cdot a_{\mathrm{H_2O}}}{K_{eq}}\right)}{\left(1+K_{\mathrm{DNBE}}\cdot a_{\mathrm{DNBE}}\right)^{2+n_\sigma}}$	**LHHW-RLS2/6b** $r_{\mathrm{DNBE}}=\frac{\hat{k}\cdot\frac{K_{\mathrm{BuOH}}^2}{K_{\mathrm{DNBE}}^{2+n_\sigma}}\left(a_{\mathrm{BuOH}}^2-\frac{a_{\mathrm{DNBE}}\cdot a_{\mathrm{H_2O}}}{K_{eq}}\right)}{\left(a_{\mathrm{DNBE}}\right)^{2+n_\sigma}}$
LHHW-RLS2/7a $r_{\mathrm{DNBE}}=\frac{\hat{k}\cdot K_{\mathrm{BuOH}}^2\left(a_{\mathrm{BuOH}}^2-\frac{a_{\mathrm{DNBE}}\cdot a_{\mathrm{H_2O}}}{K_{eq}}\right)}{\left(1+K_{\mathrm{H_2O}}\cdot a_{\mathrm{H_2O}}\right)^{2+n_\sigma}}$	**LHHW-RLS2/7b** $r_{\mathrm{DNBE}}=\frac{\hat{k}\cdot\frac{K_{\mathrm{BuOH}}^2}{K_{\mathrm{H_2O}}^{2+n_\sigma}}\left(a_{\mathrm{BuOH}}^2-\frac{a_{\mathrm{DNBE}}\cdot a_{\mathrm{H_2O}}}{K_{eq}}\right)}{\left(a_{\mathrm{H_2O}}\right)^{2+n_\sigma}}$

Table S3. Simplified kinetic models for the LHHW formalism considering the rate limiting step (RLS) the desorption of DNBE.

LHHW – RLS: DNBE desorption	
LHHW-RLS3/1a $r_{\mathrm{DNBE}} = \dfrac{k_{\mathrm{DNBE}}\left(K_{eq}\dfrac{a_{\mathrm{BuOH}}^2}{a_{\mathrm{H_2O}}} - a_{\mathrm{DNBE}}\right)}{1+K_{\mathrm{BuOH}}\cdot a_{\mathrm{BuOH}} + K_{\mathrm{DNBE}}\cdot\left(K_{eq}\dfrac{a_{\mathrm{BuOH}}^2}{a_{\mathrm{H_2O}}}\right) + K_{\mathrm{H_2O}}\cdot a_{\mathrm{H_2O}}}$	**LHHW-RLS3/1b** $r_{\mathrm{DNBE}} = \dfrac{\dfrac{k_{\mathrm{DNBE}}}{K_{\mathrm{DNBE}}}\left(K_{eq}\dfrac{a_{\mathrm{BuOH}}^2}{a_{\mathrm{H_2O}}} - a_{\mathrm{DNBE}}\right)}{\dfrac{K_{\mathrm{BuOH}}}{K_{\mathrm{DNBE}}}\cdot a_{\mathrm{BuOH}} + K_{eq}\dfrac{a_{\mathrm{BuOH}}^2}{a_{\mathrm{H_2O}}} + \dfrac{K_{\mathrm{H_2O}}}{K_{\mathrm{DNBE}}}\cdot a_{\mathrm{H_2O}}}$
LHHW-RLS3/2a $r_{\mathrm{DNBE}} = \dfrac{k_{\mathrm{DNBE}}\left(K_{eq}\dfrac{a_{\mathrm{BuOH}}^2}{a_{\mathrm{H_2O}}} - a_{\mathrm{DNBE}}\right)}{1+K_{\mathrm{BuOH}}\cdot a_{\mathrm{BuOH}} + K_{\mathrm{DNBE}}\cdot\left(K_{eq}\dfrac{a_{\mathrm{BuOH}}^2}{a_{\mathrm{H_2O}}}\right)}$	**LHHW-RLS3/2b** $r_{\mathrm{DNBE}} = \dfrac{\dfrac{k_{\mathrm{DNBE}}}{K_{\mathrm{DNBE}}}\left(K_{eq}\dfrac{a_{\mathrm{BuOH}}^2}{a_{\mathrm{H_2O}}} - a_{\mathrm{DNBE}}\right)}{\dfrac{K_{\mathrm{BuOH}}}{K_{\mathrm{DNBE}}}\cdot a_{\mathrm{BuOH}} + K_{eq}\dfrac{a_{\mathrm{BuOH}}^2}{a_{\mathrm{H_2O}}}}$
LHHW-RLS3/3a $r_{\mathrm{DNBE}} = \dfrac{k_{\mathrm{DNBE}}\left(K_{eq}\dfrac{a_{\mathrm{BuOH}}^2}{a_{\mathrm{H_2O}}} - a_{\mathrm{DNBE}}\right)}{1+K_{\mathrm{DNBE}}\cdot\left(K_{eq}\dfrac{a_{\mathrm{BuOH}}^2}{a_{\mathrm{H_2O}}}\right) + K_{\mathrm{H_2O}}\cdot a_{\mathrm{H_2O}}}$	**LHHW-RLS3/3b** $r_{\mathrm{DNBE}} = \dfrac{\dfrac{k_{\mathrm{DNBE}}}{K_{\mathrm{DNBE}}}\left(K_{eq}\dfrac{a_{\mathrm{BuOH}}^2}{a_{\mathrm{H_2O}}} - a_{\mathrm{DNBE}}\right)}{K_{eq}\dfrac{a_{\mathrm{BuOH}}^2}{a_{\mathrm{H_2O}}} + \dfrac{K_{\mathrm{H_2O}}}{K_{\mathrm{DNBE}}}\cdot a_{\mathrm{H_2O}}}$
LHHW-RLS3/4a $r_{\mathrm{DNBE}} = \dfrac{k_{\mathrm{DNBE}}\left(K_{eq}\dfrac{a_{\mathrm{BuOH}}^2}{a_{\mathrm{H_2O}}} - a_{\mathrm{DNBE}}\right)}{1+K_{\mathrm{DNBE}}\cdot\left(K_{eq}\dfrac{a_{\mathrm{BuOH}}^2}{a_{\mathrm{H_2O}}}\right)}$	**LHHW-RLS3/4b** $r_{\mathrm{DNBE}} = \dfrac{\dfrac{k_{\mathrm{DNBE}}}{K_{\mathrm{DNBE}}}\left(K_{eq}\dfrac{a_{\mathrm{BuOH}}^2}{a_{\mathrm{H_2O}}} - a_{\mathrm{DNBE}}\right)}{K_{eq}\dfrac{a_{\mathrm{BuOH}}^2}{a_{\mathrm{H_2O}}}}$

Table S4. Simplified kinetic models for the LHHW formalism considering the rate limiting step (RLS) the desorption of water.

LHHW – RLS: H_2O desorption	
LHHW-RLS4/1a $r_{\mathrm{DNBE}} = \dfrac{k_{\mathrm{H_2O}}\left(K_{eq}\dfrac{a_{\mathrm{BuOH}}^2}{a_{\mathrm{DNBE}}} - a_{\mathrm{H_2O}}\right)}{1 + K_{\mathrm{BuOH}}\cdot a_{\mathrm{BuOH}} + K_{\mathrm{DNBE}}\cdot a_{\mathrm{DNBE}} + K_{\mathrm{H_2O}}\cdot\left(K_{eq}\dfrac{a_{\mathrm{BuOH}}^2}{a_{\mathrm{DNBE}}}\right)}$	**LHHW-RLS4/1b** $r_{\mathrm{DNBE}} = \dfrac{\dfrac{k_{\mathrm{H_2O}}}{K_{\mathrm{H_2O}}}\left(K_{eq}\dfrac{a_{\mathrm{BuOH}}^2}{a_{\mathrm{DNBE}}} - a_{\mathrm{H_2O}}\right)}{\dfrac{K_{\mathrm{BuOH}}}{K_{\mathrm{H_2O}}}\cdot a_{\mathrm{BuOH}} + \dfrac{K_{\mathrm{DNBE}}}{K_{\mathrm{H_2O}}}\cdot a_{\mathrm{DNBE}} + K_{eq}\dfrac{a_{\mathrm{BuOH}}^2}{a_{\mathrm{DNBE}}}}$
LHHW-RLS4/2a $r_{\mathrm{DNBE}} = \dfrac{k_{\mathrm{H_2O}}\left(K_{eq}\dfrac{a_{\mathrm{BuOH}}^2}{a_{\mathrm{DNBE}}} - a_{\mathrm{H_2O}}\right)}{1 + K_{\mathrm{BuOH}}\cdot a_{\mathrm{BuOH}} + K_{\mathrm{H_2O}}\cdot\left(K_{eq}\dfrac{a_{\mathrm{BuOH}}^2}{a_{\mathrm{DNBE}}}\right)}$	**LHHW-RLS4/2b** $r_{\mathrm{DNBE}} = \dfrac{\dfrac{k_{\mathrm{H_2O}}}{K_{\mathrm{H_2O}}}\left(K_{eq}\dfrac{a_{\mathrm{BuOH}}^2}{a_{\mathrm{DNBE}}} - a_{\mathrm{H_2O}}\right)}{\dfrac{K_{\mathrm{BuOH}}}{K_{\mathrm{H_2O}}}\cdot a_{\mathrm{BuOH}} + K_{eq}\dfrac{a_{\mathrm{BuOH}}^2}{a_{\mathrm{DNBE}}}}$
LHHW-RLS4/3a $r_{\mathrm{DNBE}} = \dfrac{k_{\mathrm{H_2O}}\left(K_{eq}\dfrac{a_{\mathrm{BuOH}}^2}{a_{\mathrm{DNBE}}} - a_{\mathrm{H_2O}}\right)}{1 + K_{\mathrm{DNBE}}\cdot a_{\mathrm{DNBE}} + K_{\mathrm{H_2O}}\cdot\left(K_{eq}\dfrac{a_{\mathrm{BuOH}}^2}{a_{\mathrm{DNBE}}}\right)}$	**LHHW-RLS4/3b** $r_{\mathrm{DNBE}} = \dfrac{\dfrac{k_{\mathrm{H_2O}}}{K_{\mathrm{H_2O}}}\left(K_{eq}\dfrac{a_{\mathrm{BuOH}}^2}{a_{\mathrm{DNBE}}} - a_{\mathrm{H_2O}}\right)}{\dfrac{K_{\mathrm{DNBE}}}{K_{\mathrm{H_2O}}}\cdot a_{\mathrm{DNBE}} + K_{eq}\dfrac{a_{\mathrm{BuOH}}^2}{a_{\mathrm{DNBE}}}}$
LHHW-RLS4/4a $r_{\mathrm{DNBE}} = \dfrac{k_{\mathrm{H_2O}}\left(K_{eq}\dfrac{a_{\mathrm{BuOH}}^2}{a_{\mathrm{DNBE}}} - a_{\mathrm{H_2O}}\right)}{1 + K_{\mathrm{H_2O}}\cdot\left(K_{eq}\dfrac{a_{\mathrm{BuOH}}^2}{a_{\mathrm{DNBE}}}\right)}$	**LHHW-RLS4/4b** $r_{\mathrm{DNBE}} = \dfrac{\dfrac{k_{\mathrm{H_2O}}}{K_{\mathrm{H_2O}}}\left(K_{eq}\dfrac{a_{\mathrm{BuOH}}^2}{a_{\mathrm{DNBE}}} - a_{\mathrm{H_2O}}\right)}{K_{eq}\dfrac{a_{\mathrm{BuOH}}^2}{a_{\mathrm{DNBE}}}}$

Table S5. Simplified kinetic models for the ER formalism where the produced DNBE remains adsorbed while water is released into solution. The rate limiting step (RLS) considered is the adsorption of 1-butanol.

ER_{DNBE}– RLS: 1-butanol adsorption	
ER_{DNBE}-RLS1/1a $r_{\mathrm{DNBE}} = \dfrac{k_{\mathrm{BuOH}}\left(a_{\mathrm{BuOH}} - \dfrac{a_{\mathrm{DNBE}}\cdot a_{\mathrm{H_2O}}}{K_{eq}\cdot a_{\mathrm{BuOH}}}\right)}{1 + K_{\mathrm{BuOH}}\cdot\left(\dfrac{a_{\mathrm{DNBE}}\cdot a_{\mathrm{H_2O}}}{K_{eq}\cdot a_{\mathrm{BuOH}}}\right) + K_{\mathrm{DNBE}}\cdot a_{\mathrm{DNBE}}}$	**ER_{DNBE}-RLS1/1b** $r_{\mathrm{DNBE}} = \dfrac{\dfrac{k_{\mathrm{BuOH}}}{K_{\mathrm{BuOH}}}\left(a_{\mathrm{BuOH}} - \dfrac{a_{\mathrm{DNBE}}\cdot a_{\mathrm{H_2O}}}{K_{eq}\cdot a_{\mathrm{BuOH}}}\right)}{\left(\dfrac{a_{\mathrm{DNBE}}\cdot a_{\mathrm{H_2O}}}{K_{eq}\cdot a_{\mathrm{BuOH}}}\right) + \dfrac{K_{\mathrm{DNBE}}}{K_{\mathrm{BuOH}}}\cdot a_{\mathrm{DNBE}}}$
ER_{DNBE}-RLS1/2a $r_{\mathrm{DNBE}} = \dfrac{k_{\mathrm{BuOH}}\left(a_{\mathrm{BuOH}} - \dfrac{a_{\mathrm{DNBE}}\cdot a_{\mathrm{H_2O}}}{K_{eq}\cdot a_{\mathrm{BuOH}}}\right)}{1 + K_{\mathrm{BuOH}}\cdot\left(\dfrac{a_{\mathrm{DNBE}}\cdot a_{\mathrm{H_2O}}}{K_{eq}\cdot a_{\mathrm{BuOH}}}\right)}$	**ER_{DNBE}-RLS1/2b** $r_{\mathrm{DNBE}} = \dfrac{\dfrac{k_{\mathrm{BuOH}}}{K_{\mathrm{BuOH}}}\left(a_{\mathrm{BuOH}} - \dfrac{a_{\mathrm{DNBE}}\cdot a_{\mathrm{H_2O}}}{K_{eq}\cdot a_{\mathrm{BuOH}}}\right)}{\left(\dfrac{a_{\mathrm{DNBE}}\cdot a_{\mathrm{H_2O}}}{K_{eq}\cdot a_{\mathrm{BuOH}}}\right)}$

Table S6. Simplified kinetic models for the ER formalism where the produced DNBE remains adsorbed while water is released into solution. The rate limiting step (RLS) considered is the surface reaction. n_σ is the number of additional active centers participating in the surface reaction ranging from 0 to 2[*]

ER$_{\text{DNBE}}$– RLS: Surface reaction	
ER$_{\text{DNBE}}$-RLS2/1a	**ER$_{\text{DNBE}}$-RLS2/1b**
$r_{\text{DNBE}} = \dfrac{\hat{k} \cdot K_{\text{BuOH}}^2 \left(a_{\text{BuOH}}^2 - \dfrac{a_{\text{DNBE}} \cdot a_{\text{H}_2\text{O}}}{K_{eq}} \right)}{\left(1 + K_{\text{BuOH}} \cdot a_{\text{BuOH}} + K_{\text{DNBE}} \cdot a_{\text{DNBE}}\right)^{1+n_\sigma}}$	$r_{\text{DNBE}} = \dfrac{\hat{k} \cdot \dfrac{K_{\text{BuOH}}^2}{K_{\text{BuOH}}^{1+n_\sigma}} \left(a_{\text{BuOH}}^2 - \dfrac{a_{\text{DNBE}} \cdot a_{\text{H}_2\text{O}}}{K_{eq}} \right)}{\left(a_{\text{BuOH}} + \dfrac{K_{\text{DNBE}}}{K_{\text{BuOH}}} \cdot a_{\text{DNBE}} \right)^{1+n_\sigma}}$
ER$_{\text{DNBE}}$-RLS2/2a	**ER$_{\text{DNBE}}$-RLS2/2b**
$r_{\text{DNBE}} = \dfrac{\hat{k} \cdot K_{\text{BuOH}}^2 \left(a_{\text{BuOH}}^2 - \dfrac{a_{\text{DNBE}} \cdot a_{\text{H}_2\text{O}}}{K_{eq}} \right)}{\left(1 + K_{\text{BuOH}} \cdot a_{\text{BuOH}}\right)^{1+n_\sigma}}$	$r_{\text{DNBE}} = \dfrac{\hat{k} \cdot \dfrac{K_{\text{BuOH}}^2}{K_{\text{BuOH}}^{1+n_\sigma}} \left(a_{\text{BuOH}}^2 - \dfrac{a_{\text{DNBE}} \cdot a_{\text{H}_2\text{O}}}{K_{eq}} \right)}{\left(a_{\text{BuOH}} \right)^{1+n_\sigma}}$
ER$_{\text{DNBE}}$-RLS2/3a	**ER$_{\text{DNBE}}$-RLS2/3b**
$r_{\text{DNBE}} = \dfrac{\hat{k} \cdot K_{\text{BuOH}}^2 \left(a_{\text{BuOH}}^2 - \dfrac{a_{\text{DNBE}} \cdot a_{\text{H}_2\text{O}}}{K_{eq}} \right)}{\left(1 + K_{\text{DNBE}} \cdot a_{\text{DNBE}}\right)^{1+n_\sigma}}$	$r_{\text{DNBE}} = \dfrac{\hat{k} \cdot \dfrac{K_{\text{BuOH}}^2}{K_{\text{DNBE}}^{1+n_\sigma}} \left(a_{\text{BuOH}}^2 - \dfrac{a_{\text{DNBE}} \cdot a_{\text{H}_2\text{O}}}{K_{eq}} \right)}{\left(a_{\text{DNBE}} \right)^{1+n_\sigma}}$

[*] For $n_\sigma = 1, 2$ the expressions are equivalent to LHHW-RLS2/2a & b, LHHW-RLS2/5a & b and LHHW-RLS6/2a & b (Table S2).

Table S7. Simplified kinetic models for the ER formalism where the produced DNBE remains adsorbed while water is released into solution. The rate limiting step (RLS) considered is the desorption of DNBE.

ER$_{\text{DNBE}}$ – RLS: DNBE desorption	
ER$_{\text{DNBE}}$-RLS3/1a	**ER$_{\text{DNBE}}$-RLS3/1b**
$r_{\text{DNBE}} = \dfrac{k_{\text{DNBE}} \left(K_{eq} \dfrac{a_{\text{BuOH}}^2}{a_{\text{H}_2\text{O}}} - a_{\text{DNBE}} \right)}{1 + K_{\text{BuOH}} \cdot a_{\text{BuOH}} + K_{\text{DNBE}} \cdot \left(K_{eq} \dfrac{a_{\text{BuOH}}^2}{a_{\text{H}_2\text{O}}} \right)}$	$r_{\text{DNBE}} = \dfrac{\dfrac{k_{\text{DNBE}}}{K_{\text{DNBE}}} \left(K_{eq} \dfrac{a_{\text{BuOH}}^2}{a_{\text{H}_2\text{O}}} - a_{\text{DNBE}} \right)}{\dfrac{K_{\text{BuOH}}}{K_{\text{DNBE}}} \cdot a_{\text{BuOH}} + K_{eq} \dfrac{a_{\text{BuOH}}^2}{a_{\text{H}_2\text{O}}}}$
ER$_{\text{DNBE}}$-RLS3/2a	**ER$_{\text{DNBE}}$-RLS3/2b**
$r_{\text{DNBE}} = \dfrac{k_{\text{DNBE}} \left(K_{eq} \dfrac{a_{\text{BuOH}}^2}{a_{\text{H}_2\text{O}}} - a_{\text{DNBE}} \right)}{1 + K_{\text{DNBE}} \cdot \left(K_{eq} \dfrac{a_{\text{BuOH}}^2}{a_{\text{H}_2\text{O}}} \right)}$	$r_{\text{DNBE}} = \dfrac{\dfrac{k_{\text{DNBE}}}{K_{\text{DNBE}}} \left(K_{eq} \dfrac{a_{\text{BuOH}}^2}{a_{\text{H}_2\text{O}}} - a_{\text{DNBE}} \right)}{K_{eq} \dfrac{a_{\text{BuOH}}^2}{a_{\text{H}_2\text{O}}}}$

Simplified models gathered in Table S7 are equivalent to models LHHW-RLS3/2a&b and LHHW-RLS3/4a&b (Table S3).

Table S8. Simplified kinetic models for the ER formalism where the produced water remains adsorbed while DNBE is released into solution. The rate limiting step (RLS) considered is the adsorption of 1-butanol.

ER_{H2O} – RLS: 1-butanol adsorption	
ER_{H2O}-RLS1/1a	**ER_{H2O}-RLS1/1b**
$r_{DNBE}=\dfrac{k_{BuOH}\left(a_{BuOH}-\dfrac{a_{DNBE}\cdot a_{H_2O}}{K_{eq}\cdot a_{BuOH}}\right)}{1+K_{BuOH}\cdot\left(\dfrac{a_{DNBE}\cdot a_{H_2O}}{K_{eq}\cdot a_{BuOH}}\right)+K_{H_2O}\cdot a_{H_2O}}$	$r_{DNBE}=\dfrac{\dfrac{k_{BuOH}}{K_{BuOH}}\left(a_{BuOH}-\dfrac{a_{DNBE}\cdot a_{H_2O}}{K_{eq}\cdot a_{BuOH}}\right)}{\left(\dfrac{a_{DNBE}\cdot a_{H_2O}}{K_{eq}\cdot a_{BuOH}}\right)+\dfrac{K_{H_2O}}{K_{BuOH}}\cdot a_{H_2O}}$
ER_{H2O}-RLS1/2a[a]	**ER_{H2O}-RLS1/2b**[a]
$r_{DNBE}=\dfrac{k_{BuOH}\left(a_{BuOH}-\dfrac{a_{DNBE}\cdot a_{H_2O}}{K_{eq}\cdot a_{BuOH}}\right)}{1+K_{BuOH}\cdot\left(\dfrac{a_{DNBE}\cdot a_{H_2O}}{K_{eq}\cdot a_{BuOH}}\right)}$	$r_{DNBE}=\dfrac{\dfrac{k_{BuOH}}{K_{BuOH}}\left(a_{BuOH}-\dfrac{a_{DNBE}\cdot a_{H_2O}}{K_{eq}\cdot a_{BuOH}}\right)}{\left(\dfrac{a_{DNBE}\cdot a_{H_2O}}{K_{eq}\cdot a_{BuOH}}\right)}$

Models ER_{H2O}-RLS1/2a&b are equivalent to models ER_{DNBE}-RLS1/2a&b (Table S5).

Table S9. Simplified kinetic models for the ER formalism where the produced water remains adsorbed while DNBE is released into solution. The rate limiting step (RLS) considered is the surface reaction. n_σ is the number of additional active centers participating in the surface reaction ranging from 0 to 2.*

ER_{H2O}– RLS: Surface reaction	
ER_{H2O}-RLS2/1a	**ER_{H2O}-RLS2/1b**
$r_{DNBE}=\dfrac{\hat{k}\cdot K_{BuOH}^2\left(a_{BuOH}^2-\dfrac{a_{DNBE}\cdot a_{H_2O}}{K_{eq}}\right)}{\left(1+K_{BuOH}\cdot a_{BuOH}+K_{H_2O}\cdot a_{H_2O}\right)^{1+n_\sigma}}$	$r_{DNBE}=\dfrac{\hat{k}\cdot\dfrac{K_{BuOH}^2}{K_{BuOH}^{1+n_\sigma}}\left(a_{BuOH}^2-\dfrac{a_{DNBE}\cdot a_{H_2O}}{K_{eq}}\right)}{\left(a_{BuOH}+\dfrac{K_{H_2O}}{K_{BuOH}}\cdot a_{H_2O}\right)^{1+n_\sigma}}$
ER_{H2O}-RLS2/2a[b]	**ER_{H2O}-RLS2/2b**[b]
$r_{DNBE}=\dfrac{\hat{k}\cdot K_{BuOH}^2\left(a_{BuOH}^2-\dfrac{a_{DNBE}\cdot a_{H_2O}}{K_{eq}}\right)}{\left(1+K_{BuOH}\cdot a_{BuOH}\right)^{1+n_\sigma}}$	$r_{DNBE}=\dfrac{\hat{k}\cdot\dfrac{K_{BuOH}^2}{K_{BuOH}^{1+n_\sigma}}\left(a_{BuOH}^2-\dfrac{a_{DNBE}\cdot a_{H_2O}}{K_{eq}}\right)}{\left(a_{BuOH}\right)^{1+n_\sigma}}$
ER_{H2O}-RLS2/3a	**ER_{H2O}-RLS2/3b**
$r_{DNBE}=\dfrac{\hat{k}\cdot K_{BuOH}^2\left(a_{BuOH}^2-\dfrac{a_{DNBE}\cdot a_{H_2O}}{K_{eq}}\right)}{\left(1+K_{H_2O}\cdot a_{H_2O}\right)^{1+n_\sigma}}$	$r_{DNBE}=\dfrac{\hat{k}\cdot\dfrac{K_{BuOH}^2}{K_{H_2O}^{1+n_\sigma}}\left(a_{BuOH}^2-\dfrac{a_{DNBE}\cdot a_{H_2O}}{K_{eq}}\right)}{\left(a_{H_2O}\right)^{1+n_\sigma}}$

Models ER_{H2O}-RLS2/2a&b are equivalent to models ER_{DNBE}-RLS2/2a&b (Table S6).

* For $n_\sigma = 1, 2$ the expressions are equivalent to LHHW-RLS2/3a & b, LHHW-RLS2/5a & b and LHHW-RLS7/2a &b (Table S2).

Table S10. Simplified kinetic models for the ER formalism where the produced water remains adsorbed while DNBE is released into solution. The rate limiting step (RLS) considered is the desorption of water.

ER$_{\mathrm{H2O}}$– RLS: H$_2$O desorption	
ER$_{\mathrm{H2O}}$-RLS3/1a	**ER$_{\mathrm{H2O}}$-RLS3/1b**
$r_{\mathrm{DNBE}} = \dfrac{k_{\mathrm{H_2O}}\left(K_{eq}\dfrac{a_{\mathrm{BuOH}}^2}{a_{\mathrm{DNBE}}} - a_{\mathrm{H_2O}}\right)}{1 + K_{\mathrm{BuOH}}\cdot a_{\mathrm{BuOH}} + K_{\mathrm{H_2O}}\cdot\left(K_{eq}\dfrac{a_{\mathrm{BuOH}}^2}{a_{\mathrm{DNBE}}}\right)}$	$r_{\mathrm{DNBE}} = \dfrac{\dfrac{k_{\mathrm{H_2O}}}{K_{\mathrm{H_2O}}}\left(K_{eq}\dfrac{a_{\mathrm{BuOH}}^2}{a_{\mathrm{DNBE}}} - a_{\mathrm{H_2O}}\right)}{\dfrac{K_{\mathrm{BuOH}}}{K_{\mathrm{H_2O}}}\cdot a_{\mathrm{BuOH}} + \left(K_{eq}\dfrac{a_{\mathrm{BuOH}}^2}{a_{\mathrm{DNBE}}}\right)}$
ER$_{\mathrm{H2O}}$-RLS3/2a	**ER$_{\mathrm{H2O}}$-RLS3/2b**
$r_{\mathrm{DNBE}} = \dfrac{k_{\mathrm{H_2O}}\left(K_{eq}\dfrac{a_{\mathrm{BuOH}}^2}{a_{\mathrm{DNBE}}} - a_{\mathrm{H_2O}}\right)}{1 + K_{\mathrm{H_2O}}\cdot\left(K_{eq}\dfrac{a_{\mathrm{BuOH}}^2}{a_{\mathrm{DNBE}}}\right)}$	$r_{\mathrm{DNBE}} = \dfrac{\dfrac{k_{\mathrm{H_2O}}}{K_{\mathrm{H_2O}}}\left(K_{eq}\dfrac{a_{\mathrm{BuOH}}^2}{a_{\mathrm{DNBE}}} - a_{\mathrm{H_2O}}\right)}{\left(K_{eq}\dfrac{a_{\mathrm{BuOH}}^2}{a_{\mathrm{DNBE}}}\right)}$

Simplified models gathered in Table S10 are equivalent to models LHHW-RLS4/2a&b and LHHW-RLS4/4a&b (Table S4).

Nomenclature

Notation

A	Preexponential factor
a_j	Activity of compound *j*
BuOHσ	1-Butanol molecule chemisorbed on an only active site
DNBEσ	Di-n-butyl ether molecule chemisorbed on an only active site
E_A	Activation energy
d_p	Particle diameter
F_0	Test statistic
$F_{distribution}$	Value of the continuous probability distribution
$H_2O\sigma$	Water molecule chemisorbed on an only active site
k	Number of regressor variables
k_α	Freundlich parameter, K
$\hat{k}$	Forward rate constant for the surface reaction
K_{eq}	Equilibrium constant of DNBE formation reaction
k_j	Adsorption rate constant of compound *j*
K_j	Adsorption equilibrium constant of compound *j*
K_s	Surface reaction equilibrium constant
K_w	Water correction factor
K_{w1}	First parameter of the water correction factor
K_{w2}	Second parameter of the water correction factor
m	Number of levels of the regressor variables
m_σ	Number of total active sites participating in the rate limiting step
n	Total number of observations
n^0_{BuOH}	Initial moles of 1-butanol
n_{DNBE}	Mole of di-n-butyl ether
n_σ	Number of additional active sites participating in the surface reaction
N_{stir}	Stirring speed
n_i	Number of observations at the *i*th level of the regressor variables
p	Number of regression coefficients
R	Ideal gas constant
R^2_{adj}	Goodness of the fit
r_{cal}	Estimated reaction rate
r_{exp}	Experimental reaction rate

r_{DNBE}	Reaction rate of DNBE formation
r^0_{DNBE}	Initial reaction rate of DNBE formation
$\hat{r}^0_{\mathrm{DNBE}}$	Fitted value of initial reaction rate of DNBE formation
$\overline{r^0_{\mathrm{DNBE}}}$	Average of the initial reaction rate of DNBE formation
SS_E	Sum of squares due to the error
SS_{LOF}	Sum of squares due to the lack of fit
SS_{PE}	Sum of squares due to pure error
SS_R	Sum of squares due to the regression
t	Time
T	Temperature
T_{ref}	Midpoint T value of the analyzed range of temperatures
W_{cat}	Mass of loaded catalyst
X_{BuOH}	1-Butanol conversion

Greek symbols

α	Freundlich constant
β_i	Parameter *i*
ε_i	Uncertainty of parameter *i*
Δ	Parameter uncertainty
ΔG_j	Adsorption free energy of compound *j*
ΔH_j	Adsorption enthalpy of compound *j*
ΔS_j	Adsorption entropy of compound *j*
θ_{H2O}	Fraction of acid sites blocked by water molecules
σ	Active site

Abbreviations

BuOH	1-Butanol
DNBE	Di-n-butyl ether
ER	Eley Rideal
$\mathrm{ER_{DNBE}}$	Eley Rideal formalism where DNBE remains adsorbed
$\mathrm{ER_{H2O}}$	Eley Rideal formalism where H_2O remains adsorbed
LHHW	Langmuir-Hinshelwood-Hougen-Watson
RLS	Rate limiting step
SSRE	Sum of squared relative errors

References

[1] Olaofe, O.; Yue, P. L. Kinetics of dehydration of 1-butanol over zeolites. *Collect. Czech. Chem. Commun.* **1985**, *501*, 1784-1800.

[2] Krampera, F.; Beránek, L. Kinetics of individual reactions in reaction network 1-butanol-di-(1-butyl) ether-butenes-water on alumina. *Collect. Czech. Chem. Commun.***1986**, *51*, 774-785.

[3] Sow, B.; Hamoudi, S.; Zahedi-Niaki, M. H.; Kaliaguine, S. 1-Butanol etherification over sulfonated mesostructured silica and organo-silica. *Microporous Mesoporous Mater*. **2005**, *79*, 129–136.

[4] Gates, B. C.; Rodriguez, W. General and specific acid catalysis in sulfonic acid resins. *J. Catal*. **1973**, *31*, 27-31.

[5] du Toit, E.; Nicol, W. The rate inhibiting effect of water as a product on reactions catalyzed by cation exchange resins: formation of mesityl oxide from acetone as case study. *App. Catal., A*. **2004**, *277*, 219-225.

[6] Limbeck, U.; Altwicker, C.; Kunz, U.; Hoffmann, U. Rate expression for THF synthesis on acidic ion exchange resin. *Chem. Eng. Sci*. **2001**, *56*, 2171-2178.

[7] Yang, B.-L.; Maeda, M.; Goto, S. Kinetics of liquid phase synthesis of tert-amyl methyl ether from tert-amyl alcohol and methanol catalyzed by ion exchange resin. J. *Chem. Kinet*. **1997**, *30*, 137-143.

[8] Balakos, M. W.; Chuang, S. S. C. Dynamic and LHHW analysis of heterogeneous catalytic hydroformylation. *J. Catal*. **1995**, *151*, 266-278.

[9] Box, G. E. P.; Hunter, J. S.; Hunter, W. H. *Statistics for experimenters. Design, Innovation and Discovery*, 2nd ed.; John Wiley & Sons Inc.: Hoboken, New Jersey, 2005.

[10] Bringué, R.; Ramírez, E.; Fité, C.; Iborra, M.; Tejero, J. Kinetics of 1-pentanol etherification without water removal. *Ind. Eng. Chem. Res*. **2011**, *50*, 7911-7919

[11] Casas, C. Synthesis of C_{10}-C_{16} linear symmetrical ethers from n-alcohols over heterogeneous acid catalysts. Ph.D. Thesis, University of Barcelona, Spain, 2013.

[12] Montgomery, D. C. Fitting regression models. *Design and Analysis of Experiments*, 5th ed.; John Wiley & Sons Inc.; 2001.

[13] Hill, C. G. Jr. Elements of heterogeneous catalysis. *An introduction to chemical engineering kinetics & reaction design*. John Wiley & Sons, Inc.: 1977.

[14] Yang, K. H.; Hougen, O. A. Determination of mechanisms of catalyzed gaseous reactions. *Chem. Eng. Prog*. **1950**, *46* (3), 146-157.

[15] Levenberg, K. A. Method for the solution of certain problems in least squares. *Quart. Appl. Math.* **1944**, *2*, 64–168.

[16] Marquardt, D. An algorithm for least-squares estimation of nonlinear parameters. *SIAM J. Appl. Math*. **1963**, *11*, 431–441.

[17] Park, H.; Stefanski, L. A. Relative-error prediction. *Statist. Probab. Lett*. **1998**, *40*, 227-236.

[18] Tofallis, C. Least squares percentage regression. *J. Mod. App. Stat. Meth*. **2008**, *7* (2), 526-534.

[19] Kittrell, J.R. Mathematical modeling of chemical reactions. *Adv. Chem. Eng*. **1970**, *8*, 97–183.

[20] Weidlicht, U.; Gmehling, J. A modified UNIFAC model. 1. Prediction of VLE, h^E, and γ^∞. *Ind. Eng. Chem. Res.* **1987**, *26* (7), 1372-1381.

[21] Gmehling, J.; Li, J.; Schiller, M. A modified UNIFAC model. 2. Present parameter matrix and results for different thermodynamic properties. *Ind. Eng. Chem. Res*. **1993**, *32*, 178-193.

[22] Gmehling, J.; Lohmann, J.; Jakob, A.; Li, J.; Joh, R. A modified UNIFAC (Dortmund) model. 3. Revision and extension. *Ind. Eng. Chem. Res.* **1998**, *37*, 4876-4882.

[23] Jakob, A.; Grensemann, H.; Lohmann, J.; Gmehling, J. Further development of modified UNIFAC (Dortmund): revision and extension 5. *Ind. Eng. Chem. Res.* **2006**, *45*, 7924-7933.

[24] Bringué, R.; Ramírez, E.; Iborra, M.; Tejero, J.; Cunill, F. Kinetics of 1-hexanol etherification on Amberlyst 70. *Chem. Eng. J.* **2014**, *246*, 71–78.

6. MODELING AND ATOMISTIC SIMULATIONS OF ION EXCHANGE RESINS[*]

---

[*] Results presented in this chapter have been published in:

Pérez-Maciá, M. A.; Curcó, D.; Bringué, R.; Iborra, M.; Alemán, C. Atomistic simulations of the structure of highly crosslinked sulfonated poly(styrene-co-divinylbenzene) ion exchange resins. *Soft Matter* **2015**, *11*, 2251–2267.

6.1. Introduction

As it has been demonstrated in the previous chapters, the catalytic performance of ion exchange resins depends critically on both the nano-environment surrounding the active centers and their accessibility. Accessibility to the active centers in these materials depends greatly on the polymeric structure and is dramatically affected by the extent of swelling of the polymer mass in contact with the reaction medium. Because of the difficulty in experimentally determining the structure of the polymeric resins and the swollen-state morphology, exploitation of ion-exchange catalysts is still based on a trial and error approach rather than on solid understanding and design of their parameters.

Employment of experimental techniques to get structural information of ion exchange resins is a complex task, therefore, atomistic computer simulations currently represent a distinctive method for answering questions related with the influence of network topology on material properties. A considerable number of atomistic computer simulation studies have been reported to stablish relationships between the structure of crosslinked networks and material properties. For example, Bandyopadhyay and Odegard[1] simulated epoxy systems demonstrating that the mechanical properties (volume shrinkage, coefficients of thermal expansion and elastic moduli values) are largely influenced by the overall crosslinking degree but not by the distribution of crosslink clusters in the bulk matrix. Koo et al.[2] investigated the relationship between the crosslinking degree and the glass transition temperature of crosslinked epoxy network (its chemical constituents being di-glycidyl ether of bisphenol F (DGEBF), di-ethylene tri-amine (DETA) and tris-(cinnamoyloxymethyl)-ethane (TCE)). They showed that glass transition temperatures increased with the crosslinking degree. Jang et al.[3] modeled vinyl ester resins, showing that the Young’s moduli and the resin density increased with increasing crosslink density. Soni et al.[4] simulated bisphenol A diglycidyl ether (DGEBA) with curing agents of different lengths, evidencing that the glass transition temperature for those resins decreased with increasing length of curing agent. Khare and Khare[5] created epoxy networks of DGEBA and 4,4’-diamineodiphenyl sulfone using a diffusion approach, characterizing the dependence between the epoxy conversion and the bond formation distance. Atomistic MD simulations on crosslinked poly(vynil alcohol) evidenced that the mechanical properties and glass transitions depend on both the network topology and crosslinking density.[6] In general, the overall of these works indicate that properties of crosslinked materials are highly dependent on network topology and generally an increase in the crosslinking provokes an increase in the elastic modulus and glass transition temperature. In spite of this extensive literature, the relationship between the topology of highly crosslinked ion-exchange P(S-DVB) resins and their properties, especially the structural ones, remains unknown.

The aim of this chapter is to offer a contribution to the understanding of the microscopic structure of ion-exchange P(S-DVB) resins using atomistic computer simulations. The next chapter deals with the swelling of ion exchange resins in 1-butanol.

6.2. Construction of the polymer network

Construction of heterogeneously ordered macromolecular multi-chain systems is always a very difficult task because the relatively high density and the connectivity of the molecular systems reduce significantly the efficiency of conventional simulation methods.[7] Additionally, construction of P(S-DVB) networks is restricted by the crosslinks formed by the divinylbenzene units. Crosslinked networks have been modeled by several authors. For example, Doherty and co-workers[8] created poly(methyl acrylate) networks using lattice-based simulations based on a polymerization MD scheme. Yarovsky et al.[9] presented a methodology to cross-link low molecular weight water-soluble phosphate-modified epoxy resins. More recently, Gou et al.[10] and Fan et al.[11] built cross-linked networks for epoxy resins (EPON-862) using Accelyrs simulation package.[12] However, no details were provided in such studies regarding the cross-linking procedure. Wu et al.[13] also performed cross-linking simulations for epoxy resin and used their model to study diffusion of water in these cross-linked networks.[14] The authors used an iterative MD/MM procedure to cross-link epoxy resin, where the newly formed topology was subjected to 1000 MD steps of relaxation. Heine et al.[15] simulated structural and mechanical properties of large polydimethylsiloxane networks, modeled as united atom model, using a dynamic cross-linking approach based on cutoff distance criterion. Here, the newly formed topology was relaxed using a modified potential which was linear at large distances and quadratic at short distances. Varshney et al.[16] used different approaches to build highly crosslinked polymer networks, the molecular topology being relaxed by applying a multistep relaxation procedure during cross-linking.

In this work, two different procedures were developed to construct P(S-DVB) networks. The first one, hereafter denoted HGA (Homogeneous Generation Approach) is based on the generation of polystyrene segments of identical length (i.e. same number of repeat copolymerized monomers) while the second approach, called CGA (Combined Growing Approach), enables the generation of segments defining internal loops by combining two growing algorithms. In both approaches, the following conditions are fulfilled: (1) molecular internal geometry restrictions (i.e. bond lengths and bond angles) are satisfied; and (2) atomic overlaps between atoms separated by three or more chemical bonds are completely avoided (i.e. interatomic distances are equal or higher than the sum of the van der Waals radii).

Amberlyst 15, which is a highly crosslinked (≈ 20% w/w), monosulfonated (presenting one sulfonic group per phenyl ring) resin, was used as reference in this work to model P(S-DVB).

Table 6.1 gathers the more relevant experimentally-determined physical properties of Amberlyst 15 for the construction and validation of atomic models.

Table 6.1. Physical properties of Amberlyst 15.

Property	Values from the literature	Own authors values
Sulfur content (% w/w)	13.8[a]	15.02 ± 0.12[b]
Porosity, θ_{Total} (%)	31.9[a]	31.7[c]
Apparent density, ρ_a (g/cm^3)	1.012[a]	0.97[d]
Average pore diameter, d_{pore} (nm)	28.8[a]; 31.8[e]	-
Exchange capacity (meq H$^+$/g)	4.3[a]	4.81[f]
DVB content (% w/w)	20[g]	-

[a] From reference 17.
[b] Determined by elemental analysis.
[c] Calculated as $\theta_{\text{Total}}= V_{pore}/(V_{pore}+1/\rho_s)$, where V_{pore} is the pore volume per mass of resin determined by adsorption of N_2 at 77 K and P/P_0 = 0.99 and ρ_s is skeletal density measured by helium displacement. V_{pore} = 0.328 cm^3/g; ρ_s = 1.416 g/cm^{-3}.
[d] Indirectly determined using V_{pore} = 0.328 cm^3/g. ρ_s = 1.416 g/cm^{-3}.
[e] From reference 18.
[f] Determined by titration against standard base following the procedure described in reference 19.
[g] Information supplied by the manufacturer as weight % of crosslinker used to prepare the network.

6.2.1. Homogeneous Generation Approach (HGA)

This strategy can be summarized in four main steps (see Figure 6.1):

(a) Construction of the first polymer chain.

The styrene monomer is constructed within the simulation box according to its chemical architecture (Figure 6.1a). After this, the *ortho, meta* or *para* position of the phenyl ring is randomly selected, according to previously defined probabilities, to attach the sulfonic acid group. Next, the position for growing the second styrene unit is randomly chosen between the two available positions (identified as 1 and 2 in Figure 6.1b). It should be noted that this selection is related with the chain growing direction. After constructing the second repeat unit, the sulfonic group is attached to its phenyl ring at a position randomly selected among the *ortho, meta* and *para*. This procedure is repeated until a polymer chain, containing *m* sulfonated styrene units, has been created (Figure 6.1c).

(b) Selection of crosslinking positions.

Among the *m* sulfonated styrene units of the first polymer chain, one is randomly selected and transformed, after eliminating its sulfonic acid group, into a divinylbenzene unit (Figure 6.1d). In order to keep the styrene/divinylbenzene ratio close to that of Amberlyst 15 manufacturer specifications, in this work *m* was fixed to 7.

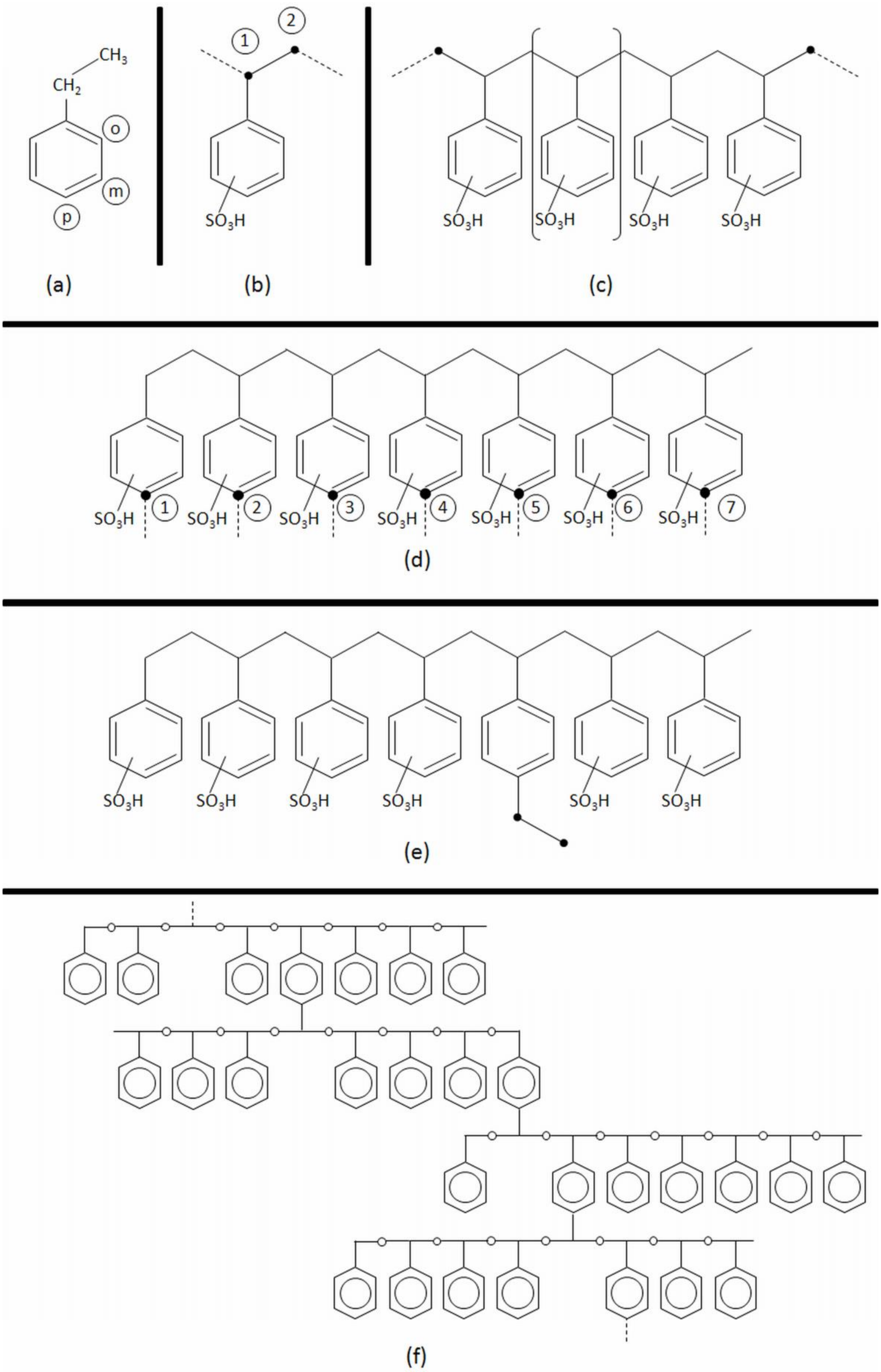

Figure 6.1. Schematic representation of the main steps involved in the construction of P(S-DVB) networks using the HGA method: (a) styrene monomer and identification of the possible positions for the sulfonic acid group (*ortho*, *meta* and *para*); (b) available positions (1 and 2) for the growing of the polymer chain by adding the second sulfonated styrene unit; (c) growing of the polymer chain; (d) selection of one crosslink position from a total of *m*; (e) transformation of the selected sulfonated styrene unit into a divinylbenzene unit; and (f) P(S-DVB) network obtained using the HGA strategy.

(c) Construction of the second polymer chain.

The divinylbenzene unit generated in the first chain is used to initiate the growing of the second polymer chain (Figure 6.1e). For this purpose, *m*-1 sulfonated styrene units were built using the procedure described in (a), one of them being transformed into a divinylbenzene unit as indicated in (b). Accordingly, in addition to the *m*-2 sulfonated styrene units, the new chain contains two divinylbenzene units: the one coming from the previous chain (which has been used to initiate the growing of this chain) and the one derived from the transformation of styrene into divinylbenzene (which will be used in (d) to initiate the growing of the next chain).

(d) Repetition.

The rest of the segments is generated using the procedures indicated in (a)-(c). Figure 6.1 provides a schematic representation of the resin network obtained using the HGA method.

In this approach, repeat units are constructed one-by-one. After constructing a repeat unit, the possible existence of steric overlaps with previously generated units is systematically examined. If such interactions are detected the generation process stops and a new position/unit is randomly selected among the remaining ones. If steric clashes still exist, the process is restarted from the previous step or so many previous steps as necessary (if the clashes persist).

6.2.2. Combined Growing Approach (CGA)

The generation of the first sulfonated polystyrene chain is identical for both the HGA and CGA procedures, differences between them starting once a minimal number, *r*, of sulfonated styrene units have been added to the first chain. After this, the CGA strategy consists on the combination of two different algorithms: the enlargement-crosslinking, which looks for suitable crosslink geometries among the generated sulfonated styrene units and grows the molecule using the existing ends, and the branching algorithm, which is applied every *k* steps of enlargement-crosslinking and creates new crosslinks increasing the number of ends in the supermolecule.

(a) Enlargement-crosslinking algorithm.

Once the *r* sulfonated styrene unit has been attached to the previous one *r*-1, the position for growing the *r*+1 sulfonated styrene unit is randomly chosen between one of the available ends. At the initial stages, the number of available ends is only two (identified as 1 and 2 in the HGA method, Figure 6.1b). However, after combining with the branching algorithm (see below), the number of available ends grows progressively. This feature represents an important difference between the CGA and HGA approaches, since in the former the increasing number of available ends enables the construction of polymer segments with different lengths while the length of all segments is identical in the latter.

After the construction of the *r*+1 sulfonated styrene unit, the surrounding of the carbon atom located at the *para* position of the phenyl ring is examined to look for a backbone tertiary carbon atom at a distance similar to that typically found for C–C bonds (i.e. bond length with a specified tolerance). If this condition is satisfied, the existence of suitable bond angles (with specified tolerances) is also checked. If these two internal geometry conditions are met, the phenyl group attached to such tertiary carbon atom and the sulfonic group of the *r*+1 styrene unit are removed while a new C–C bond connecting the two units is created. If the conditions are not satisfied, the whole *r*+1 styrene unit is removed and re-constructed. This re-construction process is repeated until a successful transformation of styrene into divinylbenzene or until a pre-specified number, *s*, of trials has been reached. In the latter case, the sulfonated styrene monomer is kept. Once the crosslinking degree has reached a pre-defined value (i.e. in this work this value corresponds to the one experimentally observed), the crosslinking algorithm becomes inactive and the structure only grows at the available ends.

Figure 6.2 provides a schematic representation of this algorithm. More specifically, two possible locations at one of the ends for the new sulfonated styrene units are displayed. As it can be seen, position 1 does not satisfy internal geometry restrictions to transform sulfonated styrene into divinylbenzene while position 2 does. This procedure allows the formation of crosslinks in a supermolecule that grows heterogeneously.

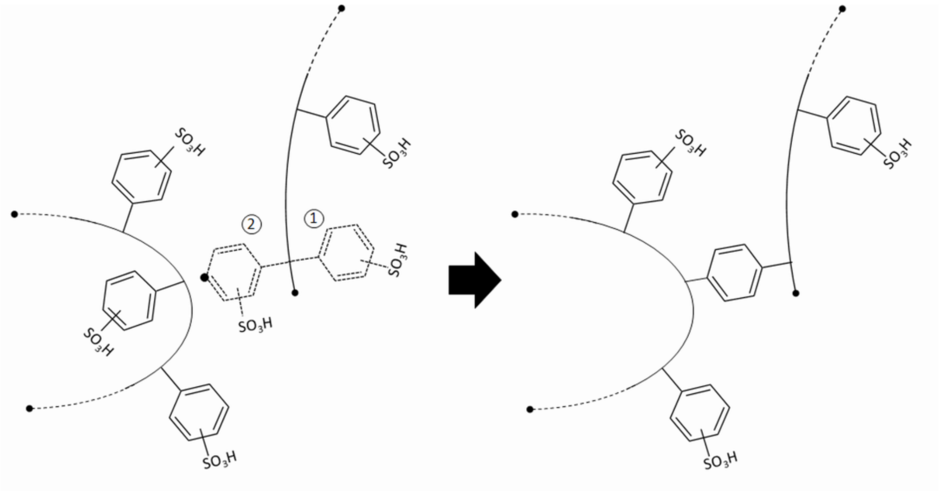

Figure 6.2. Application of the enlargement-crosslinking algorithm involved in the CGA method. The enlargement-crosslinking algorithm is illustrated through the selection of position 2 for the formation of a new crosslink.

(b) Branching algorithm.

Application of the enlargement-crosslinking algorithm is not enough to construct a P(S-DVB) resin with the physical characteristics described in Table 6.1. Accordingly, such algorithm has been combined with the branching algorithm, which is applied after a previously specified number of repeat units, *k*, has been generated. In the branching algorithm, a carbon atom located at the *para* position of the phenyl ring is randomly selected among all the sulfonated styrene units contained in the simulation box. Then, the sulfonic group is removed and the styrene unit is transformed into a divinylbenezene unit. This strategy gives place to the generation of two new end positions to grow the polymer chain, as is schematically represented in Figure 6.3.

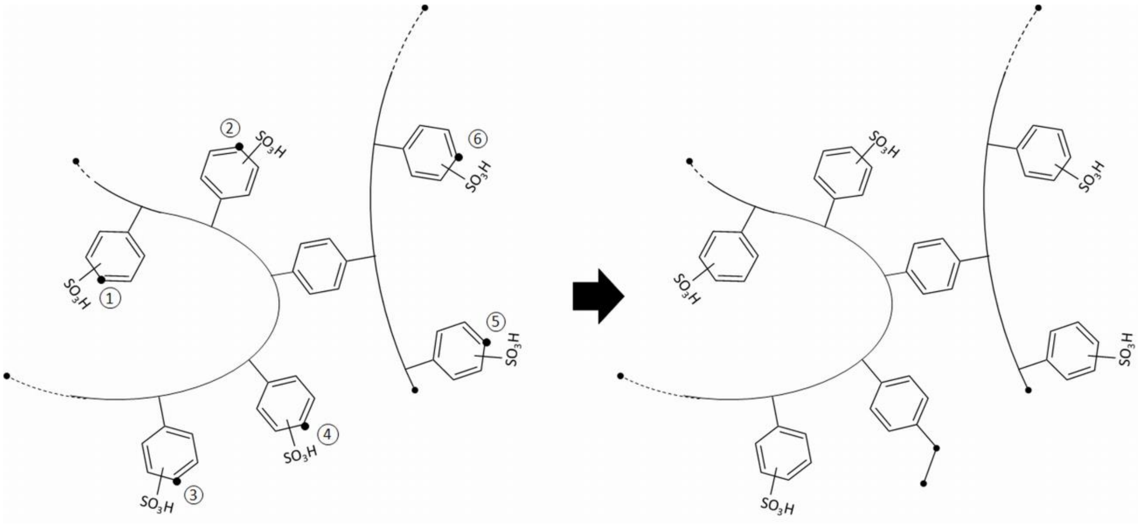

Figure 6.3. Application of the branching algorithm involved in the CGA method. The branching algorithm is applied by randomly choosing the *para* carbon atom 4 (among a total of 6) to remove the sulfonic acid group and transform the sulfonated styrene unit into divinylbenzene, giving place to the creation of two new ends.

6.3. Computational methods

All MD simulations were performed using the GROMACS 4.6.5 program.[20] The energy was calculated using the force-field expression previously introduced in Section 2.4.1.1:

$$U = \frac{1}{2}\sum_{\text{bonds}} k_b \left(b - b_0\right)^2 + \frac{1}{2}\sum_{\text{angles}} k_\theta \left(\theta - \theta_0\right)^2 + \sum_{\text{dihedrals}} k_\varphi \left(1 + \cos\left(n\varphi - \varphi_0\right)\right) + \sum_{\text{non-bonded}} 4\in_{ij}\left(\left(\frac{\sigma_{ij}}{r_{ij}}\right)^{12} - \left(\frac{\sigma_{ij}}{r_{ij}}\right)^{6}\right) + \frac{q_i q_j}{4\pi\varepsilon_0\varepsilon_r r_{ij}} \tag{2.6}$$

where the first two sums represent the harmonic approximation for stretching and bending contributions, followed by a Fourier series expansion for the torsional term. In these bonding terms k_b, k_θ and k_φ are the bond, angle and dihedral angle force constants, respectively; b, θ and

φ are the bond length, bond angle and dihedral angle, respectively; the subindex zero represents the equilibrium values for such geometric parameters; and n is the dihedral multiplicity. The second part of expression (2.6) contains the non-bonding interactions, which are represented by the sum of Coulomb and 6-12 Lennard-Jones terms. In these contributions ϵ_{ij} is the depth of the potential well for the interaction of atoms i and j, σ_{ij} is the distance where the Lennard-Jones potential is exactly zero, q_i is the partial atomic charge of atom i, ε_0 is the electric constant, ε_r is the effective dielectric constant and r_{ij} is the distance separating atoms i and j. The Lennard-Jones parameters between pairs of different atoms are obtained from the Lorentz-Berthelot mixing rules, in which ϵ_{ij} values are based on the geometric mean of ϵ_i and ϵ_j and σ_{ij} values are based on the arithmetic mean of σ_i and σ_j. For 1-4 interactions (those between atoms separated by three chemical bonds), the strength of the Lennard-Jones and electrostatic interactions were scaled down by a factor of 0.5 and 0.8333 respectively.

Stretching, bending, torsional and van der Waals force field parameters were extracted from the general AMBER force field (GAFF).[21] Atomic charges were computed at the HF/6-31G(d) level using the Restrained ElectroStatic Potential (RESP) strategy.[22] Charges, which were calculated on different model molecules, were scaled (c = 0.71) to reflect that the polarization in condensed media is smaller than in the gas-phase.[23,24] Figure 6.4 provides the atomic charges used in this work to represent electrostatic interactions involving styrene, sulfonated styrene and divinylbenzene units.

Periodic boundary conditions were applied using the nearest image convention. Newton's equations of motion were integrated using the leap-frog algorithm using a numerical integration step of 1 fs. An atom pair distance cut-off of 14.0 Å was applied to compute the van der Waals interactions. Beyond such cut off distance, electrostatic interactions were calculated by using Particle Mesh Ewald method, with a points grid density of the reciprocal space of 1 Å^3.[25] The Nosé-Hoover thermostat[26,27] was used with a temperature time constant of 0.5 ps. The Parrinello-Rahman[28] barostat was used to keep the pressure at 1 bar, the pressure time constant being set at 1 ps (see Section 2.4.1 for a description of: periodic boundary conditions, leap-frog algorithm, evaluation of the non-bonded energy and temperature and pressure couplings).

Before MD trajectories, all generated P(S-DBV) microstructures were submitted to 5000 steps of energy minimization using the steepest descent method to relax conformational and structural tensions[*]. Next, configurations were heated up to 300 K during 500 ps in a NVT-MD

---

[*] During the construction of the polymeric network, molecular internal geometry restrictions are satisfied and atomic overlaps between atoms separated by three or more chemical bonds are completely avoided. However, the energy of interaction is not taken into account. In order to avoid large energies that could lead to instabilities during MD simulation, an energy minimization on the generated conformation was carried out to find the best nearby conformation. The minimized structure has smaller forces on each atom and therefore serves as an excellent starting point for molecular dynamics simulations.

simulation. Finally, 500 ps NPT-MD were run for density relaxation at 300 K with a pressure of 1 bar. For each microstructure, the last snapshot (system configuration) of the last NPT-run was the starting point for NPT-MD productive trajectories, the production time ranging from 30 to more than 60 ns.

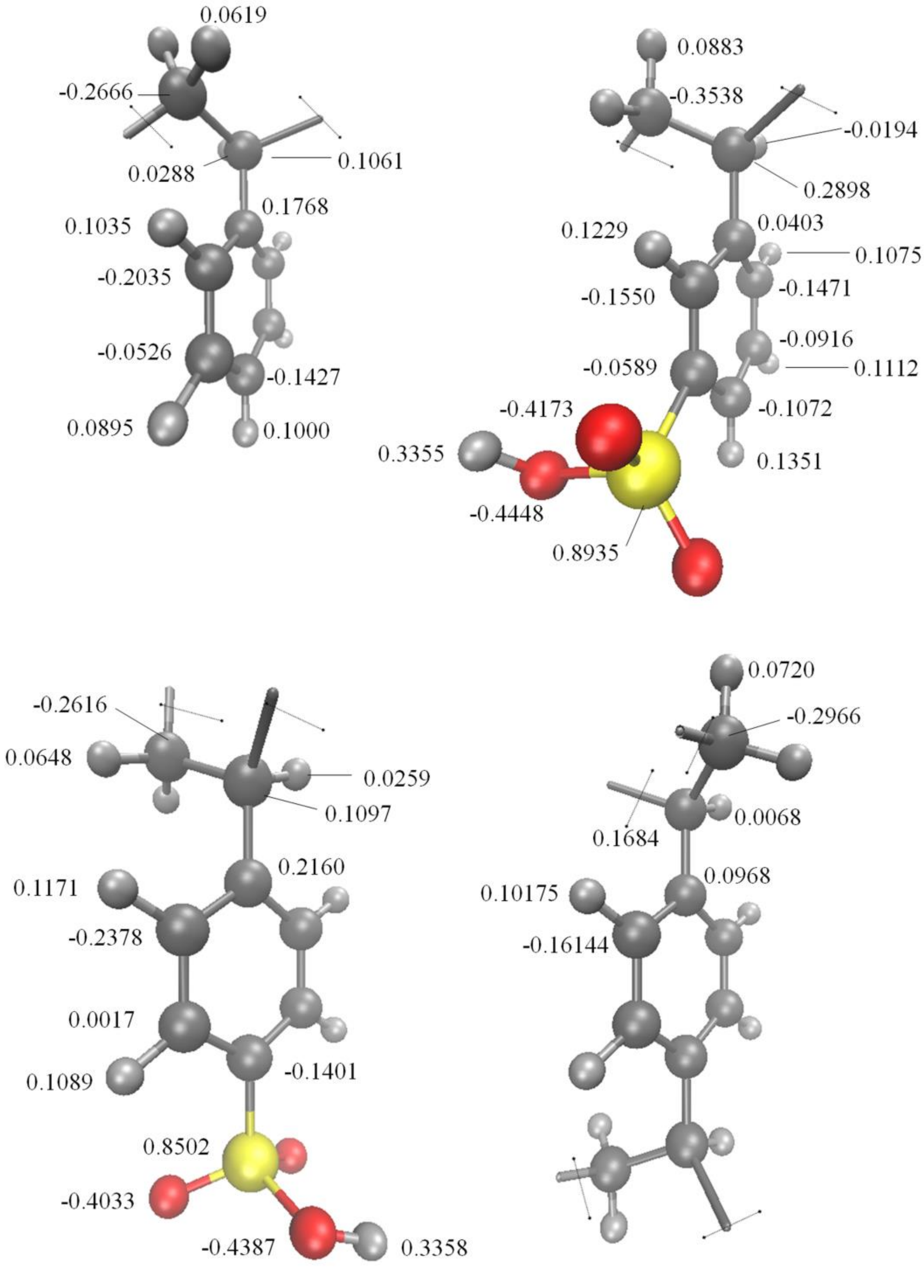

Figure 6.4. Electrostatic parameters for styrene, *m*-sulfonic styrene, *p*-sulfonic styrene and divinylbenzene units.

6.4. Results and discussion

6.4.1. Topology-density relationship

The HGA and CGA procedures described above were applied for the generation of many sulfonated P(S-DVB) microstructures. The topology of these microstructures and its relationship with the density of the system is discussed in this sub-section.

Tens of microstructures were generated using the HGA method, which was applied using m = 7. Two systems of different size were examined by considering the following numbers of styrene (N_S) and divinylbenzene (N_{DVB}) units: {N_S = 727; N_{DVB} = 144} and {N_S = 1787; N_{DVB} = 356}. According to the imposed value of m, microstructures with N_S = 727 and 1787 were distributed in 145 and 357 small chains, respectively, of identical chemical composition (i.e. each chain contains 2 divinylbenzene units, which are shared through crosslinks with another two chains, and 5 styrene units). In general, the number of sulfonic groups (N_{Sulf}) was slightly lower than N_S since steric effects precluded the sulfonation of all styrene units (i.e. N_{Sulf} was ~721 and ~1761 for N_S= 727 and 1787, respectively). The main characteristic of the microstructures obtained using the HGA method (hereafter denoted as HGA-145 and HGA-357 depending on the number of small chains) is the homogeneous distribution of the styrene and divinylbenezene unit. This is evidenced in Figure 6.5a, which displays one HGA-357 microstructure after MD relaxation.

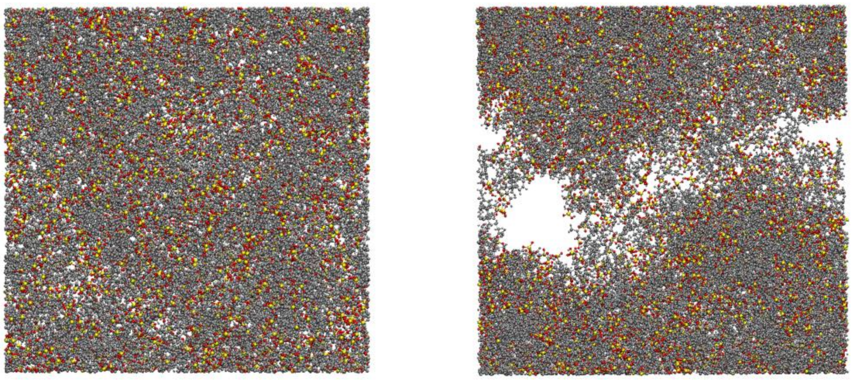

Figure 6.5. Representative microstructures obtained using the (a) HGA and (b) CGA procedures and, subsequently, relaxed with MD. Figure (a) corresponds to the microstructure HGA-357 generated using {N_S= 1787; N_{DVB}= 356} while Figure (b) corresponds to the microstructure CGA-14/2 which was constructed using {N_S= 2141; N_{DVB}= 358} and involves 14 super-crosslinks and 2 inter-crosslinks.

Homogeneous structures derived from the HGA method systematically led to very unsatisfactory density values, as it can be seen in Figure 6.6, where the temporal evolution of the apparent density (ρ_a) for representative HGA-145 and HGA-357 microstructures is shown. As it can be seen, the ρ_a values of the relaxed structures are around 1.25-1.28 g/cm^3, representing an overestimation close to 30% with respect to the experimental value (Table 6.1). These high density values are due to the homogeneous topology of the resin that is motivated by the own HGA algorithm. Thus, detailed topological analyses of the HGA microstructures indicates that, independently of the number of small chains, all crosslinks are identical, as is schematically depicted in Figure 6.7a. HGA microstructures, which do not reflect the characteristics and inhomogeneity typically associated to highly crosslinked resins, systematically fail in the reproduction of essential properties, as the apparent density and porosity. According to these features, the rest of this work has been exclusively focused on the microstructures generated by the CGA method.

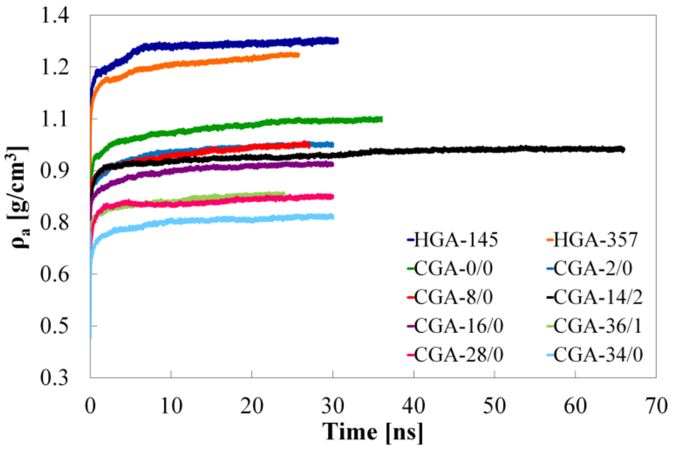

Figure 6.6. Temporal evolution of the apparent density (ρ_a) during the MD relaxation process for representative microstructures generated using the HGA and CGA methods.

Several microstructures were generated using the CGA method considering $\{N_S = 2141; N_{DVB} = 358\}$. Inspection of the topologies of the generated structures indicates that this procedure facilitates the formation not only of simple crosslinks, like those obtained using the HGA method (Figure 6.7a), but also of "*super-crosslinks*". The name super-crosslink refers to the cyclic topology defined when the formation of one or more simple crosslinks close a loop (Figure 6.7b). The total number of super-crosslinks in the generated microstructures was found to vary between 0 and 37. In addition, the CGA approach sporadically generates crosslinks that connect molecular fragments located at the own simulation box and its image, hereafter denoted "*inter-crosslinks*". The number of these inter-crosslinks (if any) is very reduced (i.e. ≤ 2). The most relevant characteristic of structures with super-crosslinks is the heterogeneity and porosity provoked by the constraints associated to the topology of the loop. This is evidenced in the representative microstructure depicted in Figure 6.5b, which contains 14 super-crosslinks and 2 inter-crosslinks. In contrast, CGA microstructures in which the crosslinked topology does not allow to define super-crosslinks are more homogeneous and relatively similar to those obtained using the HGA method.

In order to evaluate the influence of the topology on both the density and the porosity (θ_{Total}), Figure 6.6 represents the temporal evolution of ρ_a during the relaxation process for a selected number of CGA microstructures. These microstructures are identified using the following label code: CGA-N_{scl}/N_{inter}, where N_{scl} and N_{inter} correspond to the number of super-crosslinks and the number of inter-crosslinks, respectively. Table 6.2 lists the main characteristics of the CGA-N_{scl}/N_{inter} microstructures as well as the values of ρ_a and θ_{Total}, which were averaged by considering the last 5 ns of the production runs. The value of θ_{Total} was calculated using the Widom insertion method.[29,30]

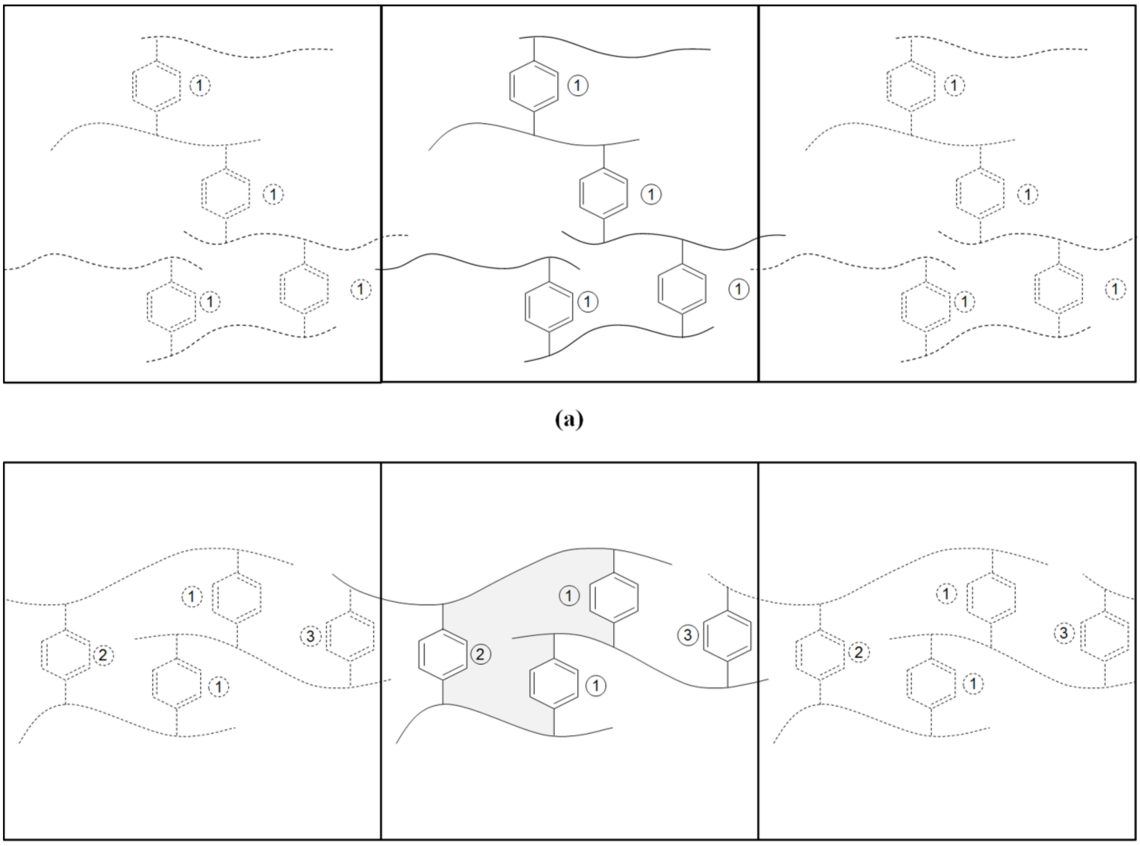

(a)

(b)

Figure 6.7. (a) Simple crosslinks in microstructures generated using the HGA method. The topology of crosslinks located at both the own simulation box (center) and its images (left and right) are identical, being labelled as 1. Simple crosslinks are also obtained using the CGA method. (b) Super- and inter-crosslinks in microstructures generated using the CGA method. Super-crosslinks, which are formed by two more crosslinks (in the image: 2 crosslinks with label 1 and one crosslink with label 2) closing a loop, define a cyclic topology (in the image: perimeter of the grey area). Inter-crosslinks (labelled as 3) connects polystyrene fragments located at the own simulation box (center) and its image (left and right).

The apparent density decreases with increasing N_{scl} while, in opposition, the porosity increases with N_{scl}. Comparison of the ρ_a values calculated for CGA-N_{scl}/0 microstructures with the experimental measure[18] (ρ_a= 0.97 g/cm^3) indicates an excellent agreement for CGA-2/0 (ρ_a= 0.97 g/cm^3) and a significant underestimation for CGA-34/0 (ρ_a= 0.77 g/cm^3). Nevertheless, the porosity predicted for CGA-2/0 ($\theta_{Total} \approx 26$ %) is slightly lower than the experimental value (θ_{Total} = 31.7%). From the theoretically estimated values of ρ_a and θ_{Total}, it is possible to compute the pore volume per mass of resin, V_{pore} (which was determined from expression 6.1) and the skeletal density ρ_s (Equation 6.2). Both values are also gathered in Table 6.2.

$$\theta_{\text{Total}} = \frac{V_{pore}}{V_{pore} + 1/\rho_s} \tag{6.1}$$

$$\rho_s = \frac{\rho_a}{(1-\theta_{Total})} \tag{6.2}$$

The experimental value of V_{pore}, estimated by nitrogen adsorption at low temperature (Table 6.1) is 0.328 cm^3/g. As it can be seen in Table 6.2, theoretical estimations of V_{pore} were 0.258 cm^3/g for CGA-2/0 increasing to 0.519 cm^3/g for CGA-34/0. Consideration of inter-crosslinks in the topology of the microstructures leads to similar results. Thus, the ρ_a calculated for CGA-14/2 (0.96 g/cm^3) agrees with the experimental measure while V_{pore} and the porosity are slightly underestimated by the theoretical model (V_{pore}= 0.271 cm^3/g and θ_{Total} = 25.7%).

Table 6.2. Characteristics and properties of selected microstructures generated using the CGA strategy and relaxed using MD. Properties were averaged considering the snapshots recorded during the last 5 ns of the MD relaxation run.

Label [a]	N_{scl} [b]	N_{inter} [c]	N_{Sulf} [d]	ρ_a [g/cm^3][e]	θ_{Total} [%][f]	V_{pore} [cm^3/g][g]	ρ_s [g/cm^3][h]
CGA-0/0	0	0	2111	1.02	18	0.176	1.24
CGA-2/0	2	0	2116	0.97	25	0.258	1.29
CGA-8/0	8	0	2110	0.94	25	0.266	1.25
CGA-16/0	16	0	2109	0.92	28	0.304	1.28
CGA-28/0	28	0	2112	0.82	35	0.427	1.26
CGA-34/0	34	0	2122	0.77	40	0.519	1.28
CGA-14/2	14	2	2120	0.96	26	0.271	1.30
CGA-36/1	36	1	2122	0.83	35	0.422	1.28

[a] The code used to identify the microestructures corresponds to CGA-N_{scl}/N_{inter}.
[b] Number of super-crosslinks.
[c] Number of inter -crosslinks.
[d] Number of sulfonic acid groups.
[e] Apparent density.
[f] Porosity calculated using the Widom insertion method.
[g] Pore volume estimated from Equation 6.1.
[h] Skeletal density estimated from Equation 6.2.

The overall of these results suggest that there is no simple direct correlation between the topology, the density and the distribution of the pores in the resin. In spite of this, the agreement between the ρ_a, θ_{Total} and V_{pore} estimations calculated for the CGA-14/2 microstructure and the experimental values indicates that the coexistence of conventional, super- and inter-crosslinks provides a reasonable microscopic description of highly crosslinked P(S-DVB) resins. On the other hand, as is evidenced in Figure 6.6, the MD trajectory of CGA-14/2 microstructure was enlarged to 66 ns. The variation of the density in the last 40 ns was found to be lower than 0.7%, corroborating that microstructures are completely relaxed after 30 ns of MD.

6.4.2. Structural properties

Although results discussed in previous sub-section reflected that the relaxed CGA-14/2 is the model that best reproduces the experimental density, pore volume and porosity, the structural analyses discussed in this sub-section have been focused no only on such reliable model but also on understanding the effect of super- and intercrosslinks on structural properties. Figure 6.9 compares the distribution of the pair of backbone dihedral angles (ξ_1 and ξ_2 in Figure 6.8) just after CGA generation, at the beginning of the relaxation process (5 ns MD) and the end of the relaxation (~30 or ~60 ns MD) for CGA-0/0, CGA-8/0, CGA-16/0, CGA-34/0, CGA-14/2 and CGA-36/1 microstructures. Analysis of the results indicates that, despite microstructures were generated following independent processes, the distribution of the dihedral angles (ξ_1,ξ_2) before density relaxation does not reflect drastic differences among them. After 5 ns of NPT-MD relaxation, the initial dihedral distributions experience important variations that are essentially provoked by the remarkable dominance of the (ξ_1,ξ_2) = (+150º,-150º) pair. Thus, the population of the latter (ξ_1,ξ_2) pair increases from 26-29% in the generated microstructures to 43-48% in the microstructures submitted to 5 ns of MD relaxation, this increment inducing significant variations in the rest of (ξ_1,ξ_2) pairs. Other (ξ_1,ξ_2) pairs with significant populations are the (+30º,+90º) and (-30º,-90º), even though their populations decrease from 21-22% to 15-19% when the generated structures are relaxed using 5 ns of MD. Enlargement of the MD simulations to ~30 ns or even more (i.e. 66 ns for CGA-14/2) only provokes very small variations (≤ 3%) in the populations. The overall of the results displayed in Figure 6.9 indicates that super- and inter-crosslinks does not affect the local atomic order of the polymeric chains in the resin, which is defined by the backbone dihedral angles.

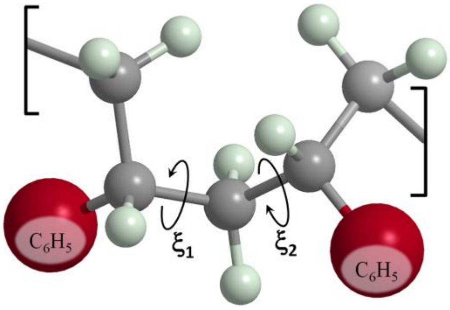

Figure 6.8. Pair of backbone dihedral angles (ξ_1 and ξ_2)

Figure 6.10, which represents the temporal evolution of the distribution of the ξ_1 and ξ_2 dihedral angles along the first 30 ns of simulation, indicates that the conformational relaxation occurs in only ~2 ns for CGA-14/2. After the initial re-arrangement, no other significant conformational change occurs during the simulation, populations remaining practically constants along the whole trajectory. Inspection of such temporal evolution for the other models (not shown) indicates that this relaxation process occurs before 5 ns in all cases, 2-3 ns being the most frequent interval.

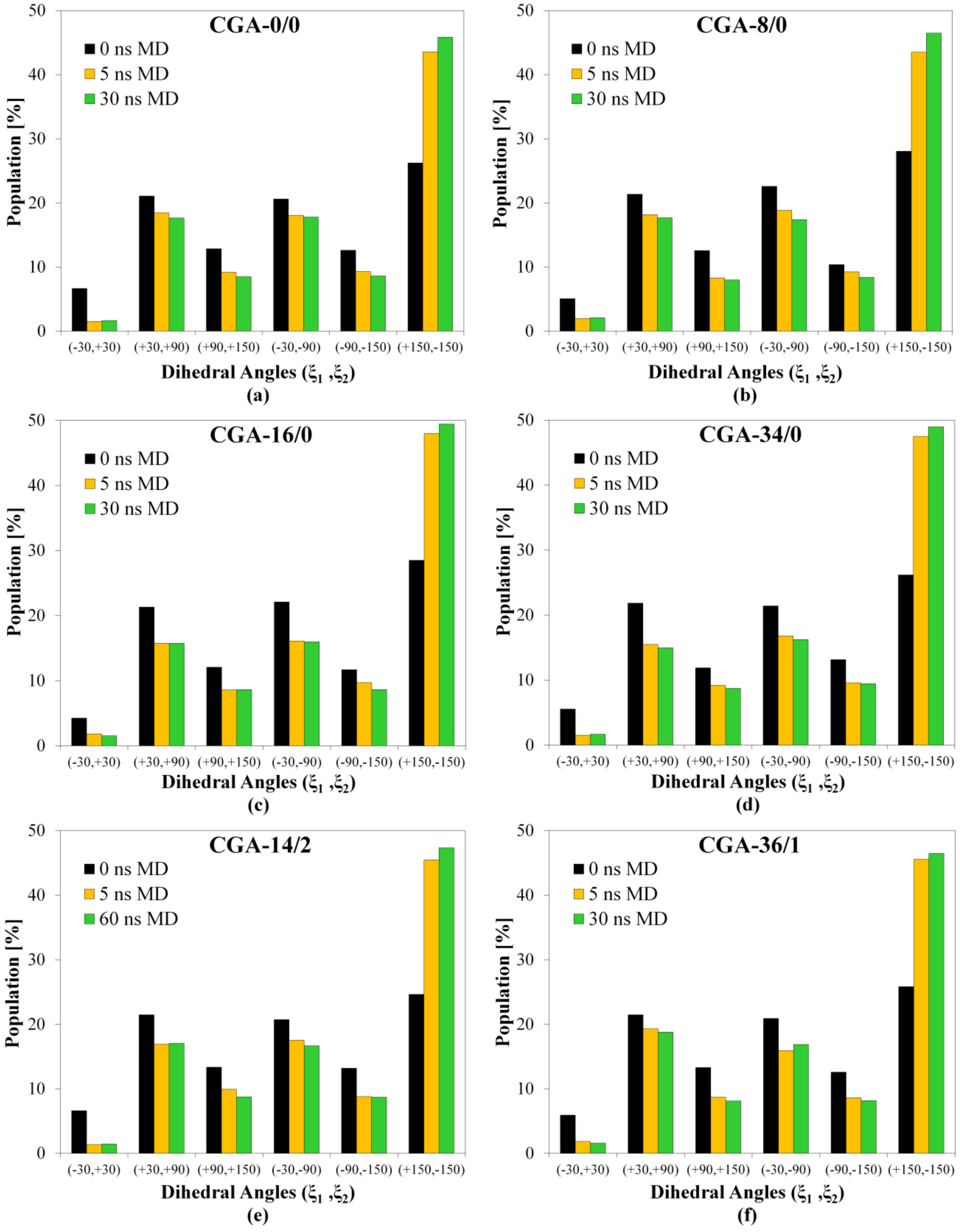

Figure 6.9. Distribution of the pair of backbone dihedral angles (ξ_1,ξ_2) (see Figure 6.8) for selected microstructures: (a)-CGA-0/0, (b) CGA-8/0, (c) CGA-16/0, (d) CGA-34/0, (e) CGA-14/2 and (f) CGA-36/1. For each case, distributions are displayed for the microstructures obtained after generation (black), after 5 ns MD relaxation (orange) and after complete MD relaxation (green).

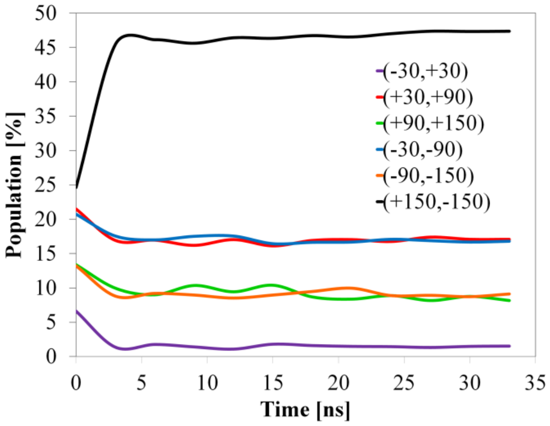

Figure 6.10. Temporal evolution of the distribution of the ξ_1 and ξ_2 dihedral angles for CGA-14/2.

In spite of topology of P(S-DVB) does not affect the short-range atomic order, the remarkable influence of N_{scl} and N_{inter} in ρ_a, θ_{Total} and V_{pore} is expected to be reflected in the medium- and long-range structural properties. Figure 6.11a and Figure 6.11b display the radial distribution function between backbone carbon atom pairs, g_{cb}-$_{cb}(r_{ij})$, for selected generated microstructures before and after MD relaxation, respectively. For all profiles the first and second sharp peaks corresponds to the C–C bond length and ∠ C–C–C bond angle, respectively. Both the third and fourth peak, which are separated by only 0.6 Å, capture the different conformational states associated to the C–C–C–C dihedral angles. These peaks show small differences between the generated microstructures (Figure 6.11a) while they are practically identical for all MD relaxed microstructures (Figure 6.11b). This corroborates the small influence of the topology in the local atomic order at the backbone discussed above. After those four peaks, the profiles displayed in Figure 6.11 present some differences, indicating that N_{scl} and N_{inter} affect the medium- and long-range order of the backbone carbon atoms. These results evidence that super- and inter-crosslinks affect the relative orientation of the repeat units located at the same segment but separated by more than two units and the relative orientation between units located at different segments, which in fact are crucial for the satisfactory description of the physical properties of the resin (i.e. distribution and size of the pores).

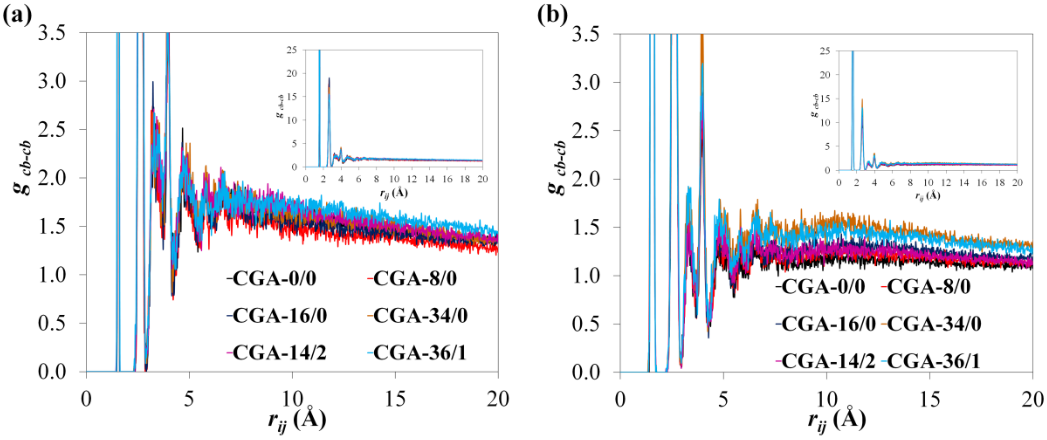

Figure 6.11. Radial distribution functions of backbone carbon···backbone carbon atom pairs for selected microstructures (a) before and (b) after MD relaxation.

In order to evaluate the effect of the relaxation at large distances, the internal distances (*R*) between pairs of repeat units separated by *L* repeat units[31] was calculated for the CGA-14/2 model using the geometric centers of the aromatic ring contained in each repeat unit. Figure 6.12 compares the profiles obtained for the microstructures obtained after generation and after 66 ns of MD. Results reveal differences at large *L* values, which should be attributed to the influence of the MD relaxation on the polymer network. However, comparison of the frequency distribution of the internal distances corresponding to the generated and MD relaxed microstructures for *L*= 5, 10 and 50 (see Figure 6.13) shows that not significant differences can be observed between the structures before and after relaxation.

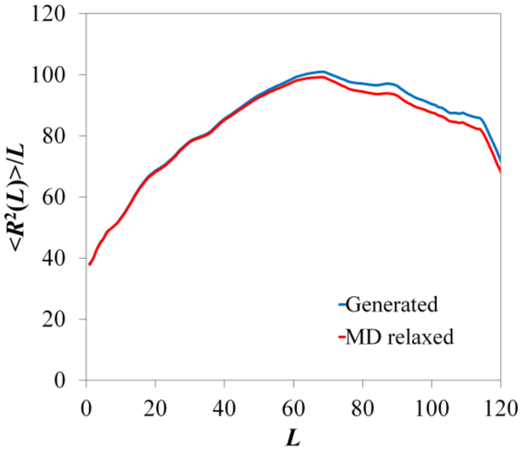

Figure 6.12.(a) Internal distance distribution for the generated and MD relaxed microstructures of CGA-14/2. The internal distance, which refers to the distance between repeat units separated by *L* repeat units, was calculated using the geometric centers of the aromatic ring contained in each repeat unit.

Results discussed in this sub-section and in the previous one reveal the importance of the super-crosslinks topology in the properties (i.e. density, porosity and structures) of highly cross-linked resins. Thus, although regular crosslinks define the local backbone structure, super-crosslinks confer rigidity and loop architecture. Furthermore, the existence of super-crosslinks affects the distribution of the sulfonic groups (see below). It should be noted that the microscopic information derived from this work can be used to improve the performance of cross-linked polymeric materials, especially in the field of catalysis, by tailoring the topology of super-crosslinks.

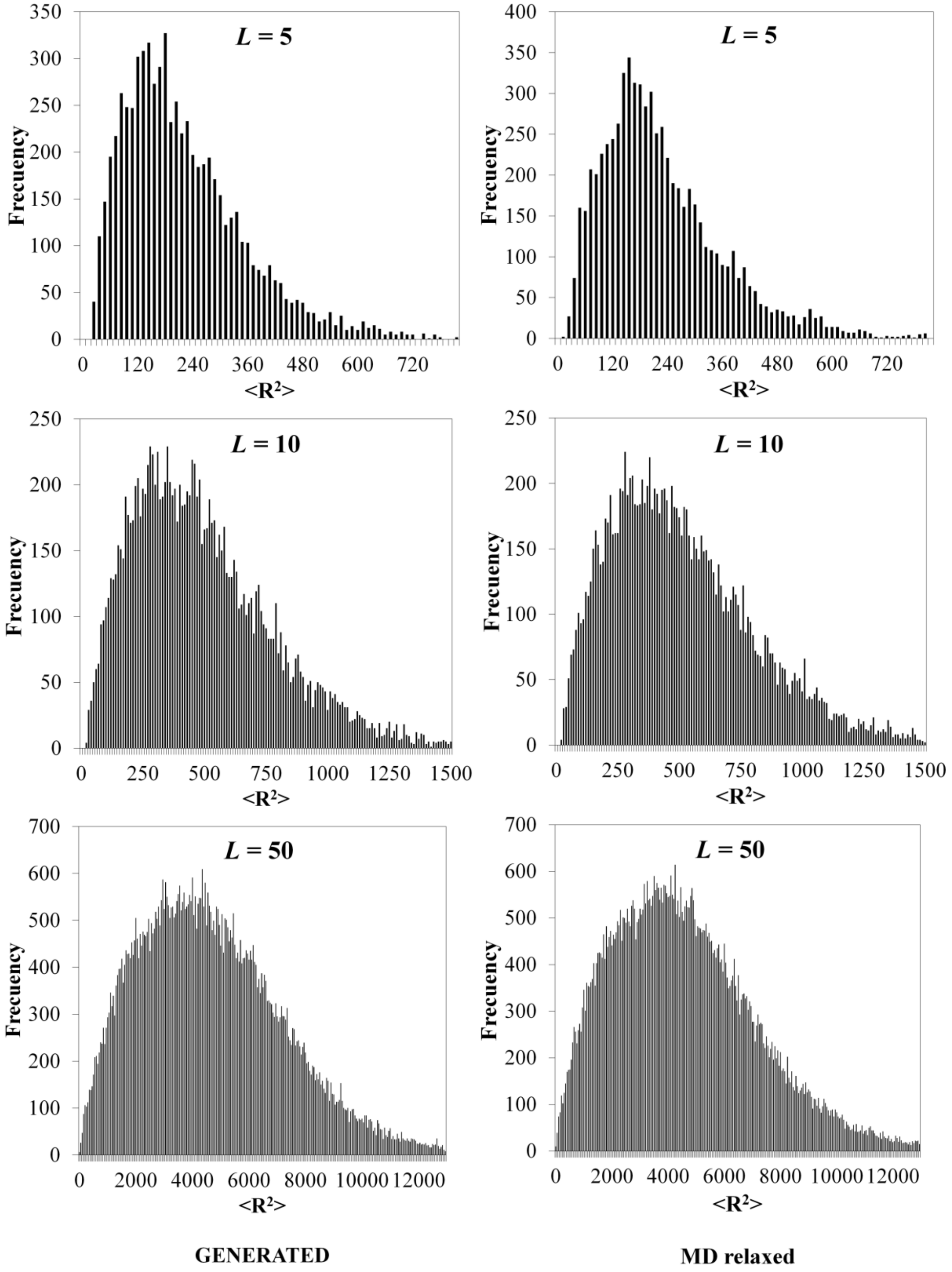

Figure 6.13. Frequencies of the internal distance distributions considering *L*= 5, 10 and 50 for the generated (left) and MD relaxed (right) microstructures of CGA-14/2.

6.4.3. Distribution of sulfonic groups

In order to ascertain the influence of N_{scl} and N_{inter} in the distribution of the sulfonic groups, the simulation boxes used to represent generated and relaxed CGA microstructures were divided into 1000 identical cells. Both the sulfonation ratio, which was defined as the ratio between the number of sulfonic groups and the total number of atoms per cell) and the local apparent density were calculated for each of these cells. After this, cells were ranked following

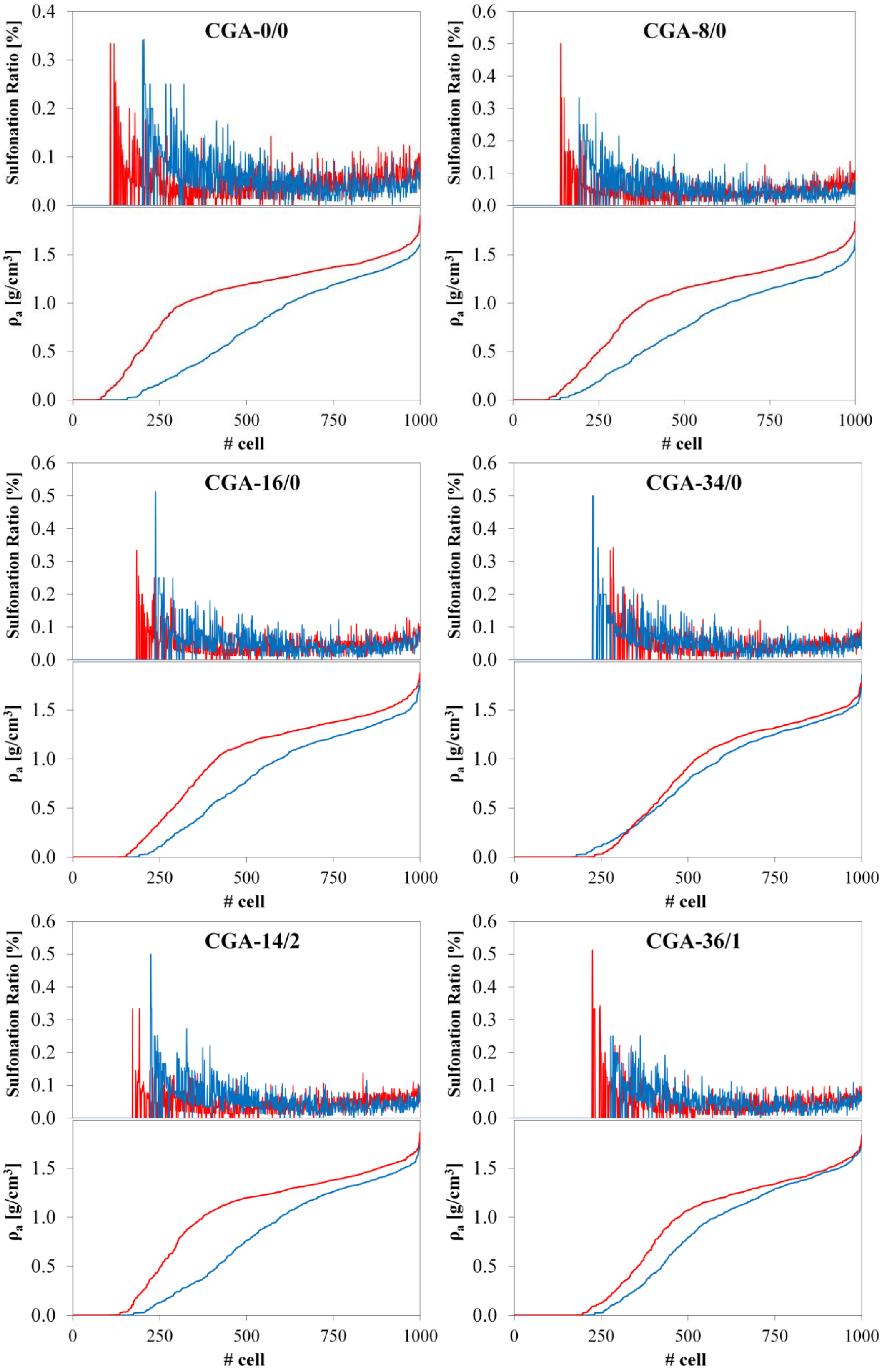

Figure 6.14. Local sulfonation ratio and local apparent density for the 1000 cells in which each microstructure was divided for CGA-0/0, CGA-8/0, CGA-16/0, CGA-34/0, CGA-14/2 and CGA-36/1. Cells were ranked following a growing local density order. Profiles for microstructures before (blue) and after complete MD relaxation (red) are displayed.

an increasing local apparent density criterion. Figure 6.14 displays the sulfonation ratio and the apparent density of the ranked cells for representative microstructures just after generation with the CGA method (blue) and after complete MD relaxation (red).

Results displayed in Figure 6.14 indicate that sulfonic groups tend to be located at the regions of lower density in all generated and relaxed microstructures, independently of N_{scl} and N_{inter}. In spite of this, important changes are detected among the different microstructures. The number of cells with negligible local apparent density values and, therefore, without sulfonic groups is higher before relaxation than after relaxation in all cases with exception of CGA-34/0. On the other hand, Figure 6.14 reveals that MD relaxation provokes a change in the slope of the local density profile in all cases. This change affects the number of cells (i.e. volumetric fraction) with local apparent densities close to the average ones (Table 6.2), which is noticeably higher for the relaxed microstructures. According to these observations, representations provided in Figure 6.14 indicate that, in general, MD relaxation produces a homogenization of the system in terms of both sulfonic groups and local density distributions.

However, detailed analyses of these results evidence that the above mentioned homogenization affects the volume of the pores in a different way (i.e. super-and inter-crosslinks enable a heterogeneous distribution of the pores). This feature is evidenced by comparing the number of void cells (with negligible local apparent density values) before and after MD relaxation. For example, in absence of super-crosslinks (CGA-0/0) the number of void cells in the generated microstructure is 139, whereas in the relaxed microstructure the number of void cells is 70. This evidences that an important fraction (≈ 50 %) of the initial pores undergoes a re-distribution of the mass and, therefore, of the sulfonic groups upon relaxation. In contrast, after incorporation of 8 super-crosslinks (CGA-8/0), the number of void cells in the generated microstructure is 120 whereas in the relaxed microstructure is 92. In this case, super-crosslinks preserve the volume of some pores and the homogenization induced by the relaxation process only affects to some regions. This “heterogeneous homogenization” also affects the distribution of sulfonic groups, the sulfonation ratio experiencing higher fluctuations in CGA-8/0 than in CGA-0/0 after MD relaxation. For the CGA-16/0 the results are similar to that of CGA-8/0 with 175 void cells before relaxation and 131 after relaxation. Finally, CGA-34/0 shows an opposite behavior with a larger number of void cells in the relaxed microstructure (210) than in the generated microstructure (164). This behavior is probably due to the low average apparent density of the relaxed microstructure (0.77 g/cm^3). For the structures that present both super-crosslink and inter-crosslinks similar features are observed: the trend shown by CGA-14/2 is similar to those described for CGA-16/0 whereas in CGA-36/1 the number of void cell that undergoes a re-distribution of the mass during the relaxation process is lower (≈ 17%) due to the higher number of super-crosslinks which preserve the volume of the pores.

6.4.4. Relative orientation of the phenyl rings

The interaction between aromatic phenyl rings is normally described in terms of center of mass –center of mass partial radial distribution function, $g_{p\text{-}p}(r_{ij})$. Figures 6.15a and b plot the $g_{p\text{-}p}(r_{ij})$functions calculated for different P(S-DVB) generated microstructures before and after MD relaxation, respectively. As it can be seen, peaks centered at around ~3.7 and ~7 Å appear in all cases, evidencing the presence of two favored orientations between the phenyl rings of P(S-DVB). The peak at ~3.7 Å, which is considerably less intense than that at ~7 Å, has been attributed to the interactions in which the aromatic rings adopt a co-facial disposition. The frequency of this kind of interaction is practically independent of the number of crosslinks and super-crosslinks in the generated microstructures (Figure 6.15a). However, after MD relaxation the abundance of co-facial interactions increases with the number of crosslinks, as is reflected by the enhancement in the height of the peak in Figure 6.15b.

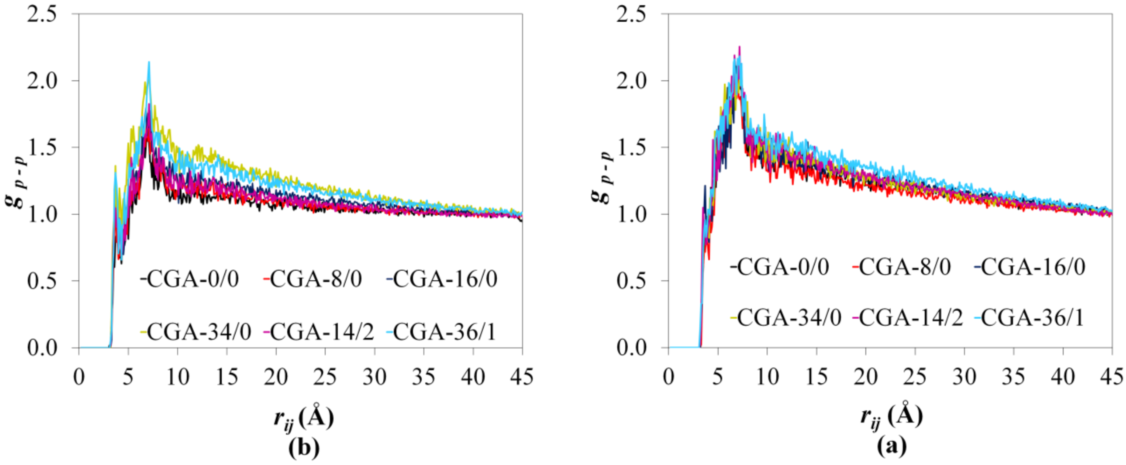

(b) **(a)**

Figure 6.15. Radial distribution functions of phenyl center of masses···phenyl center of masses pairs for selected microstructures (a) before and (b) after MD relaxation.

On the other hand, the peak at ~7 Å has been associated to the T-shape disposition adopted by the two aromatic rings. This kind of interaction is considerably more frequent than that in which the two rings are co-facial. As occurred for co-facial interactions, the abundance of T-shape interactions seems to be relatively independent of the number of crosslinks for generated microstructures, whereas it increases with the number of crosslinks for relaxed microstructures. The small and remarkable influence of MD relaxation on the peaks at ~3.7 and ~7 Å, respectively, is clearly reflected in Figure 6.16, which compares the $g_{p\text{-}p}(r_{ij})$functions obtained for CGA- 14/2 microstructures before and after relaxation.

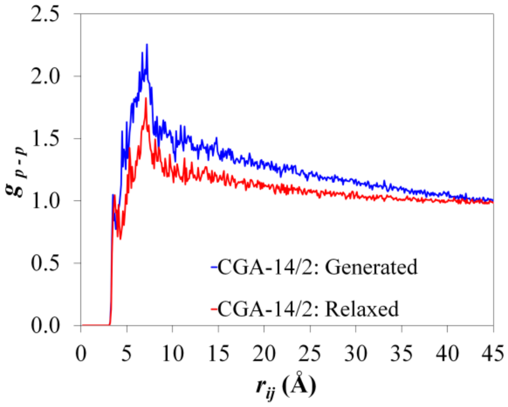

Figure 6.16. Radial distribution functions of phenyl center of masses···phenyl center for CGA-14/2 microstructures before and after relaxation.

In order to get more insights about the influence of N_{scl} and N_{inter} in the relative orientation of close phenyl rings, all pairs of phenyl rings with the centers of masses separated by a distance lower than 10 Å (d_{p-p}) were selected and the angle defined by their corresponding planes (θ_{p-p}) subsequently determined. The variation of d_{p-p} against θ_{p-p} (Figure 6.17) indicates that the two phenyl rings prefer a co-facial disposition when they are separated by less than ~ 5 Å, both parallel and antiparallel configurations (i.e. $\theta_{p-p} \approx 0^o$ and 180º, respectively) being detected. However, a homogeneous distribution of θ_{p-p} is obtained for d_{p-p} values higher than ~5 Å, indicating that co-facial, T-shaped ($\theta_{p-p} \approx 90^o$) and tilted or herringbone (θ_{p-p} comprised between 30º and 60º as well as between 120º and 150º) inter-ring orientations coexist in the same microstructure. Moreover, these results, which are very similar before and after MD relaxation, are practically independent of N_{scl} and N_{inter}. The latter features are reflected in Figure 6.17, which compares the results obtained for CGA-0/0, CGA-34/0 and CGA-16/2 generated and relaxed microstructures.

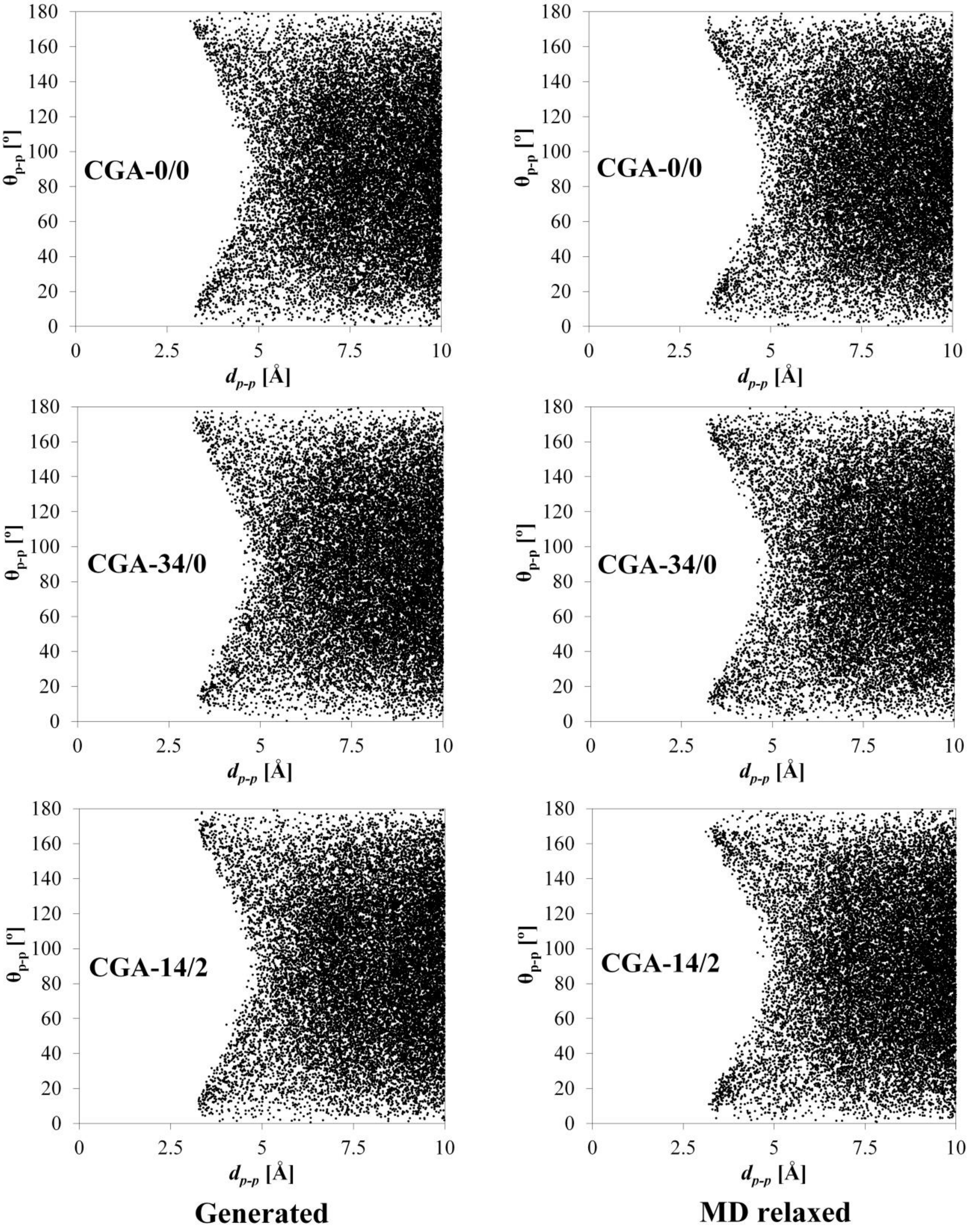

Figure 6.17. Variation of d_{p-p} against θ_{p-p} for CGA-0/0, CGA-34/0 and CGA-14/2 microstructures before (left) and after MD relaxation (right).

6.5. Conclusions

Highly crosslinked sulfonated P(S-DVB) resins were modeled using a generation-relaxation strategy. Two different approaches were used for the generation of initial microstructures, which were subsequently relaxed using MD simulations. The simplest strategy, called HGA, is based on the generation of homogeneous polymeric matrices constituted by short chains of identical lengths that are connected through conventional crosslinks. This homogeneous topology, which is maintained after MD relaxation, leads to an overestimation of the density and to an underestimation of the porosity with respect to the experimental values. On the other hand, the CGA strategy combines two different algorithms that allow the heterogeneous growing and branching of the chains. The combination enables the formation of complex topological features through super- and inter-crosslinks, which are essential for the satisfactory description of the density, porosity and pore volume of the studied P(S-DVB) resins.

Although super-crosslinks do not affect local structural properties, the topological loops associated to them largely affect the distribution of the sulfonic group, the local distribution of the density, the medium- and long-range structural properties, and the frequency of co-facial and T-shape disposition adopted by two aromatic rings. Thus, constraints associated to the topology of super-crosslinks are responsible of preserving the pore volume of the generated microstructures upon MD relaxation and, consequently, of the porosity typically associated to this kind of polymeric matrices.

Nomenclature

Notation

b	Bond length
c	Charges scaling factor
d_{pore}	Pore diameter
$d_{p\text{-}p}$	Distance between two phenyl rings center of mass
$g_{cb\text{-}cb}$	radial distribution function between backbone carbon atom pairs
$g_{p\text{-}p}$	partial radial distribution function between aromatics phenyl rings
k	Number of steps of enlargement-crosslinking (in the CGA)
k_b	Bond force constant
k_θ	Angle force constant
k_φ	Dihedral angle force constant
L	Repeat units
m	Monomers per chain in the HGA
n	Dihedral multiplicity
N_{DVB}	Number of divinylbenzene units
N_{inter}	Number of inter-crosslinks
NPT	Isobaric-isothermal ensemble
N_S	Number of styrene units
N_{scl}	Number of super-crosslinks
N_{Sulf}	Number of sulfonic groups
NVT	Canonical ensemble
q_i	Partial atomic charge of atom i
r	Minimal number of sulfonated styrene units (in the CGA)
R	Internal distances between pairs of repeat units separated by L repeat units
r_{ij}	Distance separating atoms i and j
s	Number of trials for the transformation of styrene into divinylstyrene (in the CGA)
V_{pore}	Pore volume determined by adsorption-desorption of N_2 at 77 K

Greek symbols

ρ_a	Apparent density
ρ_s	Skeletal density
ϵ_{ij}	Depth of the potential well for the interaction of atoms i and j

ε_0	Electric constant
ε_r	Effective dielectric constant
θ	Bond angle
θ_{Total}	Porosity
θ_{p-p}	Angle defined by the planes of two phenyl rings
ξ_1 and ξ_2	Pair of backbone dihedral angles
σ_{ij}	Distance between atoms *i* and *j* where the Lennard-Jones potential is exactly zero
φ	Dihedral angle

Abbreviations

CGA	Combined Growing Approach
DETA	Di-ethylene tri-amine
DGEBA	Bisphenol A diglycidyl ether
DGEBF	Di-glycidyl ether of bisphenol F
GAFF	General Amber Force Field
HGA	Homogeneous Generation Approach
MD	Molecular dynamics
MM	Molecular Mechanics
P(S-DVB)	Poly(styrene-divinylbenzene)
RESP	
TCE	Tris-(cinnamoyloxymethyl)-ethane

References

[1] Bandyopadhyay, A.; Odegard, G. M. Molecular modeling of crosslink distribution in epoxy polymers. *Model. Simul. Mater. Sci. Eng*. **2012**, *20*, 045018.

[2] Koo, B.; Liu, Y.; Zou, J.; Chattopadhyay, A.; Dai, L. L. Study of glass transition temperature (T_g) of novel stress-sensitive composites using molecular dynamic simulation. *Model. Simul. Mater. Sci. Eng*. **2014**, *22*, 065018.

[3] Jang, C.; Lacy, T. E.; Gwaltney, S. R.; Toghiani, H.; Pittman, C. U. Jr. Relative reactivity volume criterion for cross-linking: Application to vinyl ester resin molecular dynamics simulations. *Macromolecules* **2012**, *45*, 4876-4885.

[4] Soni, N. J.; Lin, P.-H.; Khare, R. Effect of cross-linker length on the thermal and volumetric properties of cross-linked epoxy networks: A molecular simulation study. *Polymer* **2012**, *53*, 1015-1019.

[5] Khare, K. S.; Khare, R. Directed diffusion approach for preparing atomistic models of crosslinked epoxy for use in molecular simulations. *Macromol. Theory Simul*. **2012**, *21*, 322-327.

[6] Sacristan-Bermejo, J.; Mijangos-Ugarte, C. Influence of cross-linking density on the glass transition and structure of chemically cross-linked PVA: A molecular dynamics study. *Macromol. Theory Simul*. **2009**, *18*, 317-327.

[7] Alemán, C.; Karayiannis, N. Ch.; Curcó, D.; Foteinopoulou, K.; Laso, M. Computer simulations of amorphous polymers: From quantum mechanical calculations to mesoscopic models. *J. Mol. Struct. (Theochem.)* **2009**, *898*, 62–72.

[8] Doherty, D. C.; Holmes, B. N.; Leung, P.; Ross, R. B. Polymerization molecular dynamics simulations. I. Cross-linked atomistic models for poly(methacrylate) networks. *Comput. Theor. Polym. Sci*. **1998**, *8*, 169-178.

[9] Yarovsky, I.; Evans, E. Computer simulation of structure and properties of crosslinked polymers: applications to epoxy resins. *Polymer* **2002**, *43*, 963-969.

[10] Gou, J.; Minaie, B.; Wang, B.; Liang, Z.; Zhang, C. Computational and experimental study of interfacial bonding of single-walled nanotube reinforced composites. *Comput. Mater. Sci*. **2004**, *31*, 225-236.

[11] Fan, H. B.; Yuen, M. M. F. Material properties of the cross-linked epoxy resin compound predicted by molecular dynamics simulation. *Polymer* **2007**, *48*, 2174-2178.

[12] Accelrys Inc., San Diego, CA.

[13] Wu, C.; Xu, W. Atomistic molecular modelling of crosslinked epoxy resin. *Polymer* **2006**, *47*, 6004-6009.

[14] Wu, C.; Xu, W. Atomistic simulation study of absorbed water influence on structure and properties of crosslinked epoxy resin. *Polymer* **2007**, *48*, 5440-5448.

[15] Heine, D. R.; Grest, G. S.; Lorenz, C. D.; Tsige, M.; Stevens, M. J. Atomistic simulations of end-linked poly(dimethylsiloxane) networks: structure and relaxation. *Macromolecules* **2004**, *37*, 3857-3864.

[16] Varshney, V.; Patnaik, S. S.; Roy, A. K.; Farmer, B. L. A molecular dynamics study of epoxy-based networks:cross-linking procedure and prediction of molecular and material properties. *Macromolecules* **2008**, *41*, 6837-6842.

[17] Kunin, R.; Meitzner, E. F.; Oline, J. A.; Fisher, S. A.; Frisch, N. Characterization of Amberlyst 15. *Ind. Eng. Chem. Prod. Res. Dev*. **1962**, *1*, 140-144.

[18] Casas, C.; Bringué, R.; Ramírez, E.; Iborra, M.; Tejero, J. Liquid-phase dehydration of 1-octanol, 1-hexanol and 1-pentanol to linear symmetrical ethers over ion exchange resins. *Appl. Catal., A.* **2011**, *396*, 129-139.

[19] Fisher, S.; Kunnin, R. Routine exchange capacity determinations of ion exchange resins. *J. Anal. Chem*. **1955**, *27*, 1191-1194.

[20] Berendsen, H. J. C., van der Spoel, D., van Drunen, R. GROMACS: A message-passing parallel molecular dynamics implementation. *Comp. Phys. Comm*. **1995**, *91*, 43–56.

[21] Wang, J.; Wolf, R. M.; Caldwell, J. W.; Kollman, P. A.; Case, D. A. Development and testing of a general Amber force field. *J. Comput. Chem*. **2004**, *25* (9), 1157-1174.

[22] Cieplak, P.; Cornell, W. D.; Bayly, C.; Kollman, P. A. Application of the multimolecule and multiconformational RESP methodology to biopolymers: Charge derivation for DNA, RNA, and proteins. *J. Comput. Chem.* **1995**, *16*, 1357-1377.

[23] Anisimov, V. M.; Lamoureux, G.; Vorobyov, I. V.; Huang, N.; Roux, B.; MacKerell, A. D. Determination of electrostatic parameters for a polarizable force field based on the classical Drude oscillator. *J. Chem. Theory Comput*. **2005**, *1*, 153-168.

[24] Vorobyov, I.; Anisimov, V. M.; Greene, S.; Venable, R. M.; Moser, A.; Pastor, R. W.; MacKerell, A. D. Additive and classical drude polarizable force fields for linear and cyclic ethers. *J. Chem. Theory Comput*. **2007**, *3* (3), 1120-1133.

[25] Toukmaji, A.; Sagui, C.; Board, J.; Darden, T. Efficient particle-mesh Ewald based approach to fixed and induced dipolar interactions *J. Chem. Phys*. **2000**, *113*, 10913-10927.

[26] Hoover, W. G. Canonical dynamics: Equilibrium phase-space distributions. *Phys. Rev. A.* **1985**, *31*, 1695-1697.

[27] Nosé, S. A unified formulation of the constant temperature molecular dynamics methods. *J. Chem. Phys*. **1984**, *81*, 511-519.

[28] Parrinello, M.; Rahman, A. Polymorphic transitions in single crystals: A new molecular dynamics method. *J. Appl. Phys*. **1981**, *52*, 7182-7190.

[29] Widom, B. Potential-distribution theory and the statistical mechanics of fluids. *J. Phys. Chem.* **1982**, *86* (6), 869-872.

[30] Widom, B. Some Topics in the Theory of Fluids. *J. Chem. Phys*. **1963**, *39*, 2808-2812.

[31] Harmandaris, V. A.; Adhikari, N. P.; van der Vegt, N. F. A.; Kremer, K. Hierarchical modeling of polystyrene: from atomistic to coarse-grained simulations. *Macromolecules* **2006**, *39*, 6708-6719.

7. 1-BUTANOL ABSORPTION IN P(S-DVB) RESINS[*][†]

---

[*] Results presented in this chapter have been submitted in:

Pérez-Maciá, M. A.; Curcó, D.; Bringué, R.; Iborra, M.; Rodríguez-Ropero, F.; van der Vegt, N. F. A.; Aleman, C. 1-Butanol absorption in poly(styrene-divinylbenzene) ion exchange resins for catalysis. *Soft Matter.* (Status: submitted and resubmitted).

[†] Part of the experiments presented in this chapter was carried out in the *Computational Physical Chemistry Group, Technische Universität Darmstadt*, under the supervision of Prof. Dr. Nico van der Vegt.

7.1. Introduction

In most applications, ion-exchange resins operate in a swollen state. As it has been said in several occasions along this text, the pore structure of P(S-DVB) ion exchange resins (and consequently their catalytic performance, activity and selectivity) is greatly dependent upon the swelling characteristics of their polymeric network.[1] Swelling creates free spaces within the resin and allows ready access and exploitation of the inner part of the network in chemical reactions. Thus, in order to comprehend the catalytic performance of ion exchange catalysts it is essential to understand their swelling behavior and structural properties in the reaction medium.

Several physico-chemical techniques were used to characterize swollen polymers during the last decade of the 20th century. However, these techniques provided a rough estimate of the accessibility and the molecular mobility into swollen resins. A valuable review of these techniques can be found in Corain et al.[1] During the last years, several works have been published related with the characterization of the swollen morphology of polymers by inverse steric exclusion chromatography (ISEC).[2-5] This method is based on measurements of elution volumes of standard solutes with known molecular sizes, by using a chromatographic column filled with the investigated swollen polymer. Then, by means of a suitable mathematical treatment of these elution volumes (model) it is possible to obtain information about the pore volume distribution of the studied material.[6] Although the obtained experimental results have significantly improved the understanding of the character of the reaction environment inside swollen polymers, a full knowledge of the details of ion exchange catalysts at the molecular level is still lacking. Furthermore, ISEC cannot be used for assessing the morphology of incompletely swollen polymers or in solvents like alcohols, where the interaction between the eluted dimensional standards and the swollen polymer is not exclusively based on steric exclusion.[3]

In Chapter 6, the relationship between the topology of highly crosslinked P(S-DVB) ion-exchange resins and their structural properties in dried state was studied by means of molecular dynamics (MD) simulations. The aim of this chapter is to study the swelling behavior of a sulfonated P(S-DVB) resin in 1-butanol by means of MD simulations and offer a contribution to the understanding of the molecular details of the structure of swollen P(S-DVB).

7.2. Methods

7.2.1. Computational methods

As stated in the previous chapter, we produced several microstructures with different topological features for a P(S-DVB) ion-exchange resin with characteristics (DVB content and acid capacity) similar to the commercial resin Amberlyst 15 (a monosulfonated, highly crosslinked macroreticular catalyst) using two stochastic algorithms developed to that end (a detailed description of these algorithms can be found in Section 6.2). From this previous work, the model that provided the best microscopic description of the resin in dry state (apparent density, porosity and pore volume) was selected in order to carry out the swelling study. This model (denoted as CGA-14/2 in Chapter 6) was composed by 2141 and 358 monomers of styrene and divinylbenzene respectively. 2120 styrene monomers were sulfonated (steric effects precluded the sulfonation of all the styrene units) at the *meta* or, preferentially, *para* positions of the aromatic ring (the *ortho* substitution is sterically hindered). Beside “simple-crosslinks” (a monomer of DVB connecting two polymer chains), the selected model also presented 14 “super-crosslinks” (internal loops that appears when one or more simple-crosslinks give rise to a closed polymer chain) and 2 “inter-crosslinks” (a DVB monomer connecting two polymer chains, one pertaining to the macromolecule and the other to its own periodic image). It should be pointed out that these topological characteristics were found to be essential to reproduce satisfactorily the experimental values of relevant morphological parameters (apparent density, porosity and pore volume) in dry state.

1-butanol molecules were randomly introduced at sterically accessible positions of the equilibrated dry resin. Seven resin/solvent systems, which only differ in the amount of 1-butanol (10%, 15%, 20%, 26.3%, 30%, 40% and 50% w/w), were considered in this work.

All MD simulations were performed using the GROMACS 4.6.5 program.[7-9] The energy was calculated by means of the same force-field expression used in Chapter 6 (see Section 6.3, Equation 2.6). Force-field parameters were taken from the General Amber Force Field (GAFF)[10] for both resin and 1-butanol. Atomic charges for the sulfonated P(S-DVB) resin were taken from the previous chapter (see Figure 6.4). Atomic charges for 1-butanol were taken from reference 11 and scaled (c = 0.71) to reflect that the polarization in condensed media is smaller than in the gas-phase.[12,13]

Before MD trajectories, the initial structures of polymer network and absorbed 1-butanol were equilibrated using the following strategy: (1) 10000 steps of energy minimization using the steepest descent algorithm were performed to relax conformational and structural tensions; (2) next, 500 ps of NVT-MD at 300K were performed for all the microstructures; (3) afterwards, 500 ps of NPT-MD at 300 K and 1 bar were run. For the highest 1-butanol concentration it was necessary to integrate the Newton's equation of motion using a numerical integration step of 0.5 fs during the first 10 ps to avoid numerical instabilities.

After this equilibration strategy, NPT-MD productive trajectories were run at 300 K and 1 bar during 10 ns. Figure 7.1 shows the temporal evolution of the systems volume.

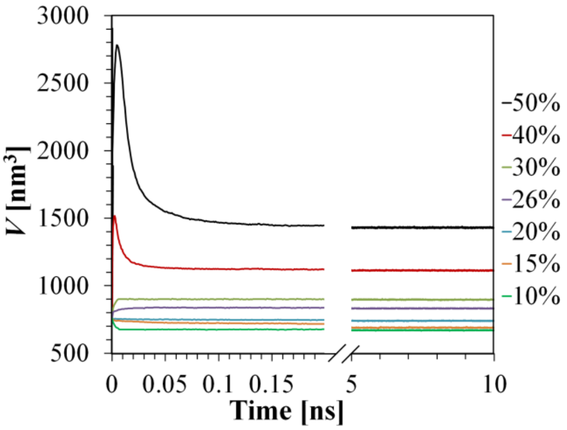

Figure 7.1. Temporal evolution of the systems volume during NPT-MD runs. All simulations beginning at V = 760 nm^3

Furthermore, a structure of pure 1-butanol system containing 821 1-butanol molecules was generated at the density of liquid 1-butanol (0.809 g/cm^3). After 1000 steps of steepest-descent minimization of the total potential energy the 1-butanol structure was equilibrated for 500 ps by MD simulation under constant NVT conditions at 300 K followed by 500 ps at constant NPT conditions (300 K and 1 bar). Finally, NPT-MD productive trajectories were run at 300 K and 1 bar during 5 ns.

In all MD simulations, periodic boundary conditions were applied using the nearest image convention. Newton's equations of motion were integrated by the leap-frog algorithm using a numerical integration step of 1fs, except in the case aforementioned. Van der Waals and electrostatic interactions were computed using an atom pair distance cut-off of 14.0 Å. Beyond such a cut-off distance, electrostatic interactions were calculated by using Particle Mesh Ewald method, with a point grid density of the reciprocal space of 1 Å^3.[14] Temperature and pressure were controlled by the Nosé-Hoover thermostat[15,16] (with a temperature time constant of 0.5 ps) and the Parrinello-Rahman barostat[17] (with a pressure time constant of 1 ps), respectively. The coordinates of all the production runs were saved every 1000 steps (1 ps).

7.2.2. Experimental methods

Particle diameter of Amberlyst 15 in dry state and swollen in 1-butanol was experimentally determined by a laser diffraction particle size analyzer (Beckman Coulter, LS 13 320). From these values, the swelling of Amberlyst 15 in 1-butanol was determined (see Table 7.1). Resin samples, previously dried at 110 ºC at 10 mbar during 24 h, were placed in 1-butanol for 2 days to assure that resins were completely swollen.

Table 7.1. Mean d_p in air and 1-butanol and volume increase with respect to air.

Mean d_p^{a} [µm]		Volume increase [%]
Air	1-butanol	1-butanol
650.1	729.1	21.1

From experimental values of resin particle diameter in dry state and swollen in 1-butanol (Table 7.1), resin skeletal density (1.416 g/cm^3, see Table 2.2) and porosity in dry state (31.9%, see Table 6.1), the estimated amount of 1-butanol absorbed by the resin Amberlyst 15 is ≈ 31% w/w.

7.3. Results

7.3.1. Thermodynamic study of 1-butanol absorption in a P(S-DVB) resin

In Section 2.4.2 the absorption of solvent molecules in polymer matrices was described from a thermodynamic standpoint. It was stated that the absorption process depends on the difference between the chemical potential of solvent molecules inside the polymer matrix ($\mu_{s,polymer}$) and the chemical potential of solvent molecules in the pure solvent system ($\mu_{s,pure}$). It was also demonstrated that the evaluation of the excess part of the chemical potential is enough to determine the absorption of solvent molecules. Several approaches to estimate the free energy change due to the process of inserting a molecule at a fixed position (i.e., the excess chemical potential) and their limitations were presented. In Section 7.3.1.1 the suitability of these approaches to study the absorption of 1-butanol in a highly crosslinked macroreticular P(S-DVB) resin is evaluated. In Section 7.3.1.2 an estimation of the absorption behavior of the P(S-DVB) resin based on simplified thermodynamic assumptions is presented.

7.3.1.1. Preliminary steps

7.3.1.1.1. Free energy perturbation. Widom's particle insertion method

As it was introduced in Section 2.4.3.1, the particle insertion method proposed by Widom[18] may be viewed as a special case of the perturbation theory, in which the addition of a single particle is handled as a one-step perturbation of the system. The Widom's method allows to estimate the excess chemical potential of a component (μ^{excess}) in a N-particles system from the total potential energy of interaction between the 'test' particle of that component placed in a random position in the simulation cell and the N particles of the system (B_{N+1}):

$$\mu^{excess} = \Delta A = -\beta^{-1}\ln\left\langle e^{-\beta B_{N+1}} \right\rangle_N \tag{7.1}$$

with:

$\beta = 1/k_BT$, where k_B is the Boltzman constant.

$$B_{N+1} = \sum_{i=1}^{N} U_{i,N+1} \tag{7.2}$$

being $U_{i,N+1}$ the potential energy of interaction between the particle N+1 and each of the other particles in the system.

The brackets $\langle ... \rangle_N$ denote the ensemble average over the original N-particle system (without the test particle).

The Widom's method was used with the aim of estimating the excess chemical potential of 1-butanol in the pure 1-butanol system and in 6 resin/1-butanol systems which only differ in the number of alcohol molecules (10%, 15%, 20%, 26.3%, 30% and 40% w/w). The construction, equilibration and production of trajectories for the different resin/1-butanol systems and the 1-butanol pure system were described in Section 7.2.1.

For all the systems, a 1-butanol "test" particle was inserted in the system snapshots stored from the corresponding MD simulations. For each insertion, the conformation of the test molecule was randomly selected from the conformations of the 1-butanol molecules in the pure alcohol system and the energies of interaction between the inserted particle and each of the N particles of the system ($U_{i,N+1}$ in Equation 7.2) were estimated as the sum of Coulomb and 6-12 Lennard-Jones potential using the *minimum-image convention* (see Section 2.4.1.2). In order to accelerate the process, after the test molecule was inserted steric overlaps with the closest atoms of the system were evaluated. For that, a cutoff distance of 2 Å was adopted. In the event that the inserted molecule presented overlapping (the distance between an atom of the inserted 1-butanol molecule and an existing atom of the system was < 2 Å), the corresponding total potential energy of interaction (B_{N+1}) was not estimated and it was assumed that it would be very high and, consequently, $e^{-\beta B_{N+1}} \approx 0$.

Specifically, 100 snapshots were considered for each system, and a test 1-butanol molecule was inserted at 10^8 random positions for each snapshot. Accordingly, 10^{10} insertions, each one with the corresponding energy evaluation, were considered for each system. This procedure was repeated 10 times (i.e., a total of 10^{11} insertions in each system). For each of these 10 series, a value of the average $\left\langle e^{-\beta B_{N+1}} \right\rangle_N$ was computed from the 10^{10} insertions and, according to the central limit theorem, it was possible to estimate the total average and the corresponding confidence interval for each system. It was observed that 10 series of insertions yielded unacceptable confidence intervals. Therefore, the number of series was increased up to 50 for the pure 1-butanol system and the resin with a 30% of 1-butanol (i.e., $5\cdot10^{11}$ insertion for each of the two systems). Table 7.2 gathers the value of ensemble average $\left\langle e^{-\beta B_{N+1}} \right\rangle_N$ for each of the studied systems as well as the confidence intervals for the pure 1-butanol system and the system with a 30% w/w of 1-butanol determined from the 50 series of insertions. As it can be seen, for the pure 1-butanol system, a reasonable confidence interval is obtained after increasing the total number of insertions up to $5 \cdot 10^{11}$. However, for the resin/1-butanol system with a 30% w/w of 1-butanol the confidence interval is still unacceptable.

Table 7.2. Results of the Widom's particle-insertion method

System	$\left\langle e^{-\beta B_{N+1}} \right\rangle_N$
Pure 1-butanol	381±71
Resin/1-butanol (10% w/w)	943094
Resin/1-butanol (15% w/w)	1438
Resin/1-butanol (20% w/w)	939
Resin/1-butanol (26.3% w/w)	581
Resin/1-butanol (30% w/w)	361±150
Resin/1-butanol (40% w/w)	505

The important uncertainty of the estimated values is attributed to an insufficient sampling. Figure 7.2 shows the probability distribution of B_{N+1} corresponding to the pure 1-butanol system and the resin/1-butanol system with a 30% w/w of 1-butanol (for the rest of systems the distribution are similar). At this point it needs to be taken into account that, due to the *acceleration process* described in the previous paragraph, an important number of insertions with high values of B_{N+1} are not included in the probability distribution of Figure 7.2. In spite of that, there is still an important number of attempted insertions of test particles that result in overlap with existing particles in the system, with B_{N+1} large and positive (as it can be seen in Figure 7.2). These insertions do not contribute significantly to the ensemble average $\left\langle e^{-\beta B_{N+1}} \right\rangle_N$, as neither do the previously discarded insertions. On the other hand, it was expected that the probability distribution of B_{N+1} had a Gaussian-like shape.[19] In Figure 7.2, one can observe that an important part of the negative tail is missing. Missing such important samples will cause significant bias in the calculated $\left\langle e^{-\beta B_{N+1}} \right\rangle_N$ and, consequently, estimates of ΔA will be inaccurate.

In conclusion, estimation of the excess chemical potential of 1-butanol in both the pure alcohol and the polymer matrix by the particle insertion method presents some difficulties. In those systems, it is very unlikely that a test particle can be successfully inserted and consequently, it will be difficult to know sufficiently well the low energy tail of the distribution resulting in inaccurate estimates of $\left\langle e^{-\beta B_{N+1}} \right\rangle_N$. Given the uncertainty regarding the number of insertions needed to achieve an acceptable sampling, the Widom's method was discarded.

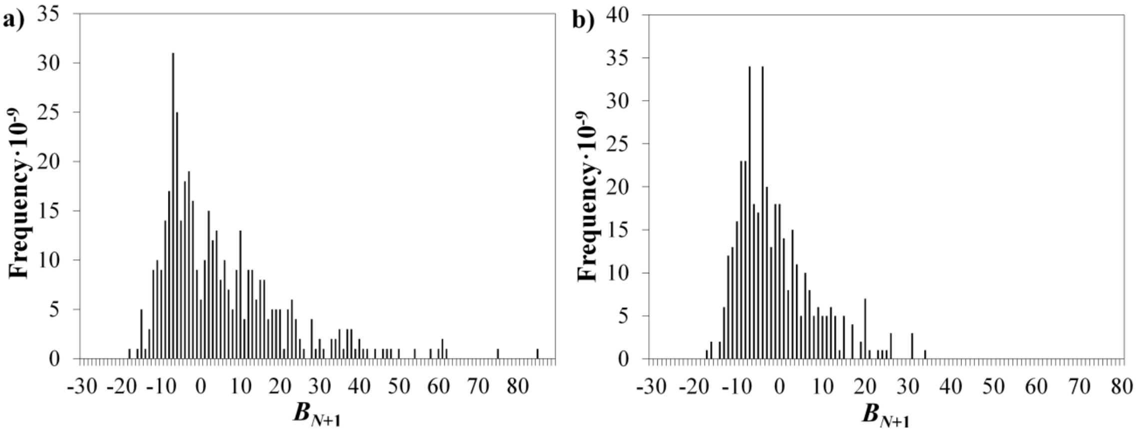

Figure 7.2. Probability distribution of B_{N+1} for the system: a) pure 1-butanol and b) resin/30% 1-butanol.

7.3.1.1.2. Thermodynamic integration

As it was introduced in Section 2.4.3.2, the thermodynamic integration (TI) method relies on a nonphysical path and a coupling parameter λ through which two states are connected. In the particular case of estimating the excess chemical potential of the specie *s*, the mentioned two states are the system with *N* particles of *s* (state A) and the system with *N*+1 particles of *s* (state B) and the coupling parameter λ slowly introduces (or removes) the binding energy B_{N+1} (attractive and repulsive interactions) between an *s* particle *N*+1 and all other particles in the system. Standard TI assumes that one obtains full equilibration along this λ-path which allows the calculation of the free energy by integrating the derivative of the Hamiltonian with respect to λ:

$$\Delta A = A_{\lambda=1} - A_{\lambda=0} = \int_0^1 \left\langle \frac{\partial H_\lambda(\vec{x},\vec{p})}{\partial \lambda} \right\rangle_\lambda d\lambda \tag{7.3}$$

Assuming that the kinetic energy term in the Hamiltonian[*] is separable and not dependent on λ (which is true for the case under study where λ introduces (or removes) the attractive and repulsive interactions keeping constant the mass of the particles, m_i), Equation 7.3 can be rewritten in terms of the potential energy *U* of the system:

$$\Delta A = A_{\lambda=1} - A_{\lambda=0} = \int_0^1 \left\langle \frac{\partial U_\lambda}{\partial \lambda} \right\rangle_\lambda d\lambda \tag{7.4}$$

---

[*] $H(\vec{x},\vec{p}) = \sum_{i=1}^{N} \frac{\vec{p}_i^{\,2}}{2m_i} + U\left(\vec{x}_1,\vec{x}_2,\ldots,\vec{x}_N\right)$

In a free-energy calculation where particles grow out of nothing, or particles disappear, using a simple linear interpolation of the Lennard-Jones and Coulomb potentials may lead to poor convergence. When the particles have nearly disappeared, or are close to appearing (at λ close to 0 or 1), the interaction energy will be weak enough for particles to get very close to each other, leading to large fluctuations in the measured values of $\partial U/\partial\lambda$ (which, because of the simple linear interpolation, depends on the potentials at both the endpoints of λ).To circumvent these problems, the singularities in the potentials need to be removed. This can be done by modifying the regular Lennard-Jones and Coulomb potentials with "soft-core" potentials that limit the energies and forces involved at λ values between 0 and 1, but not at $\lambda = 0$ or 1. In GROMACS the soft-core potentials U_{sc} are shifted versions of the regular potentials, so that the singularity in the potential and its derivatives at $r = 0$ is never reached:[20]

$$U_{sc}(r) = (1-\lambda)U^A(r_A) + \lambda U^B(r_B) \tag{7.5}$$

$$r_A = \left(\alpha\sigma_A^6\lambda + r^6\right)^{\frac{1}{6}} \tag{7.6}$$

$$r_B = \left(\alpha\sigma_B^6(1-\lambda) + r^6\right)^{\frac{1}{6}} \tag{7.7}$$

where U^A and U^B are the normal "hard core" Van der Waals and electrostatic potentials in state A ($\lambda = 0$) and state B ($\lambda = 1$) respectively, α is the soft-core parameter, and σ_i is the radius of the interaction. For intermediate λ, r_A and r_B alter the interactions very little for $r_i > \alpha^{1/6}\sigma$ and quickly switch the soft-core interaction to an almost constant value for smaller r_i.

Pure 1-butanol system

On the first place, the excess chemical potential of pure 1-butanol was estimated by means of thermodynamic integration. For that, the last configuration of the equilibrated 1-butanol system (the construction and equilibration of the 1-butanol pure system was described in Section 7.2.1.) was used as the initial configuration for the subsequent MD simulations with the different force fields (different values of λ). 26 values of λ were considered (i.e. $\Delta\lambda = 0.04$). For each of these 26 MD simulations all the 1-butanol molecules were coupled with the corresponding value of λ. This approach is based on the same principles that have been used for studies of the transfer of a single molecule, in which the interactions between one molecule and all other molecules in the sample are varied. When the interactions between all molecules in the sample are varied, accuracy is improved, as the statistical error per molecule is less.[21]

Each of the 26 systems with all the molecules coupled to the corresponding value of λ were re-equilibrated for 500 ps at constant NPT conditions (300 K and 1 bar). After that, 4 ns of NVT-MD simulations were performed to obtain the trajectories. For each value of λ the average $\left\langle \partial U_\lambda/\partial\lambda \right\rangle_\lambda$ was estimated. Figure 7.3 shows $\left\langle \partial U_\lambda/\partial\lambda \right\rangle_\lambda$ as a function of λ.

Finally, for the pure 1-butanol system a value of the Helmholtz free energy difference ΔA = 29.23 kJ/mol was computed from Equation 7.4 as the integral over the values of $\left\langle \partial U_\lambda / \partial \lambda \right\rangle_\lambda$ obtained at the 26 equidistant values of λ.

Ben-Naim and Marcus[22] estimated, from experimental data[*], the Gibbs free energy of pure 1-butanol, ΔG = 25.7 kJ/mol.

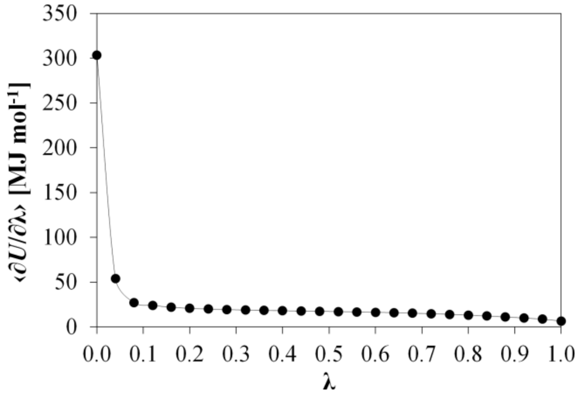

Figure 7.3. $\left\langle \partial U_\lambda / \partial \lambda \right\rangle_\lambda$ as a function of λ. Error bars are smaller than the markers. Integration of the curve provides the excess chemical potential of pure 1-butanol.

The difference between the Helmholtz free energy (ΔA) and the Gibbs free energy (ΔG) is the term $p\Delta V$. However, at low pressures this term can be neglected and the Helmholtz free energy and the Gibbs free energy can be considered equals. Therefore, the free energy corresponding to pure 1-butanol estimated from thermodynamic integration (29.23 kJ/mol) slightly overestimates (13.5 %) the experimental value determined by Ben-Naim and Marcus[22] (25.7 kJ/mol).

Resin/1-butanol system

As it was previously mentioned in Section 2.4.3.2, TI relies on exhaustively sampling the phase space at each intermediate λ point to meet the requirement of being always in equilibrium and fully reversible. When TI method is used to compute the excess chemical potential of a solvent in a polymer matrix, the accuracy of the phase space sampling could become quite poor. In these cases the major problem to overcome is related to the sampling of the state in which the coupled solvent molecule is completely (or almost completely) interacting. When the interaction between the penetrant solvent molecule and the polymer structure is sufficiently strong the solvent molecule may end up in a local free minimum, that is, the solvent molecule occupies a cavity in the polymer from which it does not move away during the simulation thus, poorly sampling the phase space.

In order to ascertain the reliability of the phase space sampling of the resin/solvent system, the diffusion coefficients (D) for 1-butanol in pure 1-butanol and in the resin/1-butanol system (with a concentration of 1-butanol of 5% w/w) were determined:

---

[*] Ben-Naim and Marcus[22] related the process of transferring (inserting) a molecule of *s* from a fixed position in the gas, into a fixed position in the liquid with the process of solvation of vapors condensing into their own liquids at 298.15 K. Although the data that they used to compute ΔG of pure 1-butanol were obtained from liquid-vapor equilibria, this thermodynamic quantity is not to be confused with the conventional condensation (or evaporation) free energy.

Table 7.3. Diffusion coefficients for 1-butanol in the pure 1-butanol and in the resin/1-butanol system

System	D [cm^2/s]
Pure 1-butanol system (estimated)	$(0.2198 \pm 0.0315) \cdot 10^{-5}$
Pure 1-butanol system (experimental)	$0.456 \cdot 10^{-5}$
Resin/1-butanol (5% w/w) system	$(0.0199 \pm 0.0051) \cdot 10^{-5}$

Two important things can be inferred from the diffusion coefficients gathered in Table 7.3: (1) the estimated diffusion coefficient for 1-butanol in the pure 1-butanol system is of the same order of magnitude as the experimental value ($D \approx 10^{-5}$ cm$^2 \cdot$s^{-1}) which validates the 1-butanol model used; (2) the estimated diffusion coefficient for 1-butanol in resin/1-butanol (5% w/w) system is significantly lower than that corresponding to the pure system. Einstein equation ($D = \left\langle x^2 \right\rangle / 6t$) predicts that the medium displacement for solvent molecules in the resin/1-butanol system in 1 ns is about 3.5 Å. This distance is very short indicating that the requirement of exhaustively sampling the phase space (in order to obtain an accurate value of $\left\langle \partial U_\lambda / \partial \lambda \right\rangle_\lambda$ at each λ point) requires very long unfeasible simulation times.

7.3.1.1.3. Fast growth thermodynamic integration

The fast growth thermodynamic integration method is based on the non-equilibrium work theorem introduced by Jarzynski. Jarzynski relates the work W_{AB} that is being performed on a system when going from state A to state B (along a coordinate λ) with the free energy change, irrespective of the reversibility of the sampling. He found that the exponentially averaged work of repeated sampling of the path from A to B is equal to the free energy difference between A and B:[23]

$$\Delta A_{AB} = -\beta^{-1} \ln \left\langle \exp(-\beta W_{AB}) \right\rangle_A \qquad (7.8)$$

where the angular bracket denotes averaging over a canonical ensemble of the initial state A.

The Jarzynski formalism and the resulting fast-growth methods bridge the gap between TI (Equation 7.3) and FEP methods (Equation 7.1), since Equations 7.3 and 7.1 can be viewed as the infinitely slow and the infinitely fast limits of Equation 7.8. As it was previously mentioned, TI relies on exhaustively sampling phase space at each intermediate λ point to meet the requirement of being always in equilibrium and fully reversible, a requirement which is difficult to meet in complex systems. In FEP, the sampling problem is a different one, and it lies in the bad sampling of low energies in the B (final) state and therefore a prediction of the free energy difference which is too high. In the case of fast-growth methods, one has to fully sample the work distribution functions, ergo all the (relevant) paths between the two states A and B. This sampling problem is in spirit similar to the typical perturbation sampling problems: in order to replace one very long equilibrium experiment to determine a free energy difference with many fast non-equilibrium experiments, the number of fast experiments required to sample the (exponentially rarely occurring) tails of the work distribution function grows exponentially with the amount of irreversible work performed during the experiment. In fast growth, one must decide whether to use many short simulation runs ('fast growth') or few long runs ('slow growth'). In general, it is expected the latter to give more-accurate results for a given amount of computer time. As a rule of thumb, the runs should be slow enough that the standard deviation in the resulting work values is about k_BT. If the standard deviation of the work is much larger, sampling errors will arise because only a few trajectories at the lower tail of the work distribution will contribute significantly to the weighted average, with all others having 'exponentially' small relative weights.[24]

The FGTI method was used with the aim of estimating the excess chemical potential of 1-butanol in the resin/1-butanol systems with 10% and 30% w/w of alcohol. The construction and equilibration of both systems, as well as the main simulation details, were described in Section 7.2.1. The last configurations of the equilibrated systems were used as the initial configurations for the subsequent fast-growth simulations.

In each fast-growth simulation a 1-butanol molecule was randomly selected and coupled to the parameter λ. The fast-growth simulations were performed in two steps. First the Coulomb interactions of the selected 1-butanol molecule were decoupled from the polymeric matrix. In this step the partial charges of the 1-butanol molecule (with full Lennard Jones interactions) were linearly changed from the normal partial charge of the force field to zero. After Coulomb interactions were completely decoupled, a second step was performed where the Lennard Jones (LJ) interactions of the 1-butanol were decoupled from the matrix using a soft-core potential identical to that used in the TI method (Section 7.3.1.1.2):

$$U_{sc}(r) = (1-\lambda)U^A(r_A) + \lambda U^B(r_B) \tag{7.5}$$

where the coupling parameter λ went from 0 (with coupled LJ, Coulomb interactions were previously decoupled) to 1 (fully decoupled), U^A and U^B are the normal "hard core" Van der Waals potential in state A ($\lambda = 0$) and state B ($\lambda = 1$) respectively, the soft-core parameter α was set to 0.7, and σ_i is the radius of the interaction.

As λ is changed, the accumulated thermodynamic work W_{AB} performed on the system (which by definition equals the change in energy of the system) is

$$W_{AB} = \int_0^{t_s} \frac{d\lambda(t)}{dt} \frac{\partial H_\lambda}{\partial \lambda} dt \tag{7.9}$$

During each simulation, for each Δt MD step the coupling parameter λ changed a value of $\Delta\lambda = \Delta t/t_s$, where t_s is the total simulation time. Thus, the work W performed during each decoupling process is the sum of the work over all the MD time steps for both decoupling steps. Then, this work needs to be averaged exponentially over all the FGTI simulations performed to obtain the free energy difference ΔA (see Equation 7.8).

During FGTI the integration step was set at Δt = 2 ft. Therefore, the only remaining parameter is the length of the fast-growth simulations, t_s. When the transformation is conducted rapidly, most trajectories do not sample relevant regions of phase space. Rapid crossing of barriers under tension and crossing over atypically high barriers result in hysteresis effects, and a broadened work distribution that reflects an increasing relevance of dissipation. As it was mentioned before, broad work distributions have two important consequences: first, the statistics will be poor; and, second, a bias in the estimator of the free energy change will result in free energy estimates that deviate systematically from the correct free energy difference.[25]

For the system with 10% w/w of absorbed 1-butanol we tried 1 ns for decoupling the Coulomb interactions and 5 ns for decoupling the LJ interactions. For the system with 30% w/w of absorbed 1-butanol 0.2 ns and 2 ns were used for decoupling the Coulomb and LJ interactions, respectively. 25 FGTI simulations (N_s) were performed for each system. Table 7.4 shows the most relevant information regarding the performed FGTI simulations as well as the corresponding results.

Table 7.4. Fast Growth Thermodynamic Integration results

System	t_s Q/LJ [ns]	N_s	$\langle W \rangle$ [kJ/mol]	$\sigma(W)$	ΔA_J [a] [kJ/mol]	ΔA_G [b] [kJ/mol]
10%	1/5	25	32.3	5.0	27.8	27.3
30%	0.2/2	25	18.7	5.9	14.3	11.9

[a] Free energy estimated by the Jarzynski non-equilibrium equality (Equation 7.8)
[b] Free energy estimated assuming a Gaussian distribution of the work (Equation 7.13)

In the limit of relatively long runs and sufficiently slow growth, the work probability distributions are expected to be approximately Gaussian as a consequence of the central limit theorem.[26] Hummer demonstrated that, for a Gaussian work distribution of variance σ^2(W) the free energy ΔA_G is[26]

$$\Delta A_G = \langle W \rangle - \tfrac{1}{2}\beta\sigma^2 \tag{7.13}$$

In Equation 7.13 the term $\langle W \rangle$ is the arithmetic average of the work distribution and $-\tfrac{1}{2}\beta\sigma^2$ is the irreversible work of the process, which is proportional to the variance of the work distribution.[24]

The last column of Table 7.4 shows the free energy value ΔA_G calculated from Equation 7.13. When the distributions are Gaussian, the effect of the missing tail can be quantified by determining the free energy for a Gaussian distribution (Equation 7.13). Therefore, comparison between ΔA_J and ΔA_G indicates how much of distribution tail is missing (assuming that the underlying distribution is really Gaussian).

Results gathered in Table 7.4 show that $\sigma(W) > 2\ k_BT$ (temperature was set to 300 K; thus k_BT = 2.49 kJ mol^{-1}), despite the simulations times (t_s) were long for both systems. In spite of that, for the system with the longest simulation time (10% w/w of 1-butanol), ΔA_J can be compared to ΔA_G. However, for the system with a 30% w/w of 1-butanol (which has the shortest simulation time), ΔA_J exceeds ΔA_G in 2.4 kJ/mol. This overestimation is related to the fact that low values of W were not accurately sampled indicating that longer simulation times are needed in order to accurately determine ΔA.

In conclusion, although FGTI seems to be a capable method to estimate the free energy of 1-butanol in the P(S-DVB) resins, the required computational effort is disproportionate to our purpose.

7.3.1.2. Thermodynamic estimation

As it has been seen in the previous section, the free energy perturbation (FEP) method, the thermodynamic integration (TI) and the fast growth thermodynamic integration (FGTI) method based in Jarzynski equality present practical limits that hinder the thermodynamic study of the absorption of 1-butanol in ion exchange resins. Therefore, and given that the main objective of this work was to study the influence of 1-butanol absorption on the polymeric structure of the resin at macroscopic and microscopic level, a detailed and rigorous thermodynamic description of the absorption process will not be pursued. However, if it is assumed, as a rough approximation, that the major factor contributing to the free energy change of the process is the energy change associated with the bonding and non-bonding interactions, ΔE, an estimate of the thermodynamic behavior of the absorption process can be obtained.

With this aim, the energy change (ΔE) corresponding to the absorption process was computed as:

$$\Delta E = E_{\mathrm{Resin}(X_{OH}\%)} - E_{\mathrm{Resin(dry)}} - n_{OH} \cdot \hat{E}_{\mathrm{Butanol}} \tag{7.14}$$

where $E_{\mathrm{Resin}(XOH\%)}$, $E_{\mathrm{Resin(dry)}}$ and $\hat{E}_{\mathrm{Butanol}}$ represent, respectively, the energy for: the resin/alcohol system; the dry resin system; and the contribution of a single molecule of 1-butanol to the total of a pure alcohol system. n_{OH} is the number of absorbed 1-butanol molecules in the resin.

Figure 7.4 represents the variation of the energy change, Δ*E*, against the amount of absorbed 1-butanol. As it can be seen, Δ*E* shows a minimum which indicates the maximum amount of 1-butanol that the polymeric matrix can absorb. This minimum corresponds to a 1-butanol concentration of ≈ 34% w/w which agrees considerably well with the value indirectly estimated from experimental data (31%, see Section 7.2.2). For higher concentrations of 1-butanol, Δ*E* increases due to the fact that the matrix is not able to accommodate all the 1-butanol forcing alcohol molecules to be closer and resulting in higher non-bonding interaction between molecules.

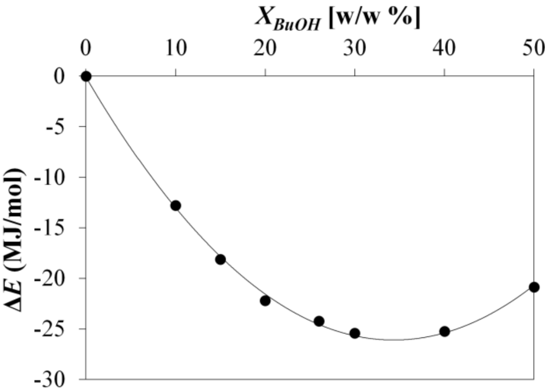

Figure 7.4. Variation of the energy change (Δ*E*) from the dried resin system to the resin/1-butanol system against the concentration of absorbed alcohol.

One could have expected that, once the resin reaches the maximum 1-butanol concentration that it can absorb, the alcohol molecules added afterwards would locate surrounding (out of) the resin particle. In that case, the system would consist of a resin particle immerse in 1-butanol and the increase of the amount of alcohol would only mean increasing the volume of alcohol in which the particle is immersed without involving a change in the stability of the system (i.e., in Figure 7.4, Δ*E* would be constant for values of X_{BuOH} higher than the equilibrium concentration). However, two circumstances prevent the formation of a resin particle immerse in 1-butanol: (1) the fact that the polymeric matrix selected to carry out the swelling study presents 2 “inter-crosslinks” (DVB monomer connecting two polymer chains, one pertaining to the macromolecule and the other to its own periodic image, see Section 7.2.1); and that periodic boundary conditions were used during MD simulations. Therefore, in this particular case, the system consists of an infinite polymeric matrix in which all the alcohol molecules have to locate inside the polymeric network. Consequently, alcohol concentrations higher than the equilibrium concentration lead to less stable systems (i.e., in Figure 7.4 Δ*E* increases for values of X_{BuOH} higher than the equilibrium concentration).

7.3.2. Influence of 1-butanol absorption on the macroscopic swelling

Figure 7.5a shows the volume variation (with respect to the dry resin volume), Δ*V*, against the concentration of absorbed 1-butanol, as well as the experimentally determined volume increase of Amberlyst 15 swollen in 1-butanol (red dot), Δ*V* = 21.1% (see Table 7.1). As it can be seen, low concentrations of alcohol lead to resin shrinkage with the highest volume reduction observed corresponding to 10% of 1-butanol (Δ*V* = -11.8%). From that point on, Δ*V* experiences a gradual increase, slight at the beginning but more pronounced from 20% w/w up. The early shrinkage of the resin (added to the mass system increment) entails a significant increase of the system density (see Figure 7.5b). However, for concentrations of 1-butanol higher than 20% the important swelling experienced by the system results in a progressive reduction of the density of the system.

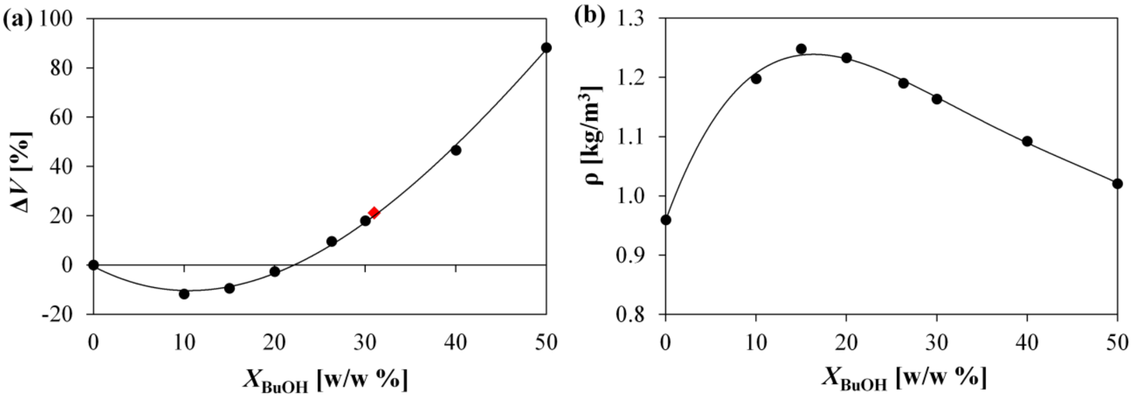

Figure 7.5. Variation of a) the percentage of swelling volume (ΔV) and b) the density against the concentration of absorbed 1-butanol in the P(S-DVB) resin. The red dot represents the experimental value of ΔV determined by laser diffraction.

Results showed in Figure 7.5a suggest that the maximum amount of 1-butanol absorbed by the resin (which causes a volume increase equivalent to that experimentally determined, $\Delta V = 21.1\%$, see red dot in Figure 7.5a) corresponds to a concentration of 31-32% w/w. This value is in good agreement with that indirectly estimated from experimental data (31%, see Section 7.2.2) and with that estimated from the thermodynamic study (Section 7.3.1.2).

7.3.3. Influence of 1-butanol absorption on the microscopic swelling

With the aim of studying the influence that 1-butanol absorption has on the structural properties of the polymeric network at molecular level, the simulation box was divided into 1000 cells of identical volume. For each cell the local apparent density of the resin, ρ_a, (without taking into account 1-butanol molecules) was calculated and, subsequently, cells were ranked following an increasing local apparent density criterion. Figure 7.6 displays the average (among 100 snapshots) apparent density of the ranked cells for several resin/solvent systems with different amounts of 1-butanol. As it can be seen, significant structural differences exist among the studied systems. Dry resin presents

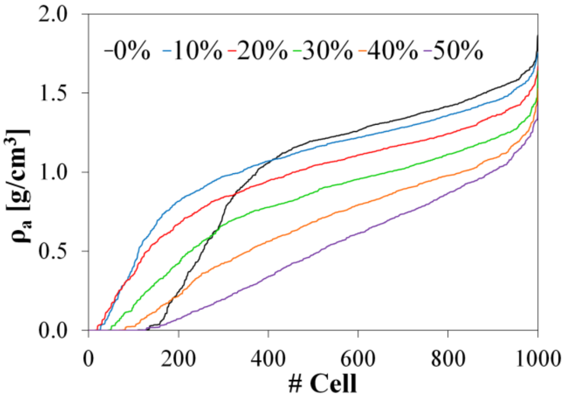

Figure 7.6. Local apparent density for the 1000 cells in which microestructures were divided. Cells were ranked following a growing local density order.

an important number of cells (more than 10%) with negligible local apparent density. This fact is clearly reflected in Figure 7.7a where the frequency histogram of the local apparent density is represented. These void cells form the network of macropores characteristic of macroreticular resins. On the other hand, dry resin also presents a considerablenumber of cells with apparent density higher than 1.5 g/cm^3 corresponding to a very dense polymer mass hardly accessible. This description of the dry resin structure is consistent with the known structure of highly crosslinked macroreticular resins.[27]

For systems with 10% and 20% of absorbed 1-butanol the number of cells with negligible apparent density remarkably decreases (Figures 7.7b and c, respectively). This decrease is mainly attributed to the shrinkage of the polymeric matrix observed in Figure 7.5a. A 10% or 20% w/w of 1-butanol is not enough to fill the macropores of the resin. In that cases the alcohol molecules seem to exert an attractive effect on the polymer chains which originates the collapse of the matrix. The polymeric matrix of the resin with a 10% w/w of 1-butanol absorbed is, in general terms, denser than the dry resin (ρ_a = 1.054 and 0.961 g/cm^3 respectively). However, if the local structure is taken into account, it can be observed that the high-dense resin zones (with ρ_a > 1.5 g/cm^3) decrease as the absorbed amount of 1-butanol increases. Therefore, small amounts of alcohol make the macropores to collapse but, at the same time, allow the polymer chain to move apart giving place to less dense zones which harbor small spaces between polymer chains. Comparing Figures 7.7a, b and c, it can be seen that the maximum frequency moves to the left (to less dense zones). For the dry resin the maximum frequency corresponds to an apparent density of 1.4 g/cm^3 whereas for the systems with 10% and 20% w/w of 1-butanol the maximum frequencies correspond, respectively, to an apparent density of 1.3 and 1.2 g/cm^3.

For the system in which the amount of absorbed 1-butanol was close to the equilibrium (30% w/w), the number of cells void of resin was significantly higher than that corresponding to the systems with 10% and 20% w/w of 1-butanol. However, this number it is still lower than the corresponding to the dry resin. More important, the number of cells with relatively low apparent density (with ρ_a < 1.0 g/cm^3) significantly increased whereas zones highly dense tended to disappear (cell with apparent densities higher that 1.5 g/cm^3 were barely detected). These features indicate that a significant part of the matrix presents important spaces between polymer chains, motivated by the presence of alcohol molecules, resulting in a more easily accessible catalyst.

Finally, for the systems in which the amount of absorbed 1-butanol is higher than the equilibrium concentration (40% and 50%) the profiles gathered in Figure 7.6 are significantly different, the slope change observed for other systems having almost disappeared. Taking a close look to the corresponding frequency histograms (Figures 7.7e and f) it can also be observed that the profiles have changed considerably and the resin porosity has remarkably increased. In those systems more 1-butanol molecules than that corresponding to the equilibrium concentration were introduced “by force” at sterically accessible positions (without initially considering intermolecular interactions). Once relaxed, the excess of alcohol leaded to the over-swelling of the resin resulting in a stretched matrix.

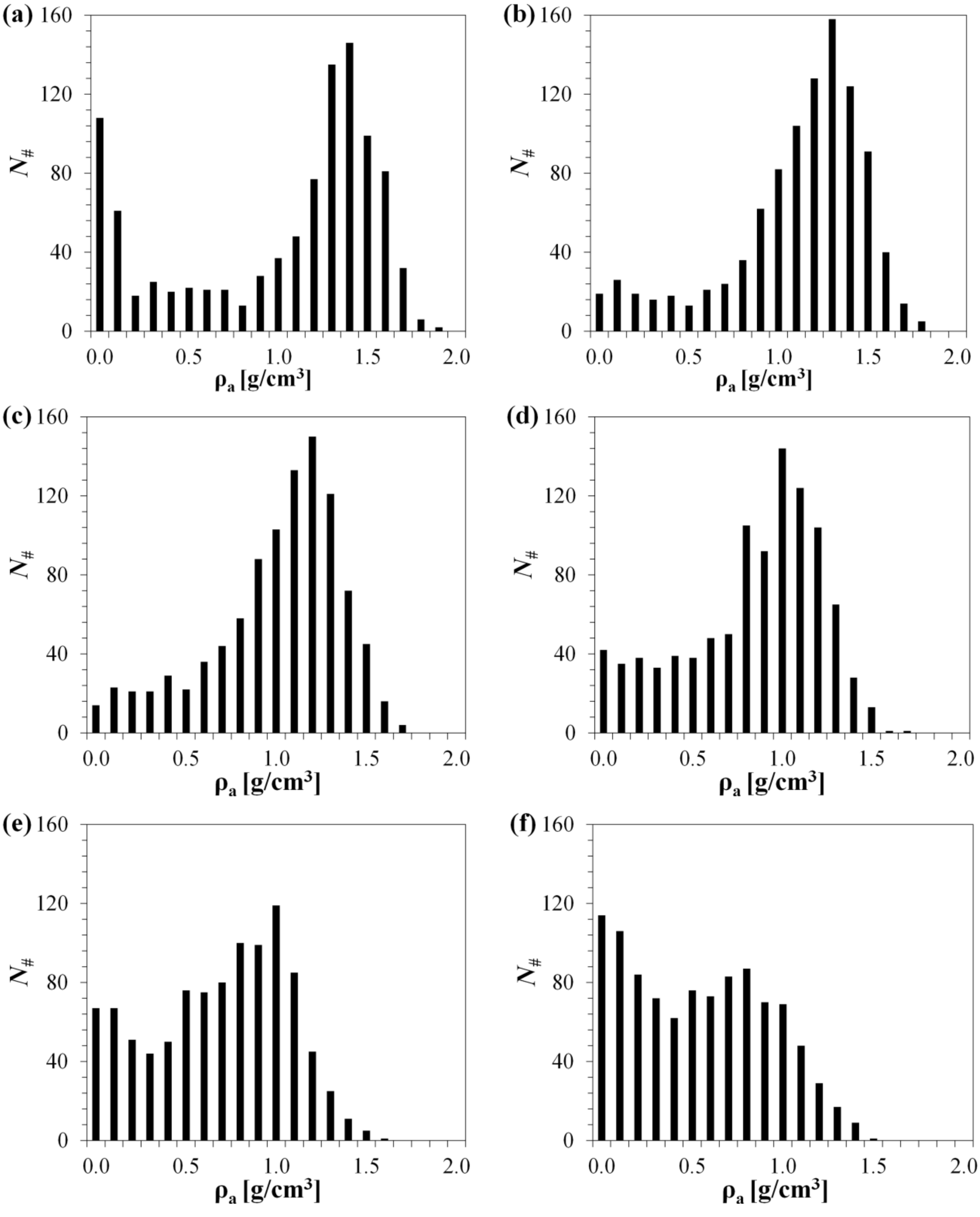

Figure 7.7. Frequency histograms of local apparent density for selected systems: a) 0%; b) 10%; c) 20; d) 30%; e) 40%; and f) 50% of 1-butanol absorbed.

7.3.4. Organization of absorbed 1-butanol

The study of the relative position of the system components shows that, independently of the alcohol concentration, 1-butanol tends to locate close to the sulfonic groups. Figure 7.8a and

Figure 7.8b display the radial distribution function between the proton of the sulfonic group and the oxygen of the alcohol molecule, $g_{Hx\text{-}OH}(r)$, for selected generated microstructures before and after MD relaxation, respectively. As it can be seen in Figure 7.8a, before relaxation the alcohol molecules are uniformly distributed and no preferential organization of the alcohol molecules around the sulfonic groups is observed for all the generated microestructures. However, after MD relaxation, the radial distribution function of the Hx-OH pair (Figure 7.8b) shows, for all the microestructures, a sharp and narrow peak at 0.19 nm and a second smaller and broader peak at 0.55 nm indicating that 1-butanol molecules tend to locate close to the sulfonic groups.

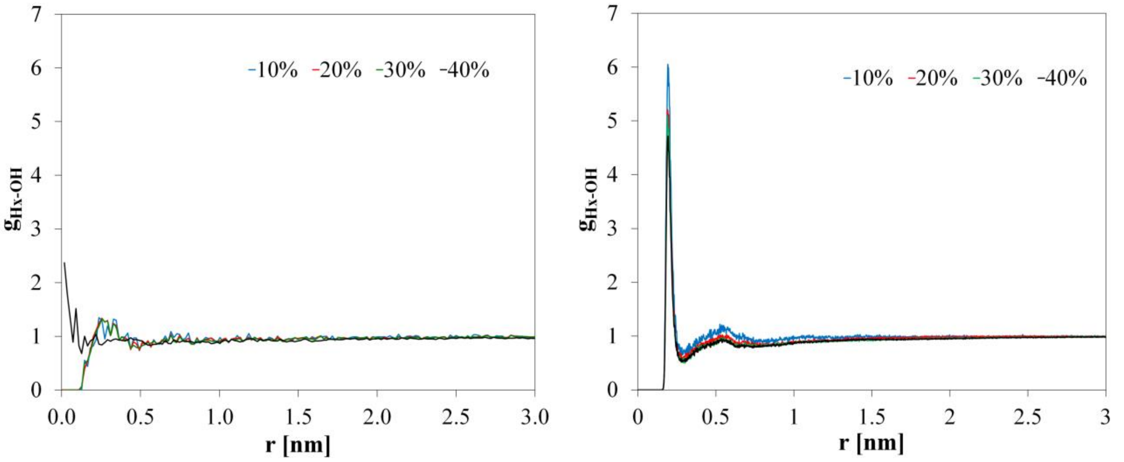

(a) **(b)**

Figure 7.8. Radial distribution functions of the Hx-OH pair where Hx refers to the hydrogen atom of the sulfonic group and OH refers to the oxygen atom of the 1-butanol for: (a) generated microstructures before relaxation; (b) after MD relaxation.

With the aim of gaining some insight on the interaction between the sulfonic groups and the alcohol molecules we calculated, for the microstructure with a 30% of 1-butanol, the time fraction that each alcohol molecule remains close to a sulfonic group (with a distance between the sulfur atom of the sulfonic group and the oxygen atom of the 1-butanol molecule lower than 5 Å) for the last 2 ns of the MD simulation (i.e. 201 snapshots recorded every 10 ps) and compared it with the time fraction that each alcohol molecule remains close to another alcohol molecule (with a distance between oxygen atoms of each 1-butanol molecule lower than 5 Å). Figure 7.9 shows the frequency distribution of the time fraction for the couples sulfonic group-alcohol (blue) and alcohol-alcohol (red). As it can be seen, the number of sulfonic group-alcohol couples that remain close a short fraction time (lower than 10%) is significantly lower than the number of alcohol-alcohol couples. However, for longer fraction times the number sulfonic group-alcohol couples that remain close is higher than the number of alcohol-alcohol couples. These observations suggest that, although alcohol molecules do not become stuck when they approach a sulfonic group, they interact to some extent with the sulfonic groups making them to remain close for a longer time. This behavior justifies the results observed in the radial distribution of Figure 7.8b.

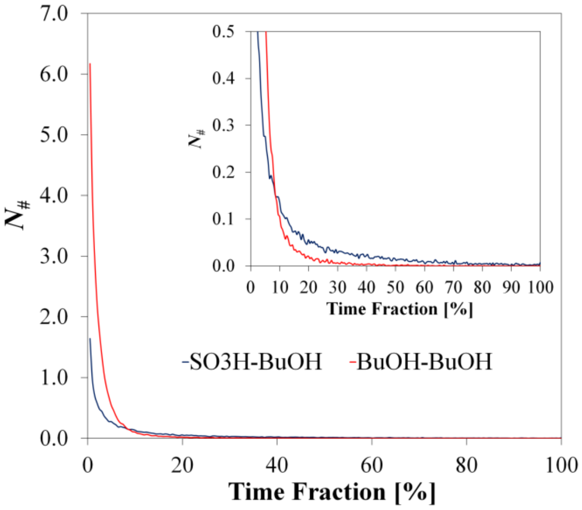

Figure 7.9. Frequency distribution of the time fraction that the couples sulfonic group-alcohol (blue) and alcohol-alcohol (red) remain close. Distributions have been divided by the number of sulfonic groups and the number of alcohol molecules respectively.

7.4. Conclusions

In this chapter, the macroscopic and microscopic swelling of a highly crosslinked macroreticular resin were studied by means of MD simulations. The macroscopic swelling predicted by the model agrees quite well with experimental results validating the performance of our resin atomistic model. The microscopic study allowed us to characterize and quantify the structure of the polymeric network at molecular level concluding that swelling creates new spaces in the matrix given as a result a less dense polymer mass where the high dense zones, characteristic of the dry resin, have disappeared. Finally, it was confirmed that alcohol molecules tend to interact with the sulfonic groups of the resin. Results obtained in this chapter are currently being used as starting point for the study of the catalytic reaction in the P(S-DVB) resin using quantum mechanics / molecular mechanics methods.

Nomenclature

Notation

B_{N+1}	Total potential energy of interaction between the ‘test’ particle and the *N* particles of the system
D	Diffusion coefficient
d_p	Particle diameter
$E_{Resin(XOH\%)}$	Energy for the resin/1-butanol system
$E_{Resin(dry)}$	Energy for the dry resin system
$\hat{E}_{\mathrm{Butanol}}$	Contribution of a single molecule of 1-butanol to the total energy of a pure alcohol system
$g_{Hx\text{-}OH}$	Radial distribution function of the Hx-OH pair
$H(x,p;\lambda)$	Hamiltonian of the system
k_B	Boltzman constant
N	Number of particles
N_s	Number of simulations
$N_{\#}$	Frequency number
n_{OH}	Number of absorbed 1-butanol molecules in the resin
r	Distance between two particles
t	Time
t_s	Total simulation time
T	Temperature
$U_{i,N+1}$	Energy of interaction between the particle *i* and the particle *N*+1
U_{sc}	Soft-core potential
W	Work
x	Distance
X_{BuOH}	Concentration of absorbed 1-butanol

Greek symbols

α	Soft-core parameter
β	$1/k_BT$
ΔA	Helmholtz free energy
ΔA_G	Helmholtz free energy estimated assuming a Gaussian work distribution
ΔA_J	Helmholtz free energy estimated from Jarzynski’s non-equilibrium equality
ΔE	Energy change associated with the bonding and non-bonding interactions
$\Delta \mathrm{G}$	Gibbs free energy
$\Delta\lambda$	Increment of λ

Δt	Time increment
ΔV	Volume increment
λ	Coupling parameter through which two states are connected
$\mu_{s,i}$	Chemical potential of the compound *s* in the system *i*
μ^{excess}	Excess chemical potential
ρ_a	Apparent density of the resin
σ_i	Radius of the interaction
σ	Standard deviation

Abbreviations

CGA	Combined Growing Approach
DVB	Divinylbenzene
FGTI	Fast-growth thermodynamic integration
FEP	Free energy perturbation
GAFF	General Amber Force Field
ISEC	Inverse Steric Exclusion Chromatography
LJ	Lennard-Jones
MD	Molecular dynamics
NPT	Isobaric-isothermal ensemble
NVT	Canonical ensemble
P(S-DVB)	Poly(styrene-divinylbenzene)
TI	Thermodynamic Integration

Reference

[1] Corain, B.; Zecca, M.; Jerábek, K. Catalysis and polymer networks—the role of morphology and molecular accessibility. *J. Mol. Catal. A: Chem*. **2001**, *177*, 3–20.

[2] Sterchele, S.; Centomo, P.; Zecca, M.; Hanková, L.; Jerábek, K. Dry-and swollen-state morphology of novel high surface area polymers. *Microporous Mesoporous Mater.* **2014**, *185*, 26–29.

[3] Centomo, P.; Jerabek, K.; Canova, D.; Zoleo, A.; Maniero, A. L.; Sassi, A.; Canton, P.; Corain, B.; Zecca, M. Highly hydrophilic copolymers of N,N-dimethylacrylamide, acrylamido-2-methylpropanesulfonic acid, and ethylenedimethacrylate: nanoscale morphology in the swollen state and use as exotemplates for synthesis of nanostructured ferric oxide. *Chem. Eur. J.* **2012**, *18*, 6632 – 6643.

[4] Hanková, L.; Holub, L.; Jerabek, K. Formation of porous polymer morphology by microsyneresis during divinylbenzene polymerization. *J. Polym. Sci., Part B: Polym. Phys*. **2015**, *53*(11), 774–781.

[5] Hanková, L.; Holub, L.; Meng, X.; Xiao, F.S.; Jerabek, K. Role of water as a coporogen in the synthesis of mesoporous poly(divinylbenzenes). *J. Appl. Polym. Sci*. **2014**, *131*(23), 41198.

[6] Jeřábek, K. Inverse steric exclusion chromatography as a tool for morphology characterization. In *Cross-evaluation of strategies, size-exclusion chromatography*; Potschka, M., Dubin, P. L., Eds.; ACS Symposium Series 635; American Chemical Society: Washington, DC, 1996; pp 211-224.

[7] Lindahl, E.; Hess, B.; van der Spoel, D. GROMACS 3.0: A package for molecular simulation and trajectory analysis. *J. Mol. Mod.* **2001**, *7*, 306–317.

[8] van der Spoel, D.; Lindahl, E.; Hess, B.; Groenhof, G.; Mark, A. E.; Berendsen, H. J. C.

GROMACS: Fast, Flexible and Free. *J. Comp. Chem*. **2005**, *26*, 1701–1718.

[9] Hess, B.; Kutzner, C.; van der Spoel, D.; Lindahl, E. GROMACS 4: Algorithms for highly efficient, load-balanced, and scalable molecular simulation, *J. Chem. Theory Comp*. **2008**, *4*(3), 435–447.

[10] Wang, J.; Wolf, R. M.; Caldwell, J. W.; Kollman, P. A.; Case, D. A. Development and testing of a general Amber force field *J. Comput. Chem*. **2004**, *25*, 1157–1174.

[11] virtualchemistry.org (accessed May 2015).

[12] Anisimov, V. M.; Lamoureux, G.; Vorobyov, I. V.; Huang, N.; Roux, B.; MacKerell, A. D. Determination of electrostatic parameters for a polarizable force field based on the classical Drude oscillator. *J. Chem. Theory Comput*. **2005**, *1*, 153-168.

[13] Vorobyov, I.; Anisimov, V. M.; Greene, S.; Venable, R. M.; Moser, A.; Pastor, R. W.; MacKerell, A. D. Additive and classical drude polarizable force fields for linear and cyclic ethers. *J. Chem. Theory Comput*. **2007**, *3* (3), 1120-1133.

[14] Toukmaji, A.; Sagui, C.; Board, J.; Darden, T. Efficient particle-mesh Ewald based approach to fixed and induced dipolar interactions *J. Chem. Phys*. **2000**, *113*, 10913-10927.

[15] Nosé, S. A unified formulation of the constant temperature molecular dynamics methods. *J. Chem. Phys.* **1984**, *81 (1)*, 511-519.

[16] Hoover, W. G. Canonical dynamics: Equilibrium phase-space distributions. *Phys. Rev. A.* **1985**, *31 (3)*, 1695-1697.

[17] Parrinello, M.; Rahman, A. Polymorphic transitions in single crystals: A new molecular dynamics method. *J. Appl. Phys*. **1981**, *52*, 7182-7190.

[18] Widom, B., Some topics in the theory of fluids, *J. Chem. Phys*. **1963**, *39*, 2808-2817.

[19] Chipot. C.; Pohorille, A. Calculating free energy differences using perturbation theory. In *Free energy calculations. Theory and applications in chemistry and biology*; Chipot. C.; Pohorille, A., Eds.; Springer Series in Chemical Physics 86; Springer-Verlag: Berlin Heidelberg, 2007; pp 37-38.

[20] van der Spoel, D.; Lindahl, E.; Hess, D. and the GROMACS development team. GROMACS User Manual version 4.6.4.

[21] Hermans, J.; Patbiaseril, A.; Anderson, A. Excess free energy of liquids from molecular dynamics simulations. Application to water models. *J. Am. Chem. Soc*. **1988**, *110*, 5982-5986.

[22] Ben-Naim, A.; Marcus, Y. Solvation thermodynamics of nonionic solutes. *J. Chem. Phys.* **1984**, *81(4)*, 2016-2027.

[23] Jarzynski, C. Nonequilibrium equality for free energy differences. *Phys. Rev. Lett*. **1997**, *78* (14), 2690-2693.

[24] Hummer, G. Nonequilibrium methods for equilibrium free energy calculations. In *Free energy calculations. Theory and applications in chemistry and biology*; Chipot. C.; Pohorille, A., Eds.; Springer Series in Chemical Physics 86; Springer-Verlag: Berlin Heidelberg, 2007; pp 184-185.

[25] Wood, R. H.; Mühlbauer, W. C. F.; Thompson, P. T. Systematic errors in free energy perturbation calculations due to a finite sample of configuration space. Sample-size hysteresis. *J. Phys. Chem*. **1991**, *95*, 6670–6675.

[26] Hummer, G. Fast-growth thermodynamic integration: Error and efficiency analysis. *J. Chem. Phys*. **2001**, *114*, 7330-7337.

[27] Sherrington, D. C. Preparation, structure and morphology of polymer supports. *Chem Commun*. **1998**, *21*, 2275–2286.

8. SUMMARY AND OUTLOOK

8.1. Summary: A unified view

As stated in the Introduction, di-n-butyl ether is considered a very attractive oxygenate compound to reformulate diesel fuel. Throughout the previous chapters it has been clearly proven the suitability of ion exchange resins in the synthesis of di-n-butyl ether from 1-butanol dehydration in liquid phase at the temperature range of 140-190 ºC. A catalyst screening of acidic poly(styrene-divinylbenzene), P(S-DVB), ion exchange resins (Chapter 3) showed that resins activity is enhanced with high acid capacities and with polymer matrices that are able to swell moderately allowing 1-butanol ready access to the active sites but without resulting in very large distance between the active centers. The resin Amberlyst 36 (oversulfonated, medium values of DVB %) proved to be the most active catalyst tested. However, in an industrial process a high selectivity to di-n-butyl ether is extremely desirable from an environmental and economic standpoint, and resins that present a more elastic polymer matrix and higher ability to swell (gel type resins and Amberlyst 70) are the ones that present higher selectivities. Among all the tested resins, Amberlyst 70 was selected as the most suitable catalyst for industrial use given its excellent property balance: satisfactory activity, high selectivity to di-n-butyl ether and thermal stability up to 463 K.

In Chapter 3, the study of the influence of typical 1-butanol impurities (isobutanol or ethanol and acetone, depending on the production process) demonstrated that isobutanol enhances the formation of branched ethers (which have worse properties as diesel components than the linear ones) whereas ethanol leads to the formation of ethyl butyl ether and di-ethyl ether and acetone hardly reacts. Thus, in an industrial process special care must be taken to avoid ethanol in the feed stream given that di-ethyl ether cannot be blended directly into commercial diesel fuels.

In Chapter 4, the relatively large value found for the thermodynamic equilibrium constant of di-n-butyl ether formation and the fact that the formation of 1-butene was extremely slow assure high conversion levels in an industrial etherification process. Di-n-butyl ether formation proved to be a slightly exothermic reaction, almost athermic, whereas 1-butene formation was found to be an endothermic reaction. A review of the literature data for di-n-pentyl ether, di-n-hexyl ether and di-n-octyl ether equilibrium constants showed that the formation reactions of these ethers tend to be more exothermic as the ether chain gets longer.

A comprehensive kinetic analysis (Chapter 5) enlightened that the reaction rate to form di-n-butyl ether on Amberlyst 70 is highly influenced by the temperature and the presence of water. Two kinetic models that are able to predict the reaction rates of di-n-butyl ether formation in the whole range of temperatures and concentrations explored were identified. One of them stems from a Langmuir-Hinshelwood-Hougen-Watson formalism in which two adsorbed molecules of 1-butanol react to yield ether and water, being the reversible surface reaction the rate limiting step. The other one stems from a mechanism in which the rate limiting step is the desorption of water and where the adsorption of di-n-butyl ether is negligible. Both models present several characteristics in common: in both water inhibition effect is correctly represented by a correction factor derived from a Freundlich adsorption isotherm; the number of free active sites is found to be negligible compared to the occupied ones; both present similar values of apparent activation energies (122 ± 2 kJ/mol).

The second general objective of this thesis, *Modeling and simulation of ion exchange resin*, was developed in Chapters 6 and 7. Throughout these two chapters it was demonstrated the suitability of molecular dynamics simulations in the understanding of the microscopic structure of P(S-DVB) ion-exchange resins and the prediction of their properties. Atomistic simulations of the structure of sulfonated P(S-DVB) resins reveled the decisive role that internal loops (closed polymer chains) play in defining the properties (i.e. density, porosity and structures) of highly cross-linked resins. Thus, although crosslinks ensure the local backbone structure, internal loops confer rigidity and loop architecture. It was also demonstrated that the developed atomistic model is able to predict the swelling behavior of ion-exchange resins in 1-butanol. From the swelling study performed by means of molecular dynamic simulation it was possible to characterize and quantify the structure of the swollen polymeric network at molecular level and to conclude that alcohol molecules tend to interact with the sulfonic groups of the resin.

8.2. Outlook: What’s next?

As it is well-known, the success of a catalytic industrial process depends significantly on the correct selection of the catalyst. However, the performance of comprehensive experimental catalytic tests is economically and timely consuming. Furthermore, in the case of ion exchange resins, their catalytic performance depends critically on their polymeric structure in the reaction medium. In this work it has been proved that molecular dynamic simulations are a useful tool to model and predict structural properties of ion exchange resins as well as their behavior in a polar solvent (1-butanol). The developed resin model together with MD simulation can provide economical and highly valuable information. In this regard, the following recommendations are proposed:

- Perform a MD study with the series of n-alcohols 1-ethanol, 1-pentanol, 1-hexanol and 1-octanol (experimental values of ion-exchange resins swelling in these alcohols can be found in the bibliography) in order to check the performance of the model and to ascertain the role that the aliphatic alcohol chain and the polar part play in the swelling process.

- Perform a MD study with 1-alcohol/water solvent mixtures to gain insight about the interactions water-alcohol-resin and the mechanism by which water influences the reaction rate of ether formation.

Furthermore, the computational chemistry realm offer other very interesting related works, among them, the study of the 1-butanol dehydration reaction mechanism over ion exchange resins by means of QM/MM (quantum mechanics/molecular mechanics) methods.

From an experimental standpoint, the proposed recommendations are focused on mitigate the important inhibitor effect of water on the reaction rate of di-n-butyl ether formation. For such purpose two paths can be investigated:

- Exploration of new ion-exchangers which can minimize the inhibitor effect of water on the reaction rate.
- Study the process of 1-butanol dehydration with parallel water removal from an industrial point of view.

And finally, for a potential industrial implementation the next recommendations are proposed:

- Study, by means of process simulations tools or the use of an experimental pilot reactor, the possible difficulties that may appear in the scale up process and look for solutions.
- Study the potential alternatives in downstream processing (recovery and purification of di-n-butyl ether from reaction mixture).

RESUMEN DEL TRABAJO
(Spanish)

Objetivos

(1) Demostrar que las resinas de poli(estireno-divinilbenceno), P(E-DVB), pueden catalizar satisfactoriamente la deshidratación de 1-butanol a di-n-butil éter, DNBE, en fase líquida.

(2) Evaluar la influencia de las características morfológicas de las resinas de P(E-DVB) en la síntesis del DNBE y, en base a estos resultados, seleccionar la resina más apropiada para uso industrial.

(3) Estudiar el efecto que las impurezas típicas del 1-butanol tienen en la reacción de deshidratación.

(4) Evaluar el equilibrio termodinámico de la reacción de deshidratación de 1-butanol a DNBE y de sus reacciones secundarias más importantes.

(5) Llevar a cabo un estudio cinético de la reacción de deshidratación de 1-butanol a DNBE sobre la resina termoestable Amberlyst 70 y proponer una ecuación cinética con base mecanística.

(6) Desarrollar un modelo atomístico realista de la matriz polimérica de las resinas de intercambio iónico.

(7) Mediante simulaciones de dinámica molecular estudiar la influencia de la topología de la matriz polimérica sobre las propiedades microscópicas de la resina.

(8) Estudiar el efecto del 1-butanol sobre la estructura polimérica de la resina y las interacciones 1-butanol/resina.

1. Introducción

La creciente demanda de combustibles (asociada al progresivo aumento de la población mundial y de la calidad de vida), la limitación de las reservas existentes, la volatilidad de los precios del crudo así como su tendencia al alza, la fuerte dependencia de las importaciones de combustibles desde regiones altamente inestables geopolíticamente y la problemática ambiental han ocasionado que algunos gobiernos redirijan sus esfuerzos al desarrollo de compuestos que puedan sustituir parcialmente a los combustibles fósiles. Dentro de la variedad de posibles aditivos para reformular los carburantes (ya sea la gasolina o el diésel), los compuestos oxigenados han demostrado ser una excelente alternativa para reducir las emisiones contaminantes sin suponer importantes pérdidas de potencia y sin la necesidad de introducir modificaciones en los motores existentes.[1-4]

Varios compuestos oxigenados (alcoholes, esteres y éteres) han sido considerados como candidatos para ser añadidos al combustible diésel. De entre ellos, los éteres, especialmente los monoéteres lineales, son los que presentan las mejores condiciones: elevado índice de cetano; temperaturas de ebullición dentro del rango del diésel; buen comportamiento en frío y; buena estabilidad de mezcla.[5] Además, se ha demostrado que la adición de éteres lineales al combustible diésel reduce las emisiones de CO, partículas sólidas e hidrocarburos y que mejora significativamente el balance entre partículas sólidas y NO_x.[6] El monoéter lineal di-n-butil éter (DNBE) presenta, además de todas estas propiedades, la ventaja de que puede ser obtenido a partir de biobutanol convirtiéndose así en un interesante candidato a biocombustible.

Los éteres lineales simétricos pueden sintetizarse mediante deshidratación bimolecular del correspondiente n-alcohol sobre un catalizador ácido;[7,8] consecuentemente el DNBE podría obtenerse a partir de 1-butanol. Actualmente el 1-butanol se produce a nivel industrial tanto por rutas biológicas (fermentación ABE[9,10] o catálisis Guerbet[11,9]) como por rutas petroquímicas (siendo la ruta más conocida el proceso Oxo[12]). La posterior deshidratación bimolecular del 1-butanol sobre un catalizador ácido daría lugar al DNBE. Hasta la fecha, la deshidratación de alcoholes a nivel industrial se ha llevado a cabo utilizando ácido sulfúrico como catalizador.[13] Sin embargo, el uso de catalizadores sólidos presenta importantes ventajas tanto medioambientales como económicas. A este respecto, varios trabajos en los últimos años han demostrado que las resinas de intercambio iónico ácidas pueden catalizar la deshidratación de alcoholes para dar lugar selectivamente al correspondiente éter lineal.[14-17] Sin embargo, no se ha encontrado en la bibliografía información relacionada con la síntesis de DNBE sobre resinas de intercambio iónico. El objetivo de este trabajo es estudiar la deshidratación en fase líquida del 1-butanol a DNBE sobre resinas de intercambio iónico.

La mayoría de las resinas de intercambio iónico comerciales están basadas en un copolímero de estireno y divinilbenceno, P(E-DVB). Dichas resinas se preparan normalmente mediante polimerización en suspensión dando lugar a pequeñas esferas de copolímero.[18] Tras la polimerización, las esferas de P(E-DVB) se someten a un proceso de funcionalización en el cual los anillos aromáticos de ambos monómeros pueden reaccionar con diferentes reactivos, principalmente electrofílicos, con la consiguiente introducción de, al menos, un grupo activo en cada anillo aromático.[19] Esta post-funcionalización puede dar lugar a resinas con elevadas capacidades de intercambio.

En base a su estructura (la cual viene determinada principalmente por las condiciones en las que se ha llevado a cabo la polimerización de la cadena polimérica) las resinas pueden clasificarse en dos grupos: las tipo gel y las macroreticulares. Las resinas tipo gel se caracterizan por presentar áreas superficiales muy bajas ($< 1\ m^2/g$) y porosidad prácticamente inexistente cuando se encuentran en estado seco. Sin embargo, en solventes polares se hinchan (estando el hinchamiento inversamente relacionado con la cantidad de DVB) creando espacios entre las cadenas de polímero. Por otro lado, las resinas macroreticulares sí que presentan porosidad, incluso en estado seco, y una mayor área superficial (hasta $100\ m^2/g$). Estas resinas también se hinchan en medio polar (aunque menos que las tipo gel) dando lugar a nuevos espacios.

Dado el importante papel que el medio en el cual están embebidas las resinas juega en la estructura polimérica de las mismas y por tanto en su accesibilidad, los métodos de porosimetría convencionales tales como intrusión de mercurio o la adsorción de nitrógeno (en los cuales las muestras deben de estar completamente secas) no proporcionan una descripción completa de dicha estructura. Hasta la fecha, la única técnica que permite aportar información de la estructura de las resinas en medio hinchado es la Cromatografía Inversa de Exclusión de tamaño (ISEC).[20-24]

La dificultad que entraña el estudio experimental de la estructura polimérica de las resinas de intercambio iónico y de su morfología en estado hinchando ha hecho que el uso de dichos catalizadores se base principalmente en estrategias de ensayo y error más que en un profundo entendimiento y diseño de sus parámetros. Sin embargo, para aprovechar todo el potencial que las resinas de intercambio iónico presentan como catalizadores es fundamental entender, describir y predecir el comportamiento de las mismas en el medio de reacción. A este respecto, la química computacional junto con el modelado molecular son actualmente herramientas muy útiles para investigar las propiedades y el comportamiento de materiales.

En esta tesis se han utilizado técnicas de química computacional con el objetivo de lograr una mayor comprensión de la estructura microscópica de las resinas de P(E-DVB) y para estudiar las interacciones resina/1-butanol.

2. Materiales y metodología

En este trabajo se utilizaron 13 resinas de P(E-DVB) con diferente grado de sulfonación, estructura, porcentaje en DVB y estabilidad térmica. Los experimentos de deshidratación se realizaron en un reactor discontinuo agitado de 100 mL de acero inoxidable 316 (Autoclave Engineers, M010SS, máxima temperatura de operación: 232 ºC; rango de presión: 0 – 150 bar). El reactor está equipado con un sistema de inyección neumático que permite cargar el catalizador, un agitador magnético y una manta calefactora de 400 W. La temperatura y la velocidad de agitación se miden mediante un termopar localizado en el interior del reactor y un tacómetro, respectivamente. Ambas variables se controlan con una precisión de ±1 ºC y ±1 rpm mediante una unidad de control electrónico. La toma de muestras se realiza mediante un sistema de muestreo conectado desde el reactor a una válvula de muestreo que inyecta 0.2 µL de líquido en un cromatógrafo de gases (Agilent Technologies, 7820A) equipado con un detector de conductividad térmica (TCD). Los detalles de la instalación se muestran en la Figura 1.

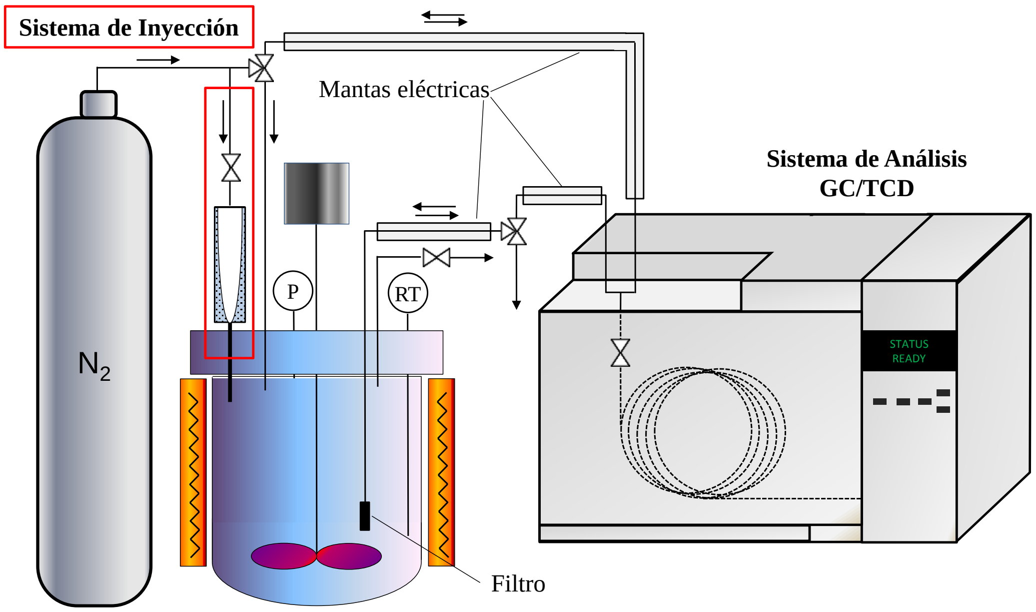

Figura 1. Esquema de la instalación.

Antes de ser usadas las resinas se sometieron a un pretratamiento: en primer lugar se secaron a temperatura ambiente durante 24 h; seguidamente se tamizaron en cuatro fracciones (<0.4, 0.4 – 0.63, 0.63 – 0.8, y >0.8); a continuación se secaron a 110 ºC y 1 bar durante 2h; y finalmente se secaron a 110 ºC y 10 mbar durante aproximadamente 15 h. En algunos experimentos las resinas se utilizaron sin tamizar (diámetro de partícula comercial).

En cada experimento el reactor se cargó con 70 mL de reactivos y, tras comprobar que no existían fugas, se fijó la velocidad de agitación y se calentó la mezcla hasta la temperatura de operación (140 – 190 ºC). Una vez alcanzada la temperatura deseada se inyectó el catalizador mediante transporte neumático y se ajustó la presión de operación a 40 bar mediante N_2 para mantener la fase líquida. En algunos experimentos el catalizador se introdujo directamente con la mezcla de reactivos. La composición del sistema se analizó a lo largo de todo el experimento (7 h para todos los experimentos excepto para los experimentos de equilibrio químico).

El estudio de la estructura molecular de las resinas (escala microscópica) y su relación con las propiedades (tanto microscópicas como macroscópicas) se llevó a cabo mediante simulaciones de Dinámica Molecular. La Dinámica Molecular es un algoritmo que intenta simular el comportamiento de un sistema sometiendo sus átomos a las leyes de la Mecánica Newtoniana. La trayectoria de la simulación se efectúa integrando las ecuaciones de Newton del movimiento (las interacciones entre las partículas se modelan con un campo de fuerza aproximado) a lo largo del tiempo para todas las partículas del sistema.[25]

3. Resultados y discusión

Del estudio sobre la deshidratación de 1-butanol sobre resinas de intercambio iónico ácidas se concluyó que además de la reacción principal de eterificación de 1-butanol a DNBE (R1), también tenían lugar otras reacciones secundarias. Las reacciones secundarias observadas fueron: la deshidratación intramolecular de 1-butanol a 1-buteno (R2); la isomerización de 1-buteno a *trans*- y *cis*- 2-buteno (R3); la hidratación de las olefinas para producir el alcohol secundario 2-butanol (R5); la reacción entre 1-butanol y las olefinas C_4 para dar lugar al éter ramificado 1-(1-metilpropoxi) butano (R6).

En la Figura 2 se muestra el esquema de reacción propuesto correspondiente a la deshidratación de 1-butanol.

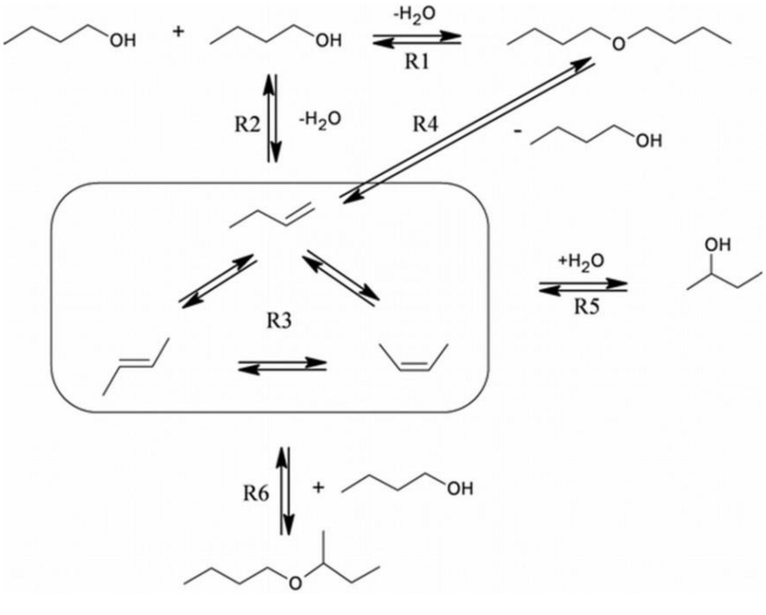

Figura 2. Esquema de reacción para la deshidratación de 1-butanol.

Análisis de la influencia de las propiedades de las resinas

Se observó que tanto la capacidad ácida de las resinas como su morfología (representada mediante el parámetro V_{sp}, volumen de polímero hinchado) juegan un papel decisivo a la hora de optimizar la producción de DNBE.

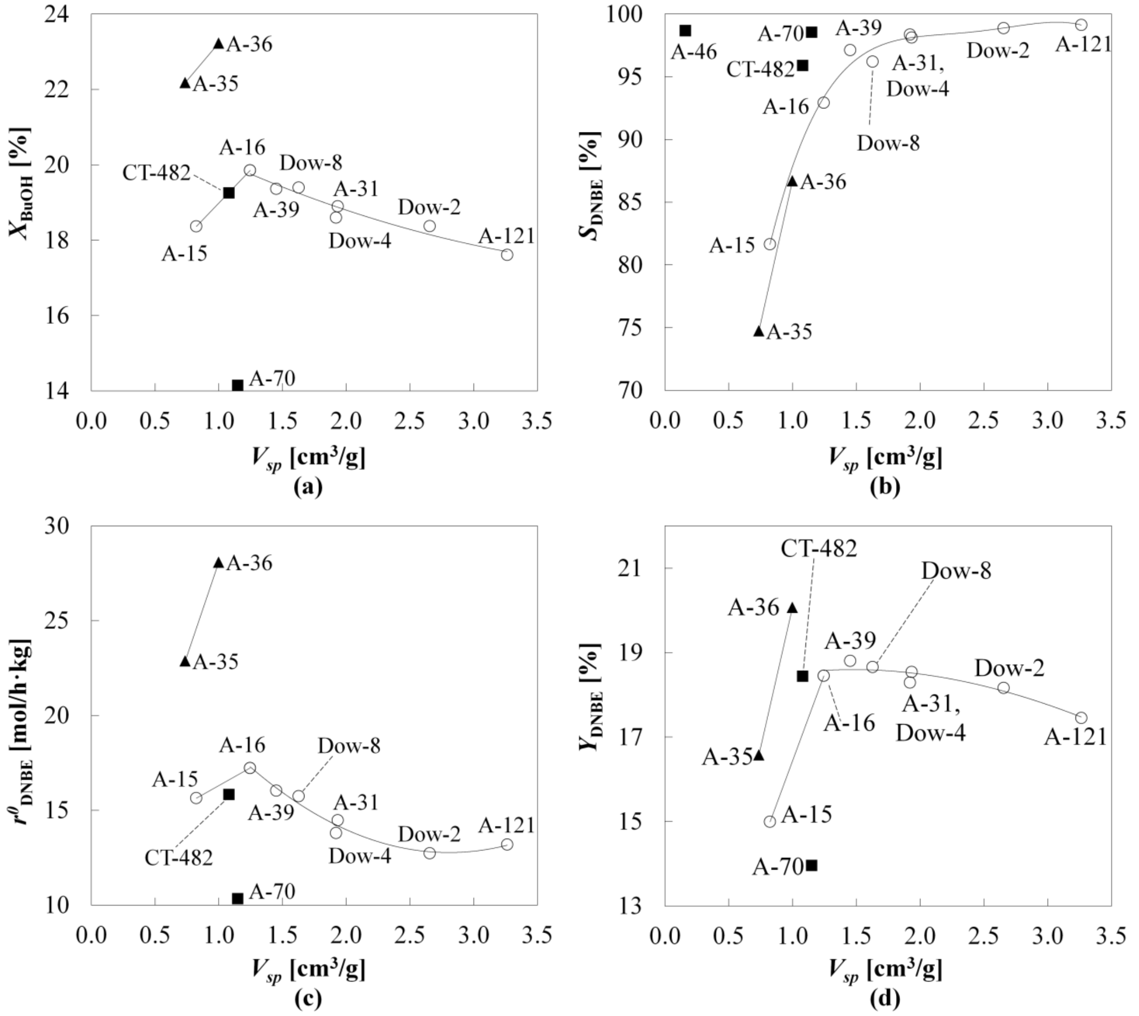

Figura 3. Influencia de la capacidad ácida y de la morfología de las resinas (V_{sp}) sobre: (a) la conversión de 1-butanol; (b) la selectividad DNBE; (c) velocidad inicial de formación de DNBE; (d) el rendimiento hacia DNBE.
Resinas con: (○) 4.8 meq.H^+/g; (♦) 5.3 meq.H^+/g; (■) otros valores de capacidad ácida.
t = 7 h, 1 g de catalizador, tamaño de partícula = 0.400 - 0.630 mm, T = 150 ºC, P = 40 bar, 500 rpm.

Una mayor capacidad ácida es esencial para lograr un catalizador más activo (Figuras 3a y c) sin embargo, también supone una menor selectividad hacia DNBE (Figura 3b). Por otro lado, la morfología de la matriz polimérica influencia en gran medida la selectividad hacia DNBE de las resinas (Figura 3b). Cuanto mayor es el espacio disponible generado en la fase gel de las resinas (lo cual se ve traducido en mayores valores de V_{sp}) mayor es la selectividad hacia el éter lineal. Por lo tanto, las resinas tipo gel que presentan elevados valores de V_{sp} (2-3 cm^3/g), son las que muestran una mayor selectividad hacia DNBE. La morfología de las resinas también influencia, aunque no tanto como la capacidad ácida, la actividad catalítica: una matriz polimérica muy densa dificulta la accesibilidad del 1-butanol a los centros activos y por lo tanto repercute negativamente en la actividad del catalizador; por otro lado, una matriz polimérica muy expandida supone una mayor distancia entre los centros activos, lo cual también puede perjudicar la conversión de 1-butanol. Se concluye por tanto que la conversión de 1-butanol se ve favorecida en resinas que presentan matrices poliméricas con densidades intermedias, tal y como reflejan las Figuras 3a y c.

Estabilidad térmica y reusabilidad de las resinas

Con el fin de estudiar la estabilidad térmica y la reusabilidad de los catalizadores, las resinas Amberlyst 31 y Amberlyst 15 (dos de las resinas que presentan temperaturas máximas de operación más bajas) fueron sometidas a tres ciclos de operación. Análisis posteriores indicaron que ambas resinas experimentaron una ligera pérdida de grupos sulfónicos. En cuanto a lo que área superficial BET se refiere, no se observó ningún cambio en la resina Amberlyst 31, sin embargo, el área superficial de la resina Amberlyst 15 aumento moderadamente. A pesar de los pequeños cambios observados en la capacidad ácida y en la morfología de las resinas, el comportamiento de ambos catalizadores (actividad y selectividad) se mantuvo constante durante los tres ciclos de operación. A pesar de ello, a la hora de diseñar un proceso industrial se recomienda utilizar la resina termoestable Amberlyst 70 (la cual presenta una excelente selectividad hacia DNBE) para reducir la pérdida de grupos sulfónicos.

Influencia de las impurezas típicas del 1-butanol

Otro factor que puede influenciar la deshidratación de 1-butanol es la existencia de impurezas en la corriente de alimentación. Las impurezas típicas del 1-butanol son isobutanol (cuando la ruta de obtención es el proceso Oxo) o etanol y acetona (cuanto se obtiene mediante fermentación ABE). Un estudio realizado sobre las resinas Amberlyst 70, Amberlyst 31 y Amberlyst 121 (tres de las resinas más selectivas) reveló que la presencia de isobutanol promueve la formación de los éteres ramificados 1-(1-metilpropoxi) butano y 1-(2-metilpropoxi) butano. La reacción entre 1-butanol y el carbocatión secundario resultante de la deshidratación y posterior transición del grupo alquilo del isobutanol da lugar a 1-(1-metilpropoxi) butano (ver Figura 4) mientras que el 1-(2-metilpropoxi) butano se forma a partir de la reacción entre 1-butanol e isobutanol (ver reacción R1).

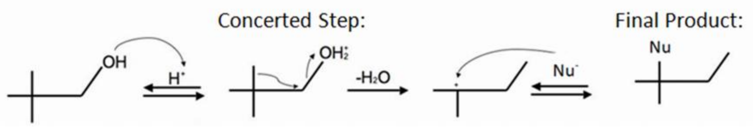

Figura 4. Mecanismo de transposición del grupo alquilo.

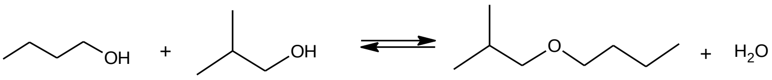

(R1)

Por otro lado, la presencia de etanol y acetona en la corriente alimentación da lugar a la formación del éter asimétrico butil etil éter (producto de la deshidratación bimolecular entre 1-butanol y etanol, reacción R2) y di-etil éter (consecuencia de la deshidratación intermolecular del etanol, reacción R3).

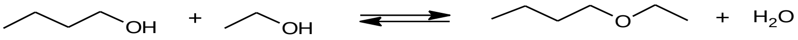

(R2)

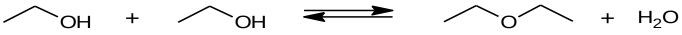

(R3)

Equilibrio termodinámico

A partir de la composición en el equilibrio de la mezcla de reacción se determinaron, de acuerdo con la ecuación (1), las constantes de equilibrio, K_{eq}, (en el rango de temperaturas 413-463 K) de la reacción de formación de DNBE a partir de 1-butanol, así como de las reacciones secundarias.

$$K_{eq} = \prod_{j=1}^{S} \left(a_j\right)_e^{\nu_j} = \prod_{j=1}^{S} \left(\gamma_j\right)_e^{\nu_j} \left(x_j\right)_e^{\nu_j} \qquad (1)$$

Los coeficientes de actividad (γ_j) para cada una de las especies (*j*) se estimaron con el método UNIFAC-Dortmund.[26-29]

Los resultados obtenidos indican que la K_{eq} correspondiente a la formación de DNBE es suficientemente alta como para asegurar que, en el equilibrio, la reacción está desplazada hacia la formación del éter. Además, la formación de 1-buteno es considerablemente lenta siendo muy baja la cantidad de olefina detectada en el medio de reacción. Consecuentemente, la cantidad del resto de subproductos es también muy baja. Todo ello aseguraría una buena conversión de 1-butanol hacia DNBE en un posible proceso de eterificación industrial.

A partir de la dependencia de las constantes de equilibrio con la temperatura (ver Figura 5) se puede concluir que las reacciones de isomerización de olefinas (Figura 5b), las de formación de 2-butanol a partir de olefinas (Figura 5c) y las de formación del éter ramificado (Figura 5d) son reacciones exotérmicas. Sin embargo, la constante de equilibrio correspondiente a la reacción de formación de DNBE es prácticamente independiente de la temperatura de operación (Figura 5a), pudiendo considerarse una reacción atérmica. En la Figura 5 no se han incluido los resultados correspondientes a la formación de 1-buteno ya que, tras más de 450 h de experimento, esta reacción no alcanzó el equilibrio; sin embargo, los datos sugieren que se trata de una reacción endotérmica.

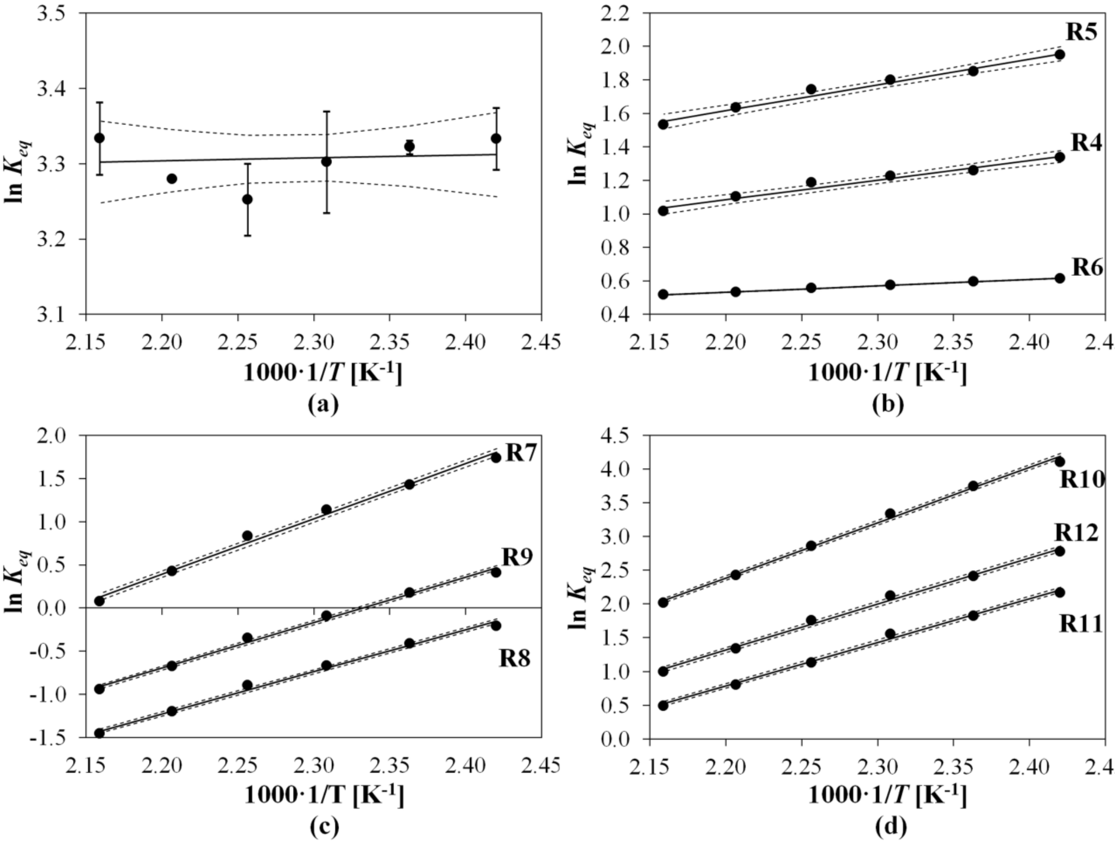

Figura 5. Variación de ln K_{eq} con 1/T considerando constantes las $\Delta_r H^0_{i,(l)}$ en el rango de temperaturas explorado. (a) R1: reacción de formación de DNBE; (b) reacciones de isomerización: 1-buteno a *cis*-2-buteno (R4), 1-buteno a *trans*-2-buteno (R5), *cis*-2-buteno a *trans*-2-buteno (R6); (c) Reacciones de hidratación de las olefinas: 1-buteno (R7), *trans*-2-buteno (R8) y *cis*-2-buteno (R9); (d) formación del éter 1-(1-metilpropoxi) butano por reacción de 1-butanol con una olefina: 1-buteno (R10), *trans*-2-buteno (R11), *cis*-2-buteno (R12).

A partir de los valores de las constantes de equilibrio y mediante la ecuación de van´t Hoff (Ecuación 2) se determinaron la entalpía standard ($\Delta_r H^0_{i,(l)}$), la entropía estándar ($\Delta_r S^0_{i,(l)}$) y la energía libre de Gibbs estándar ($\Delta_r G^0_{i,(l)}$) para cada una de las *i* reacciones. Para ello se asumió que las entalpías de reacción no varían en el rango de temperaturas estudiado. El valor experimental encontrado correspondiente a la entalpía de la reacción de deshidratación de 1-butanol a DNBE es de -0.3 ± 2.9 kJ·mol^{-1}. Dicho valor concuerda con: el valor teórico estimado a partir de las entalpías de formación de los compuestos implicados en la reacción (-7.8 ± 9.8 kJ·mol^{-1}); el carácter atérmico de la reacción; y con la tendencia mostrada por otros éteres simétricos lineales (al disminuir la longitud del éter el valor de la entalpía de la reacción es menos negativo, es decir, la reacción es menos exotérmica).[30-31] Con respecto a la entropía de reacción, el valor experimental obtenido fue 26.8 ± 6.7 J·mol^{-1}·K^{-1}. A partir de los valores experimentales de entalpia y entropía de reacción se estimó el valor de la entalpia del formación del DNBE a 25 ºC, $\Delta_f H^0_{\mathrm{DNBE,(l)}}$ = -370.5 ± 10.9 kJ·mol^{-1} (el cual concuerda con el valor obtenido por Colomina et al.[33] a partir de entalpias de combustión) y el valor de la entropía de formación del DNBE a 25 ºC, $S^0_{\text{DNBE,(l)}}$ = 408.3 ± 6.8 J·mol^{-1}·K^{-1}(este valor es un 3% menos que el valor predicho mediante el método de estimación de Benson modificado por Verevkin[34]).

$$\ln K_{eq,i} = \frac{-\Delta_r G_i^0}{RT} = \frac{-\Delta_r H_i^0}{RT} + \frac{\Delta_r S_i^0}{R} \qquad (2)$$

Estudio cinético sobre Amberlyst 70

Con el objetivo de comprobar que los valores de velocidad de reacción observados no estaban influenciados por el efecto de la transferencia de materia o de la distribución de sólidos, se realizó un estudio preliminar para determinar las condiciones de operación óptimas (velocidad de agitación, masa de catalizador y diámetro de partícula). A partir de los resultados obtenidos se concluyó que operando con una masa de Amberlyst 70 de 1g, diámetro de partícula de 0.4-0.63 mm y velocidad de agitación de 500 rpm aseguramos que los valores de velocidad de reacción observados no están afectados por procesos físicos de transferencia.

82 modelos cinéticos basados en los mecanismos Langmuir-Hinshelwood-Hougen-Watson (LHHW) y Eley Rideal (ER) se tuvieron en cuenta para describir la formación de DNBE. Todos ellos se ajustaron a los datos de velocidad de reacción minimizando la suma de los errores relativos cuadráticos (*SSRE*). Además, con el fin de cuantificar el efecto desactivador/inhibidor del agua en la velocidad de reacción se incorporaron factores correctores de la constante de reacción. Dichos factores correctores se basan en cuantificar la fracción de centros activos bloqueados por el agua mediante isotermas de adsorción. Las isotermas consideradas en el presente trabajo derivan de las isotermas de Langmuir (Ecuaciones 3 y 4) y de Freundlich (Ecuación 5).[35-37] De nuevo, los modelos modificados con los factores de corrección se ajustaron a los datos de velocidad de reacción minimizando la suma de los errores relativos cuadráticos. Se analizaron todos los ajustes, descartando inicialmente los modelos cuyas constantes de adsorción implicaban entalpías y/o entropías de adsorción positivas así como aquellos modelos con energías de activación negativas. Una vez seleccionados los modelos con coherencia fisicoquímica se procedió a evaluar y seleccionar el modelo que más se ajustaba a los datos experimentales por criterios matemáticos de ajuste (suma mínima de errores relativos cuadráticos, *SSRE*, distribución aleatoria de los residuos y menor incertidumbre en sus parámetros, Δ).

$$\left(\frac{1}{1+K_w \cdot a_{\mathrm{H_2O}}}\right)^{m_\sigma} \qquad (3)$$

$$\left(\frac{1}{1+K_w \cdot a_{\mathrm{H_2O}}^{0.5}}\right)^{m_\sigma} \qquad (4)$$

$$\left(1\text{-}K_w\cdot a_{\mathrm{H_2O}}^{1/\alpha}\right)^{m_\sigma} \qquad \text{con } \alpha = K_\alpha/T \tag{5}$$

A continuación se muestran los modelos que mejor se ajustan a los datos cinéticos. Los resultados de dichos ajustes se recogen en la Tabla 1:

$$r_{\mathrm{DNBE}} = \frac{\hat{k}\cdot\dfrac{K_{\mathrm{BuOH}}^{2}}{K_{\mathrm{BuOH}}^{2+n_\sigma}}\left(a_{\mathrm{BuOH}}^{2} - \dfrac{a_{\mathrm{DNBE}}\cdot a_{\mathrm{H_2O}}}{K_{eq}}\right)}{\left(a_{\mathrm{BuOH}} + \dfrac{K_{\mathrm{DNBE}}}{K_{\mathrm{BuOH}}}\cdot a_{\mathrm{DNBE}}\right)^{2+n_\sigma}}\left(1\text{-}K_w a_{\mathrm{H_2O}}^{1/\alpha}\right)^{2+n_\sigma} \tag{6}$$

$$r_{\mathrm{DNBE}} = \frac{\dfrac{k_{\mathrm{H_2O}}}{K_{\mathrm{H_2O}}}\left(K_{eq}\dfrac{a_{\mathrm{BuOH}}^{2}}{a_{\mathrm{DNBE}}} - a_{\mathrm{H_2O}}\right)}{\dfrac{K_{\mathrm{BuOH}}}{K_{\mathrm{H_2O}}}\cdot a_{\mathrm{BuOH}} + K_{eq}\dfrac{a_{\mathrm{BuOH}}^{2}}{a_{\mathrm{DNBE}}}}\left(1\text{-}K_w a_{\mathrm{H_2O}}^{1/\alpha}\right) \tag{7}$$

Se consideró que la dependencia de las constantes de velocidad ($\hat{k}$ and k_j) con la temperatura sigue la ley de Arrhenius (Ecuación 8) mientras que las constantes de adsorción (K_j) siguen la ley de Van’t Hoff (Ecuación 9). Con respecto a la constante K_w, se consideró que su dependencia con la temperatura viene dada por la Ecuación 10. Las tres Ecuaciones (8-10) se reparametrizaron para evitar una fuerte correlación entre sus parámetros.

$$\hat{k}, k_j = A\cdot\exp\left[-\frac{E_A}{R}\left(\frac{1}{T} - \frac{1}{T_{ref}}\right)\right] \tag{8}$$

$$K_j = \exp\left[\frac{\Delta S_j}{R} - \frac{\Delta H_j}{R}\left(\frac{1}{T} - \frac{1}{T_{ref}}\right)\right] \tag{9}$$

$$K_w = \exp\left[K_{w_1} - K_{w_2}\left(\frac{1}{T} - \frac{1}{T_{ref}}\right)\right] \tag{10}$$

El primer modelo (Ecuación 6) es el resultado de considerar un mecanismo LHHW en el cual dos moléculas de 1-butanol adsorbidas sobre la superficie del catalizador reaccionan para dar lugar a una molécula de DNBE y agua siendo la reacción en superficie la etapa limitante (a partir de los resultados es difícil distinguir el número de centros activos que participan en la reacción en superficie). La Ecuación 6 considera que el número de centros activos libres es muy inferior al número de centros activos ocupados y que la adsorción de agua es despreciable, sin embargo, el agua bloquea los centros activos inhibiendo la reacción de formación de DNBE.

La Ecuación 7 deriva de un mecanismo en el cual la etapa limitante es la desorción del agua y donde la adsorción del DNBE y el número de centros activos libres son despreciables. A partir de la Ecuación 7 es imposible discernir si se trata de un mecanismo LHHW o un mecanismo ER donde al agua permanece adsorbida en la superficie del catalizador (ambos mecanismos dan lugar a la misma expresión cinética).

Tabla 1. Resultados de los ajustes correspondientes a las Ecuaciones 6 y 7.

Ecuación 6			
n_σ	**0**	**1**	**2**
SSRE:	1.24	1.38	1.50
R^2_{adj} :	0.99	0.99	0.99
Δ:	2.50	0.84	0.54
Parámetros			
A:	25.4 ± 1.1	24.9 ± 1.0	24.7 ± 1.0
E_A [kJ/mol]:	121.7 ± 1.8	122.2 ± 1.9	122.6 ± 2.0
$\Delta S_{DNBE}–\Delta S_{BuOH}$ [J/mol·K]:	-9.6 ± 1.7	-7.2 ± 0.9	-6.3 ± 0.7
$\Delta H_{DNBE}–\Delta H_{BuOH}$ [kJ/mol]:	61.2 ± 12.9	42.6 ± 7.5	36.1 ± 5.4
K_{w1}:	-0.08 ± 0.03	-0.20 ± 0.03	-0.29 ± 0.02
K_{w2}:	73.3 ±180.4	233.1 ± 184.6	364.2 ± 178.6
K_α:	563.2 ± 42.4	499.4 ± 31.5	471.8 ± 26.2

Ecuación 7						
SSRE = 1.34			R^2_{adj} = 0.98		Δ = 2.54	
Parámetros						
A	E_A [kJ/mol]	ΔS_{BuOH} - ΔS_{H2O} [J/mol·K]	ΔH_{BuOH} - ΔH_{H2O} [kJ/mol]	K_{w1}	K_{w2}	K_α
29.7±2.1	121.3±1.8	22.8±2.0	83.7±15.4	0.09±0.02	36.8±92.5	1018±128

Los cuatro modelos (con n_σ = 0, 1 y 2 en Ecuación 6) presentan valores muy similares de energías de activación aparente (E_A = 122 ± 2 kJ/mol). Este valor es ligeramente superior al encontrado en la bibliografía para la deshidratación sobre Amberlyst 70 de 1-pentanol a di-n-pentil éter[38] (114.0 ± 0.1 kJ/mol) y 1-octanol a di-n-octil éter[39] (110 ± 5 kJ/mol) y muy similar a la energía de activación correspondiente a la deshidratación de 1-hexanol a di-n-hexil éter[40] (121 ± 3 kJ/mol). Por otro lado, los valores de los parámetros obtenidos indican que el proceso de adsorción de 1-butanol está más favorecido termodinámicamente que el de adsorción de DNBE (Ecuación 6) mientras que el proceso de adsorción de agua está más favorecido termodinámicamente que el de adsorción de 1-butanol. Esta tendencia concuerda con la polaridad de los compuestos y la elevada afinidad del agua por la resina.

En la Figura 6 se puede observar que las Ecuaciones 6 (con n_σ = 0) y 7 son capaces de predecir satisfactoriamente los resultados experimentales.

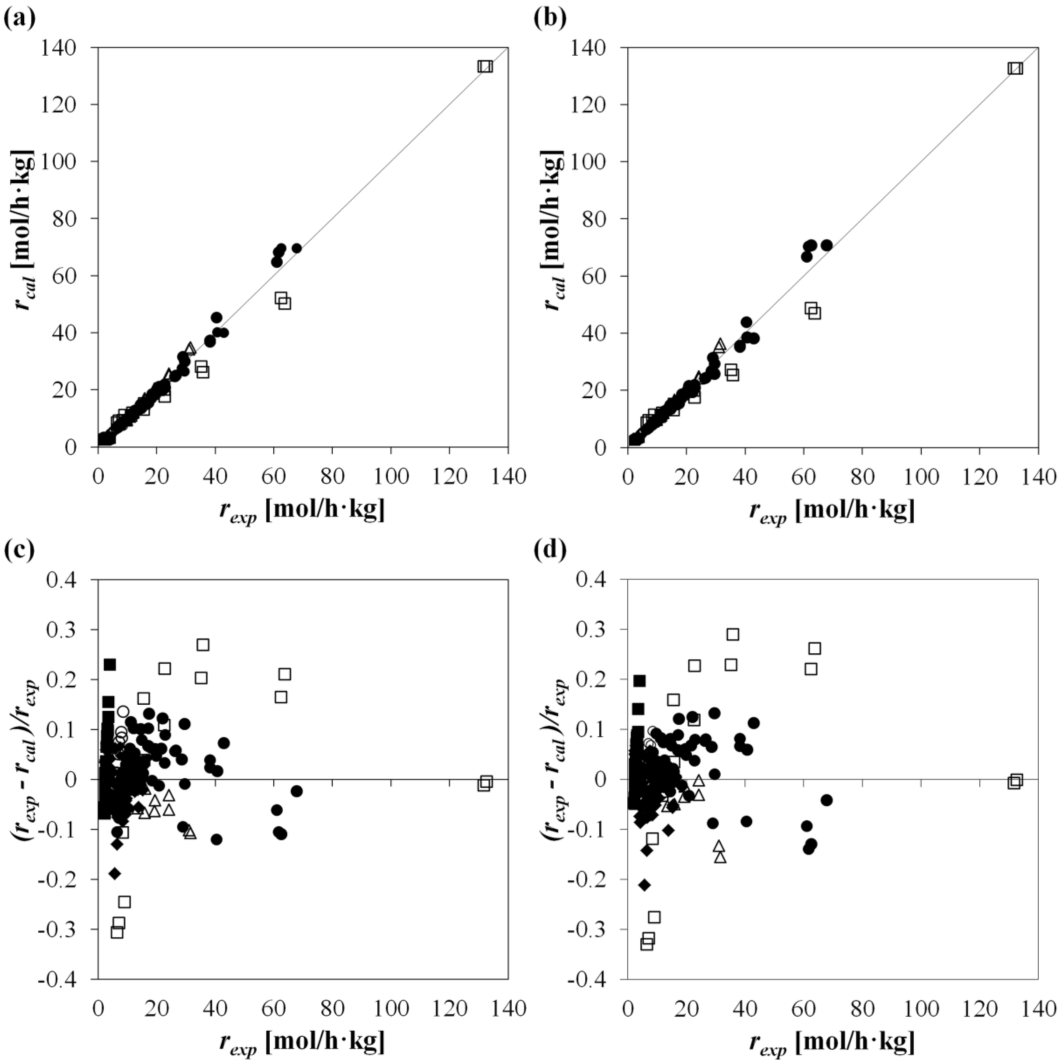

Figura 6. Velocidades de reacción calculadas mediante la Ecuación 6 con $n_\sigma = 0$ (a) y la Ecuación 7 (b) versus velocidades experimentales. Distribución de residuos correspondientes a los modelos Ecuación 6 con $n_\sigma = 0$ (c) y Ecuación 7 (d).

Modelado y simulación de las resinas de P(E-DVB)

Uno de los objetivos de este trabajo era obtener un modelo atomístico realista de la matriz polimérica de las resinas de intercambio iónico. Con este fin se desarrollaron dos algoritmos de tipo estocástico: el primero de ellos, denominado HGA (de Homogeneous Generation Approach), permite la construcción de matrices de P(E-DVB) formadas por cadenas poliméricas de la misma longitud (mismo número de monómeros); el segundo algoritmo, denominado CGA (de Combined Growing Approach), permite generar matrices de polímero las cuales presentan una topología compleja caracterizada por una muy heterogénea distribución de entrecruzamientos y de longitudes de cadena polimérica y por la existencia de ciclos (cadenas de polímero cerradas) de diferente tamaño.

Como referencia para modelar la resina de P(E-DVB) se seleccionó la resina comercial Amberlyst 15 (macroreticular, monosulfonada y con un alto grado de entrecruzamiento). Las microestructuras generadas con el algoritmo HGA y posteriormente relajadas utilizando dinámica molecular, las cuales no reflejan la heterogeneidad típicamente asociada a la resinas con alto grado de entrecruzamiento, no son capaces de reproducir propiedades esenciales tales como la densidad aparente o la porosidad. Estas estructuras tienden a sobreestimar la densidad aparente y subestimar la porosidad con respecto a los valores experimentales. Por otro lado, las matrices heterogéneas en las cuales las cadenas poliméricas se cierran formando ciclos (tales como las que se obtienen con el algoritmo CGA) sí que consiguen reproducir los valores experimentales de densidad y porosidad.

Un estudio detallado de la estructura de la resina reveló que, a pesar de que la existencia de ciclos en la red polimérica de la resina no afecta a las propiedades estructurales locales, sí que afecta a la distribución de densidad local y por lo tanto a la distribución de los grupos sulfónicos (los grupos sulfónicos tienden a estar localizados en las regiones de la matriz que presentan menor densidad), a las propiedades estructurales a medio y largo alcance y a la disposición relativa de los anillos bencénicos.

Absorción de 1-butanol en resinas de P(E-DVB)

Mediante simulaciones de dinámica molecular se llevó a cabo el estudio del hinchamiento de una resina de P(E-DVB). A partir de los modelos generados en el apartado anterior (los cuales se construyeron con el grado de entrecruzamiento y la capacidad ácida correspondientes a la resina Amberlyst 15) se seleccionó la estructura polimérica que mejor reproducía los valores experimentales de densidad aparente, porosidad y volumen de poro de la resina Amberlyst 15 en estado seco. A continuación se añadió a dicha estructura diferentes concentraciones de 1-butanol y se estudió tanto la variación de volumen experimentada por la resina como el efecto que tiene la absorción de 1-butanol sobre la estructura polimérica de la resina a nivel molecular.

La Figura 7a muestra la variación de volumen (con respecto al volumen de la resina seca), ΔV, en función de la concentración de 1-butanol absorbida, así como el incremento de volumen que experimenta la resina Amberlyst 15 hinchada en 1-butanol determinado experimentalmente mediante difracción laser. Como puede observarse, bajas concentraciones de alcohol hacen que la resina se contraiga, lo cual supone un aumento importante de la densidad del sistema (Figura 7b). Sin embargo, concentraciones de 1-butanol superiores al 20% dan lugar a un rápido hinchamiento de la resina, traduciéndose en un progresivo descenso de la densidad (Figura 7b).

Los resultados mostrados en la Figura 7a sugieren que la máxima cantidad de 1-butanol absorbida por la resina (la cual causa un incremento de volumen equivalente al determinado experimentalmente) es de un 31-32%. Dicho valor reproduce muy bien el valor estimado indirectamente (31%) a partir de datos experimentales de diámetro de partícula (en seco e hinchada en 1-butanol), porosidad (en seco) y densidad de esqueleto de la resina.

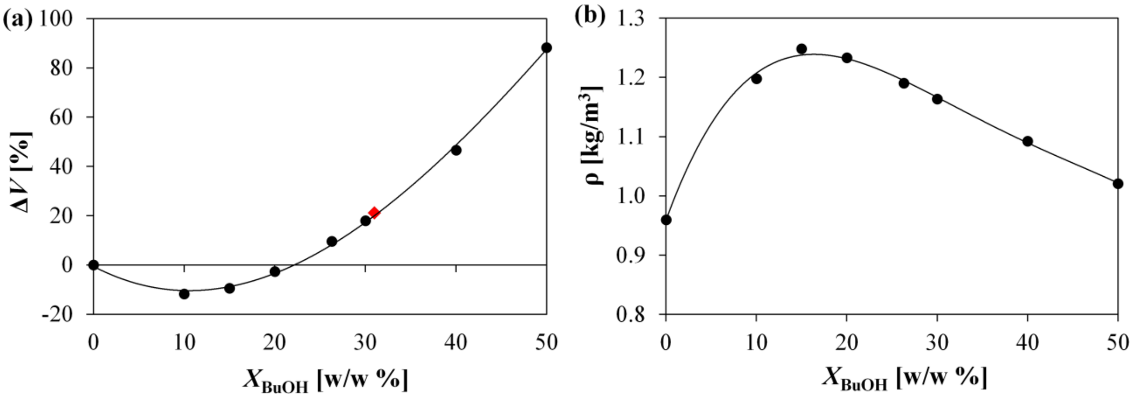

Figura 7. Variación de a) porcentaje de hinchamiento (Δ*V*) y b) densidad del sistema en función de la concentración de 1-butanol absorbida en la resina de P(E-DVB). El punto rojo representa el valor experimental de Δ*V* determinado mediante difracción laser.

Con el fin de estudiar el efecto de la absorción de 1-butanol sobre la estructura polimérica de la resina a nivel molecular se dividió la caja de simulación en 1000 celdas y para cada una de estas celdas se determinó la densidad aparente (ρ_a) de la resina. La Figura 8 muestra los histogramas de frecuencias de la densidad aparente de las 1000 celdas de la resina correspondientes a los sistemas resina/1-butanol con diferentes concentraciones de 1-butanol absorbido.

Como puede observarse, existen importantes diferencias estructurales entre los sistemas estudiados. En primer lugar, la resina seca (Figura 8a) presenta una importante cantidad de celdas vacías (con ρ_a muy próxima a 0 g/cm^3) las cuales forman la red de macroporos característica de las resinas macroreticulares. Pero además, la resina seca también presenta un importante número de celdas con $\rho_a > 1.5$ g/cm^3 correspondiente a zonas de la resina altamente densas y con difícil accesibilidad. Esta descripción de la estructura de la resina seca es consistente con la conocida estructura de las resinas macroreticulares con alto grado de entrecruzamiento.[18]

Para los sistemas en los cuales la concentración de 1-butanol absorbido es inferior a la concentración de equilibrio (10%, Figura 8b y 20%, Figura 8c) el número de celdas vacías disminuye considerablemente. Este descenso se atribuye a la contracción de la matriz polimérica observada en la Figura 7a. El colapso de los macroporos en los sistemas con 10 y 20% de 1-butanol da lugar, en términos generales, a resinas más densas que la resina seca. Sin embargo, si se tiene en cuenta la estructura local se puede concluir que las zonas altamente densas tienden a disminuir según aumenta la concentración de 1-butanol absorbida. Las moléculas de 1-butanol hacen que las cadenas de polímero se separen generando espacios libres entre ellas y dando paso a zonas ligeramente menos densas.

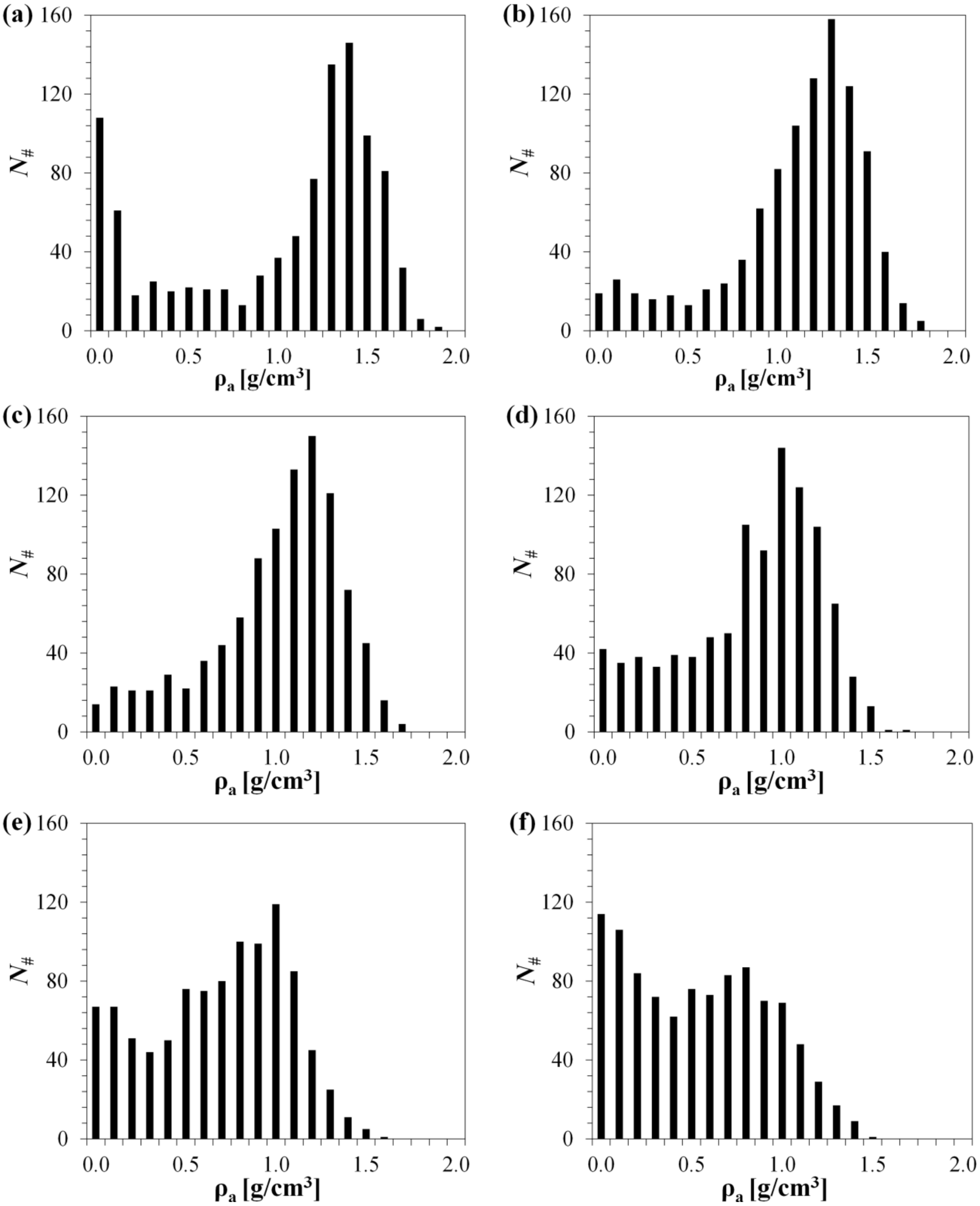

Figura 8. Histograma de frecuencias de la densidad aparente de la resina correspondiente a los sistemas con una concentración de 1-butanol absorbida de: a) 0%; b) 10%; c) 20%; d) 30%; e) 40%; y f) 50%.

Para el sistema en el cual la cantidad de 1-butanol absorbido es próxima a la concentración de equilibrio (30%, Figura 7d) se puede observar que la porosidad ha aumentado de manera significativa. Este sistema presenta una matriz polimérica expandida y más fácilmente accesible (como se deduce del elevado número de celdas con $\rho_a < 1.0$ g/cm^3). Además, las zonas altamente densas ($\rho_a > 1.5$ g/cm^3) tienden a desaparecer.

Finalmente, en los sistemas en los cuales la cantidad de alcohol absorbida es superior a la concentración de equilibrio (40 y 50%, Figuras 7e y f respectivamente) se puede observar que los perfiles han cambiado significativamente y la porosidad de la resina ha aumentado considerablemente. Sin embargo, esta estructura de la matriz polimérica es ficticia puesto que más moléculas de alcohol de las correspondientes a la concentración de equilibrio se han introducido “a la fuerza” y, una vez relajado el sistema, el exceso de alcohol da lugar a un sobre hinchamiento de la matriz.

A partir del estudio de la posición relativa de los componentes del sistema se puede concluir que, independientemente de la concentración de alcohol absorbida, las moléculas de 1-butanol tiende a localizarse cerca de los grupos sulfónicos.

4. Conclusiones

Se ha demostrado que las resinas de intercambio iónico son catalizadores apropiados para llevar a cabo la síntesis de DNBE a partir de 1-butanol. Las resinas con mayor capacidad ácida han demostrado ser catalizadores más activos. Sin embargo, las resinas tipo gel y la resina Amberlyst 70 son considerablemente más selectivas. Además de su excelente selectividad, la resina Amberlyst 70 presenta una mayor estabilidad térmica por lo que se considera el catalizador más adecuado para uso industrial.

El estudio termodinámico ha revelado que la constante de equilibrio correspondiente a la deshidratación bimolecular de 1-butanol a DNBE es relativamente alta e independiente de la temperatura de operación (en los límites del error experimental). Además, la formación de 1-buteno es considerablemente lenta y, por lo tanto, la cantidad de subproductos formada es muy baja. Todo ello asegura altos niveles de conversión en un proceso industrial.

El estudio cinético sobre la resina Amberlyst 70 ha permitido proponer dos modelos cinéticos que son capaces de predecir las velocidades de reacción experimentales. En los dos casos el importante efecto inhibitorio del agua se tiene en cuenta por medio de un factor de corrección. Ambos modelos presentan energías de activación aparente similares (122 ± 2 kJ/mol).

El modelado y las simulaciones de dinámica molecular revelaron que la heterogénea distribución de entrecruzamientos y de longitudes de cadena polimérica y la existencia de ciclos (cadenas de polímero cerradas) de diferente tamaño definen y caracterizan la estructura de las resinas de intercambio iónico y su comportamiento. Los modelos generados consiguen reproducir satisfactoriamente tanto importantes propiedades estructurales (densidad aparente y porosidad) como el hinchamiento de las resinas en 1-butanol.

El estudio microscópico del hinchamiento de la resina permitió caracterizar y cuantificar la estructura de la matriz polimérica a nivel molecular y confirmar que las moléculas de alcohol tienden a interaccionar con los grupos sulfónicos de la resina.

Nomenclatura

Notación

A	Factor preexponencial
a_j	Actividad correspondiente al compuesto *j*
E_A	Energía de activación
k_α	Parámetro K de Freundlich
$\hat{k}$	Constante de velocidad de la reacción en superficie directa
$K_{eq,i}$	Constante de equilibrio de la reacción *i*
k_j	Constante de velocidad de adsorción del compuesto *j*
K_j	Constante de equilibrio de adsorción del compuesto *j*
K_s	Constante de equilibrio de la reacción en superficie
K_w	Factor de corrección del agua
K_{w1}	Primer parámetro del factor de corrección del agua
K_{w2}	Segundo parámetro del factor de corrección del agua
m_σ	Número total de centros activos que participan en la reacción en superficie
$N_\#$	Frecuencia de las celdas
n_σ	Número de centros activos adicionales que participan en la reacción en superficie
R^2_{adj}	Bondad del ajuste
r_{cal}	Velocidad de reacción estimada
r_{exp}	Velocidad de reacción experimental
r_{DNBE}	Velocidad de la reacción de formación del DNBE
r^0_{DNBE}	Velocidad inicial de la reacción de formación de DNBE
S_{DNBE}	Selectividad hacia DNBE
$S^0_{j,(\mathrm{l})}$	Entropía molar estándar del compuesto *j* (en fase líquida)
T	Temperatura
T_{ref}	Valor central del rango de temperaturas analizado
v_j	Coeficiente estequiométrico del compuesto *j*
V_{sp}	Volumen de polímero hinchado
X_{BuOH}	Conversión del 1-butanol
x_j	Fracción molar del compuesto *j*
Y_{DNBE}	Rendimiento hacia di-n-butil éter

Símbolos griegos

α	Constante de Freundlich

γ_j	Coeficiente de actividad del compuesto *j*
Δ	Incertidumbre de los parámetros
$\Delta_f H^0_{j,(\mathrm{l})}$	Entalpía de formación standard del compuesto *j*(en fase líquida)
ΔG_j	Energía libre de Gibbs de adsorción del compuesto *j*
ΔH_j	Entalpía de adsorción del compuesto *j*
ΔS_j	Entropía de adsorción del compuesto *j*
$\Delta_r G^0_{i,(\mathrm{l})}$	Energía libre de Gibbs estándar de la reacción *i*
$\Delta_r H^0_{i,(\mathrm{l})}$	Entalpía estándar de la reacción *i*
$\Delta_r S^0_{i,(\mathrm{l})}$	Entropía estándar de la reacción *i*
ΔV	Incremento de volumen
ρ_a	Densidad aparente de la resina

Abreviaturas

ABE	Acetona-Butanol-Etanol
BET	Brunauer-Emmet-Teller
CGA	Algoritmo de crecimiento combinado (del inglés Combined Growing Approach)
DNBE	Di-n-butil éter
DVB	Divinilbenceno
ER	Eley Rideal
HGA	Algoritmo de generación homogénea (del inglés Homogeneous Generation Approach)
ISEC	Cromatografía inversa de exclusión de tamaño (del inglés Inverse Steric Exclusion Chromatography)
LHHW	Langmuir-Hinshelwood-Hougen-Watson
P(E-DVB)	Poli(estireno-divinilbenceno)
SSRE	Suma cuadrática de errores relativos
TCD	Detector de conductividad térmica

Bibliografía

[1] Nabi, M. N.; Kannan, D.; Hustad, J. E.; Rahman, M. M. Role of oxygenated fuel to reduce diesel emissions: A Review. *Proceedings of the International Conference on Mechanical Engineering*, Dhaka, Bangladesh, Dec 26-28, 2009.

[2] Golubkov, A. Motor fuel for diesel engines. Patent WO 2001018154 A1, March 15, 2001.

[3] Alander, T. J. A.; Leskinen, A. P.; Raunemaa, T. M.; Rantanen, L. Characterization of diesel particles: effects of fuel reformulation, exhaust aftertreatment, and engine operation on particle carbon composition and volatility. *Environ. Sci. Technol*. **2004**, *38*, 2707 -2714.

[4] Arteconi, A.; Mazzarini, A.; Di Nicola, G. Emissions from ethers and organic carbonate fuel additives: A Review. *Water, Air, Soil Pollut*. **2011**, *221*, 405 - 423.

[5] Pecci, G. C.; Clerici, M. G.; Giavazzi, F.; Ancillotti, F.; Marchionna, M.; Patrini, R. Oxygenated fuel diesel. Part-1 structure and properties correlations. *9th Int. Symp. Alcohol Fuels* **1991**, *1*, 321 - 326.

[6] Marchionna, M.; Patrini, R.; Giavazzi, F.; Pecci, G. C. Linear ethers as high-quality components for reformulated diesel fuels. *Symposium on Removal of Aromatics, Sulfur and Alkenes from Gasoline and Diesel*, 212th National Meeting, American Chemical Society: Washington DC, **1996**, 585 - 589.

[7] Starkey, L. S. In *Introduction to strategies for organic synthesis*, 2nd ed.; John Wiley & Sons, Inc., Hoboken: New Jersey, 2012; pp 67-71.

[8] Sheldon, R. A.; van Bekkum, H. In *Fine chemical through heterogeneous catalysis*, Wiley-VCH: Weinheim, Germany, 2001; Chapter 6.5.

[9] European biofuels technology platform. http://www.biofuelstp.eu/butanol.html (accessed April 2015)

[10] AIChE. BP, ABF, and DuPont unveil plans for grassroots biofuels plant. *Chem. Eng. Prog.* **2007**, *103*, 14. New York: American Institute of Chemical Engineers.

[11] Tsuchida, T.; Sakuma, S.; Takeguchi, T.; Ueda, W. Direct synthesis of n-butanol from ethanol over nonstoichiometric hydroxyapatite. *Ind. Eng. Chem. Res.* **2006**, *45*, 8634-8642.

[12] Report Abstract. Oxo Alcohols PERP06/07-8, February 2009. http://www.chemsystems.com

[13] Guilera, J. Ethyl octyl ether synthesis from 1-octanol and ethanol or diethyl carbonate on acidic ion-exchange resins. Ph.D. Thesis, University of Barcelona, June 2013.

[14] Tejero, J.; Cunill, F.; Iborra, M.; Izquierdo, J. F.; Fité, C. Dehydration of 1-pentanol to di-n-pentyl ether over ion-exchange resin catalysts. *J. Mol. Catal. A: Chem*. **2002**, *182*, 541-554.

[15] Bringué, R.; Iborra, M.; Tejero, J.; Izquierdo, J. F.; Cunill, F.; Fité, C.; Cruz, V. F. Thermally stable ion-exchange resins as catalysts for the liquid-phase dehydration of 1-pentanol to di-n-pentyl ether (DNPE). *J. Catal*. **2006**, *244*, 33-42.

[16] Medina, E.; Bringué, R.; Tejero, J.; Iborra, M.; Fité, C. Conversion of 1-hexanol to di-n-hexyl ether on acidic catalysts. *Appl. Catal., A*. **2010**, 374, 41-47.

[17] Casas, C.; Bringué, R.; Ramírez, E.; Iborra, M.; Tejero, J.; Liquid-phase dehydration of 1-octanol, 1-hexanol and 1-pentanol to linear symmetrical ethers over ion exchange resins. *Appl. Catal., A*. **2001**, 396, 129-139.

[18] Sherrington, D. C. Preparation, structure and morphology of polymer supports. *Chem Commun*. **1998**, *21*, 2275–2286.

[19] Coutinho, F. M. B.; Rezende, S. M.; Soares, B. G. Characterization of sulfonated poly(styrene–divinylbenzene) and poly(divinylbenzene) and its application as catalysts in esterification reaction. *J. Appl. Polym. Sci*. **2006**, *102*, 3616–3627.

[20] Jerabek, K. in *Cross-evaluation of strategies, size-exclusion chromatography. (Inverse steric exclusion chromatography as a tool for morphology characterization)*, ACS Symposium Series 635, American Chemical Society, Washington, DC, USA, 1996; 211.

[21] Jerabek, K. Determination of pore volume distribution chromatography data from size exclusion. *Anal. Chem.* **1985**, *57,* 1595–1597.

[22] Jerabek, K. Characterization of swollen polymer gels using size exclusion chromatography. *Anal. Chem*. **1985**, *57,* 1598–1602.

[23] Centomo, P.; Jerabek, K.; Canova, D.; Zoleo, A.; Maniero, A. L.; Sassi, A.; Canton, P.; Corain, B.; Zecca, M. Highly hydrophilic copolymers of N,N-dimethylacrylamide, acrylamido-2-methylpropanesulfonic acid, and ethylenedimethacrylate: nanoscale morphology in the swollen state and use as exotemplates for synthesis of nanostructured ferric oxide. *Chem. Eur. J.* **2012**, *18*, 6632 – 6643.

[24] Corain, B.; Zecca, M.; Jerabek, K. Catalysis and polymer networks - the role of morphology and molecular accessibility. *J. Mol. Catal. A Chem*. **2001**, *177*, 3–20.

[25] Alemán, C.; Muñoz-Guerra, S. Aplicaciones de los Métodos Computacionales al Estudio de la Estructura y Propiedades de Polímeros. Polímeros: Ciência e Tecnologia, **2003**, *13* (4), 250-264.

[26] Weidlicht, U.; Gmehling, J. A modified UNIFAC model. 1. Prediction of VLE, h^E, and γ^∞. *Ind. Eng. Chem. Res.* **1987**, *26* (7), 1372-1381.

[27] Gmehling, J.; Li, J.; Schiller M. A modified UNIFAC model. 2. Present parameter matrix and results for different thermodynamic properties. *Ind. Eng. Chem. Res*. **1993**, *32*, 178-193.

[28] Gmehling, J.; Lohmann, J.; Jakob, A.; Li, J.; Joh, R. A modified UNIFAC (Dortmund) model. 3. Revision and extension. *Ind. Eng. Chem. Res.* **1998**, *37*, 4876-4882.

[29] Jakob, A.; Grensemann, H.; Lohmann, J.; Gmehling, J. Further development of modified UNIFAC (Dortmund): revision and extension 5. *Ind. Eng. Chem. Res.* **2006**, *45*, 7924-7933.

[30] Bringué, R.; Tejero, J.; Iborra, M.; Fité, C.; Izquierdo, J. F.; Cunill, F. Study of the chemical equilibrium of the liquid-phase dehydration of 1-hexanol to di-hexyl ether. *J. Chem. Eng. Data* **2008**, *53*, 2854-2860.

[31] Bringué, R.; Tejero, J.; Iborra, M.; Izquierdo, J.F.; Fite, C.; Cunill, F. Experimental study of the chemical equilibria in the liquid-phase dehydration of 1-pentanol to di-n-pentyl ether. *Ind. Eng. Chem. Res*. **2007**, *46*, 6865-6872.

[32] Casas, C.; Fité, C.; Iborra, M.; Tejero, J.; Cunill, F. Chemical equilibrium of the liquid-phase dehydration of 1-octanol to 1-(Octyloxy)octane. *J. Chem. Eng. Data* **2013**, *58*, 741-748.

[33] Colomina, M.; Pell, A.S.; Skinner, H.A.; Coleman, D.J. Heats of combustion of four dialkylethers. *Trans. Faraday Soc*. **1965**, *61*, 2641.

[34] Verevkin S. P. Improved Benson increments for the estimation of standard enthalpies of formation and enthalpies of vaporization of alkyl ethers, acetals, ketals, and ortho esters. *J. Chem. Eng. Data* **2002**, *47*, 1071-1097.

[35] du Toit, E.; Nicol, W. The rate inhibiting effect of water as a product on reactions catalysed by cation exchange resins: formation of mesityl oxide from acetone as case study. *App. Catal., A.* **2004**, *277*, 219-225.

[36] Limbeck, U.; Altwicker, C.; Kunz, U.; Hoffmann, U. Rate expression for THF synthesis on acidic ion exchange resin. *Chem. Eng. Sci*. **2001**, *56*, 2171-2178.

[37] Yang, B.-L.; Maeda, M.; Goto, S. Kinetics of liquid phase synthesis of tert-amyl methyl ether from tert-amyl alcohol and methanol catalyzed by ion exchange resin. J. *Chem. Kinet.* **1997**, *30*, 137-143.

[38] Bringué, R.; Ramírez, E.; Fité, C.; Iborra, M.; Tejero, J. Kinetics of 1-pentanol etherification without water removal. *Ind. Eng. Chem. Res*. **2011**, *50*, 7911-7919

[39] Casas, C. Synthesis of C_{10}-C_{16} linear symmetrical ethers from n-alcohols over heterogeneous acid catalysts. Ph.D. Thesis, University of Barcelona, Spain, 2013.

[40] Bringué, R.; Ramírez, E.; Iborra, M.; Tejero, J.; Cunill, F. Kinetics of 1-hexanol etherification on Amberlyst 70. *Chem. Eng. J.* **2014**, *246*, 71–78.

LIST OF PUBLICATIONS

Pérez, M. A.; Bringué, R.; Iborra, M.; Tejero, J.; Cunill, F. Ion exchange resins as catalysts for the liquid-phase dehydration of 1-butanol to di-n-butyl ether. *Appl. Catal., A.* **2014**, *482*, 38-48.

Pérez-Maciá, M. A.; Curcó, D.; Bringué, R.; Iborra, M.; Alemán, C. Atomistic simulations of the structure of highly cross-linked sulfonated poly(styrene-co-divinylbenzene) ion exchange resins. *Soft Matter* **2015**, *11*, 2251–2267.

Pérez-Maciá, M. A.; Bringué, R.; Iborra, M.; Tejero, J.; Cunill, F. Thermodynamic equilibrium for the dehydration of 1-butanol to di-n-butyl ether. *Chem. Eng. Res. Des.* **2015**, *102*, 186–195.

Pérez-Maciá, M. A.; Bringué, R.; Iborra, M.; Tejero, J.; Cunill, F. Kinetic study of 1-butanol dehydration to di-n-butyl ether over Amberlyst 70. Submitted to the journal: *AIChE J.* on May 30th, 2015. Publication Status: Accepted.

WORK IN PROGRESS

Pérez-Maciá, M. A.; Curcó, D.; Bringué, R.; Iborra, M.; Rodríguez-Ropero, F.; van der Vegt, N. F. A.; Aleman, C. 1-Butanol absorption in poly(styrene-divinylbenzene) ion exchange resins for catalysis. Submitted to the journal: *Soft Matter* on August 2015. Publication status: Revised and resubmitted.

CONGRESSES PARTICIPATION

Sociedad Española de Catálisis, SECAT'13, *Resinas de intercambio iónico para la deshidratación de 1-butanol a di-n-butil éter.* Pérez, M. A.; Bringué, R.; Iborra, M.; Tejero, J.; Cunill, F. Sevilla (Spain), 2013. Oral Communication.

I Encuentro de Jóvenes Investigadores de la SECAT , *Resinas de intercambio iónico como catalizadores para la deshidratación selectiva del 1-butanol* . Pérez, M. A.; Bringué, R.; Iborra, M.; Tejero, J.; Cunill, F. Malaga (Spain), 2014. Flash oral communication + Poster

XXXI Annual Meeting of Reference Network of R+D+i on Theoretical and Computational Chemistry, *1-Butanol absorption in P(S-DVB) ion exchange resins*. Pérez-Maciá, M. A.; Curcó, D.; Bringué, R.; Iborra, M.; Alemán, C. Girona (Spain), 2015. Oral Communication.

Sociedad Española de Catálisis, SECAT'15, *Utilización de Amberlyst 70 en la síntesis de DNBE*. Pérez-Maciá, M. A.; Bringué, R.; Iborra, M.; Tejero, J.; Cunill, F. Barcelona (Spain), 2015. Poster.

12th European Congress on Catalysis –EuropaCat-XII, *Kinetics of the dehydration of 1-butanol to di-n-butyl ether: a next generation biofuel*. Pérez-Maciá, M. A.; Bringué, R.; Iborra, M.; Tejero, J.; Cunill, F. Kazan (Russia), 2015. Poster.

AGRADECIMIENTOS

Durante la elaboración de esta tesis he recibido la ayuda de muchísima gente. Por ello al menos quiero reflejar mi agradecimiento a las personas e instituciones que, de una manera u otra, han contribuido a que esta tesis pudiera ver la luz.

En primer lugar me gustaría dar las gracias al grupo de *Catálisis y Cinética Aplicada*: Fidel, Javier, mis directores de tesis Montse y Roger, Carles y Eliana. Gracias por confiar en mí y darme la oportunidad de formar parte del grupo. Gracias también por todos los consejos y la ayuda prestada. Sobre todo a ti, Roger, por tu ayuda durante aquellas etapas iniciales donde todo eran problemas…como tu bien me has dicho más de una vez "las puestas en marcha siempre son difíciles".

Estos cuatro últimos años no hubiesen sido lo mismo sin mis compañeros de laboratorio. Gracias a Rodrigo, Jordi Badia, Jordi Guilera, Marta y en especial a Carlos por compartir ideas, opiniones, discusiones transcendentales, risas y anécdotas. Compartir despacho/laboratorio con vosotros no podría haber sido más fácil. Seguid siendo igual de *easy-going*!

Una parte importante de esta Tesis (y también una de mis favoritas) no hubiese sido posible sin la inestimable ayuda de David Curcó. Gracias por introducirme y guiarme en el mundo de la química computacional, por todas las buenas ideas, por las clases magistrales y por todo el tiempo dedicado (que no ha sido poco). Siempre es un placer trabajar contigo.

Gracias también a Carlos Alemán, por darme la oportunidad de trabajar con su grupo, *Innovación, Modelización e Ingeniería en (BIO) Materiales*, por todos los consejos y toda la ayuda, por presentarme a Nico van der Vegt y ayudarme a realizar mi estancia en el grupo *Computational Physical Chemistry*, *Technische Universität Darmstadt*. Y, sobre todo, gracias por tenerme en cuenta.

And of course, to finish with the realm of computational chemistry, I can not forget to thank Nico van der Vegt and Francisco Rodriguez-Ropero. Thank you for accepting a newly initiated in the world of computational chemistry, for listening my engineering point of view and help me to understand your theoretical point of view. And thanks to the other members of the *Computational Physical Chemistry Group*, especially to my office mates, Fereshte Taherian-Tabasi and Timir Hajari. We shared some nice moments. Timir! I don't forget it! I still owe you a monument! Understand free energy computations would have been impossible without you!

Quisiera darles las gracias a todos los compañeros y compañeras del departamento de Ingeniería Química por los buenos momentos que hemos compartido. En el transcurso de estos años he encontrado algunas buenas amistades que sé que perdurarán.

Mi interés por el mundo de la investigación comenzó en el grupo de *Residuos, Pirólisis y Combustión* de la *Universidad de Alicante*. Por ello me gustaría dar las gracias a toda la gente que formo parte de aquel grupo y, en especial, a Andrés Fullana. Sin lugar a dudas, sin aquella primera oportunidad, hoy no estaría escribiendo estas líneas.

Finalmente quiero dar las gracias a mi familia. Gracias a mis padres y a mi hermana por estar siempre ahí y apoyarme incondicionalmente en todo. Mención especial quiero hacer de mi madre, sin ella no sería quien soy. Y por supuesto, gracias a ti, Helios, por compartir tanto los buenos como los malos momentos de este largo camino, por tolerar mis cambiantes estados de ánimo, entenderme con una mirada, darme mi espacio cuando lo he necesitado, hacerme reír hasta quedarme sin aliento e infundirme ánimo.

AYUDA FINANCIERA

Esta tesis ha sido financiada por el Ministerio de Economía y Competitividad a través de los proyectos CTQ2010-16047 y MAT2012-34498 y de la beca BES-2011-048815.